Investigation of the Abl regulatory core dynamics by single-molecule FRET and solution NMR

Inauguraldissertation

zur
Erlangung der Würde eines Doktors der Philosophie
vorgelegt der
Philosophisch-Naturwissenschaftlichen Fakultät
der Universität Basel

von

Johannes Schlotte
aus Deutschland

Basel, 2021

Genehmigt von der Philosophisch-Naturwissenschaftlichen Fakultät
auf Antrag von

Prof. Dr. Stephan Grzesiek

Prof. Dr. Daniel Häussinger

Basel, den 15.09.2020

_____

Prof. Dr. Martin Spiess (Dekan)

Thesis Summary

The physiological activity of Abelson tyrosine kinase (Abl) is linked to many cellular processes, such as control of cell growth and survival, oxidative stress response, DNA repair and F-actin-dependent mechanisms. Therefore, Abl requires a tight and fine-tuned regulation under healthy conditions, whereas deregulation leads to disease. In particular, the deregulated fusion protein Bcr-Abl, which results from an abnormal reciprocal translocation between chromosomes 22 and 9, causes chronic myeloid leukemia (CML). The molecular details of Abl's normal regulation and of deregulation in Bcr-Abl are not well understood.

Most knowledge on Abl regulation stems from a combination of structural methods and effects of mutations on kinase activity. It seems clear that in the inactive form, Abl is autoinhibited by interactions within its N-terminal half that consists sequentially of the myristoylated N-cap, the SH3 and SH2 domains, and the catalytic kinase domain (KD). In the autoinhibited state, this part of Abl adopts an assembled conformation where the SH3 and SH2 domains dock onto the KD. In contrast in the active conformation, the SH3 and SH2 domains are thought to disassemble from the KD. Very little is known about this active state, since under normal condition its population is very low and hard to detect by biophysical bulk methods. Furthermore, due to their large size and partially dynamic character, no successful structural or biophysical studies have been reported on full-length Abl or Bcr-Abl.

The central aim of this thesis was to obtain information on the conformational exchange between the inactive and active state of Abl by single-molecule FRET (Förster resonance energy transfer) experiments.

These experiments required Abl molecules labeled by FRET donor and acceptor fluorophores. After exploring many approaches, the labeling could be established by introducing the unnatural amino acid propargyl-lysine into Abl^{core} (consisting of the SH3, SH2 and KD domains) at two positions via amber codon reassignment and a subsequent copper(I)-catalyzed alkyne-azide cycloaddition (CuAAC, 'click') reaction with Alexa Fluor 488 and 647 donor and acceptor fluorophores, respectively. Two different FRET pairs were introduced: Abl^{core}-196*-510* and Abl^{core}-225*-297*, which were positioned to maximally distinguish between different proposed structural models of the activated state.

The single-molecule FRET experiments carried out on these labeled Abl^{core} molecules revealed that the apo form is in dynamic equilibrium on the submillisecond time scale between the assembled conformation and a highly dynamic disassembled conformation of about 30 % population. This dynamic opening has not been observed before and presumably presents the first step in the activation mechanism. Adding the allosteric myristoyl-pocket inhibitors asciminib or GNF-5 to apo Abl^{core} almost completely abolishes this tendency to open, thereby explaining their inhibitory effects. In contrast, addition of type II ATP-site inhibitors disassembles Abl^{core} to a highly dynamic conformation on the submillisecond timescale, which is brought back to a mainly closed conformation by the further addition of the allosteric inhibitors. Such ternary complexes with type II ATP-site and allosteric myristoyl-pocket inhibitors, however, have still a higher tendency for opening than the apo form.

In addition to these main results, the following side projects provided insights into the effects of various factors on the Abl^{core} conformational equilibrium by solution NMR:

1) The KD C-terminal αI-helix adopts a bent conformation in the crystal structure of the assembled myristoyl-bound Abl^{core}, which was proposed to allow docking of the SH2 domain onto the KD. Without myristoyl, the αI-helix is flexible and was proposed to exert an entropic force toward the SH2 domain, thereby assisting Abl activation. We investigated this mechanism by stepwise truncation of the αI-helix and subsequent quantification of the Abl^{core} disassembly and activity. The results show that the length of the αI-helix correlates with the degree of imatinib-induced core opening and the enzymatic activity. This firmly establishes that the αI-helix is an essential part of the disassembly and activation mechanism and that the type II inhibitor-induced opening occurs via an allosteric coupling from αI to the ATP site.

2) The influence of the Abl N-cap and its myristoylation on the core conformation had not been investigated in detail before in solution. Using isotope-labeled, N-terminally myristoylated Abl^{cap} comprising the N-cap, SH3, SH2, and KD (Abl residues 2-531) expressed in insect cells, we showed by NMR that the myristoylated N-cap additionally stabilizes the assembled conformation in solution. Intriguingly, the myristoyl pocket in the kinase domain is not permanently occupied by the myristoyl, but is in exchange with an empty state. Furthermore, we also investigated the non-myristoylated Abl^{cap} G2A mutant, which also adopted mainly the assembled conformation.

3) We observed an interaction of the isolated C-terminal F-actin binding domain with the disassembled Abl^{core} complex. This pushes the equilibrium of the Abl^{core} to a more open state, which is also observed when the interaction between the SH3 domain and the SH2-KD linker is disturbed by point mutations. Thus, the interaction of the FABD with the Abl^{core} presumably involves this interface. This interaction, however, is not strong enough to open the assembled core.

4) We observed a disassembly of the apo form under high (~750 bar) pressure, which is probably due to empty cavities between the individual domains visible in the crystal structure of the assembled core. This pressure-induced conformational switch between the inactive assembled and active disassembled conformation shows that these interdomain cavities are important for Abl regulation.

In summary, we have established single-molecule FRET experiments on Abl^{core} by using unnatural amino acids and bioorthogonal labeling chemistry and further investigated the influence of several factors on Abl's conformational equilibrium by solution NMR. The results give many new insights into the dynamic opening of the Abl regulatory core, which is the essential step in Abl's activation.

The established fluorophore labeling technology will allow to study Abl's dynamic conformational equilibria at the single-molecule level under many conditions. In particular, it should be possible to follow the structural transitions of not only Abl^{core}, but also of full-length Abl and Bcr-Abl both *in vitro* and in living cells. Such experiments should provide a much deeper understanding of the molecular mechanisms causing CML and possibly lead to new therapeutic approaches.

Planned publications resulting from this thesis:

- J. Schlotte, S. Felekyan, J. M. Habazettl, I. Hertel-Hering, R. Sonti, J. Kubiak, O. Hantschel, C. Seidel, S. Grzesiek, Activation and inhibition conformational dynamics of the Abl tyrosine kinase regulatory core investigated by single-molecule FRET (Chapter 2)
- J. Schlotte, A. Maier, J. M. Habazettl, I. Hertel-Hering, R. Sonti, O. Hantschel, S. Grzesiek, The entropic spring mechanism of the αI-helix in the regulation of Abelson kinase (Chapter 3.1)
- J. Schlotte, B. Franke, C. Opitz, I. Hertel-Hering, N.N., S. Grzesiek, Effect of the Abl N-cap and its myristoylation on the Abl regulatory core conformation in solution (Chapter **3.2**)

- J. Schlotte, N.N., S. Grzesiek, NMR reveals an interaction of the Abl's C-terminal F-actin binding domain with the Abl regulatory core influencing its conformational equilibrium (Chapter 3.3)
- J. Schlotte, L. A. Abiko, S. Grzesiek, High pressure shifts the conformational equilibrium of the multidomain Abl regulatory core from the inactive assembled to the active disassembled form (Chapter 4)

Acknowledgments

In the past 5 years, I have been accompanied by numerous people, who made this work possible or even made my life a better one. I am deeply grateful to you all. I would like to spend a few lines to express my gratitude to a few specifically, knowing that I cannot fully do justice to everyone's contributions.

First of all, I thank Prof. Dr. Stephan Grzesiek for giving me the opportunity and the freedom to conduct this work, for providing the environment, his knowledge and experience, critical monitoring, as well as his guidance in research and writing. I highly appreciate his patience and confidence that, in the end, this work will be a success.

I would kindly like to thank Prof. Dr. Daniel Häussinger for accepting to co-referee my thesis, but also for helpful discussions about my project.

I also thank my PhD committee members and collaborators Prof. Dr. Oliver Hantschel and Prof. Dr. Claus Seidel for all the assistance, expertise and critical evaluation of my progress. Oliver Hantschel also shared his tremendous expertise of Abelson kinaseand technical details required to establish the Abl kinase activity assay in our lab.

Claus Seidel and his lab members always warmly welcomed me in Düsseldorf, introduced me to fluorescence spectroscopy, in particular FRET, and generously provided their infrastructure and working hours for a lot of our experiments. I would like to specifically thank Dr. Suren Felekyan for performing so many FRET experiments and analyses and all his thoughts on our project. My gratitude also goes to Dr. Jakub Kubiak, who initially showed me the secrets of fluorophore labeling.

I further want to thank Dr. Timothy Sharpe and Dr. Ludovit "Lajko" Pavel Zweifel from the Biozentrum Biophysics Core Facility for their help with performing FRET experiments that led to important steps forward on the long road to a final Abl FRET sample.

I would also like to thank Dr. Alexander Schmidt and Ulrike Lanner from the Biozentrum Proteomics Core Facility for providing mass spectrometric analysis of various Abl samples.

All members of the Grzesiek lab have been of great importance for my work. Foremost, I would like mention Ines Hertel-Hering. I am deeply grateful for her help in Abl sample production. She taught me how to express and purify Abl, and produced uncountable Abl samples herself. No moody sample stops her and she continues until

she succeeds. Whenever Ines was busy with some other lab magic, Marco Rogowski filled in the gap and helped with cloning and purification of some of the Abl samples. I do not only appreciate the hard work and the great help of the two, but also the amazing atmosphere in the lab. It has always been a pleasure to work in the lab.

Dr. Rajesh Sonti earns my thanks for being my Abl mentor and leading the path for many of my experiments. I thank Dr. Christian Opitz for teaching me how to produce Abl in insect cells and providing help whenever needed with whatever problem in the lab. Those two guys also became great companions for life in and outside the lab. Dr. Bastian Franke was very helpful with production of Abl samples in insect cells for NMR studies. I am thankful for Dr. Hans-Jürgen Sass for invaluable discussions and for asking the right questions, which always led to something new. I am also very happy about Dr. Layara Akemi Abiko's membership in the 'Abl team', and for her contribution to the high-pressure experiments with Abl. Annalena Saskia Maier did a great job in the αI-helix project during her internship, learning incredibly fast, and working independently. I have rarely seen such a talented student at that level of education. Alexandra Meng Dürr earns my gratitude for all her proof-reading of my manuscript.

Furthermore, special thanks go to Dr. Judith Maria Habazettl for her direct contributions to our projects, for caring about my work and future, for all her teaching in NMR, and for all the valuable discussions.

The above mentioned contributions to this work obviously had a huge impact on the success of this work. But that is not the whole story. There is much more to success and that is friendship, family, and love. This cannot be valued high enough and is indispensable, not only for this work. It can also not be seen separately from the lab life, since many of the above mentioned people became very good friends. There is also Johanna Ude, whose friendship I greatly appreciate, and Dr. Vineet Panwalkar, and many more. I am very lucky to make new friendships 'outside the lab' and maintain old ones during the last few years, although having moved to a different country. Here, I would like to express my biggest thanks to my climbing partner and very good friend Laura and to my best friend Nicole. I wish you and your young family all the best for your future.

I cannot put into words how much I owe to my family- my beloved parents and my sister Feli and our dog Socke - for all their love, inspiration, education, support and time.

Last but not least, I cannot be happier for sharing my life with my wonderful fiancée Rebecca. Thank you very much for your unconditional support and love. I also appreciate the warm welcome into her family. The visits to Schänis are always a great pleasure and relaxation from everyday work.

Finally, I would like to wish all those mentioned all the best for their future and that everybody achieves whatever they hope for in life.

Contents

Abbreviations and Symbols

A	FRET acceptor fluorophore
Å	0.1 nm
(V)LF	(very-)low-FRET state
a.u.	arbitrary unit
aa	amino acid
aaRS	aminoacyl-tRNA synthetase
Abl	Abelson tyrosine kinase
Abl^{cap}	aa 2-531 of human Abl 1b isoform
Abl^{core}	aa 83-534 of human Abl 1b isoform
AMP-PNP	adenylyl imidodiphosphate
Arg	Abl related gene
ATP	adenosin triphosphate
AV	accessible volume
Bcr	breakpoint cluster region
CC	coiled coil
CML	chronic myeloid leukemia
CrkL	Crk-like protein
CTK	cytoplasmic tyrosine kinase
CuAAC	copper(I)-catalyzed alkyne-azide cycloaddition
D	FRET donor fluorophore
Da	Dalton
DH	Dbl-homology
DMSO	dimethyl sulfoxide
DNA	deoxyribonucleic acid
DNABD	DNA-binding domain
DOL	degree of labeling
DTT	1,4-dithiothreitol
dynPDA	dynamic photon distribution analysis

E.coli	*Echerichia coli*
EDTA	ethylenediaminetetraacetic acid
E_{FRET}	FRET efficiency
ESI	electrospray ionization
FABD	F-acting binding domain
FCS	fluorescence correlation spectroscopy
fFCS	filtered FCS
FITC	fluoresceine
FLCS	fluorescence lifetime correlation spectroscopy
FPS	FRET positioning and screening
FRET	Förster resonance energy transfer
FT	Fourier transformation
GABD	G-actin binding domain
GEF	guanine nucleotide exchange factor
GFP	green fluorescent protein
GPCR	G-protein-coupled receptor
GST	glutathione S-transferase
HDX MS	hydrogen-deuterium exchange mass spectrometry
HF	high-FRET state
HSQC	heteronuclear single quantum coherence
IC_{50}	half maximal inhibitory concentration
IPTG	isopropyl β-d-1-thiogalactopyranoside
JAK	Janus kinase
KD	kinase domain
LB	lysogeny broth
LC	liquid chromatography
LPP	lampda phosphatase
MD	molecular dynamics
MF	mid-FRET state
MFD	multiparameter fluorescence detection

mRNA	messenger RNA
MS	mass spectrometry
MT	microtubule
myr	myristoylation
ncAA	noncanonical amino acid
N-cap	Abl residues 1-82 (1b isoform)
NES	nuclear export signal
NLS	nuclear localization signal
NMR	nuclear magnetic resonance
NMT	N-myristoyltransferase
PAGE	polyacrylamide gel electrophoresis
PCA	principal component analysis
PDB	protein data bank
PH	Pleckstrin-homology
Ph^+	Philadelphia chromosome detected
PIE	pulsed interleaved excitation
PK	protein kinase
ppm	parts per million
PrK	propargyl-lysine
PTM	post translational modifications
PxxP	proline-X-X-proline motif
PylRS	pyrrolysine tRNA synthetase
R_{DA}	donor-acceptor distance
RDC	residual dipolar coupling
RNA	ribonucleic acid
RTK	receptor tyrosine kinase
SAXS	small-angle X-ray scattering
SDS	sodium dodecyl sulfate
se	sub-ensemble
SH2, SH3, SH4	Src homology domains 2,3,4

sm	single-molecule
Src	Sarcoma tyrosine-protein kinase
STAT	signal transducer and activator of transcription
TB	terrific broth
TCEP	tris(2-carboxyethyl)phosphine
TCSPC	time correlated single-photon counting
TEV	tobacco etch virus
TH	Tec-homology
THPTA	Tris(3-hydroxypropyltriazolylmethyl)amine
TK	tyrosine kinase
TKI	tyrosine kinase inhibitor
TOF	time-of-flight
Tris	Tris(hydroxymethyl)aminomethan
tRNA	transfer RNA
TROSY	transverse relaxation-optimized spectroscopy
UAA	unnatural amino acid
wt	wild-type
Δδ	chemical shift difference
τ_D	donor flourescence lifetime

1 Introduction

1.1 Protein kinases

Enzymes are one of the fundamental biological elements that make life of higher complexity possible by increasing the rates of chemical reactions by many orders of magnitude. An important class of enzymes comprises protein kinases (PKs), which promote the phosphorylation of proteins by transferring a phosphate from a donor (often ATP) to the hydroxyl group of an amino acid residue of a protein. Thereby, PKs transduce signals by regulating protein activity and consequently control various cellular processes such as metabolism, transcription, cell cycle and apoptosis, cell movement and differentiation [1]. Due to their central role in cell function, many PKs are involved in disorders such as cancer, diabetes, as well as in inflammatory, infectious, and cardiovascular diseases [2-5]. Since the first discovery of reversible protein phosphorylation in 1954 [6, 7] and the first purification of a PK [8], hundreds of kinases have been unraveled with the advent of modern cloning and sequencing techniques. The human kinome alone, which is the complete set of human kinases, comprises 518 kinases encoded by 2 % of the total genome [1].

Based on sequence homology, eukaryotic PKs can be classified into 10 major groups, each further differentiated into families and possibly subfamilies [1]. One major group is that of tyrosine kinases (TK) [9]. TK members can be further classified into receptor and cytoplasmic tyrosine kinases.

Receptor Tyrosine Kinases

Receptor tyrosine kinases (RTKs) are associated to the cell membrane, where they mediate cell-to-cell-communication and regulate various cellular processes [10-13]. In particular, formation of the vascular system relies on RTK function [14]. The human kinome includes 58 known RTKs. In all RTKs, the intracellularly located highly conserved TK domain is connected via a single transmembrane helix to an extracellular ligand binding domain. In most cases, the receptor kinase dimerizes/oligomerizes upon ligand binding, which results in an activated kinase, either through trans-autophosphorylation or deactivation of autoinhibition mechanisms of the kinase domain.

Cytoplasmic Tyrosine Kinases

In contrast to RTKs, cytoplasmic tyrosine kinases (CTKs), also referred to as non-receptor tyrosine kinases (NRTKs), are located in most cell compartments, including the nucleus. However, some members of the CTKs can be membrane-associated or function in protein complexes tethered to the cell membrane, where they play important roles in signal cascades triggered by RTKs, G-protein-coupled receptors (GPCRs), and receptors of the immune system [14]. As many other kinases, the CTKs are implicated in many diseases due to their central role in the cell.

The human genome encodes 34 CTKs, which can be further grouped into 10 CTK families based on their overall domain organization (Figure 1.1). All CTKs contain a highly conserved catalytically active kinase domain (KD) which consists of about 300 amino acids. The first crystallized KD was that of cyclic AMP-dependent protein kinase (cAPK) [15, 16]. This basic KD structure has been found in all subsequent kinase structures [17].

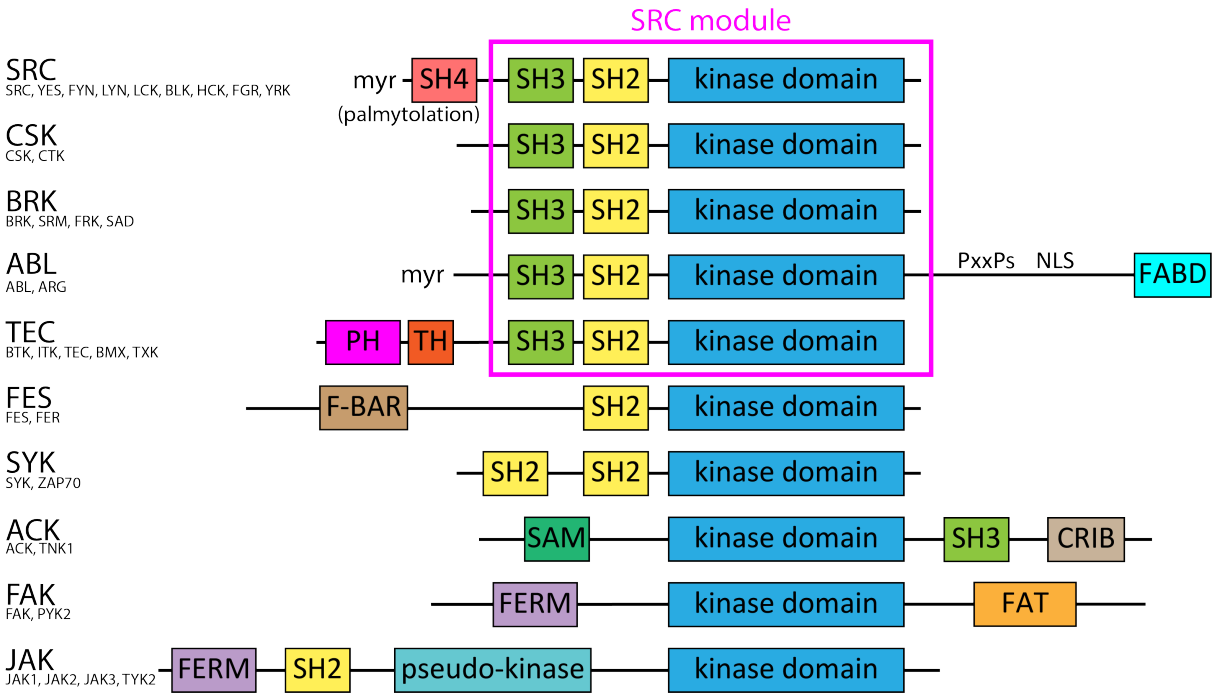

Figure 1.1. Overview of the ten cytoplasmic tyrosine kinase (CTK) families. The schematic domain organization is shown for each of the 10 families. The 'Src module', which comprises an SH3, SH2 and the KD, is highlighted where present. Abbreviations of domain names are as follows: SH2/3/4: Src-homology 2/3/4, myr: myristoylation, NLS: nuclear localization signal, FABD: F-actin binding domain, PH: Pleckstrin-homology, TH: Tec-homology, F-BAR: FCH-Bin-Amphiphysin-Rvs, SAM: Sterile-α-motif, CRIB: Cdc42/Rac-interactive-binding-motif, FERM: 4.1 protein-ezrin-radixin-moesin, FAT: focal adhesion targeting.

Kinase Domain

The KD can be divided into two smaller domains, the so-called N- and C-lobes [18] (Figure 1.5). A catalytic cleft for ATP binding is formed between the two lobes. Importantly, both lobes are connected by a flexible hinge, which allows relative motions between the two lobes [18].

The C-lobe contains a highly flexible loop, the so-called activation loop. This loop can switch between two conformations, a closed (inactive) and an open (active) one [17]. It starts with a highly conserved Asp-Phe-Gly (DFG) motif, whose orientation is crucial for phosphate transfer. In the inactive conformation, the activation loop blocks both ATP and substrate binding [19]. In the active conformation, however, it serves as a platform for substrate binding [20]. A kinase-specific phosphorylation site located on the activation loop plays a central role in kinase activation by stabilizing the active conformation [16, 21-23]. The total number of KD phosphorylation sites and their locations differ among distinct kinases [18].

Non-catalytic domains

While the KD is shared by all CTKs, the different CTK families are classified according to the homology of their KD, but also to the presence of additional structural elements (non-catalytic domains), their respective organization and further unstructured parts (Figure 1.1). These domains and unstructured parts fulfill several important functions such as substrate binding, kinase regulation and cellular localization.

Seven out of ten families have a Src-homology 2 (SH2) domain preceding the KD. It is termed SH2 due to its sequence homology to an originally uncharacterized part in Src (sarcoma) kinase [24, 25]. SH2 domains specifically recognize tyrosine-phosphorylated proteins (or peptides). In several CTKs, SH2 domains have been described to enhance kinase activity by forming a specific SH2-KD interface [26]. More than one hundred proteins from various protein classes have been identified in humans that contain one or more SH2 domains [27]. Among them are kinases (e.g. Src and Abl families) and adaptor proteins (e.g. CrkL) [28]. Due to their occurrence in diverse proteins, SH2 domains have been designated as ‘modular building blocks’ [25].

Five CTK families (Src, Abl, Brk, Tec, Sck) share the same core domain architecture, which comprises an SH3 domain preceding the SH2-KD arrangement.

This is also referred to as the ‘Src module’. SH3 (Src-homology 3) domains, like SH2 domains, are modular binding proteins present in various proteins such as CTKs, myosin, and cortactin. The SH3 domains specifically bind proline-rich motifs (in particular PxxP) in proteins [29, 30]. In some cases, they are important for kinase regulation by forming intramolecular interactions such as in Src [31, 32] and Abl [33].

Other non-catalytic domains in CTKs mediate membrane localization through phospholipid binding (PH and FERM domains), F-actin binding (FABD) [34] or further protein-protein interactions (SAM and CRIB domains).

1.2 Abelson tyrosine kinase (Abl)

Abl family

The Abl family of the CTKs comprises two members, Abl and its paralogue Arg (‘Abl related gene’), which are encoded by the ABL1 and ABL2 genes, respectively [35]. Abl and Arg ‘are found in all metazoans, which suggests that their structure and function were fixed relatively early in tyrosine kinase evolution’ [35]. They are ubiquitously expressed and related to various cellular processes, like cell motility and morphogenesis, neuronal and immune system development, genotoxic stress and apoptosis [36, 37].

Both Abl and Arg are required for normal development of the organism [35, 38]. The absence of Abl in mice leads to several defects such as low viability [39, 40], osteoporosis [41], cardiac abnormalities [42, 43], and reduced numbers and responsiveness of B- and T-cells [44-46], whereas missing Arg leads to less severe neuronal effects, but otherwise normal development [47, 48]. However, double knockout in mice leads to embryonic lethality [47].

Malfunction of Abl has been attributed to several diseases. The main driver of Abl research is its role in different forms of leukemia in humans, including chronic myelogenous leukemia (CML) and acute lymphocytic leukemia (ALL), and also some forms of T-cell acute lymphoblastic leukemia (T-ALL), and acute myeloid leukemia (AML) [38, 49-51]. Furthermore, there is evidence that aberrant function of Abl plays a role in solid tumors, neurodegenerative diseases, inflammatory disorders and microbial pathogenesis [37, 51, 52].

Domain organization

Both Abl and Arg share the above described SH3-SH2-KD cassette with high sequence identity (>90 %) [37] (Figure 1.2). Although these parts of the Abl proteins are structurally similar to Src kinase [33], they share only 52 % sequence identity with Src in the KD and 37 % in the SH3-SH2 domains [37].

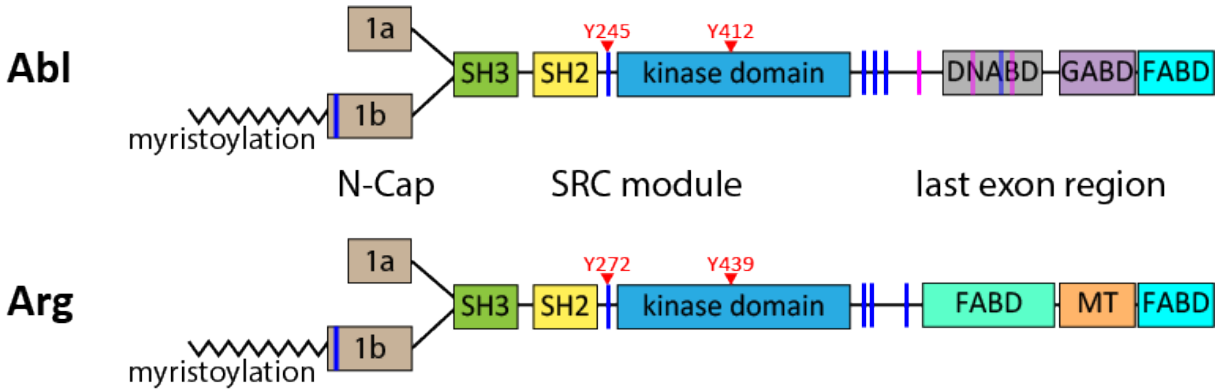

Figure 1.2. Overview of the structural elements and organization of Abl and Arg paralogues. Both paralogues share the highly similar N-terminal half of the protein, which comprises the 'Src module', i.e. SH3, SH2 and KD, and about 80-100 N-terminal residues referred to as the N-cap, which exists as two different splice variants, 1a and 1b. The 1b isoform is myristoylated in both, Abl and Arg. Two important phosphorylation sites, which are located in the activation loop and SH2-KD linker, respectively, are marked with red triangles. Both paralogues contain a PxxP motif, which mediates protein-protein interactions, in the 1b N-cap and an imperfect, but nevertheless important, PxxP motif in the SH2-KD linker (shown as blue vertical bars). The C-terminal halves of the protein differ to a larger extent. The C-terminal half, named 'last exon region', of Abl harbors a DNA binding domain (DNABD), a G-actin binding domain (GABD), an F-actin binding domain (FABD), four PxxP motifs, and three nuclear localization signals (NLS; shown as magenta vertical bars). Arg lacks the NLS, DNABD, and GABD, but comprises a microtubule (MT) binding domain and a second FABD, which differs slightly from the other one.

N-cap – two splice variants

The N-terminus of both Abl genes is expressed as two different splice variants [53]. The so-called N-cap of isoform 1b of Abl is myristoylated at Gly-2 and 19 amino acids longer than isoform 1a. The same applies to Arg. Interestingly, the expression level of the Abl isoform 1b is rather constant in different tissues and cell types in mice, whereas that of 1a may vary by a factor of 10 [53].

Last exon region

The long C-terminal tail, also called 'last exon region' (Figure 1.2), which spans half of the protein and contains several functional units, is unique to the Abl family [35, 36, 38]. In Abl, this C-terminal tail bears an F-actin binding domain (FABD) [34, 54], a G-actin binding domain (GABD) [54], nuclear localization signals (NLS) [55], several

PxxP sequences for protein-protein interactions [56], and a DNA binding region (DNABD) [57-60].

Nuclear localization

Early studies on the subcellular localization of Abl have shown that it is located in both the cytoplasm and the nucleus [61], but in different proportions with respect to the cell type [62]. Additionally, three independently acting NLS [63, 64] and a DNA binding region [57, 59, 60] have been identified in the C-terminal tail of Abl. Furthermore, Abl has been found to play a role in several nuclear processes related to DNA repair, cell proliferation, cell-cycle control and apoptosis [35, 36, 38, 62, 65]. Several binding partners have been identified that are known DNA-repair mediators [35]. Abl overexpression leads to arrest of cell growth [66] and apoptosis [67].

Of note, structural analysis of the FABD has shown that a nuclear export signal (NES) located within the FABD sequence, which was proposed based on sequence analysis, cannot be functional unless the FABD unfolds, for which there is no evidence so far [34].

Protein-protein interaction

Abl features several protein interaction sites, which are crucial for its function in signal transduction processes. As mentioned earlier, on the one hand, protein-protein interactions are possible through binding of tyrosine-phosphorylated proteins to the Abl SH2 domain or, vice versa, binding of the SH2 domain of another protein to a phosphotyrosine in Abl [35]. On the other hand, interactions can be mediated by binding of SH3 domains to PxxP motifs and proline-rich amino acid stretches [68-71]. This can be again either binding of the Abl SH3 domain to a PxxP motif of a partner protein or binding of an SH3-domain-containing protein to one of the four C-terminal Abl PxxP motifs [29, 35]. Notably, the Abl SH3 domain also interacts with an additional intramolecular PxxP motif in the SH2-KD linker. Identified functional interaction partners of Abl are, among others, the Abl interactor proteins Abi1 [72] and Abi2 [73], the Ras and Rab interactor Rin1 [74], and adaptor proteins such as Crk, CrkL, and Nck1 [50, 56, 75-80].

Although a number of interactions of Abl with partners were described, their functionality is not always clear. The Abi proteins bind to the Abl SH3 domain as well as to Abl C-terminal PxxP motifs [72, 73]. On a functional level, they were reported to

inhibit, but strikingly also sometimes to enhance, Abl kinase activity and v-Abl (a viral form of Abl) transforming activity in certain situations [72, 81-84]. Recently, Abl•Abi signaling was associated with regulation of synaptic development [85]. Abi1 was also linked to acquired drug resistance in Bcr-Abl-induced chronic myeloid leukemia (CML) [86], where Bcr-Abl is a fusion protein, whose expression leads to CML (see Chapter "Bcr-Abl" of this introduction).

Rin1 is an activator of Abl which is thought to work by binding of a Rin1 PxxP motif to the Abl SH3 domain and eventually, after subsequent Abl-mediated Rin1 phosphorylation, to the Abl SH2 domain, thereby stabilizing an activated conformation of Abl [74, 87]. Interestingly, two new therapeutic approaches for the treatment of CML are based on the concept to target and interrupt the Abl-Rin1 interaction. In one case, small molecules were screened [88] to bind Rin1 and consequently exclude binding of Rin1 to Bcr-Abl. In another case, an SH3 domain that was modified for tighter binding was used to capture Rin1 [89]. Both approaches represent alternatives to the classic therapeutic strategy of directly inhibiting the kinase activity by small molecules.

Adaptor proteins such as Crk, CrkL and Nck1 have no catalytic function on their own. However, they are indispensable in cellular signaling processes, because they recruit and mediate signaling assemblies with several signaling proteins and thereby temporarily and spatially control signal transduction pathways [90-92]. Adaptor proteins can be classified into two groups [92, 93]. Members of the first group are composed of domains that bear phosphotyrosine sites for binding other proteins, but can contain further domains. The other group contains proteins which are only built from SH3 and SH2 domains in a modular way, with which they bind other signaling proteins. The first described example of an adaptor protein is Crk [50, 79]. It occurs as two different splice forms CrkI and CrkII, as well as Crk-like (CrkL), which is translated from a different gene, but shares high sequence similarity with CrkII [77, 94]. CrkI consists of one SH2 and one SH3 domain, whereas CrkII and CrkL bear a second SH3 domain, which differs in sequence from the other SH3 domain.

CrkL has been described to be constitutively phosphorylated in human CML cells [80, 95, 96] and absolutely necessary for oncogenic transformation by binding to Bcr-Abl [50, 97-99]. However, CrkII is not necessary for oncogenic transformation [50]. A structural study revealed different domain organizations and SH3-SH2 accessibilities for both proteins and thereby explained the different preferences for binding of CrkII and CrkL to PxxP motifs of Bcr-Abl [80]. Notably, the phosphorylation level of CrkL is

used to predict the clinical outcome in CML patients [100] and as a general biomarker for Bcr-Abl activity in cells [101, 102].

F-actin interaction

An F-actin binding domain (FABD) is located at the end of the Abl C-terminus (Figure 1.2) through which Abl can directly bind and interact with the cytoskeleton [34, 103]. Abl kinase activity seems to affect the F-actin cytoskeleton. This is supported by reports showing that Abl is involved in membrane ruffling, filopodia formation, neurite extension and cell migration [104-107]. Reversely, it has been shown that binding to F-actin inhibits the kinase activity of Abl *in vitro* and *in vivo* [108]. However, the molecular mechanism for this allosteric inhibition is still unclear.

The solution structure of FABD has been determined by NMR [34]. It forms a four-helix bundle stabilized by a mainly aliphatic core. Two of the helix-connecting loops are highly flexible. Despite low sequence similarity with other FABDs such as the vinculin head and tail domain, the dimerization and adhesion modulating domain of α-catenin, the vinculin binding domain of talin, and the focal adhesion targeting domain of focal adhesion kinase, all these structures are surprisingly similar [34].

The Arg C-terminal domain organization

In contrast to the highly similar N-terminal halves of the paralogs Abl and Arg, their C-terminal halves differ in their domain organization (Figure 1.2). Arg does not contain any nuclear localization or export signal, which is consistent with its primary cytoplasmic localization [109, 110]. However, Arg contains additionally a second F-actin binding domain (FABD), which differs in sequence from the first, and a microtubule (MT) binding domain [35]. This allows Arg to directly bind and bundle F-actin by binding to two F-actin molecules [109] and to modify the cytoskeleton by F-actin-MT crosslinking [111]. Both are required for the formation of lamellipodial membrane protrusions [35, 109, 111].

Implications of Abl kinases in cancer

Chromosomal abnormalities were first linked to human cancers in 1960, when the so-called ‘Philadelphia Chromosome’ was discovered in cells from chronic myeloid leukemia (CML) patients (Figure 1.3) [50, 112, 113]. This abnormal chromosome is the result of a reciprocal translocation between chromosomes 9 and 22 [114]. The

molecular consequence is the expression of the fusion protein Bcr-Abl, which consists of Abl with the N-cap replaced by the breakpoint cluster region protein (Bcr) [115-118]. Thereby, an important regulatory element of Abl, the myristoylation, is lost (Figure 1.3).

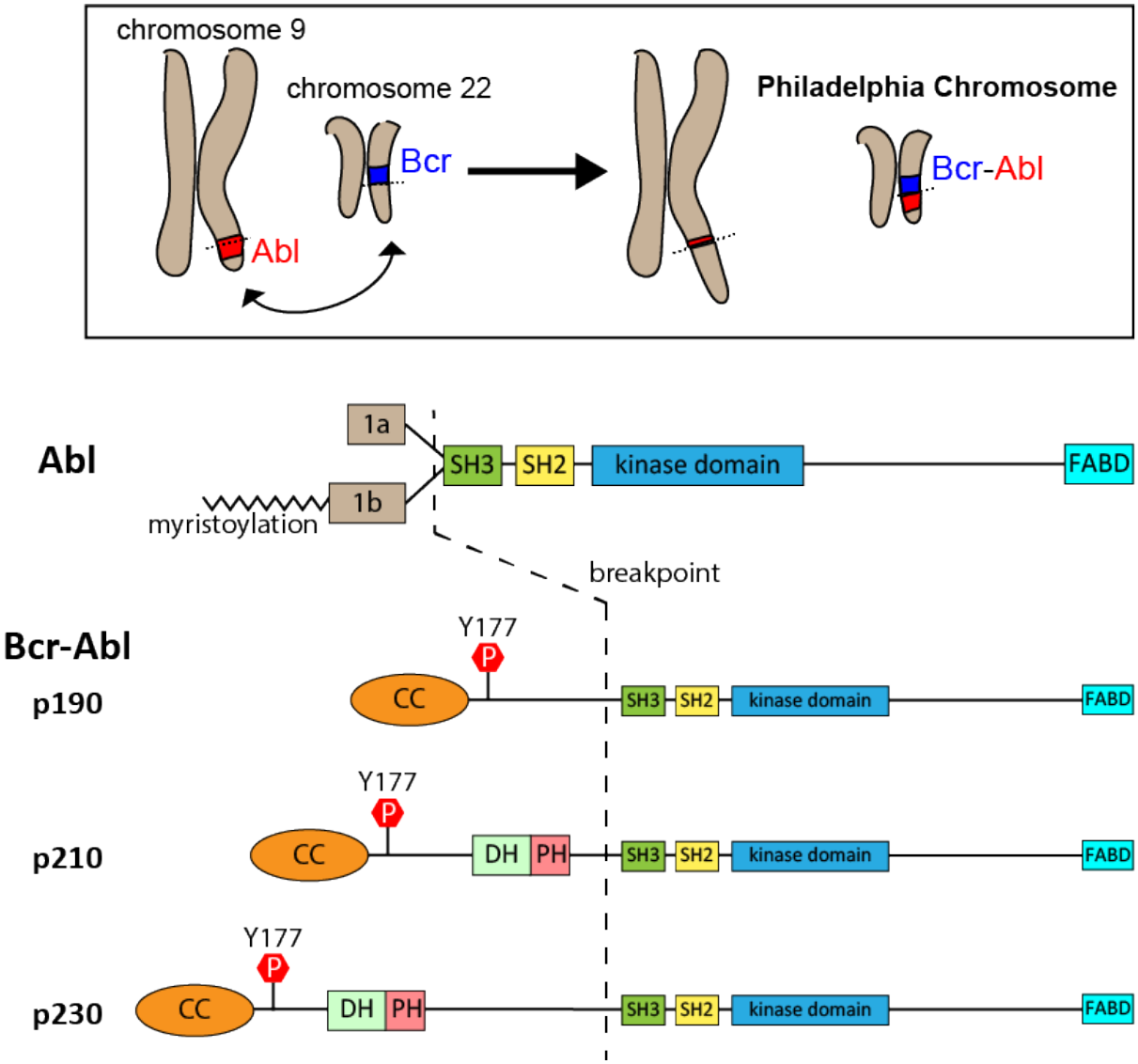

Figure 1.3. The Philadelphia chromosome and its molecular consequences. Top: The pathological Philadelphia chromosome results from a reciprocal chromosomal translocation between chromosomes 9 and 22. The breakpoint of chromosome 9 is located within the Abl gene and the one of chromosome 22 is found within the breakpoint cluster region (Bcr). The molecular consequence is the fusion protein Bcr-Abl, which leads to different types of leukemia. Bottom: overview of the structural organization of the Bcr-Abl fusion proteins resulting from the Philadelphia chromosome. The breakpoint within Bcr can vary and results in three different forms of Bcr-Abl: p190, p210, and p230. The numbers correspond to their respective molecular weights. All three forms contain an N-terminal coiled coil (CC) domain, which promotes dimerization, and an important phosphorylation site at Tyr-177. Additionally, a DH-PH module (DH: Dbl-homology domain; PH: Pleckstrin-homology domain) is present in the two longer Bcr-Abl variants. Notably, the three Bcr-Abl variants are typical for different forms of leukemia.

Bcr-Abl is not the only Abl fusion protein identified in humans. Several rare chromosomal translocations were identified, which lead to fusion of Abl with NUP214,

ETS variant 6 (ETV6), echinoderm microtubule-associated protein-like 1 (EML1), zinc finger MIZ-type containing 1 (ZMIZ1), RCSD1, the splicing factor SFPQ, forkhead box P1 (FOXP1), and sorting nexin 2 (SNX2) [38, 49, 50]. Also a fusion of Arg to ETV6 is known. These different fusions are related to different types of cancer, explicitly CML, neutrophilic-CML, B-cell acute lymphoblastic leukemia (B-ALL), T-cell acute lymphoblastic leukemia (T-ALL), acute myeloid leukemia (AML), refractory anemia with excess blasts (RAEB), and myeloproliferative neoplasms (MPN) [38, 50].

Besides its long known role in various types of leukemia, there has been increasing evidence over the past decade that Abl also plays a role in solid tumors [38, 119, 120]. While Abl fusion proteins lead to leukemias, in solid tumors activated wt Abl and/or Arg facilitate tumor progression. Activated Abl and Arg proteins were identified in various tumors such as melanoma, gastric, liver, prostate, colon, breast, ovary, pancreatic, and cervical cancers [120]. The activation of Abl originates from enhanced Abl/Arg expression, increased kinase activity due to external stimuli or loss of negative regulators, and genomic alterations, like specific amplification, somatic mutations, and increased mRNA levels [38, 119, 120].

Chronic myeloid leukemia

Patients with chronic myeloid leukemia (CML) show uncontrolled proliferation of the full lineage of bone marrow myeloid cells [121]. This first phase of the disease is called the chronic phase and typically lasts 3-5 years. This is followed by a less clearly defined accelerated phase and eventually progresses to a blast crisis, which is characterized by extensive proliferation of ‘blast cells’ (immature cells) in the peripheral blood and bone marrow, as well as the blocking of hematopoietic stem cell differentiation [117, 121, 122].

Bcr-Abl

The fusion protein Bcr-Abl is the main driver of transformation in CML patients. In fact, three different forms of Bcr-Abl arise from different breakpoints in the *bcr* gene. Besides Bcr-Abl p210, which is found in 90 % of CML patients, there is Bcr-Abl p185 and, less frequently, Bcr-Abl p230 [123]. The numbering suffix indicates the molecular weight of the gene product in kDa (Figure 1.3). As already mentioned, Bcr-Abl p210 is detected in nearly all patients with CML. Furthermore, it is also present in about one third of all B-ALL cases, which are Ph^+, i.e. the Philadelphia chromosome was

detected in the cancer cells. Bcr-Abl p185 is present in the remaining two third of Ph^+ B-ALL cases and Bcr-Abl p230 is mainly associated with neutrophilic-CML [50, 123]. Thus, there is a certain correlation between the three Bcr-Abl forms and specific different clinical consequences.

Several interrelating molecular mechanisms contribute to the Bcr-Abl-driven transformation in CML. Observed effects of the Bcr-Abl fusion are increased Abl kinase activity and subsequent substrate phosphorylation, downstream signaling pathway activation by Bcr moieties and strong Abl auto-phosphorylation. The latter renders Abl a binding partner for phosphotyrosine-binding proteins and thereby initiates multiprotein complexes serving as starting points for signaling cascades [50].

A coiled-coil (CC) oligomerization domain is located at the N-terminus of all three Bcr-Abl proteins. This CC was found to activate Abl kinase by oligomerizing Bcr-Abl molecules [124-126], thereby possibly increasing the auto-phosphorylation of critical tyrosine residues, which results in an active Abl kinase conformation. A potential therapeutic strategy against CML was developed and constantly improved over the last years. It involves targeting the CC dimerization interface by a peptide which mimics the CC interface-forming helix and thereby blocking CC-mediated Bcr-Abl oligomerization [127-131].

The Bcr portion of Bcr-Abl p210 further contains a Dbl-homology (DH) and Pleckstrin-homology (PH) tandem domain. Bcr-Abl p185 lacks the DH-PH unit, which could account for the different disease outcomes of the two Bcr-Abl proteins. Recently, the structures and function of the DH-PH tandem units have been elucidated and biophysically characterized [132]. Thus, the structures of all well-folded parts of Bcr-Abl polypeptide sequence are solved by now. DH-PH domains are canonical motifs of Dbl-family guanine nucleotide exchange factors (GEF) for Rho GTPases. The DH domain mediates the GEF activity [132, 133], where the PH domain has lipid-binding capacity and thereby mediates membrane localization [134]. In the context of the DH-PH unit, the PH domain was also reported to affect DH GEF activity [135]. However, in Bcr-Abl neither significant DH GEF activity or binding to different RhoGTPases, nor PH-mediated membrane localization could be observed [132]. Nonetheless, in particular the PH domain seems to play a role in mediating p210-specific signaling by altering the subcellular localization of Bcr-Abl [132].

As mentioned above, one mechanism by which Bcr-Abl promotes cell proliferation and apoptosis inhibition is the activation of various downstream signaling pathways.

Among others, phosphorylated Y177 (pY177) of Bcr-Abl plays an important role in oncogenic transformation [136, 137]. By the binding of adaptor protein Grb2 to pY177, several important oncogenic pathways get either activated or disturbed. These are e.g. the pathways of mitogen-activated protein kinase (MAPK), PI3K, and JAK/STAT [50].

Bcr-Abl targeting drugs

Due to their high structural conservation it is very difficult to target specific kinases by drugs. Off-target binding is prevalent and usually leads to severe and inacceptable side effects in the clinic [138-141] by affecting unwanted pathways.

For many decades, CML patients were treated by chemotherapy, interferon α therapy or allogenic bone marrow transplantation, which represents the only curative therapy [142]. However, all these therapies were suffering from low success rates and possible severe side effects including high mortality rates in the case of bone marrow transplantation [142-147].

At the end of the 1990's, the development of a small molecule that effectively inhibits Abl with high specificity [146, 148, 149] revolutionized CML drug development and cancer research in general [150]. This compound, named imatinib (Figure 1.4), was the first tyrosine kinase inhibitor (TKI) approved by the US Food and Drug Administration (FDA). It is called the 'magic bullet' due to its tremendous success in CML therapy. Imatinib binds to the ATP-binding pocket of Abl, thereby acting as an ATP-competitive inhibitor.

Imatinib

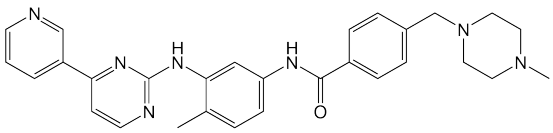

Dasatinib

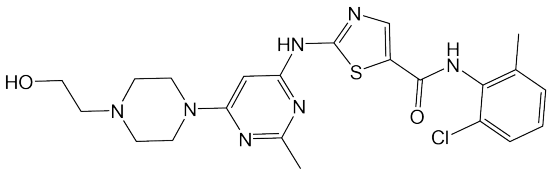

Nilotinib

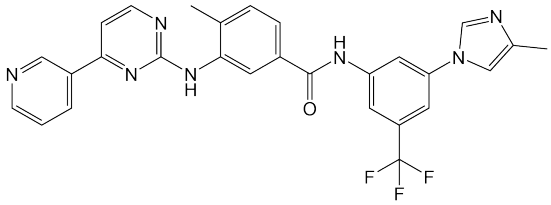

Ponatinib

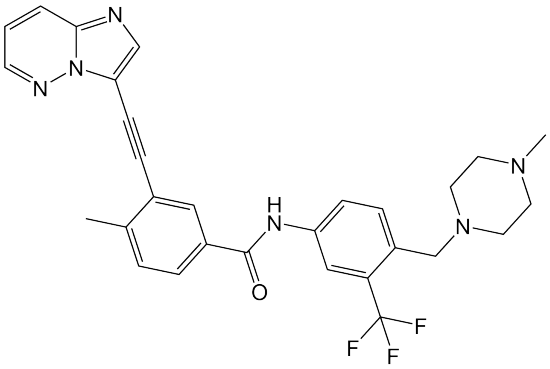

Bosutinib

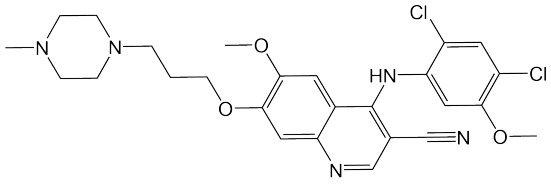

Asciminib

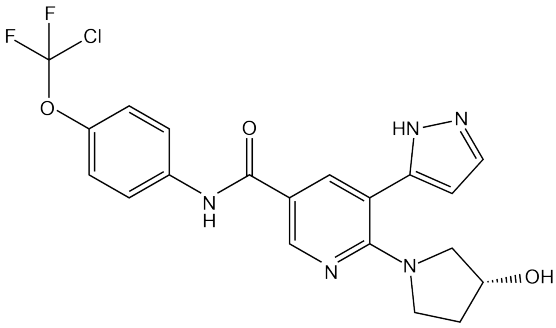

GNF-5

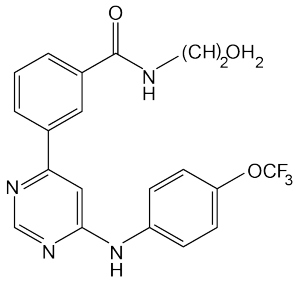

Figure 1.4. Chemical structure of several FDA-approved ATP-competitive Bcr-Abl drugs and two, not yet approved, allosteric inhibitors. Shown are the first-generation inhibitor imatinib (brand name Gleevec/Glivec®, Novartis), the second-generation inhibitors nilotinib (Tasigna®, Novartis), bosutinib (Bosulif®, Pfizer), and dasatinib (Sprycel®, Brystol-Myers Squibb), the third-generation, and gatekeeper-targeting inhibitor ponatinib (Iclusig®, Ariad Pharmaceuticals), as well as the allosteric inhibitors GNF-5 and asciminib (Novartis), the latter is currently undergoing clinical trials with promising results [151].

Early after the development of imatinib, Bcr-Abl mutations, which reduce imatinib sensitivity to Abl, were discovered in cell lines *in vitro* [152] and, shortly thereafter, also in patients with CML [153]. While resistance mechanisms exist that are independent of Bcr-Abl mutations such as Bcr-Abl overexpression or the activation of other oncogenic pathways, clinical drug resistance is most commonly caused by Abl mutations, which alter drug binding [101, 121, 154-157].

Most imatinib-resistant mutations are found in the KD and can be related to drug binding. They act either directly through blocking space that is usually occupied by imatinib, or by eliminating critical hydrogen bonds that are required for imatinib binding, or they act indirectly by destabilizing the conformation in which imatinib binding occurs [158]. The most prominent one is the so-called 'gatekeeper' mutation T315I (isoform 1a numbering). In this case, the hydroxyl group of the threonine forms a hydrogen bond with imatinib, and consequently its absence, as well as the introduction of the bulkier residue isoleucine, leads to a strong increase of the IC_{50} of imatinib and ergo insensitivity of Abl towards imatinib.

Further imatinib-resistant mutations appear in the P-loop or alternatively named Gly-rich loop, which is directly involved in imatinib binding, in the activation loop, whose conformation plays a role in imatinib binding, and other parts of the kinase [150]. Interestingly, imatinib-resistant mutations are also located in distinct parts of Bcr-Abl that are far away from the ATP-binding pocket, such as the N-cap, SH3 and SH2 domains [159, 160].

The occurrence of imatinib resistance drives the continuous search for alternative drugs to overcome these therapeutic setbacks. This has led to the development of the second generation Abl inhibitors: nilotinib, dasatinib and bosutinib (Figure 1.4) [150, 161]. These drugs are efficient against most imatinib-resistant mutants. Interestingly, all of them show distinct sensitivities against the different mutations [101, 150]. However, none of them turned out to be effective against the gatekeeper mutant.

Therefore, a third-generation of TKIs was developed that specifically target the gatekeeper mutant. Among those is ponatinib (Figure 1.4), which is a potent inhibitor of the gatekeeper mutant, but can only be used with restrictions due to its severe and recurrent side effects [162].

In order to overcome the drawback of ATP-pocket point mutations and the high sequence conservation among TKs in this part of the protein, which often results in unwanted off-targets of newly developed inhibitors, researchers seek for alternatives to target Bcr-Abl. One currently promising option is to target the myristoyl (allosteric) pocket. Since the myristoyl is missing in Bcr-Abl as a result of the protein fusion, one regulatory mechanism is lost. As discussed in more detail later, myristoyl binding induces a bend of the C-terminal αI-helix and thereby stabilizes the auto-inhibited conformation of the Abl core [33].

One such recently discovered allosteric inhibitor targeting the myristoyl pocket is asciminib (formerly ABL001) (Figure 1.4) [102, 163]. Importantly and in contrast to an earlier developed preceding class of allosteric inhibitors such as GNF-2 and GNF-5 (Figure 1.4) [164], asciminib is also potent against the gatekeeper Bcr-Abl mutant. Currently, asciminib shows promising results in clinical trials with heavily, but unsuccessfully, pretreated patients [151].

Of note, myristoyl pocket mutations can render asciminib ineffective as well [101, 102, 165]. However, dual targeting of Bcr-Abl is now possible due to the distinct mechanisms of action of ATP-competitive and myristoyl-allosteric inhibitors: asciminib was tested in combination with nilotinib, imatinib, dasatinib [102], and ponatinib [101]. The combinatorial approach is a promising solution for treatment of so far untreatable compound mutants, i.e. mutants that bear two or more drug resistance mutations. Although asciminib is effective against most single mutations, it remains insensitive to several compound mutations [101]. The combination of asciminib and ponatinib is potent against these compound mutations at much lower ponatinib concentrations, which potentially reduces its toxicity [101].

Despite the anticipated success of the new anticancer drug asciminib, it is reasonable to assume that there will be remaining patients with still untreatable Bcr-Abl mutants or drug resistances, mediated by other mechanisms than point mutations, as it has always been before. Thus, there is ongoing need for development of Bcr-Abl drugs and divergent therapeutic strategies.

1.3 Abl structures and known regulation mechanism

The preceding chapters demonstrated the importance of Abelson kinase activity in cancer research and underlined the ongoing demand for new drug development. Many of the abovementioned drug developments have been strongly assisted by the knowledge about structural features and molecular behavior of Abelson kinase. Structures have been solved for all structured parts Abl and Bcr-Abl individually and for assemblies of the Abl core, which comprises the N-cap, SH3, SH2 and KD, in complex with various inhibitors. However, a structure of full-length Abl or even Bcr-Abl is not available. In the following chapters, I will describe the known structures of the Abl core, the structured N- and C-terminal elements of Abl/Bcr-Abl, i.e. the CC, PH, DH, and FABD domains.

Abl kinase domain

The kinase domain (KD) of Abl is the catalytically active domain and therefore its structure has been studied extensively. Knowledge about the active-site architecture is invaluable for drug design. Over 50 structures of the Abl KD in complex with various ligands, e.g. potential drugs, are available in the protein data bank (PDB).

The Abl KD resembles the classical kinase domain structure (Figure 1.5), as anticipated from the high structural conservation of kinases. It can be divided into a smaller N-lobe and a bigger C-lobe, both separated by the ATP-binding pocket. The N-lobe is composed of five stranded β-sheets and one α-helix, which is named αC-helix. An important feature of the N-lobe is the P-loop (phosphate-binding-loop), sometimes also called glycine-rich (Gly-rich) loop, which coordinates ATP binding. The C-lobe is mostly α-helical. It carries several indispensable structural elements.

The so-called activation loop of the C-lobe, which starts with a crucial Asp-Phe-Gly (DFG) motif, is highly dynamic [166], but nevertheless exists predominantly in two distinct conformations in most ligand-bound complexes. It either adopts the ‘active’ open conformation, where the activation loop is oriented towards the αC-helix, or the Abl unique ‘inactive’ closed conformation, where the activation loop is oriented towards the P-loop [150]. In the ‘active’ conformation, the aspartate of the DFG motif is oriented ‘in’ or ‘flipped’ towards the ATP-pocket, whereas in the ‘inactive’ conformation, the aspartate orients ‘out’ of the ATP pocket and the activation loop somehow blocks the ATP pocket [167]. Inhibitors of Abl are categorized as ‘active’ conformation binders (type I inhibitors, e.g. dasatinib [168]) or ‘inactive’ conformation binders (type II inhibitors, e.g. imatinib [169]).

A unique structural feature of the Abl KD is a deep hydrophobic pocket at the bottom of the C-lobe, into which a myristoyl moiety or allosteric inhibitors such as asciminib can bind [33] (Figure 1.6). It is formed by four C-lobe helices, including the so-called αI’-helix, which results from a kink of the C-terminal αI-helix. This kink is induced by myristoyl binding. The newly formed helix at the C-terminus is named the αI’-helix. In crystal structures of the myristoyl-free KD, the αI-helix adopts an extended conformation [169, 170]. In solution, however, the αI’-helix is highly flexible in the apo protein, as evident from NMR [171, 172].

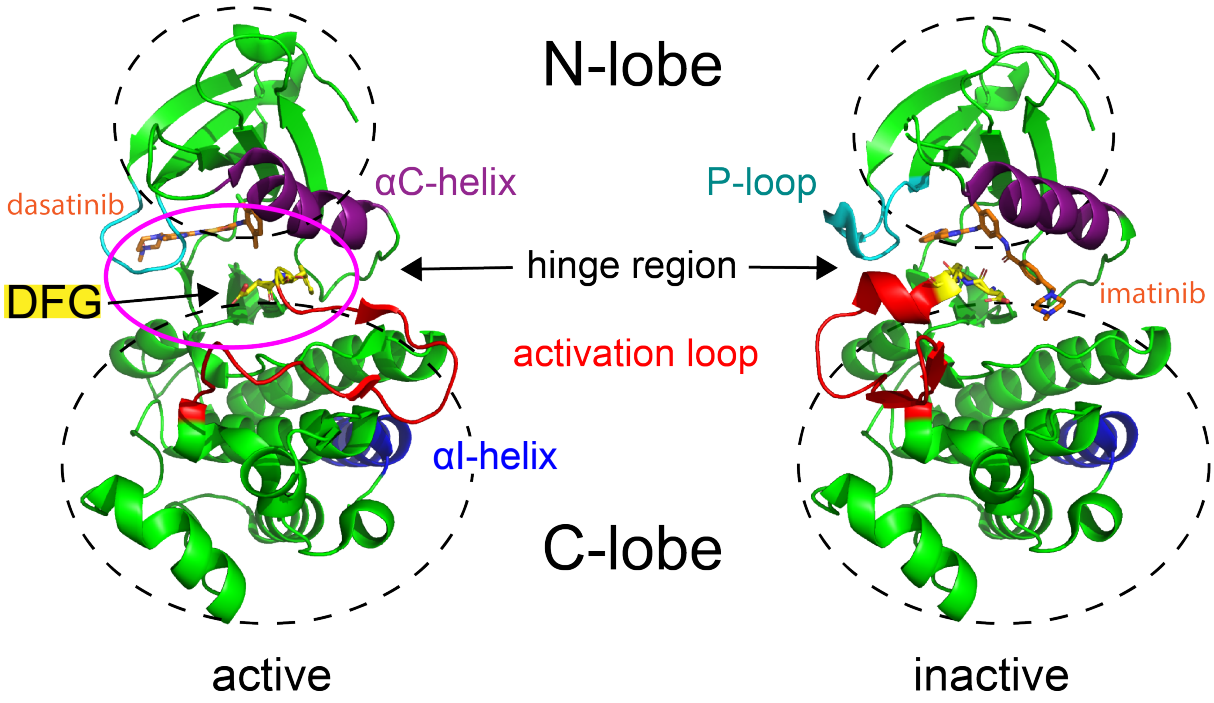

Figure 1.5. Structures of the Abl kinase domain (KD) in the active and inactive conformation. The KD consists of two subdomains (highlighted by dashed circles), the smaller N-lobe (top) and the larger C-lobe (bottom), which are flexibly connected by the 'hinge region'. The ATP-binding pocket is located between the two domains in the vicinity of the hinge region. The positioning of the N-lobe's αC-helix (purple) and P- loop (light blue) as well as the C-lobe's activation loop (red) is crucial for ATP binding and hence enzymatic turnover. The activation loop starts with the important DFG motif (yellow sticks). The C-lobe further contains the C-terminal αI-helix (blue), which is important for allosteric regulation. Left: the active conformation of the dasatinib·Abl KD complex (PDB code 2GQG [168]). Right: the inactive conformation of the imatinib·Abl KD complex (PDB code 2HYY [167]). Abl KD and ligands are shown in cartoon and orange stick representation, respectively.

Assembled autoinhibited Abl core

The intrinsic high catalytic activity of the isolated Abl KD is strongly reduced in the presence of the SH3 and SH2 domains [173, 174]. Native regulation is achieved with a construct spanning the myristoylated N-cap, the SH3 and SH2 domains, and the KD [175]. Notably, the C-terminal half is not required, as demonstrated by *in vitro* kinase assays, where deletion of the C-terminal half did not increase the kinase activity [175]. Thus, the N-terminal half of Abl is called the regulatory core. The structure of this regulatory core in complex with the type I inhibitor PD166326 was solved by X-ray crystallography [33, 173]. The regulatory core forms a tight assembly, wherein the SH3 and SH2 domains dock onto the back of the KD N- and C-lobes, respectively (Figure 1.6). This structure is highly similar to the autoinhibited form of Src kinase [32], although Abl lacks a critical phosphotyrosine of the Src C-terminus, which binds to the SH2 domain and thereby stabilizes the assembled conformation of Src. However, this clamping mechanism in Src appears functionally replaced by the N-terminal

myristoylation in Abl [176], which binds to a pocket at the kinase bottom, as described above. The resulting kink of the αI-helix allows the SH2 to dock tighter to the KD C-lobe. This conformation is stabilized by a network of hydrogen bonds between the SH2 and the KD C-lobe [33].

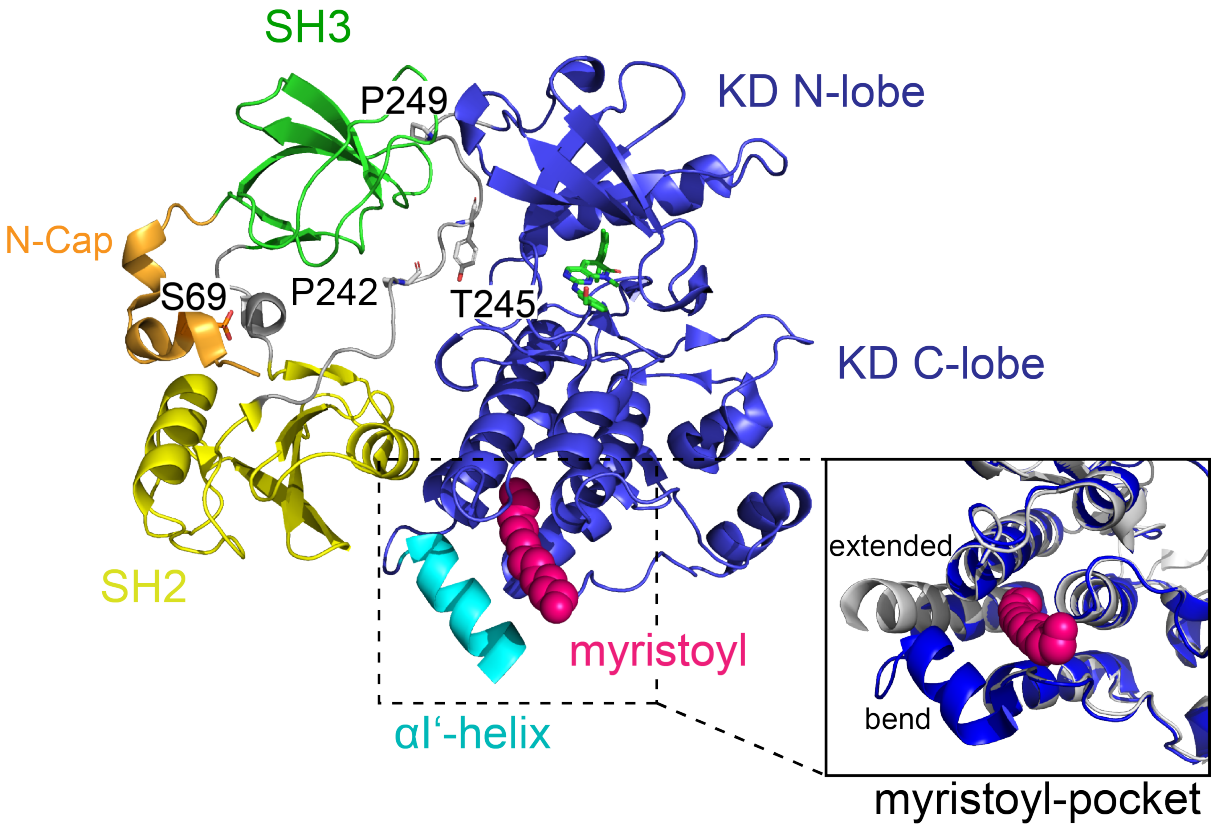

Figure 1.6. Structure of the autoinhibited assembled Abl core (PDB code 2FO0 [173]) in complex with the inhibitor PD166326 (green sticks). The SH3 (green) and SH2 (yellow) domains dock tightly onto the KD (blue) N- and C-lobe, respectively. This assembly is stabilized by three linchpins: i) the interaction of the SH2 domain with the KD C-lobe, ii) interaction of the SH3 domain with the proline-rich SH2-KD linker and consequently docking onto the KD N-lobe, and iii) the clamp around the SH2 domain, which is formed by the N-cap (orange) and facilitated by interaction of the phosphorylated S69 with the SH2-KD linker [173]. The docking of the SH2 onto the KD C-lobe is facilitated by a kink in the αI-helix (light blue), which is induced by intramolecular binding of the N-terminal myristoylation (magenta spheres) to a hydrophobic pocket at the C-lobe bottom. In KD-only crystal structures, an extended conformation of the αI-helix is observed, which reaches into the space occupied by the SH2 domain in the assembled conformation, whereas it is evident from NMR that this part of the helix is flexible in solution. However, in solution it will also sample the extended and other conformations that clash with the SH2 domain and thereby exert an entropic force onto the SH2 domain.

Residues 56-82 were found to be necessary for proper regulation in cellular activity *in vitro* assays [176], and the crystal structure shows a possibly stabilizing interaction between the N-terminal cap and the SH2 domain, mediated by phosphorylated S69 [173]. The remaining N-cap, however, is not crucial for forming the assembled conformation in crystals. Omitting either residues 1-45 or 15-56 did not change the assembled conformation [33, 173]. These residues were also shown in *in vitro* cellular

activity assays to be irrelevant for regulation [176]. Importantly, the construct used for crystallization either contained the N-terminal myristoylation or a short myristoylated peptide that comprised the first 16 amino acids of Abl 1b isoform, which was added *in trans* before crystallization.

Surprisingly, it was found later by NMR and SAXS experiments that a construct, which misses the entire N-cap including the myristoyl (SH3-SH2-KD; Abl^{83-534}, 1b numbering; named Abl^{core} herein), nevertheless adopts the assembled conformation in solution [172].

The presence of the SH3 domain is of elementary importance for Abl regulation. The crystal structures [33, 173] show that the SH3 domain interacts with the SH2-KD linker through which it docks onto the back of the KD N-lobe, thereby stabilizes the assembled conformation. Interestingly, in Hck, another tyrosine kinase with an SH3-SH2-KD core, the SH3 domain interacts with a proper PxxP motif of the SH2-KD linker in a classical SH3-PxxP interaction [177], whereas in Abl, as well as in Src, the second proline of this motif is replaced by tyrosine ($P^{242}xxY^{245}$) or glutamine, respectively. These two residues are distorted such that they can pack within a hydrophobic crevice of the KD [32, 33]. The phosphorylation of this tyrosine (Y245) in Abl results in increased kinase activity [178], which can be clearly rationalized by the disruption of the hydrophobic interaction between Y245 and the KD through the charged phosphate [33].

The first proline (P242) of the SH2-kinase linker's imperfect PxxP motif ($P^{242}xxY^{245}$) is as well essential for formation of the assembled conformation, together with a further proline (P249) of the SH2-KD linker. Mutation of both prolines to glutamates leads to a highly active kinase [173, 176], and thus most likely induces a non-assembled conformation.

Based on the crystal structures of the inactive conformation of Abl, three linchpins that stabilize the formation of the assembled conformation have been proposed: (i) docking of the SH2 domain to the KD C-lobe, which is facilitated by myristoyl-induced bending of the αI-helix, (ii) docking of the SH3 domain to the poly-proline motif of the SH2-KD linker and consequently docking onto the KD N-lobe, and (iii) the clamp formed by the N-cap [173]. However, the latter, is dispensable for assembled core formation as shown by NMR [172]. The latter results also indicated that bending of the αI-helix is not solely achieved in the presence of the myristoylation, since the myristoylation is not necessary for adopting the assembled conformation in

solution. The αI-helix is rather flexible in solution in the absence of myristoyl pocket ligand [171, 172] and thus allows for SH2 docking onto the KD C-lobe.

Disassembled Abl core

To date, there is no comprehensive structural or dynamical model available of the activated wt (wild-type) Abl regulatory core. This is very likely due to highly dynamic nature and/or low population of the activated state in wt Abl. All available studies had to introduce artificial modifications to make the activated conformation observable: either mutations that disrupt the autoinhibited assembled conformation or addition of inhibitors that induce disassembly. SAXS data of these modified constructs show that it adopts a disassembled, extended conformation [26, 172, 173], which allows for substrate access, binding and phosphorylation. Several biophysical studies suggest how such a disassembled conformation may look like (Figure 1.7). On the one hand, NMR data suggest a disassembled dynamic conformation with high SH3 and SH2 mobility on the nanosecond time scale [172], whereas on the other hand, a more static so-called 'top-hat' conformation is observed under certain conditions in crystals [173, 179] and in solution [26, 180].

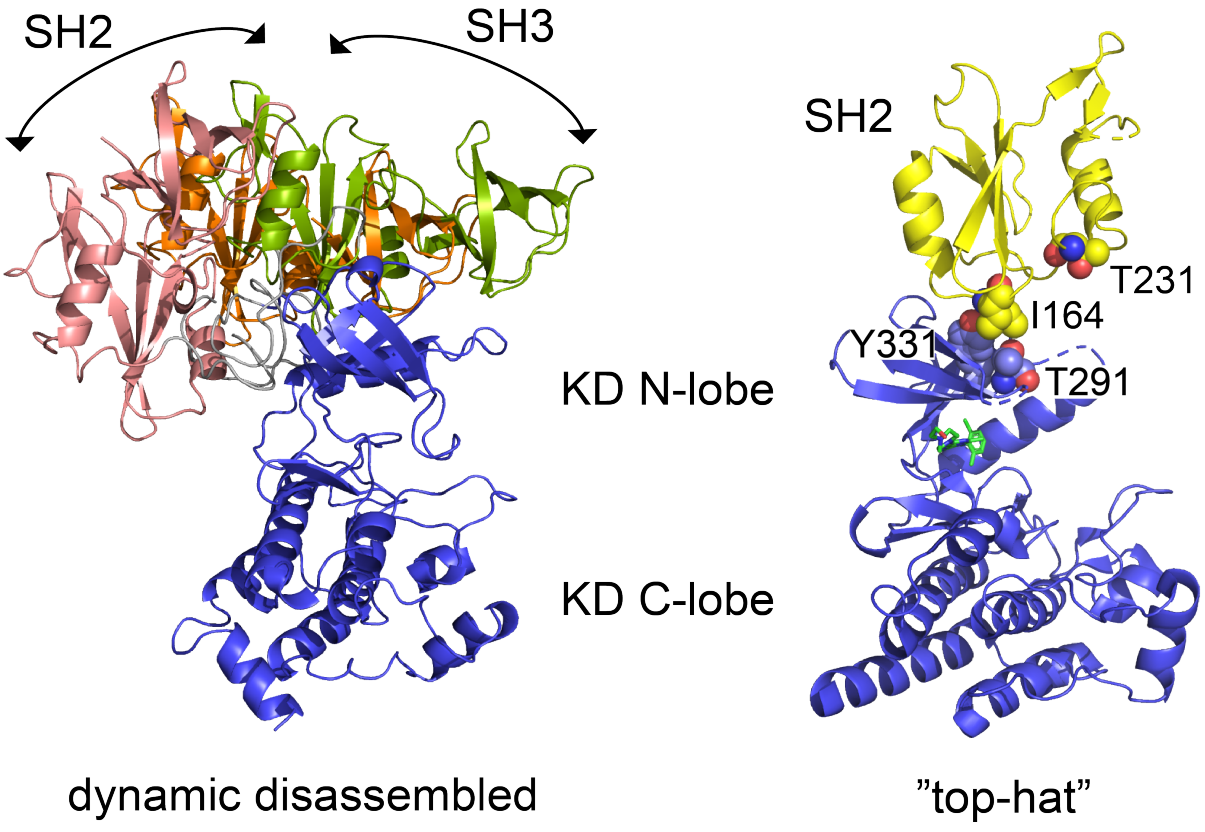

Figure 1.7. Structural models for the activated KD domain. Left: a dynamically disassembled model derived from NMR and SAXS data [172]. The SH3 and SH2 domains disassemble from the KD and

exhibit nanosecond motions as evident from NMR ^{15}N relaxation data. The best three models are displayed with the SH3-SH2 module shown in red, orange and green, respectively. Right: crystal structure (PDB code 4XEY [179]) of a construct comprising only the SH2 (yellow) and kinase domains (blue) in complex with dasatinib (green sticks). The SH2 domain sits on top of the KD N-lobe. This 'top-hat' conformation appears stabilized by the interaction of Ile-164 (yellow spheres), T291 and Y331 (blue spheres).

NMR residual dipolar coupling (RDC) and ^{15}N relaxation data in combination with SAXS data show that addition of imatinib to the SH3-SH2-KD construct, which is in the assembled conformation in the apo state, leads to an unexpected disassembly of the Abl core with high SH3 and SH2 mobility on the nanosecond timescale [172]. The kinase is effectively inhibited by imatinib, but still resembles a conformation expected for an active kinase conformation.

In contrast, the 'top-hat' conformation was observed for Abl in certain crystal [33, 160, 179] and solution conditions [26, 180], which included activating mutations or certain constructs such as SH2-KD [179] or SH3-SH2 [180]. In this conformation, the SH3 and SH2 domains are disengaged from the KD side. However, in contrast to the dynamic conformation described before, the SH2 domain forms a static interaction with a hydrophobic patch at the top of the KD N-lobe, called the 'αC patch' [179]. In several kinases this hydrophobic region has been shown to participate in inter- or intramolecular interactions, thereby activating the kinase. These kinases include EGFR [181], cyclin-dependent kinase (CDK) [182], protein kinase A (PKA) [15], Aurora-A kinase [183], and Fes (Feline sarcoma) [184]. For Fes [184], Bruton's tyrosine kinase (Btk) [185], and Abl [26, 179, 184], a structural and functional coupling between the SH2 domain and the KD's αC patch was observed under certain conditions.

For Abl, the 'top-hat' conformation was observed under certain crystal conditions in constructs that lacked the SH3 domain [179] or, in constructs comprising the myristoylated N-cap, SH3, SH2, and KD, but with no electron density observed for the SH3 domain [33]. However, SAXS data suggest that the SH3 domain sits on top of the SH2-KD assembly, i.e. the Abl core aligns in a fully extended conformation [173].

The main interaction between the SH2 and the KD N-lobe in the 'top-hat' conformation involves I164 from the SH2 domain and the KD N-lobe's T291 and Y331 (Figure 1.7). Mutation of these residues in an activated Abl construct, which misses all three assembly linchpins [173], led to a slightly less extended, but yet not fully assembled conformation in SAXS experiments [173].

Later, mutations at the SH2-KD such as T231R were found in CML patients and conferred with increased kinase activity [160]. The I164E mutation, which was thought to destabilize the 'top-hat' interface, inhibits downstream signaling pathways that are important for CML maintenance and abolishes leukaemogenesis in a CML mouse model [186].

The *in vitro* kinase activity is indeed impaired by this interaction in a construct comprising the SH2 and KD [26, 179]. The presence of the SH2 domain increases the KD's activity by a factor of approximately 2 [26, 179]. The interaction-destabilizing mutation I164E decreases the activity again to the KD-only level, whereas an interaction-stabilizing mutation, T231R, even further increases the activity by a factor of 3 [179].

However, these rather small effects cannot explain the much larger physiological effects [179]. Possibly, other mechanisms in the cell, which enhance the effect of the interface mutations, play an important role. These may be post translational modifications (PTMs) such as phosphorylation or interactions of downstream signaling partners with the Abl C-terminal tail. Very little is known of their effects on Abl regulation [179]. Nevertheless, the mentioned structural and biophysical studies have proven the relevance of the 'top-hat' conformation in Abl. To which extent, the 'top hat' conformation exists under physiological and pathological conditions as well as a comprehensive understanding of its functionality remain subject to further studies.

Structural investigations of the 'regulatory module' (RM) of Abl, i.e. N-cap, SH3 and SH2 domains, by solution-state NMR indirectly support the extended elongated 'top-hat' conformation of active Abl [180]. Here, the solution structure of RM-only was solved by NMR. It was found that the RM has two populations: one matches the conformation that this module adopts in the auto-inhibited Abl structure and the other was assigned to the activated conformation, which appeared to fit the 'top-hat' arrangement. In this active RM conformation, a region close to the N-terminus, comprising amino acids 14-20, which contains a PxxP motif (P15-S16-L17-P18), binds to the SH3 domain and thereby competes with binding of the SH3 domain to the SH2-KD linker in the assembled conformation. Importantly, this RM construct used in this study was not myristoylated. Strikingly, the apo form was found in equilibrium of roughly 50 % activated-state population, which is in stark contrast to the finding that the apo SH3-SH2-KD module is mainly in the inhibited conformation in solution [172].

Inhibitor-induced conformational changes of the regulatory core

As mentioned above, imatinib binding induces the disassembled Abl core conformation with highly mobile SH3 and SH2 domains [172]. A follow-up study, which combined NMR data with systematic analysis of all available KD crystal structures, revealed that the Abl core conformation strictly correlates with the ATP-competitive inhibitor-induced activation loop conformation [174]. Binding of all type II inhibitors such as imatinib, nilotinib, and ponatinib results in the disassembled core conformation, whereas binding of type I inhibitors such as dasatinib induces the assembled conformation.

The core disassembly upon binding of type II inhibitors has been explained by an induced push on the kinase N-lobe via A- and P-loop onto the SH3 domain [174]. This can explain the strongly reduced kinase activity in the assembled state, since similar N-lobe and P-loop motions are expected during nucleotide exchange [174, 187], but hindered due to the tight SH3 docking to the N-lobe [174].

1.4 Methods to study protein dynamics at atomic resolution

In many cases, static structures of proteins can be obtained by X-ray crystallography, cryo electron microscopy (EM), and for smaller to mid-sized proteins (up to about 80 kDa) also by NMR. However, besides the static structure, knowledge of the conformational variations and dynamics is crucial to understand the action and regulation of enzymes. Several methods exist that provide such dynamic information. Fluorescence spectroscopy [188] can probe the local environment of a fluorophore, rotational diffusion (fluorescence anisotropy) and distances between two fluorophores (Förster resonance energy transfer, FRET) in single-molecule experiments on time scales from picoseconds to hours. Nuclear magnetic resonance (NMR) can determine motions at atomic level on pico- to nanosecond, >microsecond and >second timescales [189]. Further experimental methods include electron paramagnetic resonance (EPR) [190] and hydrogen-deuterium exchange mass spectrometry (HDX MS) [191]. In addition, computational methods such as molecular dynamics (MD) calculations can simulate the dynamics of biomolecules at atomic level based on physical principles. In the following chapters, I will discuss the three major methods, single-molecule FRET, NMR, and MD, and their advantages and limitations in more detail.

Single-molecule FRET

Introduction

Förster resonance energy transfer (FRET) [192, 193] is an increasingly popular method to measure time-dependent distances of a few nanometers (nm) between two fluorophores [194]. For fluorescence correlation spectroscopy (FCS), accessible timescales range from picoseconds (ps) to hours (h) [195]. Together with the high sensitivity of fluorescence detection [196] fluorescence spectroscopy and in particular FRET is a very useful technique for studying the relationship between protein function and structure and conformational exchange on single molecules [197]. A network of several FRET distances within a protein may even be used for structure determination when this is combined with information from covalent geometry, x-ray crystallography, NMR, MD or other techniques [198-200].

The application of FRET is not limited to measuring distances within a single biomolecule. FRET has been used to analyze binding equilibria [201-203], complex stoichiometries [204-206], arrangement and function of multiprotein complexes and molecular machines [207-209], enzymatic reactions [210, 211], protein nucleic acid interactions [212, 213], protein and RNA folding und unfolding [214-216] and intrinsically disordered proteins [217, 218]. Moreover, all these studies are also possible in living cells [219-221].

Single-molecule vs. ensemble measurements

The high sensitivity of fluorescence spectroscopy as well as of a few other methods, such as atomic force microscopy, allows single-molecule detection [222-225]. The advantage of single-molecule experiments over ensemble measurements is that one can observe sub-ensemble populations and their dynamics, which are averaged out in the ensemble. Thus e.g. single-molecule observations show that enzymes purified to homogeneity exhibit different turnover rates over time and between molecules, although their average follows classic Michaeli-Menten kinetics [226-230]. The disadvantage of single-molecule detection is often poor sensitivity.

In ensemble measurements, average parameters are determined for the whole ensemble of molecules being observed. Such parameters can be for example average molecular coordinates (crystallography), rotational diffusion rates (bulk fluorescence), distances (bulk FRET), and shape (SAXS). Possibly existing sub-states and their

dynamics are not visible. In that case, biophysical methods with single-molecule resolution can be advantageous.

One major field with single-molecule resolution uses force-based detection and manipulation [231]. It comprises atomic force microscopy (AFM) [232, 233], optical tweezers [234-238] and magnetic tweezers [239, 240]. These techniques are sensitive to forces in the picoNewton (pN) range and therefore suitable to study RNA, DNA and protein folding and unfolding, movements of molecular machines such as myosin and kinesin, and RNA and DNA polymerase action [231, 241]. AFM can also be used to scan the topology of protein complexes and membranes, which possibly include membrane proteins. Recently, the very fast scanning of surfaces by high-speed AFM (HS-AFM) has allowed to produce movies of the dynamics of (membrane) proteins [242, 243]. The combination of AFM with fluorescence techniques is possible as well. Thereby, e.g., biomolecular conformations can be manipulated by AFM and the response detected by fluorescence [244, 245]. Despite all possibilities offered by AFM to study the topology and dynamics of biomolecules, several disadvantages limit its applicability. The sample has to be fixed on a surface, which is possibly difficult to achieve and can easily change the molecule's behavior. Furthermore, the scanning mode of HS-AFM limits spatiotemporal resolution significantly, and fast dynamical processes are not accessible [246].

Electrophysiological methods are also capable of recording currents through single ion-channels, pumps and transporters. In fact, patch-clamp recordings of single ion-channels were the first real single-molecule experiments ever [247, 248]. However, the observable systems are very limited. Only proteins involved in ion transport across membranes can be studied.

Among all the methods with single-molecule sensitivity, fluorescence spectroscopy stands out as the most versatile. Single-molecule fluorescence experiments can be carried out in principle with any type of biomolecule, especially with any given protein, attached to a surface or freely diffusing, given that the molecule emits fluorescence itself or can be labeled with a fluorophore. It covers all timescales from picoseconds onwards. It is easy to use and highly sensitive.

FRET theory

FRET is the transfer of energy from one chromophore (donor, D) in its electronic excited state to an acceptor chromophore (acceptor, A). This energy transfer is

nonradiative and based on the dipole-dipole interaction between the two chromophores. The acceptor eventually emits a photon (fluorescence), which can be measured (Figure 1.8**)**, or relaxes via other nonradiative mechanisms to its ground state. The efficiency of the energy transfer between the two chromophores is called FRET efficiency. It depends on i) the extent of overlap between the donor emission and the acceptor absorption spectra, ii) the relative orientation of the donor and acceptor transition dipoles, iii) the donor quantum yield, and iv) the spatial distance between the two chromophores [188].

Due to this distance dependence FRET is often called a 'spectroscopic ruler' [249]. However, a careful experimental procedure and analysis is required to reliably, precisely, and accurately measure distances with FRET [194, 199].

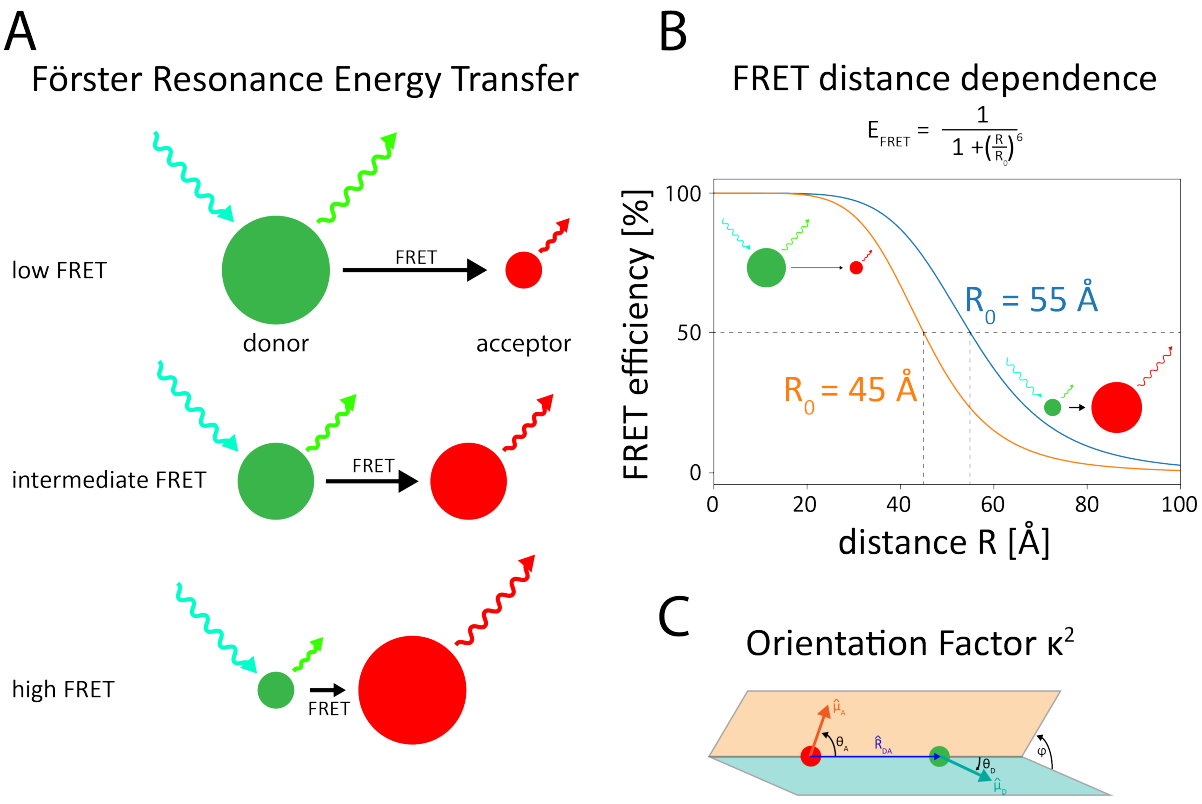

Figure 1.8. Basics of Förster Resonance Energy Transfer (FRET). A) A donor fluorophore (indicated as green spheres) absorbs a photon and may transfer energy to an acceptor molecule (red spheres) or emit the photon itself. If the acceptor is a fluorophore as well, the transferred energy may appear as acceptor fluorescence. For efficient energy transfer, the acceptor excitation spectrum needs to overlap with the donor emission spectrum. B) The energy transfer is highly distance-dependent. It is inversely proportional to the sixth power of the donor-to-acceptor distance. The Förster radius R_0 of the donor-acceptor pair is defined as the radius at which the transfer efficiency is 50 %. C) Additionally, the relative orientation of the transition dipoles of the two fluorophores, $\hat{\mu}_{A,D}$, which defines the orientation factor κ^2, is important for the rate of energy transfer.

The FRET transfer rate $k_T(r)$ from donor to acceptor depends on their distance as

$$k_T(r) = \frac{1}{\tau_{D(0)}}\left(\frac{R_0}{r}\right)^6 \quad (1)$$

where R_0 is the Förster radius for a given FRET pair.

The FRET efficiency E_{FRET} is defined as the ratio of energy transferred from the donor to the acceptor and the total amount of photons absorbed by the donor:

$$E_{FRET} = \frac{k_T(r)}{k_{D,0} + k_T(r)} \quad (2)$$

where $k_{D,0}$ is the overall relaxation rate of the donor in absence of an acceptor:

$$k_{D,0} = 1/\tau_{D(0)} \quad (3)$$

The transfer efficiency can be rewritten as

$$E_{FRET} = \frac{R_0}{R_0 + r^6} \quad (4)$$

which shows the strong r^{-6} distance dependence of FRET (Figure 1.8). From this equation it becomes also clear that the Förster radius is the distance at which the transfer efficiency equals 50 %.

Eq. 4 can also be expressed in terms of the change of the measurable donor lifetimes or relative fluorescence intensities in presence and absence of the acceptor:

$$E_{FRET} = 1 - \frac{\tau_{D(A)}}{\tau_{D(0)}} = 1 - \frac{F_{D(A)}}{F_{D(0)}} \quad (5)$$

Importantly, these equations are only valid for a single static donor-acceptor distance.

Orientation factor

A major uncertainty in calculating the Förster radius is the orientation factor κ^2, which depends on the relative orientation of the transition dipoles of the donor $\vec{\mu}_D$ and acceptor $\vec{\mu}_A$ (Figure 1.8) [250]:

$$\begin{aligned}\kappa^2 &= \left[\hat{\mu}_A\hat{\mu}_D - 3\left(\hat{\mu}_D\hat{R}_{DA}\right)\left(\hat{\mu}_A\hat{R}_{DA}\right)\right]^2 \\ &= \left(\sin\theta_D \sin\theta_A \cos\varphi - 2\cos\theta_D \cos\theta_A\right)^2\end{aligned} \quad (6)$$

Here, $\hat{\mu}_A$ and $\hat{\mu}_D$ are the unit vectors of the acceptor and donor transition dipoles, respectively. $\hat{R}_{DA}$ is the unit vector connecting donor and acceptor. θ_D and θ_A are the angles between the respective transition dipoles and $\hat{R}_{DA}$ and φ is the angle between the two planes spanned by $\hat{R}_{DA}$ and the respective transition dipole (Figure **1.8**).

From Eq. 6 it is clear that κ^2 can have values between 0 (perpendicular transition dipoles, no FRET) and 4 (head-to-tail parallel transition dipoles, maximum FRET).

Usually, free rotational diffusion is assumed for calculating the Förster radius: the orientation is randomized prior to energy transfer and results in $\kappa^2 = 2/3$. When static averaging is assumed, $\kappa^2 = 0.476$. Here, a range of all possible orientations, which are not changing during the donor lifetime, is averaged. Although it is impossible to calculate the exact κ^2 value without a priori knowledge about the symmetry and rotational behavior of the transition dipoles, limits can be determined by anisotropy measurements [250, 251]. However, if only relative FRET efficiencies are considered and the exact donor-acceptor distance is not of interest, any error in κ^2 will be a systematic error and not relevant for the results, however assuming κ^2 is the same in all conformations and at all fluorophore positions [250].

FRET experiments

Confocal FRET setup

In typical single-molecule FRET experiments, the excitation beam of linearly polarized light, produced by a pulsed laser, is focused to a small confocal volume of few femtoliters (fL) by a confocal microscope. The small observation volume in combination with highly diluted fluorescently labeled molecules in the picomolar range (~50 pM) guarantees that only one molecule is observed at a time. Furthermore, a crucial pinhole within the detection beamline selects for photons, which originate solely from the confocal volume [252]. The emitted photons are collected with the same optics used for illuminating the sample and eventually separated by a dichroic beam splitter from the excitation beam. This is possible due to the Stokes shift, i.e. red-shifted emission spectrum. To observe the fluorescence anisotropy, the beam is further separated by a polarization beam splitter into its parallel and perpendicular components, which are then again separated by a dichroic beam splitter into the respective relevant donor and acceptor wavelength ranges. Thus, the emitted photons are detected by four detectors: donor$_\perp$, donor$_\parallel$, and acceptor$_\perp$, acceptor$_\parallel$.

TCSPC and MFD

In time-resolved recordings, the output of the single photon counting avalanche photodiode (APD) is registered via time correlated single-photon counting (TCSPC) electronics [253, 254]. With modern electronics two timescales can be measured in one high-resolution experiment. For every photon not only the channel ID is registered, but also its arrival ‘microtime’, which is the time between excitation pulse and photon

detection, and the ‘macrotime’, which is the number of excitation pulses since the start of the experiment. With this information and the defined time delay between two excitation pulses (laser repetition time), the real arrival time of each photon according to the laboratory time can be calculated with picosecond precision over several hours [195]. This results in a full time trace of fluorescence intensity, i.e. number of photons, for each individual channel or combinations of channels, e.g. both green and both red channels. Within these time traces, one can identify single-molecule events, i.e. one fluorescently labeled molecule diffusing through the observation volume as so-called photon bursts and use that for ‘burst-wise analysis’. For each burst, one can create the fluorescence decay histograms for each individual channel. Thereby, one can in parallel determine all possible fluorescent parameters for a single molecule during the time of observation (typically a few ms for a protein).

The described approach is called multiparameter fluorescence detection (MFD) [255]. Detected parameters are, without claim for completeness, spectral absorption and fluorescence properties, brightness and quantum yield, fluorescence lifetime, anisotropy, stoichiometry, FRET efficiency, and timescales other than fluorescence lifetimes. Furthermore, pulsed interleaved excitation (PIE) [256], where donor and acceptor are alternatingly excited, can be used to discriminate differently labeled species resulting from sample heterogeneity due to incomplete labeling, aggregation, etc. [250]. Due to the simultaneous detection of the parameters many uncertainties of FRET measurements, such as dye mobility and quenching, may be avoided.

Fluorescence Correlation Spectroscopy (FCS)

Another method suitable to observe single molecules or at least a small number of molecules (n<10) is fluorescence correlation spectroscopy (FCS) [257]. FCS analyzes the variations of fluorescence intensities over time. Simply spoken, it compares the intensities at two different times within the experiment. The amplitude and frequency of the variations are described by calculating the autocorrelation function. Classically, these variations arise from molecules diffusing in and out of the observation volume. Here, FCS describes the average number of molecules in the observation volume (inverse of amplitude at zero time) and the diffusion time (time at half amplitude of the FCS curve). The faster the diffusion, the lower is the probability to observe the same intensity of a signal at time t, F(t), and at a later time F(t+τ). Besides translational diffusion the intensity variations can have various sources such as ligand-

macromolecule binding, rotational diffusion, molecule dynamics, photochemistry and –physics, and chemical reactions. However, each problem requires its own mathematical description and some of these processes influence each other.

Being developed in the 1970s, FCS became widely used only after major technological advances in optical detection (confocal microscopes) and excitation sources in the 1990s. More recently, FCS has been developed further to overcome limitations arising from mixtures of fluorescence species, in particular when their diffusion constants are similar [258].

In normal FCS analysis, different species within a mixture are separated by diffusion times. However, these need to be significantly different, which is usually not the case for distinct conformations of a protein. An improvement of FCS is fluorescence lifetime correlation spectroscopy (FLCS) [259-261], which can separate different species in a mixture by their fluorescent lifetime. Using this method, one can also differentiate protein conformations, if the attached fluorophore shows sufficiently distinct fluorescent lifetimes. 'Sufficiently distinct' typically means that the lifetimes differ by at least 1.0-1.5 ns [258]. As common dyes have only few nanoseconds lifetime, the number of species that can be separated by this method is nevertheless quite limited [258]. Filtered FCS (fFCS) takes advantage of multiparameter fluorescence detection and adds a further dimension, in which different species can be separated. In addition to diffusion and lifetime information, fFCS can select for anisotropy and spectral properties. This makes the method more precise and selective [258]. It was shown that even in the case of very similar lifetimes, species can be differentiated based on their anisotropy [258]. Finally, cross-correlation of the distinct species can eventually resolve the dynamical exchange between them and further dynamical processes in the nanosecond to diffusion time range.

Nowadays, FCS-based methods are applied to investigate the mobility of molecules in solution and membranes, protein interactions and aggregation, DNA hybridization, and many more experiments *in vitro* and even *in vivo* in living organisms [262, 263].

FRET dynamics – timescales, methods, examples

The data recorded with MFD can be readily analyzed for molecule dynamics in timescales ranging from sub-microseconds to hours [195, 199]. However, in confocal spectroscopy with freely diffusing particles, the observed processes are limited by the time of diffusion through the confocal volume. For freely diffusing molecules this is in

the range of a few milliseconds. However, for observation of slower processes, one may immobilize the protein or nucleic acid. This allows to record FRET trajectories of single molecules over hours. Of note, the time is limited by the photobleaching of the fluorophore.

If the system contains a limited number of well separated FRET states, one can easily deduce kinetics from the time-traces [264-268]. If the system is more complicated and a 'by eye' investigation is no longer possible, more sophisticated analyses such as Hidden Markov Modeling may be performed [269].

Dynamic processes on the millisecond timescale, such as large domain motions, can be analyzed by burst-wise analysis and 2D plotting [250], as well as dynamic photon distribution analysis (dynPDA) [270]. Since one burst of photons in TCSPC originates from one molecule diffusing through the confocal volume, the length of a burst is on the timescale of the diffusion (few milliseconds), and the FRET parameters of the molecule are averaged over this time period. Therefore, dynamic processes that take place on this timescale lead to smeared populations in 2D plots of FRET efficiency versus fluorescence-weighted mean donor lifetime $\langle \tau_{D(A)} \rangle_F$. If the exchange between two conformations is slower than the diffusion time, one observes only the two states located on a theoretical 'static FRET line'. This FRET line represents the theoretical relation between donor lifetime $\tau_{D(A)}$ and intensity-based FRET efficiency E_{FRET} (Eq. 5). If the process is much faster, one observes a single population that is shifted from the static FRET line. In this way, an estimation of the dynamical processes of a molecule and its timescales can be made. Analysis by dynPDA [270-272] can yield exchange rates in the order of ± 1 relative to the order of diffusion time [273].

Exchange processes, which are faster than the diffusion time, can be further analyzed by fFCS [258] as described above.

FRET labels

Fluorophores

Any type of fluorescence experiment requires a fluorescent probe – a fluorophore. Fluorophores can be categorized into two main groups: intrinsic and extrinsic [188]. Intrinsic fluorophores are naturally occurring in the molecule of interest (e.g. tryptophan in proteins) or could be the molecule of interest itself. Extrinsic fluorophores are fluorescent molecules, which are attached to the molecule of interest, because it

exhibits no fluorescence or its intrinsic fluorescence is of no use to answer the specific question. E.g. DNA is free of any fluorescence and requires fluorophore labeling [188]. Despite the fluorescence properties of tryptophan, tyrosine and phenylalanine, which occur naturally in most proteins, it is often required to use specialized extrinsic fluorophore labels for investigations of proteins, too [188]. An armada of specialized fluorophores is available and research into new compounds is still on-going [274, 275]. The fluorophore's properties such as spectral properties, fluorescence lifetime, photostability, solubility, size, etc. define possible applications [188].

For example, fluorophores with longer fluorescent lifetimes can be used to probe processes on different timescales; common organic fluorophores have lifetimes in the time range of 1-10 ns, whereas lanthanides have lifetimes up to ms [276-278]. Fluorophores with red-light and near-IR excitation can be used for fluorescence imaging in biological tissues with high auto-fluorescence and high (blue) light scattering [279-281]. Fluorescent proteins such as green fluorescent protein (GFP) [282], which spontaneously form a chromophore upon expression, have been proven to be useful for in-cell studies, since they can be easily expressed as fusion together with the target protein. This allows easy expression, localization and binding studies. However, native GFP is of limited use for quantitative structural studies with single-molecule detection due to its relatively large size and suboptimal photo-physical and -chemical properties [221]. As such it has been used in ensemble measurements to study structural features of protein complexes [220, 283] and protein folding [284] in live cells. However, newly developed fluorescent unnatural amino acids overcome the limitations of GFP and may facilitate single-molecule FRET studies in live cells [285-287]. Their advantage lies in their small size and superior photophysical and -chemical properties over GFP variants. They are simply introduced into proteins during expression without the need for labeling reactions. Labeling reactions are required for classical fluorescent dyes in smFRET studies, and are hardly feasible *in vivo*. Nevertheless, small organic dye molecules are still widely used for *in vitro* and in-cell smFRET studies due to their superior easiness and versatility to date.

Cysteine chemistry for site-specific labeling

While GFP fusions are simply generated by adding GFP C- or N-terminally to the gene of interest and co-translating both in any expression host, the widely used small

organic fluorophores such as rhodamine derivatives, Bodipy-dyes and cyanine dyes require a labeling reaction to covalently bind to a biomolecule of interest.

Typically, the fluorophores are attached to cysteines via a thiol-maleimide coupling reaction [288-291]. This approach is very successful since it uses naturally occurring cysteines in the protein as an attachment point. The reaction is easy to perform in aqueous solution at physiological pH and highly effective. Furthermore, the number of cysteines occurring in proteins is comparably low, which increases specificity. However, if more cysteines than desired labeling sites exist in the protein, or if they are located at wrong positions in the protein, one needs to prepare cysteine mutations, which in turn may affect protein integrity.

Unnatural amino acids and their potential for fluorophore labeling

An alternative to cysteines for site-specific labeling are unnatural amino acids (UAAs) (alternatively named noncanonical amino acids ncAAs) [292-295] with unique reaction groups such as alkynes, azides, acetyles, and cyclo-octynes. UAAs get usually incorporated into proteins by reassigning the least frequent stop codon, which is the amber codon TAG, to recognize a bioorthogonal aminoacyl-tRNA synthase aaRS/tRNA [296]. This aaRS/tRNA pair needs to uniquely recognize the desired UAA within the context of the expression host. E.g. PylRS/$tRNA_{CUA}$ pairs, where the subscript stands for the TAG anticodon, from certain methanogens are orthogonal in bacteria and eukaryotic cells, i.e. they do not recognize any of the host's natural tRNAs or any natural amino acid [296]. The aaRS can often be evolved to recognize several UAAs specifically as demonstrated for PylRS/$tRNA_{CUA}$ [297-299]. While the development of UAAs with improved properties or new functionalities and applications is ongoing, there is already a large number of UAAs available for various applications in studying the structure and function of proteins, covalently attaching small moieties, controlling protein function, designing and evolving proteins, and therapeutic applications [296].

Crosslinking UAAs have been used to identify GPCR-activating ligands [300, 301] the binding site of antidepressant drugs in the serotonin receptor [302], and key protein-protein interaction necessary for lipopolysaccharide (LPS) transport to the bacterial outer membrane [303]. The unique IR-active vibrational modes of the UAA azidophenylalanine, which was incorporated at several sites in rhodopsin, were used to study helix movements upon light-induced rhodopsin activation [304]. Photocaged

lysine was incorporated into Cas9, which enabled illumination-controlled gene activation and deactivation of exogenous gene reporters in mammalian cell cultures [305]. Recently, an UAA, conjugated to FITC, was incorporated into antibodies specific for a tumor antigen. The FITC moiety is able to bind an engineered chimeric T cell receptor. Thus, the UAA-containing antibody bridges the chimeric antigen receptor (CAR)-T cell with the tumor cell. This allows for CAR-T cell therapy with reduced toxicity, since the interaction of the CAR-T cell is well controlled [306].

UAAs can be very helpful for fluorescence spectroscopy and particularly for FRET studies since they usually require that a protein is labeled with a fluorophore. There exist UAAs that are fluorophores themselves such as coumarin, dansyl, naphthyl, terphenyl, and prodan derivatives, which have been incorporated in both prokaryotes and eukaryotes [296]. The advantages are that no labeling reaction is required and there is minimal perturbation of the protein structure. One such genetically encoded fluorophore, ANAP, was even used in a FRET pair within mammalian cells to study proteolysis and internal pore opening of ion channels [307, 308].

A currently still more versatile approach for site-specific protein labeling especially for FRET labeling of proteins is the use of UAAs that bear bioorthogonal chemical reactive groups. Various such UAAs have been developed [296]. Propargyl-lysine and other acetylenic UAAs can react with azido-conjugated fluorophores by the copper(I)-catalyzed alkyne-azide cycloaddition (CuAAC) ‘click’ reaction [309]. Of note, the reactivity can be exchanged by incorporation of azido UAAs such as azido-phenylalanine into proteins. However, the azido group is prone to reduction to an amine [310, 311] and thus sensitive to the reducing cytosolic environment and possible reducing agents required to maintain protein integrity. The need for copper as a catalyst makes this reaction less applicable to in-cell labeling, since copper ions are considered toxic to *E. coli* in their free form, although the THPTA-chelated copper(II) is reported to be non-toxic to the cell [312, 313]. Nevertheless, strained alkenes and alkynes have recently been developed, which allow for rapid and specific copper-free labeling with tetrazines in live cells [299, 313, 314]. Another UAA, p-acetyl-phenylalanine, can be labeled with a wide range of reagents such as hydrazides and hydroxylamine derivatives [315]. However, the required reaction conditions, that is mainly low pH, limit the applications to sufficiently stable proteins. Various other UAAs have been developed that can be bioorthogonally labeled using different chemical reactions [296], including carbohydrate coupling to alkenyl UAAs [316], hydroxyl-

tryptophan residues for azo-couplings [317], and p-borono-phenylalanine and p-iodo-phenylalanine used in Suzuki and other transition metal-based couplings [318].

The use of UAAs is interesting for FRET applications for several reasons. The main advantage is that one can improve site specificity of the labeling, which can improve the data meaningfulness. If one uses two cysteines, it is very hard and often impossible to have the donor and the acceptor always at one of the two spots specifically. With the use of UAAs, however, one can either use one cysteine and one UAA with orthogonal chemical reactivity [319] or two orthogonal UAAs [320] to ensure site-specific donor and acceptor labeling. Another advantage is that one can address proteins which contain cysteines that are relevant for function or protein integrity and can thus not be mutated or used for labeling. This applies in particular to larger proteins, which naturally contain more cysteines. Here, the use of UAAs can make FRET studies possible at all [321]. Nevertheless, due to complications coming along with the use of UAAs (which I describe below) and the simplicity of cysteine-based labeling, the latter is yet the most popular method to produce FRET samples.

Despite the many advantages of UAAs, their application in real-life situations with difficult-to-handle proteins is often challenging; from the selection of the most suitable UAA to the expression and labeling reaction. Advanced highly specialized UAAs are potentially costly or organic chemistry equipment and know-how is required to synthesize the UAA. Expression systems for incorporation of various UAAs using the amber codon are readily available for bacterial, yeast and mammalian expression. The UAA expression machinery was even delivered to primary cells and tissues using viral vectors [296, 322-324]. Nevertheless, the de novo development of a working aaRS/tRNA pair may be necessary, if no existing UAA system is suitable for one's purpose. This requires again special know-how in advanced molecular biology techniques and can be time-consuming.

Furthermore, the expression level can be reduced dramatically compared to wild-type expression, and expression conditions such as time, medium and supplement concentrations, and expression host need to be optimized. A major hurdle lies in the very basics of the technology. The recoded amber codon still codes for expression termination. Either high levels of amino-acetylated $tRNA_{CUA}$ that outcompete the release factor 1 (RF1) in *E. coli* or the respective termination factors of other expression hosts, or recently developed engineered strains that lack RF1 [325, 326], and consequently do not terminate expression at the amber codon, can

help to improve the expression of proteins with incorporated UAAs, particular when more than one UAA is incorporated.

Finally, the labeling reaction needs to be highly efficient for applications such as FRET, where site-specific labeling of two sites close to 100 % is needed for high-resolution studies. Additionally, the reaction conditions can be potentially harmful for the protein itself as in the case of CuAAC, where reactive Cu(I) can mediate unwanted oxidation reactions. This may require extensive optimization of reaction conditions like time, temperature, concentrations of reactants and possibly additives to prevent oxidative or other damage [327].

Nuclear Magnetic Resonance (NMR)

Nuclear Magnetic Resonance (NMR) is a powerful technique to investigate the structure, interaction and dynamics of proteins at atomic resolution in their natural solution state [328]. The physics of NMR is well understood and provides the basis for continuous developments of new experiments with increased sensitivity and resolution, which largely increase the range of possible biological targets and questions that can be addressed by NMR [329].

New technical advances and strategies, as well as novel biochemical methods for isotope labeling, have further fueled the field of biomolecular NMR [328]. The most apparent improvement concerns the size of the protein that can be studied by solution NMR. Starting with small peptides some decades ago, it is now in principle possible to investigate protein complexes with a molecular mass on the order of 1 MDa under certain conditions [329-331].

Spectrometers with larger fields and in particular the NMR technique TROSY (transverse relaxation-optimized spectroscopy) [332] together with suitable isotope labeling schemes have improved the NMR sensitivity and spectral resolution with large molecules in solution tremendously. First, ^{1}H-^{15}N TROSY was developed for studies on backbone amides in proteins and subsequently extended for methyl groups in the ^{1}H-^{13}C TROSY experiment [333] as probes for structure, dynamics, and function.

With the introduction of a paramagnetic tag in a protein new effects can be observed with NMR, which include pseudocontact shifts (PCS) and paramagnetic relaxation enhancement (PRE) [334]. PCSs yield structural restraints for distances up to more than 100 Å, and PREs use the effect of line broadening that depends on the distance between the paramagnetic center and the observed nucleus.

The development of residual dipolar coupling (RDC) in protein NMR uses the information of magnetic dipole-dipole interaction vectors of a partially aligned protein [335]. It reports on internuclear vector orientations irrespective of their distance separation. RDCs provide valuable information for refining a single protein structure as well as ensemble refinement to represent protein structure and disorder in solution, protein-substrate interaction as well as oligomeric states.

NMR does not require external probes such as fluorophores, because most (bio)-molecules naturally contain large numbers of NMR-active nuclei like hydrogen ^{1}H. In order to increase the resolution by two- or more-dimensional NMR, e.g. ^{15}N and ^{13}C isotopes can be incorporated into proteins without significantly changing their

physicochemical and biological properties. Due to the high abundance of H, C, and N in proteins, a single measurement can provide information about the whole system.

New isotope labeling strategies are still one key driver in the field of protein NMR [336]. Proteins can be easily expressed uniformly labeled with ^{15}N and ^{13}C. For larger systems, this approach becomes inapplicable because of signal crowding and broadening due to slow molecular tumbling and resulting fast relaxing signals. Perdeuteration of proteins improves their relaxation properties and has strongly increased the size of biomacromolecules that can be investigated by NMR. The number of signals, and thereby also the complexity of the data, can also be reduced by specifically labeling the protein at defined positions such as a certain type of amino acid or specific chemical groups in amino acids. This requires knowledge of the metabolic pathways in order to avoid scrambling. Especially, specific labeling of methyl groups ($^{13}CH_3$) in an otherwise perdeuterated environment has contributed enormously to the advances made in the investigation of protein complexes larger than 100 kDa [337-339]. This is due the high symmetry of the three methyl protons and their fast rotation on the picosecond time scale, which further slows relaxation rates [340].

E. coli is the preferred expression system for NMR sample production for various reasons. Among other things, its metabolism is well characterized, which enables specific isotope labeling, and most importantly, it can grow in fully deuterated medium. However, some proteins cannot be easily produced in *E. coli*, especially if PTMs are required, which are less common to prokaryotes. In these cases, the proteins can be expressed in eukaryotic systems such as insect cells and mammalian cells. Yet, isotope labeling can, hence, be more challenging and become much more expensive. Nevertheless, the costs for uniform ^{15}N- and ^{13}C-isotope labeling in insect cells could recently be reduced by using isotope-labeled yeast [341, 342] or algal extract [343] as amino acid source, instead of directly feeding isotope-labeled amino acids. Deuteration levels of >60 % have also been achieved by this approach [341].

Dynamics

One major advantage of NMR over other structural methods such as X-ray crystallography and cryo-EM is its ability to study the dynamical behavior of proteins in their natural solution state with atomic resolution on timescales ranging from picoseconds to years [328, 329, 331, 344].

The dynamics of proteins can be characterized by spin relaxation methods, i.e. quantifying how a spin system returns to its Boltzmann equilibrium. Depending on the process that causes the spins to relax, one can observe relaxation and thus dynamics by NMR on two timescales: picosecond-nanosecond and microsecond-millisecond [189]. When reaction times are slower than the duration of a typical NMR observation, i.e. several hundred milliseconds, also continuous real-time monitoring of dynamics is possible. It is important to note that, while in smFRET, TCSPC allows for extracting dynamical processes of all available timescales from one experiment/dataset, in NMR, different types of experiments have to be performed in order to elucidate specific dynamical processes that occur on different timescales.

Picosecond-nanosecond dynamics

Motions on the picosecond-nanosecond timescale – the timescale of the spin's Larmor frequency – can be investigated by spin relaxation resulting from stochastic variations of the spin Hamiltonian mainly caused by time-dependent dipole-dipole (DD), chemical-shift anisotropy (CSA), and quadrupolar interactions [189]. Thereby, rotational tumbling of the protein, fast diffusion of individual domains or fast local dynamics can be observed.

This was used to characterize the dynamics of the Abl core conformation in complex with different ligands in solution [172]. ^{15}N longitudinal (R_1) and transverse (R_2) relaxation rates were determined for Abl^{core} in complex with imatinib, GNF-5 and for the ternary complex that is Abl•imatinib/GNF-5. From that, isotropic rotational correlation times, τ_c, between 20 and 30 ns were calculated for the individual domains – SH3, SH2, and kinase domain (KD) N- and C-lobe. In both GNF-5-containing complexes, the rotational correlation times ranged between 27 ns (SH3) and 31 ns (KD), which excludes large interdomain motions on the ns timescale. In contrast, τ_c of the SH2 and SH3 domains in the Abl•imatinib complex dropped to 25 ns and 21 ns, respectively. This shows that these domains move with respect to the KD within nanoseconds. Together with SAXS data, which showed an increased radius of gyration for Abl•imatinib and thus a less compact conformation compared to the apo state and Abl•GNF-5 complexes, these data indicate a disassembled dynamic conformation of the Abl core induced by imatinib, but the assembled conformation with bound GNF-5.

Microsecond-millisecond dynamics

Motions on the microsecond-millisecond timescale are accessible to spin relaxation arising from chemical exchange phenomena, which means modulation of isotropic chemical shifts [189]. The timescale here is defined by the frequency difference of the spin within the two (or more) interchanging chemical environments, which is often the result of conformational changes for protein NMR.

If an NMR-active nucleus experiences a change in its chemical environment within two different conformations, it will give rise to two resonance lines with differing chemical shifts. Depending on the exchange rate k_{ex} between the two conformations, two separate resonances with intensities depending on the populations, $p_{A,B}$, of the two states will appear at their respective position in the case of slow exchange, or they will broaden and eventually merge into one resonance in between the two original ones, when the exchange rates get faster [344].

Slow conformational exchange in the millisecond time range, such as ligand binding and release and domain movement, can be observed by magnetization exchange (ZZ-exchange experiments). It can be used in cases where the different conformations are sufficiently populated and can be quantified by NMR [345, 346]. Slowly exchanging systems with low populated states – as low as 0.5 % – can be studied with chemical- and dark-state exchange saturation (CEST) experiments [347, 348].

Chemical exchange in the microsecond-to-millisecond time range of intermediate-to-fast exchange processes such as side-chain reorientation, loop motions, secondary-structure changes, and hinged-domain movements, can be studied by CPMG relaxation dispersion or $R_{1\rho}$ rotating-frame relaxation dispersion experiments.

Such NMR relaxation experiments have recently identified functional dynamics in GPCRs [349] and the unexpected switch between Watson-Crick and Hoogsteen base pairs [350].

Paramagnetic relaxation enhancement (PRE) provides information on lowly populated states of macromolecules and their complexes, non-specific interactions, ligand binding sites, and fast dynamic processes in the microsecond range [351].

The H/D exchange of labile protons of a globular protein gives information on the solvent accessibility of the labile protons and on the network of intramolecular hydrogen bonds, their strength, opening and reforming. It reports on the slow internal motions in the protein usually in the seconds-to-minutes range [352].

Molecular Dynamics Simulations

Computational approaches provide a powerful complement to experiments [353]. Molecular Dynamics (MD) simulations calculate the positions and velocities of atoms as a function of time based on the interatomic forces. Thus, MD simulations yield a 3D movie of all simulated atoms of a biomolecule in a given time interval [354, 355]. This cannot be achieved by any other biophysical method [355]. As the conditions are fully controlled, starting conditions, chemical nature of the molecule, including posttranslational modifications (PTMs) and mutations as well as the molecule's environment, i.e. solvent and ligands, pH, temperature, voltage, pressure, etc. can be set at will. Thus, the influence of such conditions can be easily investigated [355].

Classical MD calculations are based on Newton's laws of motion. Therefore, one needs to set the starting conditions, i.e. position and velocity of every atom, and define the forces that drive the motions of the atoms. The forces are described by so-called molecular mechanics (MM) force fields (FF), which usually combine terms for Coulombic, i.e. electrostatic, interactions between atoms, spring-like terms describing the covalent bonds, and additional terms for further interatomic interactions [355]. These force field terms are usually derived from results of quantum mechanical calculations on small molecules or from experimental data such as NMR spin relaxation methods, which give good information on fast (ps-ns) motions. Although force fields are constantly being improved [356-359], the force fields are inherently approximate [355], in particular for longer timescales (μs-ms), and the force field accuracy needs to be considered in any interpretation of MD data [355].

Of note, covalent bond breaks and formation, i.e. chemical reactions, are not considered in classical MD simulation. However, in quantum mechanics/molecular mechanics (QM/MM) simulations, a small part of the molecule is modeled by quantum mechanics and the remainder by classical mechanics. Thus, chemical reactions of enzymes for example can be studied in the context of the whole protein [360].

Another practical aspect to be considered is computational power. Time steps of MD simulations fundamentally need to be smaller than the timescale of the fastest protein dynamical processes. Thus, time steps are a few femtoseconds only. In order to reach timescales of biologically interesting processes such as protein-domain movements or folding, which take place on the microseconds, milliseconds and longer timescales, a huge number of time points need to be simulated, which is computationally very demanding [355].

However, recent technological and computational advances have tremendously increased the accessible computational power and enabled longer simulations up to milliseconds [355].

For example, MD simulations were applied to follow protein folding in detail [361], unravel an allosteric activation mechanism between rhodopsin and visual arrestin-1 [362] and, together with NMR chemical-shift data, to interpret protein structure dynamics at atomic resolution [363].

2 Investigation of the Abl regulatory core dynamics by single-molecule FRET

The following Chapter consists of the preliminary manuscript entitled “Activation and inhibition conformational dynamics of the Abl tyrosine kinase regulatory core investigated by single-molecule FRET” by J. Schlotte, S. Felekyan, J. M. Habazettl, I. Hertel-Hering, R. Sonti, J. Kubiak, O. Hantschel, C.A.M. Seidel, and S. Grzesiek. In this work, single-molecule FRET experiments are applied to investigate the dynamics of the Abl^{core} conformational equilibrium at the single-molecule level on timescales ranging from nanoseconds to milliseconds. The manuscript contains a Section ‘Preliminary results’, which describes a preliminary more-detailed analysis of the presented data with respect to the sub-millisecond dynamics of the conformational equilibrium of the Abl. This analysis will be further pursued in the near term and the manuscript updated with the finalized results. The same applies to the Section ‘Conclusion and Perspective’, which represents the current state of the research.

Activation and inhibition conformational dynamics of the Abl tyrosine kinase regulatory core investigated by single-molecule FRET

Johannes Schlotte[1], Suren Felekyan[2], Judith Maria Habazettl[1], Ines Hertel-Hering[1], Rajesh Sonti[1], Jakub Kubiak[2], Oliver Hantschel[3], Claus A.M. Seidel[2,*], Stephan Grzesiek[1,*]

[1] Focal Area Structural Biology and Biophysics, Biozentrum, University of Basel, 4056 Basel, Switzerland

[2] Institut für Physikalische Chemie, Lehrstuhl für Molekulare Physikalische Chemie, Heinrich-Heine-Universität, 40225 Düsseldorf, Germany.

[3] Institut für Physiologische Chemie, Philipps Universität Marburg, 35043 Marburg, Germany

*Address correspondence to:

Stephan Grzesiek
Focal Area Structural Biology and Biophysics, Biozentrum
University of Basel, CH-4056 Basel, Switzerland
Phone: ++41 61 267 2100
FAX: ++41 61 267 2109
Email: Stephan.Grzesiek@unibas.ch

Claus A.M. Seidel
Institut für Physikalische Chemie, Lehrstuhl für Molekulare Physikalische Chemie, Heinrich-Heine-Universität, Universitätsstraße 1, 40225 Düsseldorf, Germany
Phone: ++49 211 81-15881
FAX: ++49 211 81-11612803
Email: cseidel@hhu.de

Keywords: Abelson kinase, CML, single-molecule FRET, protein dynamics, unnatural amino acid, asciminib

Abstract

Abelson tyrosine kinase (Abl) is involved in many cellular processes. Its activity is regulated by the specific arrangement of its regulatory core SH3, SH2, and kinase domains, where an assembled or disassembled core corresponds to a low or high kinase activity, respectively. The inactive, assembled core structure has been well characterized by crystallography and NMR spectroscopy. In contrast, the structural and dynamical characteristics of the disassembled form and the underlying activation mechanism are not clear.

Here we present an analysis of the regulatory core dynamics by single-molecule Förster resonance energy transfer (smFRET) experiments using multiple donor-acceptor pairs introduced via unnatural amino acids and bioorthogonal fluorophore labeling. We show that the apo core is in dynamic equilibrium on the (sub)millisecond time scale between the assembled conformation and a highly dynamic disassembled conformation of about 30 % population. The addition of the allosteric myristoyl-pocket inhibitors asciminib or GNF-5 almost completely abolishes this tendency to open, thereby explaining their inhibitory effects. As observed previously, the addition of type II ATP site inhibitors disassembles the core to a highly dynamic conformation on the submillisecond timescale, which again can be shifted by the addition of the allosteric inhibitors to a closed conformation, which, however, shows considerably more opening than the apo form. The availability of robust FRET labeling for Abl and other kinases opens the way for detailed *in vitro* and *in vivo* studies of their regulation under healthy conditions and misregulation in cancer.

Introduction

Abelson tyrosine kinase (Abl) plays an important role in numerous cellular processes including proliferation, division, survival, DNA repair and migration[1,2]. Under non-pathological conditions, Abl is tightly regulated with very low intrinsic activity in unstimulated cells[3]. However, the oncogenic t(9;22)(q34;q11) chromosomal translocation (Philadelphia chromosome) leads to the expression of the highly active fusion protein Bcr-Abl and subsequently to chronic myeloid leukemia (CML)[4-6]. The ATP site inhibitors imatinib (Gleevec), nilotinib (Tasigna), and dasatinib (Sprycel) are very efficient against CML[7-9], but the emergence of drug-resistant point mutations in a fraction of patients has created a strong need for alternatives[8,10]. In particular, the recently developed allosteric inhibitor asciminib (ABL001)[11], which targets the myristoyl binding pocket (see below), shows high promise in clinical trials to overcome these resistances[12]. The exact functional mechanism of allosteric inhibitors is unclear.

Under healthy conditions, Abl regulation is achieved by a set of interactions within its regulatory core consisting sequentially of the SH3, SH2 and kinase (KD) domains and the preceding ~60-80-residue-long N-terminal tail (N-cap)[13] (Figure 1A). The N-cap varies between splice variants 1a and 1b, with Abl 1b being 19 residues longer and N-terminally myristoylated. The crystal structure of the autoinhibited Abl core with the myristoylated N-cap (Figure 1B)[13,14] reveals a tight, almost spherical assembly, in which the SH3 domain binds the proline-rich linker between the SH2 domain and the KD N-lobe and the SH3 and SH2 domains form extensive contacts to the KD C- and N-lobes, respectively. This assembly appears further stabilized by the docking of the N-terminal myristoyl of the Abl 1b variant into a hydrophobic cleft at the bottom of the KD C-lobe[15]. The assembly of the core impedes efficient substrate binding[13], presumably by hindering hinge motions between the KD C- and N-lobes[16], and reduces the kinase activity by 10- to 100-fold relative to the isolated kinase domain[3,16]. The precise role of the myristoyl docking for the stabilization of the assembled core and for downregulation is unclear, since this core assembly is also observed in solution for an SH3-SH2-KD construct lacking the N-cap (residues 83-534, 1b numbering; hereafter called Abl^{core} or regulatory core)[17] and since both the non-myristoylated Abl 1a and Abl^{core} have low kinase activity[14,16]. Abl's long, mostly unstructured C-terminal tail, aka last exon region, which is absent in all other closely related cytoplasmic tyrosine kinase (CTK) families, such as Src, has not been reported to have regulatory function, but rather harbors protein localization and protein-protein interaction sites[13,18].

In contrast to the well characterized, inactive assembled state of the Abl regulatory core, the nature of the active state remains unclear. The activated form has been mimicked by disrupting the internal SH3 polyproline binding site in the SH2-KD linker by P242E,P249E point mutations in an SH3-SH2-KD construct[14]. SAXS solution data of this form are compatible with an arrangement of the SH2 domain "on top" of the KD N-lobe[14], the so-called 'top-hat' conformation (Figure 1D), which has also been observed under certain conditions by crystallography, in particular for constructs lacking the SH3 domain[14,19,20]. A recent NMR study has modeled the activation mechanism by a simple two-site exchange between the assembled form and the 'top-hat' conformation[21]. The *in vitro* effects of point mutations in the top-hat SH2-KD-N-lobe interface on kinase activity are, however, rather small as compared to strong *in vivo* effects[20].

Surprisingly, the addition of ATP site inhibitors such as imatinib also opens the assembled conformation of the unmodified SH3-SH2-KD core, as evident from solution NMR and SAXS data[16,17] (Figure 1C). The opening strictly correlates with the activation loop (A-loop) conformation induced by the inhibitors, as only type II inhibitors with an inactive A-loop conformation but not type I inhibitors with an active A-loop conformation open the core[16]. The binding of type II inhibitors also leads to increased phosphorylation of residue Y245 in the SH2-KD linker in Ba/F3 cells, presumably due to the disassembly of the core[17]. This may be relevant as a priming mechanism for enhanced Abl activity after inhibitor washout. The opening by type II inhibitors can be explained by a push of the A-loop onto the KD N-lobe, which breaks the interface between the KD and the SH3/SH2 domains[16]. A similar motion is expected for substrate binding and would be impeded in the closed conformation. Solution NMR residual dipolar coupling (RDC) and ^{15}N relaxation data[17] show unequivocally that this inhibitor-induced disassembled state is highly dynamic, with the SH3 and SH2 domains moving with large amplitudes on the nanosecond timescale relative to the KD (Figure 1C). Addition of the allosteric inhibitor GNF-5 brings the inhibitor-induced disassembled state back to the assembled state[17].

This account shows that precise knowledge on the activated state is scarce and has so far mostly been insinuated indirectly by using non-natural mutations or type II ATP site inhibitors, which open the assembled core. Moreover, the large-amplitude nanosecond domain motions observed in the inhibitor-induced disassembled state are incompatible with a static 'top-hat' conformation or a two-site exchange between 'top-hat' and assembled form. The lack of precise structural and dynamical data on the activated state results from limitations of NMR and SAXS solution techniques to detecting small subpopulations of the activated state within

the predominantly assembled conformation of regulated Abl. In contrast, the high sensitivity of Förster resonance energy transfer (FRET) in combination with modern time-correlated single photon counting (TCSPC[22]) and multiparameter fluorescence detection (MFD[23]) allows to follow the conformation of single molecules on timescales from nanoseconds to the diffusion time through the confocal volume (several milliseconds). Thereby also rare dynamical events can be detected.

Here we have used single-molecule FRET (smFRET) to follow the structural dynamics of the Abl regulatory core under uninhibited and inhibited conditions. FRET donor-acceptor pairs were introduced into Abl via unnatural amino acids and bioorthogonal fluorophore labeling, since conventional cysteine-based chemistry was not possible due to the Abl's low stability in solution. The use of the unnatural amino acids allowed the labeling at strategic positions to distinguish clearly between assembled, 'top-hat', and other disassembled conformations. The results reveal that the apo form, although adopting mainly the assembled conformation, disassembles to about 30 %. The addition of allosteric inhibitors almost completely pushes this equilibrium to the assembled conformation, which explains their inhibitory power. In contrast, the addition of the type II ATP site inhibitors imatinib, ponatinib, and nilotinib disassembles the core to a state with sub-millisecond dynamics as observed previously[16,17]. Adding allosteric inhibitors to the type II complexes then shifts the equilibrium back to a mainly assembled conformation, which still undergoes occasional disassembly.

Results and Discussion

Abl SH3-SH2-KD is not amenable to FRET labeling via cysteine chemistry

We initially sought to label the Abl regulatory core (Abl^{core}) by conventional ligation of cysteines with FRET donor and acceptor fluorophores. Abl^{core} contains six cysteines (C119 in SH3, and C324, C349, C388, C483, C494, all in the KD), none of which is involved in disulfide bonds. Screening by the FRET Positioning and Screening (FPS) software[24] predicted that C349 and C483 should be accessible and therefore reactive in the assembled crystal structure (PDB 2FO0[14]), whereas C324 should be additionally accessible in the 'top-hat' structure (PDB 4XEY[20], molecule B). The remaining cysteines C119, C388 and C494 were predicted to be inaccessible in all conformations. To test these predictions, we reacted Abl^{core} with an excess of Alexa Fluor 488 maleimide. An LC-MS/MS analysis revealed that at least four of the six cysteines had reacted with Alexa Fluor 488 (C119: 47 %, C324: 98 %, C388: 6 %, C483: 64 %), whereas peptides containing C349 or C494 could not be detected. To follow the core disassembly by FRET, one of the dyes needs to be either located in the SH3 or SH2 domain and the other in the KD. Since C119 is buried in the SH3 structure, its use for labeling appeared problematic. Indeed, even the conservative C119S mutation led to a strong decrease in solubility. Further tests showed that Abl^{core} tolerated the mutations C324V and C349S, but the mutations C483A, C483V, and C483S also led to dramatic reductions in solubility. Due to these imponderables of the cysteine replacement and labeling on the stability of the Abl^{core} structure and function, we sought to rather attempt bioorthogonal fluorophore labeling of unnatural amino acids (propargyl-lysine, PrK) introduced into the Abl^{core} by amber codon reassignment (see below), which would give complete flexibility on the positions of the FRET donor and acceptor dyes.

In silico screening for suitable FRET pairs in Abl^{core} to distinguish core conformations.

Making use of this freedom, we screened the assembled conformation (PDB 2FO0[14]), the 'top-hat' conformation (PDB 4XEY[20]), and the best three models for the inhibitor-induced, dynamic, disassembled conformation[17] by the FPS software[24] for Alexa Fluor 488/647-labeled PrK FRET pairs that would be well suited to distinguish between the different expected conformations of the Abl core. Residues known to be relevant for kinase function and integrity as well as the SH3 domain, which is not contained in the known 'top-hat' structures, were excluded from the screen. From several possible FRET pairs with high distinguishing power, we chose N196(SH2)-Q510(KD C-lobe) and A225(SH2)-M297(KD N-lobe) for

implementation as PrK_2 mutants into the Abl^{core}. The predicted FRET average distances $<R_{DA}>$ for the fluorophore-labeled Abl^{core}-196*-510* PrK_2 mutant are 33 Å for the assembled, 57 ± 5 Å for the disassembled, and 82 Å for the 'top-hat' conformation (Table 1, Figure 3B). These distances translate to respective high-, mid- and low-FRET states for the 52-Å Förster radius of the used Alexa Fluor 488/647 pair. An inverted distance and FRET behavior are expected for the fluorophore-labeled Abl^{core}-225*-297* mutant.

Table 1. Expected FRET-averaged interdye distances for several FRET pair mutants within the assembled, disassembled, and 'top-hat' conformations.

Conformation/PDB code	N196-Q510[a]		A225-M297[a]	
	$<R_{DA}>$ [Å][b]	E_{FRET}	$<R_{DA}>$ [Å][b]	E_{FRET}
Assembled/2FO0[c]	33.0	0.94	81.5	0.06
Disassembled[d]	56.8 ± 5.1	0.38 ± 0.13	58.6 ± 8.7	0.36 ± 0.19
'Top-hat'/4XEY[e]	82.0	0.06	31.2	0.96

[a] Labeling positions of the two dyes.
[b] The FPS program[24] was used to dock the donor (Alexa Fluor 488) and acceptor (Alexa Fluor 647) molecules to their respective labeling positions in different Abl structures/models. The used dye parameters are given in Materials and Methods. Thereby, the accessible volumes (AVs) of the dye molecules were simulated and the resulting expected FRET efficiencies, E_{FRET}, and FRET-averaged interdye distances, $<R_{DA}>$, derived.
[c] Input structure for the assembled core conformation[14].
[d] The best three models of the disassembled conformation derived from solution NMR/SAXS data[17] were used to calculate a mean value and standard deviation of $<R_{DA}>$ and E_{FRET}.
[e] Input structure for the 'top-hat' conformation[20].

Abl SH3-SH2-KD expression with two propargyl-lysines and labeling with FRET donor and acceptor pair for smFRET experiments

The PrK pairs were introduced into the two mutants Abl^{core}-196^{TAG}-510^{TAG} and Abl^{core}-225^{TAG}-297^{TAG} using the PylRS/$tRNA^{Pyl}$ expression system for amber codon reassignment[25]. After extensive screening for expression conditions starting from published protocols[25], we obtained yields of the purified Abl^{core}-PrK_2 mutants close to those of wild-type Abl^{core}. These mutants were then labeled with Alexa Fluor 488 and 647 as FRET donor and acceptor, respectively, via the copper(I)-catalyzed alkyne-azide cycloaddition (CuAAC, "click") reaction[26]. Of note, due to the low stability of the PrK mutants, the CuAAC reaction had to be carried out in the presence of imatinib, which was later washed out during the preparation of the picomolar FRET samples. Also due to this low stability, the labeling was performed as a one-step procedure, i.e. through reaction with a mixture of donor and acceptor fluorophores. This resulted in a mixture of donor-only (D_{only}), acceptor-only (A_{only}), and FRET-

labeled donor-acceptor (DA) Abl^{core} molecules (Figure 2A), which was enriched in the DA fraction by a further ion-exchange chromatography step. Single-molecule fluorescence events arising from DA molecules were then separated from the remaining D_{only} and A_{only} molecules by a two-dimensional digital filter of the MFD data according to FRET efficiency and the donor-acceptor stoichiometry (Figure 2B).

FRET distance distributions of apo Abl and its complexes with ATP site and allosteric inhibitors reveal opening and closing of the regulatory core

The conformational dynamics of the Abl regulatory core was analyzed from the single-molecule MFD data recorded on the FRET-labeled Abl^{core}-PrK_2 mutants in apo form and in complexes with type II ATP site and allosteric inhibitors. A basic analysis of the one-dimensional FRET efficiency histograms reveals the following (Figure 3). Apo Abl^{core}-196*-510* (the asterisk marks fluorophore-labeled residues) exhibits a bimodal population distribution. The main peak (~60 % population) is narrow and centered around a maximum at 96 % FRET efficiency (E_{FRET}) corresponding to a distance of ~31 Å. This distance agrees well with the 33 Å expected for the assembled conformation (Table 1). However, also a second, minor (~34 %) broad population peak is observed, which is centered around E_{FRET} = 65 % (47-Å distance). This population apparently corresponds to an occasional opening of the core, which is corroborated by the detailed kinetic analysis of the MFD data (see below). When asciminib is added to apo Abl^{core}-196*-510*, this second broad peak almost vanishes, resulting in a unimodal distribution with a maximum at 96 % FRET efficiency that is identical to the main population peak of apo Abl^{core}-196*-510*. This important observation shows the efficacy of asciminib to suppress the opening of the core and to stabilize its assembled, inhibited conformation.

The addition of imatinib to apo Abl^{core}-196*-510* shifts the FRET histogram towards a broad unimodal distribution centered at E_{FRET} = 40 % (56-Å distance), which must be a mainly disassembled core conformation. This corroborates the earlier NMR and SAXS findings that type II inhibitors disassemble the core[16,17]. A further addition of asciminib shifts the conformational equilibrium back to a mainly high-FRET state with maximum at E_{FRET} = ~92-96 %, showing the power of this drug to induce an assembled core even against the destabilizing action of the type II inhibitor. However, as compared to the apo form and the asciminib complex, the FRET distribution of the ternary imatinib•asciminib complex is considerably more smeared out towards lower FRET values, which indicates an enhanced occasional opening of the core. Identical observations were made for all conformations of

Abl^{core}-196*-510*, when the allosteric inhibitor asciminib was replaced by one of its precursor molecules, GNF-5, to form the complexes Abl^{core}-196*-510*•GNF-5 and Abl^{core}-225*-297*•imatinib•GNF-5 (Supplementary Figure S1). Notably, the results are highly similar for two other type II ATP site inhibitors: ponatinib and nilotinib (Supplementary Figure S2).

For all investigated forms of Abl^{core}-196*-510*, analogous observations were obtained for the second FRET pair mutant, Abl^{core}-225*-297*. Similar to apo Abl^{core}-196*-510*, the distribution for apo Abl^{core}-225*-297* is bimodal with a main peak at the maximum ~20 % E_{FRET}, which is in the range expected for the assembled conformation. A second, very broad peak extends from 40 % to 100 % E_{FRET}, which must correspond to a distribution of disassembled conformations. Both the disassembled conformations calculated from NMR and SAXS data and the 'top-hat' conformation agree with this wide distribution of E_{FRET} values. Clearly, this disassembled conformation is suppressed by the action of asciminib in the asciminib complex, and a unimodal distribution corresponding to the assembled conformation with its maximum at ~20 % E_{FRET} remains. Again, the addition of imatinib to Abl^{core}-225*-297* induces a dramatic change in the FRET histogram with a very broad unimodal distribution with maximum at E_{FRET} = 60 %, indicating a heterogeneous, probably dynamic ensemble of disassembled conformations. This disassembly is then reversed by asciminib in the ternary imatinib•asciminib, leading to a unimodal distribution at low E_{FRET} values similar to the assembled form of the asciminib complex.

It has previously been speculated that the T231R mutation found in cancer patients[27] stabilizes the 'top-hat' conformation[19, 20], which may explain its increased catalytic activity. To investigate this effect, we also produced a FRET Abl^{core}-196*-510* T231R mutant. Interestingly, this mutant shows identical FRET efficiency histograms for apo Abl^{core} and its asciminib, imatinib and imatinib•asciminib complexes as the 'wild-type' Abl^{core}-196*-510* (Figure 3). Stabilization of the 'top-hat' conformation should have shifted the FRET histograms to lower efficiency values. Since this is not observed, other explanations for the increased activity of the T231R mutant are more likely.

The disassembled conformation of Abl is highly dynamic

In order to better understand the dynamics of the conformational equilibrium of Abl, we expanded the one-dimensional FRET efficiency histograms with the fluorescence-weighted donor lifetime in presence of the acceptor, $<\tau_{D(A)}>_F$, to two-dimensional MFD histograms (Figure 4). Events located on the 'static FRET line' (orange line)[28] in these two-dimensional

MFD histograms correspond to donor-acceptor pairs that are not changing during the observation. In contrast, events shifted to the right of this static FRET line result from conformational exchange.

For all investigated Abl mutants, the main populations of the apo form and of complexes with either asciminib or GNF-5 (Supplementary Figure S1) are centered on the static FRET line (Abl^{core}-196^{*}-510^{*}: E_{FRET} = 94 %, $<\tau_{D(A)}>_F$ = 0.44 ns; Abl^{core}-225^{*}-297^{*}: E = 23 %, $<\tau_{D(A)}>_F$ = 3.15 ns), i.e. the molecules do not disassemble during their diffusion through the confocal volume for a few milliseconds. Importantly, the two-dimensional histograms clearly show that the apo form of Abl^{core}-PrK_2 does not adopt this single static conformation, but rather exchanges with a disassembled conformation, as seen from the smeared-out populations off the static FRET line for Abl^{core}-196^{*}-510^{*} (center: E_{FRET} ~ 62 %, $<\tau_{D(A)}>_F$ = 2.86 ns) and to a lesser extent, but still clearly visible, for Abl^{core}-225^{*}-297^{*} (center: E_{FRET} ~ 60 %, $<\tau_{D(A)}>_F$ ~ 2.5 ns). Since the population peak is rather smeared-out and not very sharp, we can conclude that this exchange rate is close to the diffusion time, i.e. on the millisecond timescale. As already observed from the FRET efficiency histograms, this dynamic population is less populated in the binary asciminib and GNF-5 complexes (Figure 4 and Supplementary Figure S1), indicating a stabilization of the assembled core by the allosteric inhibitors. In contrast to the apo and the binary allosteric inhibitor complexes, the population centers of the imatinib complexes are shifted away from the static FRET line (Abl^{core}-196^{*}-510^{*}: E_{FRET} = 37 %, $<\tau_{D(A)}>_F$ = 3.48 ns; Abl^{core}-225^{*}-297^{*}: E_{FRET} = 58 %, $<\tau_{D(A)}>_F$ = 2.64 ns), indicating that these molecules are not static on the millisecond timescale (Figure 4). A similar observation is made for the Abl^{core}-196^{*}-510^{*}•ponatinib and •nilotinib complexes (Figure S2). Since these distributions are relatively narrow and unimodal, the exchange dynamics must be considerably faster than the diffusion time of the protein within the confocal volume (few milliseconds). This dynamic disassembled conformational equilibrium is then shifted toward the assembled conformation by asciminib in all ternary Abl^{core}•type II inhibitor•asciminib complexes (Figure 4 and S2). However, as compared to the apo form, the population distribution of the ternary Abl^{core}-196^{*}-510^{*} complexes is more smeared out off the static FRET line towards the low-FRET states, which indicates stronger opening with dynamics close to the millisecond diffusion time.

As already observed in the one-dimensional E_{FRET} histograms, the T231R mutant behaves almost identically to the wildtype except for a small fraction of events with E_{FRET} = 0, which also appears in various other measurements and may most likely be attributed to an artefact.

Preliminary results: 'Kinetic analysis of FRET data'

So far, we can conclude from the presented results that the assembled conformation is in equilibrium with at least one disassembled state. However, the MFD data contain further information that can be used to derive an in-depth kinetic description of the conformational equilibria[29]. Using filtered fluorescence correlation spectroscopy (fFCS), the minimal number of interconverting states and their exchange dynamics from nanoseconds to milliseconds can be determined. Furthermore, the limiting states at nanosecond resolution can be determined from ensemble or sub-ensemble time-resolved fluorescence (TCSPC) via fitting the donor fluorescence lifetime. These analyses are currently ongoing with our collaborators at the University of Düsseldorf.

A preliminary analysis of the Abl^{core}•imatinib complex by fFCS (Figure 5A) reveals three relaxation times, t_{Ri} (t_{R1} = 129 ns, t_{R2} = 7.17 µs, t_{R3} = 129.5 µs with respective amplitudes 0.42, 0.28, 0.30). This indicates at least four interconverting states. Possibly, these states may be assigned by thorough analysis of all inhibitor complexes for the three measured samples.

In order to define the limiting states in the ensemble, we performed a preliminary unbiased sub-ensemble donor fluorescence lifetime fitting (seTCSPC, Figures 5B, 5C and Table 2) of the respective ensemble (denoted 'FRET' in Table 2), and sub-ensembles high-FRET (HF), mid-FRET (MF), and very-low-FRET (VLF) for apo Abl^{core}-196*-510*, Abl^{core}-196*-510*•imatinib, and Abl^{core}-196*-510*•asciminib. Since the fFCS analysis had revealed four interconverting states, we globally fitted four states, each with a fixed distribution width (σ = 6 Å) taking dye mobility into account. The fitted distances of the four states were R_1 = 21.3 Å, R_2 = 39.0 Å, R_3 = 54.4 Å, and R_4 = 121.1 Å with varying fractions χ_i for the different (sub-)ensembles of the 3 samples (Figure 5C and Table 2). Both the smallest and largest distances are not well defined due to the R^{-6} dependency and the Förster radius of 52 Å of the used FRET pair.

In the following, we give a very speculative interpretation of these initial fit results. The smallest distance (R_1 = 21.3 Å) is most likely associated with the assembled conformation. The deviation from the expected R_1 of ~30 Å may be attributed to the insensitivity to distance variations of the FRET pair at this short distance. The second distance (R_2 = 39.0 Å) might be a less tightly assembled conformation, possibly arising from a push of the C-terminal αI-helix onto the SH2 domain. This conformation is most prominent in the apo form. Addition of imatinib and the associated KD N-lobe push may lead to an immediate disassembly from this conformation. Accordingly, this state is less populated in the imatinib complex. It also is less populated in the Abl^{core}-196*-510*•asciminib complex, in agreement with the fact that in the

latter the αI-helix is bent away and does not push onto the SH2 domain. The third state (R_3 = 54.4 Å) fits surprisingly well to the expected value for the disassembled conformation and is most prominent in the Abl^{core}-196*-510*•imatinib complex. The meaning of the largest distance (R_4 = 121.1 Å) is the least clear. It may be associated with the 'top-hat' conformation or just be an artefact as discussed above for the small population at E_{FRET} = 0. Interestingly, in the sub-ensemble fits of the VLF population, significant amplitudes only occur for R_1 and R_4, indicating an exchange between these seemingly contrasting states. A possible explanation is that the dyes may have physical contact in the tightly assembled conformation, which could lead to acceptor quenching and consequently a VLF artefact.

Table 2. Global sub-ensemble TCSPC decay fit of a 4-state model of Abl^{core}-196*-510* in various complexes.

	Species fractions χ_i [%] (DA distance R_i of state i)[a]			
	χ_1 (21.3 Å)	χ_2 (39 Å)	χ_3 (54.4 Å)	χ_4 (121.1 Å)
Complex/ sub-ensemble[b]				
Apo				
FRET	53	22	3	23
HF	87	10	0	3
MF	44	13	11	32
VLF	48	0	0	52
Imatinib				
FRET	57	6	10	26
HF	89	7	2	3
MF	56	4	13	27
VLF	54	0	0	46
Asciminib				
FRET	84	9	0	7
HF	91	7	0	2
MF	60	19	0	21
VLF	61	0	0	39

[a] The TCSPC decay histograms of the below listed ensembles were globally fitted with two D_{only} lifetimes ($\langle\tau_{D(0)}\rangle_{F,1}$ = 4.17 ns and $\langle\tau_{D(0)}\rangle_{F,2}$ = 1.57 ns) and four Gaussian-shaped FRET species distributions with species fractions χ_i and donor-acceptor (DA) distances R_i. The distribution width σ was kept constant at 6 Å allowing for dye motion due to its flexible linker.

[b] The TCSPC decay diagrams of apo Abl^{core}-196*-510*, Abl^{core}-196*-510*•imatinib, and Abl^{core}-196*-510*•asciminib were fitted for the following sub-ensembles, which were selected from the two-dimensional MFD E_{FRET} vs. stoichiometry (S_{PIE}) plots. 'FRET' includes all events with $0.33 < S_{PIE} < 0.67$. HF (high-FRET) selects additionally all events with $E_{FRET} > 0.8$, MF (mid-FRET) selects all events with $0.2 < E_{FRET} < 0.8$, and VLF (very-low-FRET) includes all events with $E_{FRET} < 0.2$.

These interpretations are very preliminary and a number of unclear questions remain: do we need four states to fit the data or is a three-state model sufficient? In an initial 3-state model

fit, the first two states, R_1 and R_2, combined to one state with a distance of roughly 30 Å, which fits well the expected value of the assembled conformation. What is the R_4 state and why is it so prominent, even though the population at VLF looks rather negligible? Why is the presumed assembled state so prominent also in the imatinib complex? Why does the disassembled R_3 state have such a narrow distribution? From the NMR relaxation data[17], we would have expected a continuum of states, i.e. a rather broad distribution around roughly 55 Å. The currently ongoing deeper analysis is expected to resolve these issues and to yield a well-founded interpretation of the data.

Conclusion and Perspective

In summary, we have followed the conformational dynamics of Abl^{core} by smFRET experiments. To be able to carry out smFRET observations, we incorporated a pair of the unnatural amino acid propargyl-lysine into the Abl^{core} and subsequently labeled the protein site-specifically with Alexa Fluor 488 and Alexa Fluor 647 using the copper-catalyzed alkyne-azide cycloaddition "click" reaction[26]. Using MFD[23] we were able to investigate the highly dynamic nature of Abl^{core} in the apo state and in complexes with various inhibitors.

Apo Abl^{core} adopts mainly the assembled conformation, which was observed in crystal structures[14] and in solution by NMR and SAXS[17]. However, a specific population of roughly 30 % was found in dynamic exchange with a disassembled conformation. This opening of the apo Abl^{core} has not been observed before. In the assembled conformation, nucleotide binding is excluded by a restricted P-loop motion due to SH3 docking onto the KD N-lobe[16]. The observed slightly open conformation probably allows for substrate and nucleotide binding and release, i.e. catalytic turnover. Possibly the Abl^{core} has to disassemble even further to allow for effective substrate binding to the Abl SH2 or SH3 domains[30]. The dynamic disassembly of the apo form would then act as a priming mechanism for full activation. The achieved fluorophore labeling together with the experimental smFRET setup will allow to investigate in real time this catalytic process with substrates, e.g. with the optimized 'Abltide' peptide containing a phosphorylation site or 'real' substrates or interaction partners like CrkL. Thereby, we hope to gain new insights into the molecular bases of Abl activation.

Upon addition of the allosteric inhibitors asciminib and GNF-5, the dynamic disassembled conformation is almost completely quenched. Asciminib is a highly promising drug candidate to overcome drug resistances of so far untreatable Abl mutations[10, 11]. This drug development was based on the finding that binding of Abl's N-terminal myristoyl to the myristoyl pocket at the bottom of the KD C-lobe induces a kink in the C-terminal αI-helix[13, 31]. This kink was

proposed to stabilize the assembled, inhibited conformation[13], an effect which would be also achieved by the developed drugs. However, the stabilizing effect on the core conformation either by myristoyl or allosteric inhibitors has never been shown directly until now. Here, we prove this hypothesis by observing a drastic reduction of the dynamic disassembled population in the presence of asciminib.

It would be interesting to compare the stabilizing effect of asciminib on the assembled conformation with that of myristoyl in a myristoylated Abl construct including the N-cap (myr-Abl^{cap}) by smFRET experiments. We hypothesize that the stabilizing effect by myristoyl is smaller, since native myr-Abl^{cap} must be capable of enzymatic turnover. This requires a partial opening of the regulatory core, which is almost abolished with bound asciminib. Production of myr-Abl^{cap} samples for FRET experiments, however, would either require expression with incorporation of PrK in insect or mammalian cells or the co-expression of a suitable myristoyl transferase in *E. coli*. The expression in higher eukaryotes may be easier and more flexible, since systems for incorporation of unnatural amino acids have already been described[32]. Once this is achieved, we will aim to produce even longer constructs such as full-length Abl (aa 1–1049) and the disease-related Bcr-Abl fusion protein for smFRET observation.

Addition of the type II ATP site inhibitors imatinib, ponatinib, and nilotinib leads to a more disassembled conformation than that of the apo form in agreement with NMR and SAXS observations[16, 17]. From the presented two-dimensional MFD plots, one can readily see that this disassembled conformation is dynamic on the submillisecond timescale. Interestingly, although the third-generation drug ponatinib is capable of treating the imatinib-resistant gatekeeper mutation (T334I), no difference in the dynamic behavior relative to imatinib is observed in the smFRET experiments. The differing drug efficacy must therefore be caused by an optimized binding of ponatinib to the gatekeeper mutant with its bulkier isoleucine located in the ATP pocket.

Further addition of the allosteric drug asciminib to the binary type II inhibitor complexes shifts the conformational equilibrium back towards the assembled conformation. However, this interaction is not strong enough to fully close the core again. We rather observed a broad conformational distribution on the millisecond timescale between the assembled and the disassembled conformation. This supports our previously proposed mechanical model[16], in which both the push of the αI-helix towards the SH2 domain and the push of the KD N-lobe towards the SH3 domain are required for core opening.

One of the motivations for this project was to investigate the ‘top-hat’ conformation, if it exists. So far, we could neither confirm nor disprove its existence by NMR experiments, due

to broadening of KD N-lobe resonances, even though claims in the literature, based on NOEs between the KD N-lobe and the SH2 domain[21], confirm the 'top-hat' conformation. However, the dynamics data from NMR relaxation experiments[17] argue against a static 'top-hat' conformation. Thus, we were hoping to observe the 'top-hat' conformation by smFRET.

So far, however, we can only exclude the presence of a static 'top-hat' conformation on the millisecond timescale from the two-dimensional FRET histograms since no significant population was observed for the Abl^{core}-225*-297* sample on the static FRET line at the respective FRET efficiency of roughly E_{FRET} = 90 %. This sample was specifically designed to show a strong FRET for the 'top-hat' conformation. Notably, in the Abl^{core}-196*-510* sample, we indeed observe a very small population (near E_{FRET} = 0), which could correspond to the 'top-hat' conformation. Also, sub-ensemble fluorescence lifetime fitting had led to a possible 'top-hat' species. Nevertheless, the small peak at almost zero FRET is most likely an artefact for many reasons: (i) its population was not reproducible; (ii) it appears independently of the ligand, and (iii) in some measurements, this population massively grew over the course of the experiment, which was always accompanied with a dramatic loss of DA-labeled molecules in the solution.

Yet, the 'top-hat' conformation could still exist in exchange with a less disassembled or fully assembled conformation on timescales faster than the diffusion time, which would account for the dynamic populations shifted away from the static FRET line. Results of the currently ongoing in-depth dynamical analysis of the MFD data may prove or disprove the presence of the 'top-hat' conformation on timescales faster than milliseconds.

An independent approach will be to investigate mutations and constructs that should stabilize or destabilize the 'top-hat' conformation. We have started on an Abl^{core}-196*-510* T231R mutant. This T231R mutation has been identified in cancer patients and confers high *in vivo* kinase activity[27]. It has recently been speculated that T231R stabilizes the 'top-hat' conformation in an SH2-KD construct[19, 20]. However, no difference in the smFRET experiments was observed between the wild-type Abl^{core} and the Abl^{core} T231R mutant. A further interesting mutant to investigate will be Abl^{core} I164E. This mutant shows decreased activity in *in vitro* kinase phosphorylation assays, inhibits downstream signaling pathways important for CML maintenance, and abolishes leukaemogenesis in a CML mouse model[19, 20, 33]. The I164E mutation also changed the overall shape of an SH2-KD construct observed by solution SAXS experiments[19]. As residue I164 is located on the KD N-lobe at the interface to SH2 domain in the 'top-hat' conformation[20], the I164E mutation is presumed to destabilize the latter. Furthermore, we plan to probe the 'top-hat' conformation by smFRET in

the absence of the SH3 domain in an $Abl^{SH2\text{-}KD}$ construct, since the 'top-hat' conformation was observed for this construct by crystallography[20] and in SAXS solution experiments[19]. Thus, we expect a shift of the conformational equilibrium in the FRET histograms of $Abl^{SH2\text{-}KD}$ relative to Abl^{core}, if indeed the 'top-hat' conformation exists for $Abl^{SH2\text{-}KD}$.

The ultimate goal of this project will be the observation of Abl dynamics inside the cell. The most promising approach is currently to fluorescence-label Abl outside of the cell, followed by cell penetration of labeled proteins caused by electroporation[34] and subsequent in-cell MFD imaging experiments[35]. This could be started immediately for the described Abl^{core} mutants and later be extended to larger parts of Abl or Bcr-Abl when suitable eukaryotic expression systems for unnatural amino acids are in place.

Material and Methods

Cloning, expression and purification

The expression plasmid encoding the 83–534 fragment (1b numbering, Abl^{core}) of Abl with an N-terminal His_6-tag and a PreScission protease (GE Healthcare) cleavage site, which leaves an N-terminal GP overhang, has been described previously[17]. For incorporation of two propargyl-lysine (PrK) amino acids and subsequent double-fluorophore labeling, two TAG amber stop codons where introduced at the respective sequence positions, namely 196+510 and 225+297, by QuikChange™ (Agilent) site-directed mutagenesis. The modified Abl^{core} plasmids were expressed based on a protocol by Lemke and coworkers[25] with some modifications. In brief, the Abl expression plasmid was co-transformed together with pEVOL-$PylRS^{wt}$ (a generous gift by E. Lemke, EMBL) into BL21-AI cells. The latter plasmid encodes the tRNA and aminoacyl-tRNA-synthetase, which are necessary for PrK incorporation at an amber codon position. Typically, 1-L expression cultures were started at OD 0.1–0.2 in terrific broth (TB) medium containing 50 mg/mL streptomycin and 34 mg/mL chloramphenicol and grown to OD 0.3–0.4 at 37 °C. At this point, 5 mM PrK (Sirius Fine Chemicals SiChem, Bremen, Germany), freshly dissolved in 0.1 M NaOH and sterile-filtered, were added to the culture and growth continued until OD 0.6. Then cultures were cooled down to 18 °C and further grown to OD 0.8, at which point expression was induced by 0.1 mM IPTG and 0.2 % L-(+)-arabinose. After about 20 h, cells were harvested and expression of Abl confirmed by SDS-PAGE or western blot.

After cell harvest, Abl was purified as described previously[16] using sequentially Ni-NTA chromatography, PreScission cleavage, ion-exchange chromatography, dephosphorylation by lambda phosphatase (LPP) and size-exclusion chromatography. The final product was homogeneous with correct protein mass and complete dephosphorylation confirmed by electrospray ionization time-of-flight (ESI-TOF) mass spectrometry (MS). Truncated Abl fragments as a result from an undesired expression stop at the amber codon were efficiently removed during the extended purification. The purified Abl^{core} PrK mutants were frozen at -80 ˚C in ~10 µM concentration with 50 mM Tris, 150 mM NaCl, 2 mM TCEP, 5 % glycerol, pH 8.0, until further use. The obtained yields reached up to 3 mg per L expression culture, which is very similar to wild-type Abl^{core}.

Fluorophore labeling

The copper(I)-catalyzed alkyne-azide cycloaddition (CuAAC) "click" reaction[26] (Figure 2A) was used for simultaneous donor-acceptor labeling of the Abl^{core} mutants containing two PrK residues (Abl^{core}-PrK_2) by the azide-coupled Alexa Fluor 488 (donor) and 647 (acceptor) dyes (Thermo Fisher Scientific, MA, USA). Reaction conditions for this system were optimized starting from previously described protocols[25, 36, 37].

It was essential to carry out the labeling reactions on the Abl^{core}-PrK_2 mutants saturated by imatinib, since the apo forms were not stable enough. For this, the thawed stock solutions were incubated with a 3-fold excess of imatinib (BioVision, Inc.) for 30 min at room temperature, buffer-exchanged 3 times by washing with a 20–50 volume excess of labeling buffer (50 mM HEPES, 200 mM NaCl, 5 % glycerol, pH 8.0), and concentrated to ~75 µM Abl in ~150 µL using a 30-kDa molecular weight cutoff centrifugal filter (Amicon). Complete removal of TCEP from the storage buffer was crucial, since TCEP effectively inhibits the labeling reaction. A reaction mixture containing the fluorophores was prepared as follows. 20 µL 100 mM Tris(3-hydroxypropyltriazolylmethyl)amine (THPTA) were incubated with 2 µL 100 mM $CuSO_4$ at room temperature for 30 min. Then, 10 µL freshly prepared 100 mM aminoguanidine, 6 µL each of 5 mM Alexa Fluor 488 azide (Invitrogen) and 5 mM Alexa Fluor 647 azide (Invitrogen) in DMSO were added. (For $Abl^{196/510PrK}$ the amount of Alexa Fluor 647 was doubled due to the poor acceptor labeling efficiency in this mutant.) This reaction mixture was added to the protein solution and the reaction was started by adding 4 µL freshly prepared 500 mM sodium ascorbate. Final concentrations for the reaction were: ~50 µM Abl, 150 µM Alexa Fluor 488 azide, 150 or 300 µM Alexa Fluor 647 azide, 1 mM $CuSO_4$, 10 mM sodium ascorbate, 10 mM THPTA, and 5 mM aminoguanidine, pH 8.0. The reaction was carried out for 4 h at 10 °C in the dark and stopped by the addition of 2 mM EDTA.

This reacted mixture was then buffer-exchanged to FRET sample buffer (50 Tris, 200 mM NaCl, 5 % glycerol, 2 mM DTT, pH 8.0) using a 30-kDa molecular weight cutoff centrifugal filter (Amicon). (Note that the reducing agent TCEP cannot be used after dye conjugation, since TCEP reacts with Alexa Fluor 647[38] and also appeared to destabilize the dye-protein bond under our conditions.) The sample was then loaded onto a Resource Q 1-mL column (GE healthcare) and eluted by a 0.05–1 M NaCl gradient in 20 mM Tris, 5 % glycerol, 2 mM DTT, pH 8.0. The fractions containing the labeled protein as indicated by simultaneous absorbances at 280, 495 (donor), and 650 (acceptor) nm were collected, concentrated and buffer-exchanged using a 30-kDa molecular weight cutoff centrifugal filter (Amicon) to 0.5-1 µM protein, 50 mM Tris, 200 mM NaCl, 2 mM DTT, 5 % glycerol, pH 8.0, and finally stored at -80 °C until

further usage. Obtained degrees of labeling (DOL) were 50–80 % for the donor and 60–100 % for the acceptor. The fraction of unreacted dye as judged by FCS experiments was lower than 5 % in these preparations.

FRET label accessibility and position screening

The FRET positioning and screening (FPS) software[24] was used to calculate the accessible volume (AV) of a fluorophore attached to the C^{β} atom of a specific residue of Abl^{core} with the following parameters for linker length, linker width, and dye radius, respectively. Donor (PrK-Alexa Fluor 488): 20 Å, 4.5 Å, 3.5 Å; acceptor (PrK-Alexa Fluor 647): 22 Å, 4.5 Å, 3.5 Å.

smFRET experiments and data analysis

For smFRET measurements, the stock solutions of FRET-labeled Abl^{core}-PrK_2 mutants were diluted to a concentration of approximately 100 pM in measurement buffer (50 mM Tris, 200 mM NaCl, 2 mM DTT, pH 8). The concentration was adjusted for every sample, which had varying degree of labeling, in order to have a maximum of one fluorophore-labeled molecule in the confocal observation volume. All smFRET multiparameter fluorescence detection (MFD) measurements were carried out at 30±0.3 °C in an 8-well Nunc™ Lab-Tek™ chamber cell with 170 µm coverslip located in thermos-stabilized microscope stage incubator (OKO UNO-controller, OKOLAB, Italy). Additionally, a heater around the objective connected to the controller was used to increase the stability of the solution temperature, which was in contact with the objective lens via the immersion water. Before sample application, the chambers were passivated by 3 µM BSA solution for 2 min, washed with measurement buffer afterwards, and placed into the incubator at least 30 min before sample application.

MFD measurements with pulsed interleaved excitation (PIE) were performed as demonstrated previously[39]. In brief, a confocal epi-illuminated setup based on an Olympus IX71 inverted microscope was used. Excitation is achieved using 485-nm and 635-nm pulsed diode lasers (LDH-D-C 485 and LDH-P-C-635B, respectively; both PicoQuant, Berlin, Germany) operated at 32 MHz and shifted by 15.625 ns (total frequency of both lasers 64 MHz). The laser beam is focused into the sample solution by a 60X/1.2NA water immersion objective (UPLAPO 60x, Olympus, Germany). Laser power in the sample was L_{green} = 55 µW and L_{red} = 8.0 µW, respectively. For confocal detection, a 100-µm pinhole was applied for spatial filtering. Excitation and fluorescence photons were separated by an excitation beamsplitter FF550/646 (AHF, Germany). The fluorescence photon train was divided into its parallel and perpendicular components by a polarizing beamsplitter cube (VISHT11, Gsänger)

and then into spectral ranges below and above 595 nm by dichroic detection beamsplitters (595 LPXR, AHF). After separating the fluorescence signal according to color and polarization, each of the four channels was split again using 50/50 beam splitters in order to get dead time free-filtered FCS curves, resulting in a total of eight detection channels. Photons were detected by eight avalanche photodiodes (green channels: τ-SPAD-100, PicoQuant; red channels: SPCM-AQR-14, Perkin Elmer). Additionally, green (HQ 530/43 nm for Alexa Fluor 488) and red (HQ 720/150 nm for Alexa Fluor 647) bandpass filters (AHF, Germany) in front of the detectors ensured that only fluorescence from the acceptor and donor molecules were registered, while residual excitation light and Raman scattering from the solvent were blocked. The detector outputs were recorded by a TCSPC module (HydraHarp 400, PicoQuant) and stored. Data were recorded for at least 120 minutes per sample. Bursts of fluorescence photons were distinguished from the background of 0.5-1 kHz by applying certain threshold intensity criteria[39]. FRET bursts, i.e. DA molecules, were selected in all samples by applying the selection criterion 0.33 < stoichiometry ($S_{PIE)}$ < 0.67 in S_{PIE} vs. E_{FRET} plots (Figure 2B). $S_{PIE,}$ and E_{FRET}, were computed per burst as described elsewhere[40].

In seTCSPC analysis, the decay histograms were analyzed as described elsewhere[40]. From S_{PIE} vs. E_{FRET} plots, we selected the following (sub-)ensembles. 'FRET' includes all events with 0.33 < S_{PIE} < 0.67. HF (high FRET) selects additionally all events with E_{FRET} > 0.8, MF (mid FRET) selects all events with 0.2 < E_{FRET} < 0.8, and VLF includes all events with E_{FRET} < 0.2. The decay histograms were then globally fitted with two D_{only} lifetimes ($<\tau_{D(0)}>_{F,1}$ = 4.17 ns and $<\tau_{D(0)}>_{F,2}$ = 1.57 ns) and four Gaussian-shaped FRET species distributions. The distribution width σ was kept constant at 6 Å allowing for dye motion due to its flexible linker.

The fFCS analysis was performed as described elsewhere[29, 41]. High-FRET species (HF, E_{FRET} > 0.8) and low-FRET species (LF, E_{FRET} < 0.15) were selected from S_{PIE} vs. E_{FRET} plots.

Reactivity of Abl^{core} intrinsic cysteines

To test the reactivity of the Abl^{core} intrinsic cysteines, wt Abl^{core} was buffer-exchanged to thiol-maleimide reaction buffer (50 Tris, 200 mM NaCl, 5 % glycerol, pH 7.0) using a 30-kDa molecular weight cutoff centrifugal filter (Amicon) and concentrated to a final volume of ~100 µL with approximately 55 µM protein. 500 µM Alexa Fluor™ 488 C_5 maleimide (Invitrogen™) was added from a 5-mM DMSO stock solution and the reaction mixture incubated for 30 min at 25 °C in the dark. The reaction mixture was then buffer-exchanged to storage buffer (50 Tris, 200 mM NaCl, 2 mM TCEP, 5 % glycerol, pH 8.0), thereby also removing unreacted dye, and stored at -80 °C until further use.

The fluorophore-labeled sample and an unreacted Abl^{core} sample were eventually digested by trypsin into peptides in-solution. For this, 5 µg of Abl^{core} were dissolved in 20 µl digestion buffer (1 M urea, 0.1 M ammoniumbicarbonate), reduced with 5 mM TCEP for 60 min at 37 °C and alkylated with 10 mM iodoacetamide for 30 min in the dark at room temperature. After digestion with trypsin (Promega) at 37 °C overnight (protein to trypsin ratio (w/w): 50/1), the samples were supplemented with 5 % TFA to a final concentration of 0.5 % and desalted on C18 reversed-phase spin columns according to the manufacturer's instructions (Microspin, Harvard Apparatus). Then, samples were dried under vacuum and stored at -80 °C until further processing.

The peptides were then analyzed by LC-MS/MS. Since the fluorophore-labeled peptides were not directly observed, we quantified the amount of unreacted peptides in both the labeled and unlabeled samples. The difference for cysteine-containing peptides accounts for the amount of fluorophore-labeled cysteine. For the LC-MS/MS analysis, aliquots containing 1 pmol of Abl were subjected to LC-MS analysis using a dual-pressure LTQ-Obitrap Elite mass spectrometer connected to an electrospray ion source (both Thermo Fisher Scientific). Peptide separation was carried out using an EASY nLC-1000 system (Thermo Fisher Scientific) equipped with an RP-HPLC column (75µm × 30cm) packed in-house with C18 resin (ReproSil-Pur C18–AQ, 1.9-µm resin; Dr. Maisch GmbH, Ammerbuch-Entringen, Germany) using a linear gradient from 95 % solvent A (0.1 % formic acid) and 5 % solvent B (80 % acetonitrile, 0.1 % formic acid) to 30 % solvent B over 60 min at a flow rate of 0.2 µl/min. The data acquisition mode was set to obtain one high-resolution MS scan in the FT part of the mass spectrometer at a resolution of 240,000 full width at half maximum (at m/z 400) followed by MS/MS scans in the linear ion trap of the 20 most intense ions. The charged state screening modus was enabled to exclude unassigned and singly charged ions and the dynamic exclusion duration was set to 20 s. The ion accumulation time was set to 300 ms (MS) and 50 ms (MS/MS). The collision energy was set to 35 %, and one microscan was acquired for each spectrum. For all LC-MS measurements, singly charged ions and ions with unassigned charge state were excluded from triggering MS2 events.

The data was then analyzed using Progenesis QI for proteomics software (Nonlinear Dynamics, Version 2.0) and an in-house developed SafeQuant R script (SafeQuant, https://github.com/eahrne/SafeQuant, PubMed-ID: 27345528).

Figure Legends

Figure 1. Abl domain organization and structural models. A) The domain organization is shown of Abl isoforms 1a and 1b, as well as of the chronic myeloid leukemia (CML)-inducing fusion protein Bcr-Abl. The Abl^{core} consists sequentially of the SH3, SH2, and kinase (KD) domains. The N-cap varies between the two splice variants, whereby that of isoform 1b is 19 amino acids longer and N-myristoylated at glycine 2. The N-cap is replaced by Bcr in the Bcr-Abl fusion. B) The crystal structure of the N-terminal half of Abl 1b isoform (aa 1-531) in complex with the ATP site ligand PD166326 (PDB 2FO0[14]) reveals a tight assembly with the SH3 and SH2 domains docking onto the KD N- and C-lobes. Stabilizing elements are highlighted in grey. C) Type II inhibitors such as imatinib induce a dynamic disassembled conformation as evident from NMR and SAXS data with nanosecond mobility of the SH3 and SH2 domains[17]. One possible conformation of the model is shown. Importantly, the activation loop is in its inactive conformation. D) The 'top-hat' conformation of an SH2-KD construct in complex with the ATP site ligand dasatinib is shown (PDB code 4XEY[20]). The SH2 domain sits on top of the KD N-lobe. Here, the activation loop adopts the active conformation.

Figure 2. Abl FRET labeling scheme and sample quality. A) Scheme for Abl FRET sample preparation. The unnatural amino acid propargyl-lysine (PrK) is twice incorporated into Abl^{core} by the PylRS/$tRNA^{Pyl}$ system that specifically incorporates PrK via an amber stop codon (TAG). The protein is subsequently labeled with Alexa Fluor 488 azide (donor) and Alexa Fluor 647 azide (acceptor) at the same time using Cu(I) as a catalyst, which yields a mixture of D_{only}, A_{only}, and DA fractions. The labeling reaction, Copper(I)-catalyzed Alkyne-Azide Cycloaddition (CuAAC), between Prk and the azide-coupled dyes, which form stable triazoles, is shown in the green box. B) Two-dimensional contour plot of the FRET efficiency versus donor-acceptor stoichiometry per molecule from the Abl^{core}-196*-510*•imatinib sample. The depicted contour levels are 0.2, 0.4, 0.6, and 0.8. The sum over all FRET efficiencies is shown as a one-dimensional stoichiometry plot on top. The stoichiometry is derived from the green and red channel photon counts after pulsed interleaved excitation (PIE) and denotes the fraction of donor molecules for a single particle. A stoichiometry of 1 corresponds to only donor molecules (D_{only}), a value of 0.5 means equal amounts of donor and acceptor molecules (DA), and a stoichiometry of 0 indicates that only acceptor molecules are attached to the particle (A_{only}). Hence, we select all detected single-molecule events with a stoichiometry between 0.33 and 0.67 as DA molecules for further analysis.

Figure 3. One-dimensional FRET efficiency histograms. A) The one-dimensional FRET efficiency histograms are shown for Abl^{core}-196*-510* and Abl^{core}-196*-510* T231R and Abl^{core}-225*-297* in the apo form and in complexes with asciminib, imatinib, or imatinib•asciminib. Histograms are normalized to a sum of 1. B) The label positions of the two FRET pairs, 196+510 (red) and 225+297 (magenta), are highlighted in the assembled, disassembled and 'top-hat' conformation, and the respective values for the expected E_{FRET} and inter-dye distance, simulated with the FPS software, are displayed.

Figure 4. Dynamic disassembly of the Abl core as observed in two-dimensional histograms of FRET efficiency versus FRET-averaged donor lifetime in presence of the

acceptor, E_{FRET} vs. $<\tau_{D(A)}>_F$. The two-dimensional histograms are shown for Abl^{core}-196*-510* and Abl^{core}-196*-510* T231R and Abl^{core}-225*-297* in the apo form and in complexes with asciminib, imatinib, or imatinib•asciminib. The depicted contour levels are 0.2, 0.4, 0.6, and 0.8 for the Abl^{core}-196*-510* samples and 0.1, 0.3, 0.5, and 0.7 for the Abl^{core} 225*-297* samples. The calculated static FRET line is shown in orange.

Figure 5. Analysis of the conformational dynamics of Abl. A) Filtered fluorescence correlation spectroscopy (fFCS) analysis of Abl^{core}-196*-510*•imatinib reveals at least four interconverting states. High-FRET species (HF, $E_{FRET} > 0.8$) and low-FRET species (LF, $E_{FRET} < 0.15$) were selected and the respective species auto correlation functions (SACFs), as well as the species cross correlation functions (SCCFs) fitted as described elsewhere[29, 41]. Three relaxation times, t_R, were identified. B) The TCSPC decay histograms of sub-ensembles 'FRET', HF, MF, and VLF (see below) of apo Abl^{core}-196*-510* (fit exemplarily shown), Abl^{core}-196*-510*•imatinib, and Abl^{core}-196*-510*•asciminib were globally fitted with two D_{only} lifetimes ($<\tau_{D(0)}>_{F,1}$ = 4.17 ns and $<\tau_{D(0)}>_{F,2}$ = 1.57 ns) and four Gaussian-shaped FRET species distributions. The following sub-ensembles were selected from the two-dimensional MFD E_{FRET} vs. stoichiometry (S_{PIE}) plots. 'FRET' includes all events with $0.33 < S_{PIE} < 0.67$. HF (high FRET) selects additionally all events with $E_{FRET} > 0.8$, MF (mid FRET) selects all events with $0.2 < E_{FRET} < 0.8$, and VLF includes all events with $E_{FRET} < 0.2$. The distribution width σ was kept constant at 6 Å allowing for dye motion due to its flexible linker. C) The distance distribution models with fitted species fractions χ_1 (values given in Table 2) and donor-acceptor (DA) distances R_1 = 21.3 Å, R_2 = 39.0 Å, R_3 = 54.4 Å, and R_4 = 121.1 Å corresponding to the fitted donor fluorescence lifetimes are displayed.

Supplementary Figure 1. smFRET data for GNF-5 complexes. A) The one-dimensional FRET efficiency histograms are shown for Abl^{core}-196*-510*•GNF-5 and Abl^{core}-196*-510*•imatinib•GNF-5. The histograms are normalized to a sum of 1. B) Two-dimensional histograms of FRET efficiency versus FRET-averaged donor lifetime in presence of the acceptor contour, E_{FRET} vs. $<\tau_{D(A)}>_F$, for Abl^{core}-196*-510*•GNF-5 and Abl^{core}-196*-510*•imatinib•GNF-5. The depicted contour levels are 0.2, 0.4, 0.6, and 0.8. The calculated static FRET line is shown in orange.

Supplementary Figure 2. smFRET data for ponatinib/nilotinib(+asciminib). The one-dimensional FRET efficiency histograms and two-dimensional E_{FRET} vs. $<\tau_{D(A)}>_F$ plots are shown for Abl^{core}-196*-510*•ponatinib, Abl^{core}-196*-510*•ponatinib•asciminib, Abl^{core}-196*-510*•nilotinib, and Abl^{core}-196*-510*•nilotinib•asciminib. The 1D histograms are normalized to a sum of 1. The depicted contour levels in the 2D plots are 0.2, 0.4, 0.6, and 0.8. The calculated static FRET line is shown in orange.

References

1. Van Etten, R. A., Cycling, stressed-out and nervous: cellular functions of c-Abl. *Trends Cell Biol* **1999,** *9* (5), 179-86.
2. Pendergast, A. M., The Abl family kinases: mechanisms of regulation and signaling. *Adv Cancer Res* **2002,** *85*, 51-100.
3. Hantschel, O., Structure, regulation, signaling, and targeting of abl kinases in cancer. *Genes Cancer* **2012,** *3* (5-6), 436-46.
4. Rowley, J. D., Letter: A new consistent chromosomal abnormality in chronic myelogenous leukaemia identified by quinacrine fluorescence and Giemsa staining. *Nature* **1973,** *243* (5405), 290-3.
5. Deininger, M. W.; Goldman, J. M.; Melo, J. V., The molecular biology of chronic myeloid leukemia. *Blood* **2000,** *96* (10), 3343-56.
6. Braun, T. P.; Eide, C. A.; Druker, B. J., Response and Resistance to BCR-ABL1-Targeted Therapies. *Cancer Cell* **2020,** *37* (4), 530-542.
7. Shah, N. P.; Tran, C.; Lee, F. Y.; Chen, P.; Norris, D.; Sawyers, C. L., Overriding imatinib resistance with a novel ABL kinase inhibitor. *Science* **2004,** *305* (5682), 399-401.
8. Hantschel, O.; Grebien, F.; Superti-Furga, G., The growing arsenal of ATP-competitive and allosteric inhibitors of BCR-ABL. *Cancer Res* **2012,** *72* (19), 4890-5.
9. O'Hare, T., A Decade of Nilotinib and Dasatinib: From In Vitro Studies to First-Line Tyrosine Kinase Inhibitors. *Cancer Res* **2016,** *76* (20), 5911-5913.
10. Eide, C. A.; Zabriskie, M. S.; Savage Stevens, S. L.; Antelope, O.; Vellore, N. A.; Than, H.; Schultz, A. R.; Clair, P.; Bowler, A. D.; Pomicter, A. D.; Yan, D.; Senina, A. V.; Qiang, W.; Kelley, T. W.; Szankasi, P.; Heinrich, M. C.; Tyner, J. W.; Rea, D.; Cayuela, J. M.; Kim, D. W.; Tognon, C. E.; O'Hare, T.; Druker, B. J.; Deininger, M. W., Combining the Allosteric Inhibitor Asciminib with Ponatinib Suppresses Emergence of and Restores Efficacy against Highly Resistant BCR-ABL1 Mutants. *Cancer Cell* **2019,** *36* (4), 431-443 e5.
11. Wylie, A. A.; Schoepfer, J.; Jahnke, W.; Cowan-Jacob, S. W.; Loo, A.; Furet, P.; Marzinzik, A. L.; Pelle, X.; Donovan, J.; Zhu, W.; Buonamici, S.; Hassan, A. Q.; Lombardo, F.; Iyer, V.; Palmer, M.; Berellini, G.; Dodd, S.; Thohan, S.; Bitter, H.; Branford, S.; Ross, D. M.; Hughes, T. P.; Petruzzelli, L.; Vanasse, K. G.; Warmuth, M.; Hofmann, F.; Keen, N. J.; Sellers, W. R., The allosteric inhibitor ABL001 enables dual targeting of BCR-ABL1. *Nature* **2017,** *543* (7647), 733-737.
12. Hughes, T. P.; Mauro, M. J.; Cortes, J. E.; Minami, H.; Rea, D.; DeAngelo, D. J.; Breccia, M.; Goh, Y. T.; Talpaz, M.; Hochhaus, A.; le Coutre, P.; Ottmann, O.; Heinrich, M. C.; Steegmann, J. L.; Deininger, M. W. N.; Janssen, J.; Mahon, F. X.; Minami, Y.; Yeung, D.; Ross, D. M.; Tallman, M. S.; Park, J. H.; Druker, B. J.; Hynds, D.; Duan, Y.; Meille, C.; Hourcade-Potelleret, F.; Vanasse, K. G.; Lang, F.; Kim, D. W., Asciminib in Chronic Myeloid Leukemia after ABL Kinase Inhibitor Failure. *N Engl J Med* **2019,** *381* (24), 2315-2326.
13. Nagar, B.; Hantschel, O.; Young, M. A.; Scheffzek, K.; Veach, D.; Bornmann, W.; Clarkson, B.; Superti-Furga, G.; Kuriyan, J., Structural basis for the autoinhibition of c-Abl tyrosine kinase. *Cell* **2003,** *112* (6), 859-71.

14. Nagar, B.; Hantschel, O.; Seeliger, M.; Davies, J. M.; Weis, W. I.; Superti-Furga, G.; Kuriyan, J., Organization of the SH3-SH2 unit in active and inactive forms of the c-Abl tyrosine kinase. *Mol Cell* **2006,** *21* (6), 787-98.

15. Hantschel, O.; Nagar, B.; Guettler, S.; Kretzschmar, J.; Dorey, K.; Kuriyan, J.; Superti-Furga, G., A myristoyl/phosphotyrosine switch regulates c-Abl. *Cell* **2003,** *112* (6), 845-57.

16. Sonti, R.; Hertel-Hering, I.; Lamontanara, A. J.; Hantschel, O.; Grzesiek, S., ATP Site Ligands Determine the Assembly State of the Abelson Kinase Regulatory Core via the Activation Loop Conformation. *J Am Chem Soc* **2018,** *140* (5), 1863-1869.

17. Skora, L.; Mestan, J.; Fabbro, D.; Jahnke, W.; Grzesiek, S., NMR reveals the allosteric opening and closing of Abelson tyrosine kinase by ATP-site and myristoyl pocket inhibitors. *Proc Natl Acad Sci U S A* **2013,** *110* (47), E4437-45.

18. Hantschel, O.; Wiesner, S.; Guttler, T.; Mackereth, C. D.; Rix, L. L.; Mikes, Z.; Dehne, J.; Gorlich, D.; Sattler, M.; Superti-Furga, G., Structural basis for the cytoskeletal association of Bcr-Abl/c-Abl. *Mol Cell* **2005,** *19* (4), 461-73.

19. Lamontanara, A. J.; Georgeon, S.; Tria, G.; Svergun, D. I.; Hantschel, O., The SH2 domain of Abl kinases regulates kinase autophosphorylation by controlling activation loop accessibility. *Nat Commun* **2014,** *5*, 5470.

20. Lorenz, S.; Deng, P.; Hantschel, O.; Superti-Furga, G.; Kuriyan, J., Crystal structure of an SH2-kinase construct of c-Abl and effect of the SH2 domain on kinase activity. *Biochem J* **2015,** *468* (2), 283-91.

21. Saleh, T.; Rossi, P.; Kalodimos, C. G., Atomic view of the energy landscape in the allosteric regulation of Abl kinase. *Nat Struct Mol Biol* **2017,** *24* (11), 893-901.

22. O'Connor, D. V.; Phillips, D., *Time-Correlated Single Photon Counting*. 1984.

23. Widengren, J.; Kudryavtsev, V.; Antonik, M.; Berger, S.; Gerken, M.; Seidel, C. A., Single-molecule detection and identification of multiple species by multiparameter fluorescence detection. *Anal Chem* **2006,** *78* (6), 2039-50.

24. Kalinin, S.; Peulen, T.; Sindbert, S.; Rothwell, P. J.; Berger, S.; Restle, T.; Goody, R. S.; Gohlke, H.; Seidel, C. A., A toolkit and benchmark study for FRET-restrained high-precision structural modeling. *Nat Methods* **2012,** *9* (12), 1218-25.

25. Tyagi, S.; Lemke, E. A., Genetically encoded click chemistry for single-molecule FRET of proteins. *Methods Cell Biol* **2013,** *113*, 169-87.

26. Liang, L.; Astruc, D., The copper(I)-catalyzed alkyne-azide cycloaddition (CuAAC) "click" reaction and its applications. An overview. *Coordination Chemistry Reviews* **2011,** *255* (23-24), 2933-2945.

27. Sherbenou, D. W.; Hantschel, O.; Kaupe, I.; Willis, S.; Bumm, T.; Turaga, L. P.; Lange, T.; Dao, K. H.; Press, R. D.; Druker, B. J.; Superti-Furga, G.; Deininger, M. W., BCR-ABL SH3-SH2 domain mutations in chronic myeloid leukemia patients on imatinib. *Blood* **2010,** *116* (17), 3278-85.

28. Kalinin, S.; Valeri, A.; Antonik, M.; Felekyan, S.; Seidel, C. A., Detection of structural dynamics by FRET: a photon distribution and fluorescence lifetime analysis of systems with multiple states. *J Phys Chem B* **2010,** *114* (23), 7983-95.

29. Sanabria, H.; Rodnin, D.; Hemmen, K.; Peulen, T. O.; Felekyan, S.; Fleissner, M. R.; Dimura, M.; Koberling, F.; Kuhnemuth, R.; Hubbell, W.; Gohlke, H.; Seidel, C.

A. M., Resolving dynamics and function of transient states in single enzyme molecules. *Nat Commun* **2020,** *11* (1), 1231.

30. Colicelli, J., ABL tyrosine kinases: evolution of function, regulation, and specificity. *Sci Signal* **2010,** *3* (139), re6.

31. Jahnke, W.; Grotzfeld, R. M.; Pelle, X.; Strauss, A.; Fendrich, G.; Cowan-Jacob, S. W.; Cotesta, S.; Fabbro, D.; Furet, P.; Mestan, J.; Marzinzik, A. L., Binding or bending: distinction of allosteric Abl kinase agonists from antagonists by an NMR-based conformational assay. *J Am Chem Soc* **2010,** *132* (20), 7043-8.

32. Young, D. D.; Schultz, P. G., Playing with the Molecules of Life. *ACS Chem Biol* **2018,** *13* (4), 854-870.

33. Grebien, F.; Hantschel, O.; Wojcik, J.; Kaupe, I.; Kovacic, B.; Wyrzucki, A. M.; Gish, G. D.; Cerny-Reiterer, S.; Koide, A.; Beug, H.; Pawson, T.; Valent, P.; Koide, S.; Superti-Furga, G., Targeting the SH2-kinase interface in Bcr-Abl inhibits leukemogenesis. *Cell* **2011,** *147* (2), 306-19.

34. Conic, S.; Desplancq, D.; Tora, L.; Weiss, E., Electroporation of Labeled Antibodies to Visualize Endogenous Proteins and Posttranslational Modifications in Living Metazoan Cell Types. *Bio-protocol* **2018,** *8* (21), e3069.

35. Kravets, E.; Degrandi, D.; Ma, Q.; Peulen, T. O.; Klumpers, V.; Felekyan, S.; Kuhnemuth, R.; Weidtkamp-Peters, S.; Seidel, C. A.; Pfeffer, K., Guanylate binding proteins directly attack Toxoplasma gondii via supramolecular complexes. *Elife* **2016,** *5*.

36. Hong, V.; Presolski, S. I.; Ma, C.; Finn, M. G., Analysis and optimization of copper-catalyzed azide-alkyne cycloaddition for bioconjugation. *Angew Chem Int Ed Engl* **2009,** *48* (52), 9879-83.

37. Kim, J.; Seo, M. H.; Lee, S.; Cho, K.; Yang, A.; Woo, K.; Kim, H. S.; Park, H. S., Simple and efficient strategy for site-specific dual labeling of proteins for single-molecule fluorescence resonance energy transfer analysis. *Anal Chem* **2013,** *85* (3), 1468-74.

38. Vaughan, J. C.; Dempsey, G. T.; Sun, E.; Zhuang, X., Phosphine quenching of cyanine dyes as a versatile tool for fluorescence microscopy. *J Am Chem Soc* **2013,** *135* (4), 1197-200.

39. Kudryavtsev, V.; Sikor, M.; Kalinin, S.; Mokranjac, D.; Seidel, C. A.; Lamb, D. C., Combining MFD and PIE for accurate single-pair Forster resonance energy transfer measurements. *Chemphyschem* **2012,** *13* (4), 1060-78.

40. Lehmann, K.; Felekyan, S.; Kuhnemuth, R.; Dimura, M.; Toth, K.; Seidel, C. A. M.; Langowski, J., Dynamics of the nucleosomal histone H3 N-terminal tail revealed by high precision single-molecule FRET. *Nucleic Acids Res* **2020,** *48* (3), 1551-1571.

41. Felekyan, S.; Kalinin, S.; Sanabria, H.; Valeri, A.; Seidel, C. A., Filtered FCS: species auto- and cross-correlation functions highlight binding and dynamics in biomolecules. *Chemphyschem* **2012,** *13* (4), 1036-53.

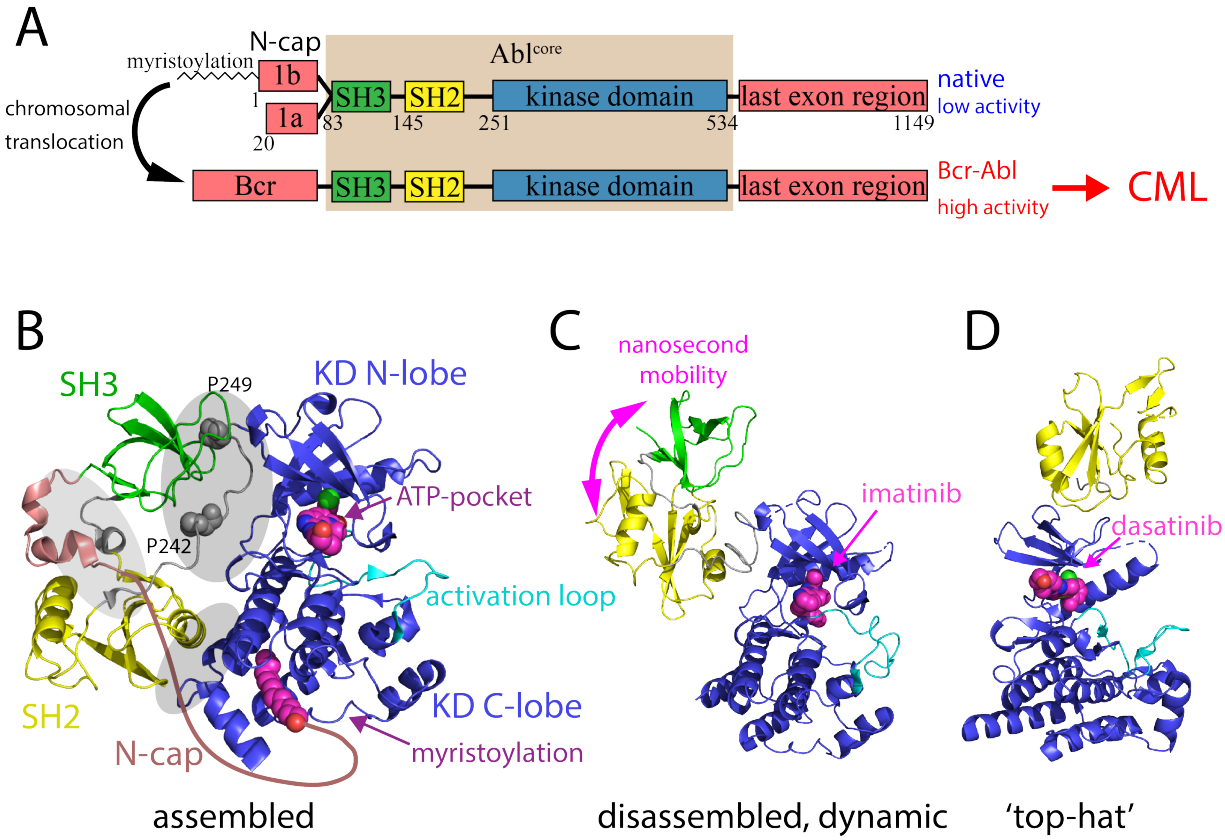
A
N-cap
myristoylation
1b
1a
1
20
Abl^core
SH3
SH2
kinase domain
last exon region
83
145
251
534
1149
native
low activity
chromosomal
translocation
Bcr
Bcr-Abl
high activity
CML
B
SH3
P249
KD N-lobe
ATP-pocket
P242
activation loop
SH2
KD C-lobe
N-cap
myristoylation
assembled
C
nanosecond
mobility
imatinib
disassembled, dynamic
D
dasatinib
'top-hat'

Figure 1

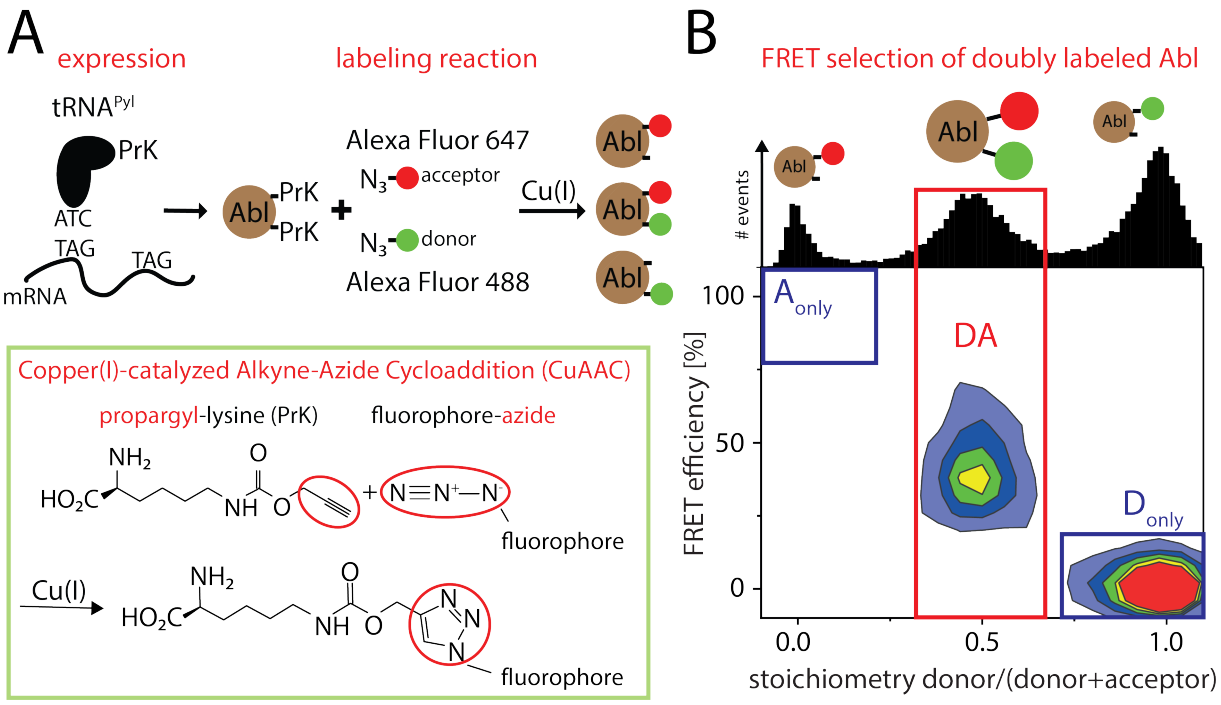
A
expression
labeling reaction
tRNA^Pyl
PrK
ATC
TAG
TAG
mRNA
Abl
PrK
PrK
Alexa Fluor 647
N3 acceptor
N3 donor
Alexa Fluor 488
Cu(I)
Abl
Abl
Abl
Copper(I)-catalyzed Alkyne-Azide Cycloaddition (CuAAC)
propargyl-lysine (PrK)
fluorophore-azide
NH2
HO2C
NH
O
O
+ N≡N+—N-
fluorophore
Cu(I)
NH2
HO2C
NH
O
O
N
N
N
fluorophore
B
FRET selection of doubly labeled Abl
events
Abl
Abl
Abl
A only
DA
D only
FRET efficiency [%]
100
50
0
0.0
0.5
1.0
stoichiometry donor/(donor+acceptor)

Figure 2

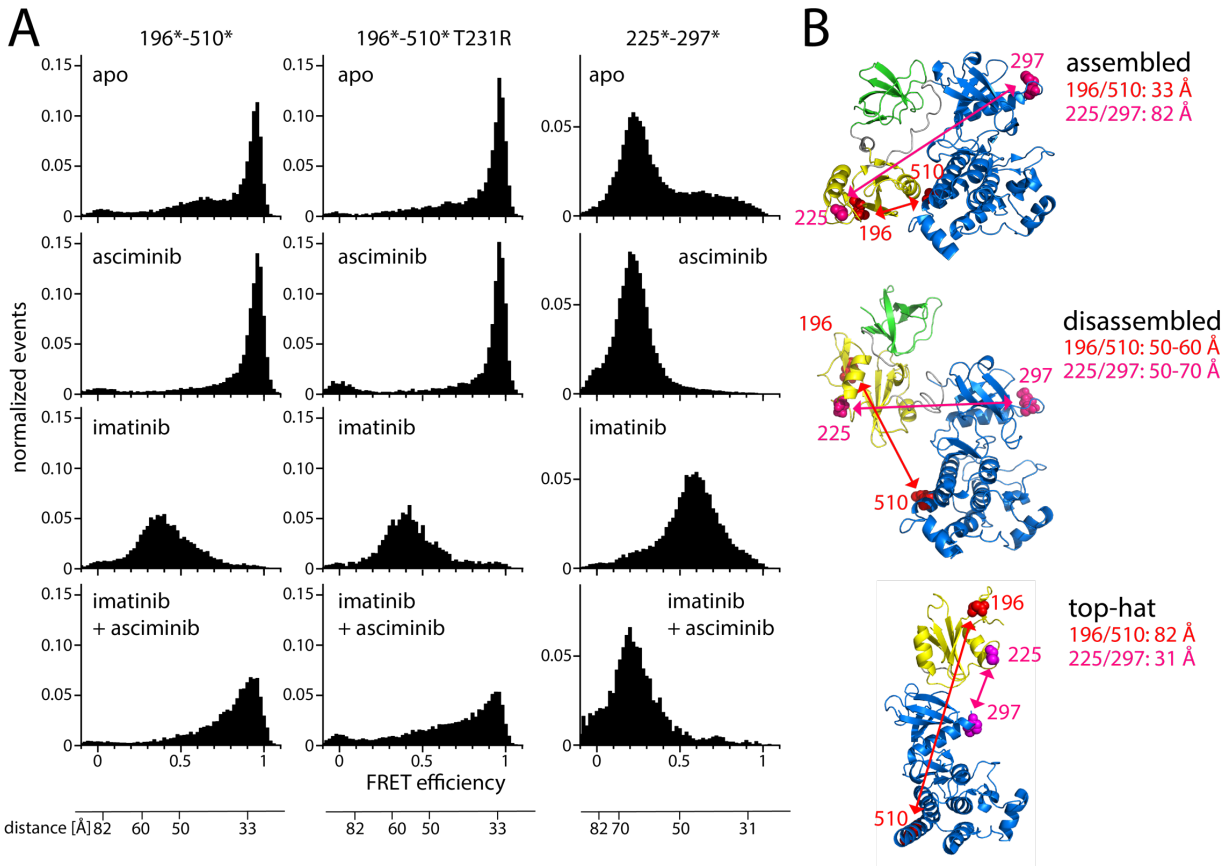
A
196*-510*
196*-510* T231R
225*-297*
apo
asciminib
imatinib
imatinib
+ asciminib
normalized events
FRET efficiency
distance [Å]
82 60 50 33
82 60 50 33
82 70 50 31
B
assembled
196/510: 33 Å
225/297: 82 Å
disassembled
196/510: 50-60 Å
225/297: 50-70 Å
top-hat
196/510: 82 Å
225/297: 31 Å
297
510
225
196

Figure 3

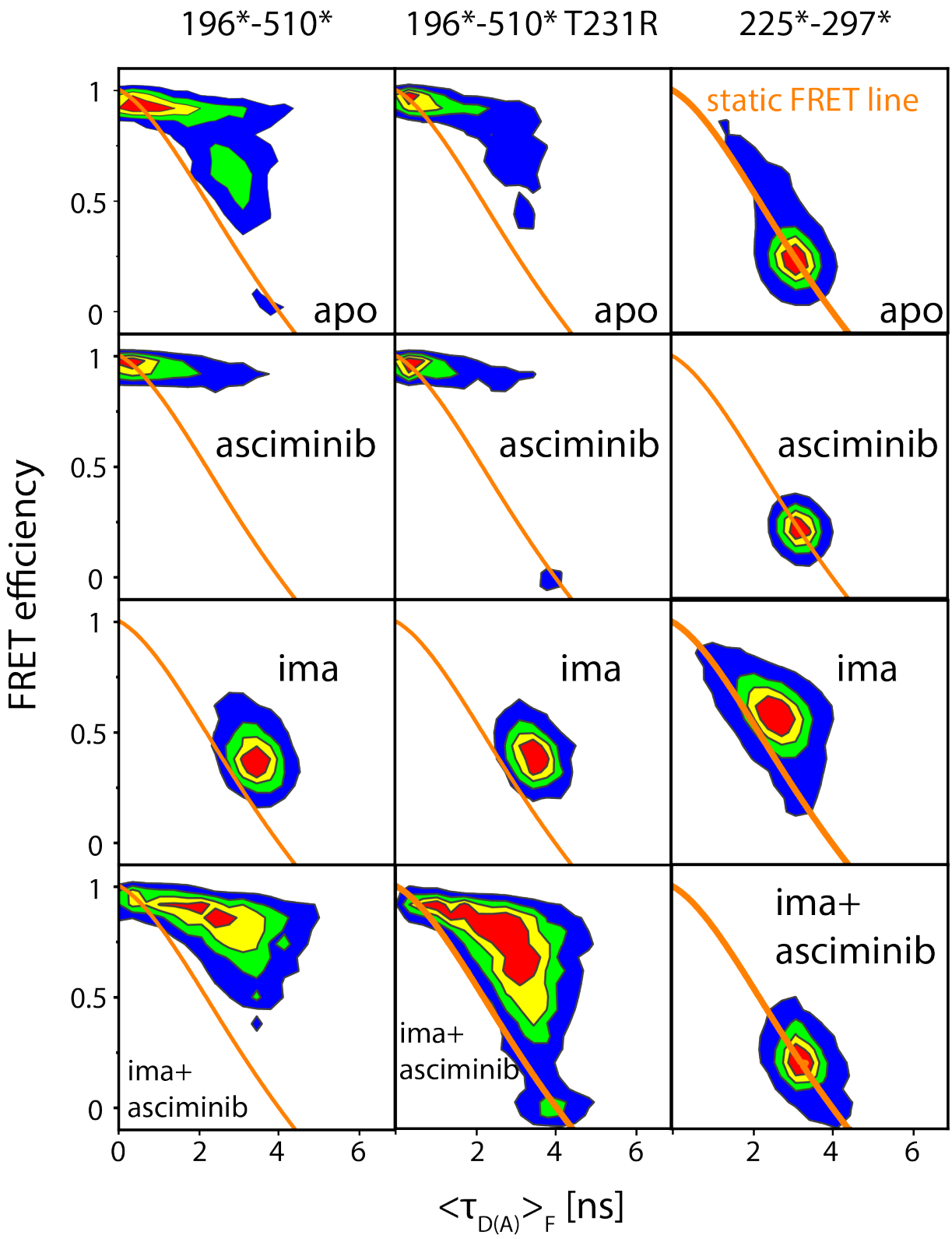
196*-510*
196*-510* T231R
225*-297*
static FRET line
apo
asciminib
ima
ima+
asciminib
FRET efficiency
0
0.5
1
2
4
6
<τD(A)>F [ns]

Figure 4

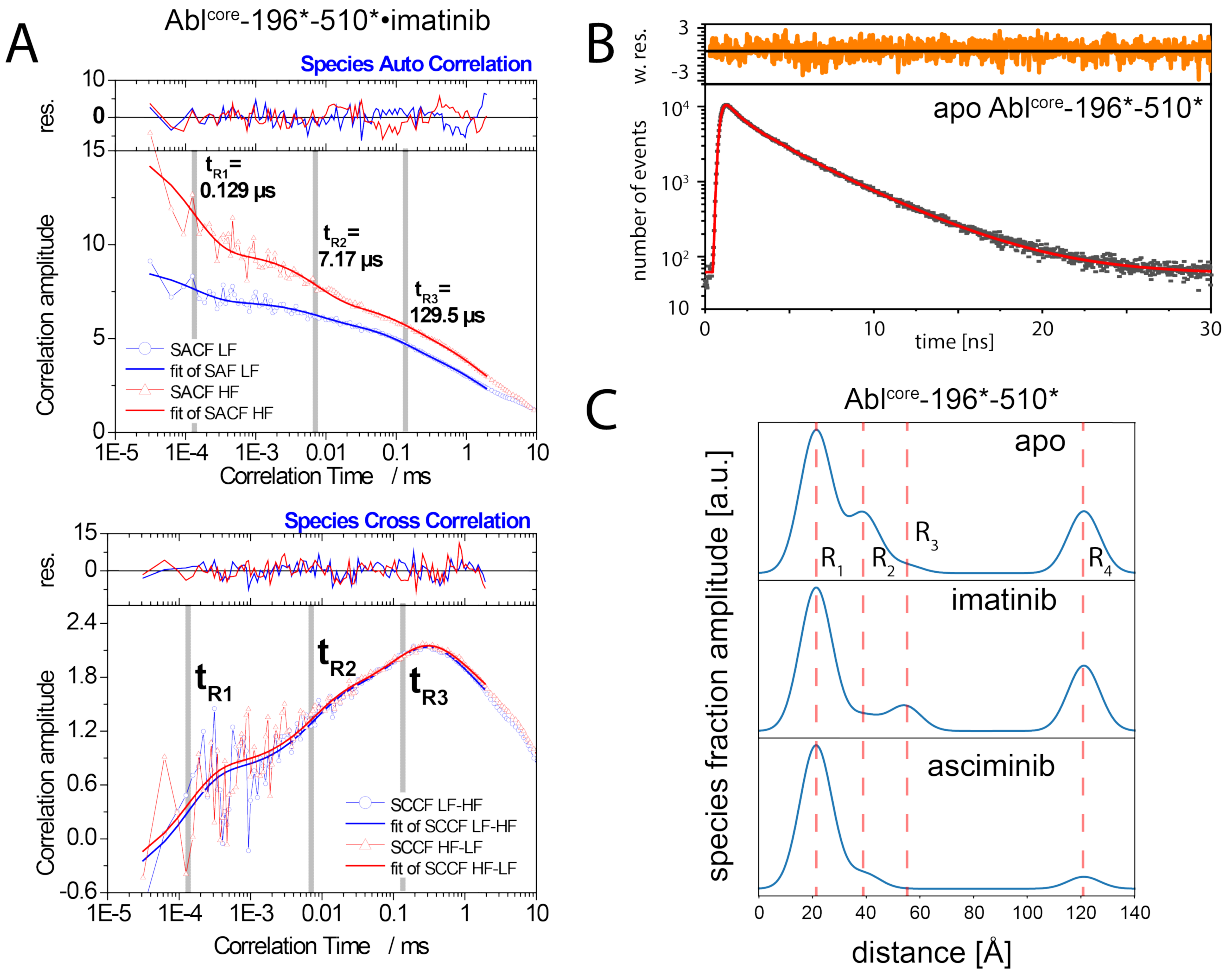
A
Abl^core-196*-510*•imatinib
Species Auto Correlation
res.
Correlation amplitude
t_R1= 0.129 µs
t_R2= 7.17 µs
t_R3= 129.5 µs
SACF LF
fit of SAF LF
SACF HF
fit of SACF HF
Correlation Time / ms
Species Cross Correlation
t_R1
t_R2
t_R3
SCCF LF-HF
fit of SCCF LF-HF
SCCF HF-LF
fit of SCCF HF-LF
B
w. res.
number of events
apo Abl^core-196*-510*
time [ns]
C
Abl^core-196*-510*
apo
imatinib
asciminib
R1
R2
R3
R4
species fraction amplitude [a.u.]
distance [Å]

Figure 5

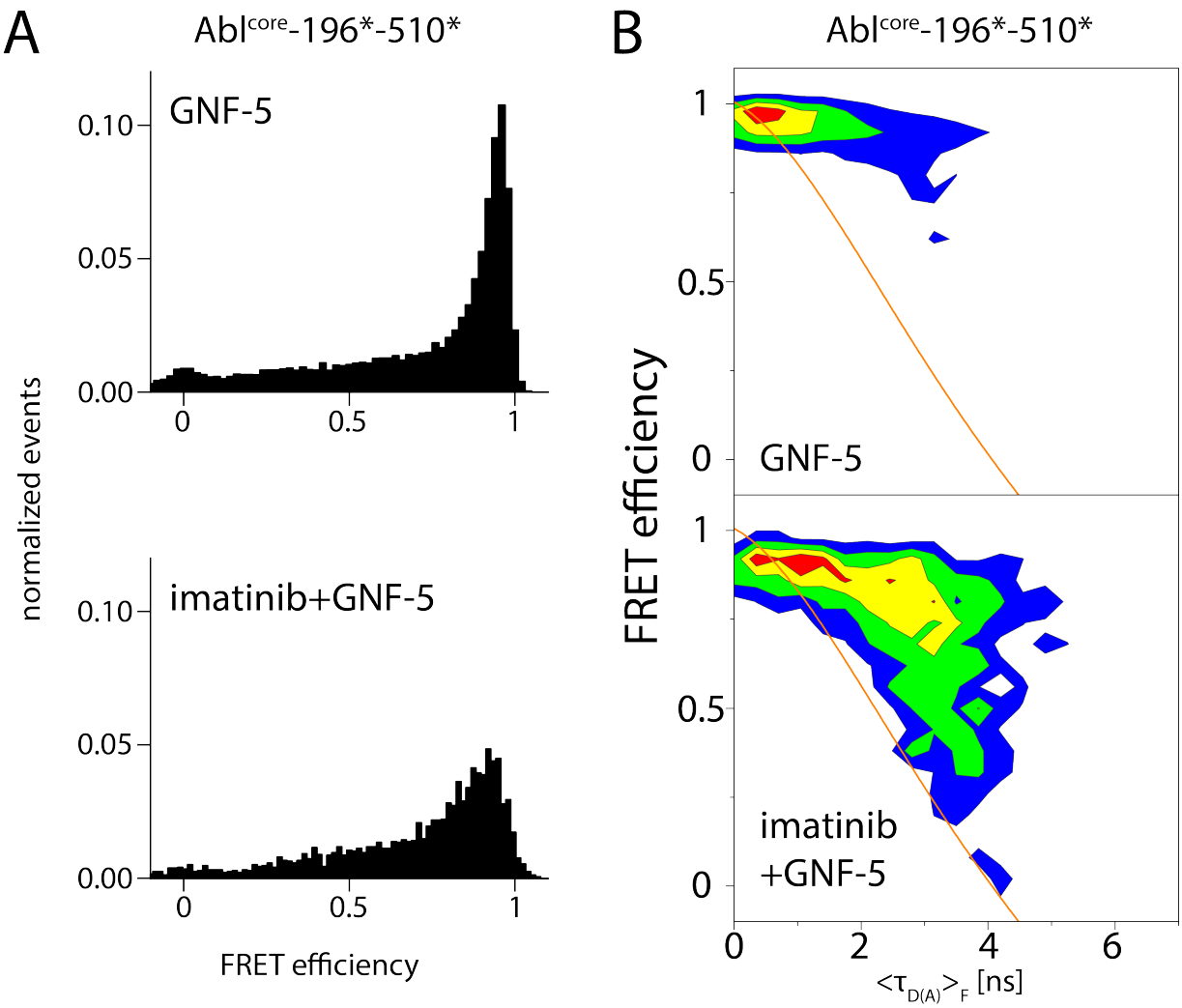

Supplementary Figure S1

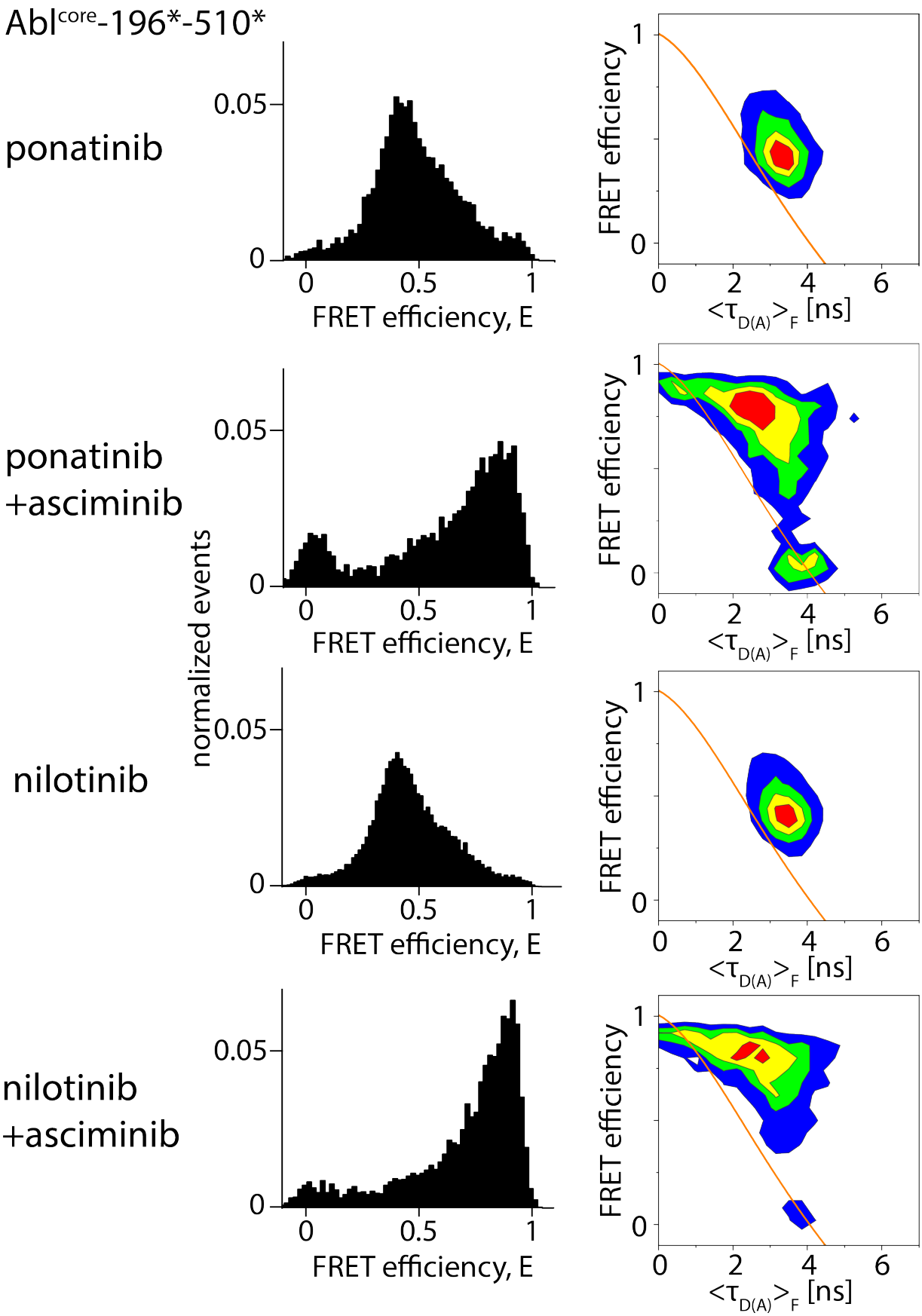

Supplementary Figure S2

3 Solution NMR studies of how various N- and C-terminal elements influence the conformational equilibrium and thereby the activity of the Abl regulatory core

In this chapter, the influence on the Abl^{core} conformational equilibrium by various Abl elements, mostly located N- and C-terminal of the Abl^{core}, is studied by solution NMR. In Chapter 3.1, it is shown how the KD C-terminal αI-helix actively supports Abl activation in a simple mechanical manner. In Chapter 3.2, the stabilizing effects of the Abl N-cap and the myristoylation on the Abl^{core} are described. In Chapter 3.3, an interaction of the C-terminal F-actin binding domain with the disassembled Abl^{core} is shown, which shifts the Abl^{core} conformational equilibrium to a more open state.

3.1 The entropic spring mechanism of the αI-helix in the regulation of Abelson kinase

The following Chapter consists of the preliminary manuscript entitled “The entropic spring mechanism of the αI-helix in the regulation of Abelson kinase” by J. Schlotte, A. Maier, J.M. Habazettl, I. Hertel-Hering, R. Sonti, O. Hantschel, and S. Grzesiek.

The entropic spring mechanism of the αI-helix in the regulation of Abelson kinase

Johannes Schlotte[1], Annalena Maier[1], Judith Maria Habazettl[1], Ines Hertel-Hering[1], Rajesh Sonti[1], Oliver Hantschel[2], Stephan Grzesiek[1,*]

[1] Focal Area Structural Biology and Biophysics, Biozentrum, University of Basel, 4056 Basel, Switzerland

[2] Institut für Physiologische Chemie, Philipps Universität Marburg, 35043 Marburg, Germany

*Address correspondence to:
Stephan Grzesiek
Focal Area Structural Biology and Biophysics, Biozentrum
University of Basel, CH-4056 Basel, Switzerland
Phone: +41 61 267 2100
Fax: +41 61 267 2109
Email: Stephan.Grzesiek@unibas.ch

Keywords: Abelson tyrosine kinase, cancer, chronic myelogenous leukemia, allosteric activation, αI-helix, asciminib, NMR

Abstract

Abelson tyrosine kinase (Abl) is involved in many cellular processes. Under healthy conditions, its activity is tightly regulated by the arrangement of its regulatory core, consisting sequentially of the SH3 and SH2 domains and the kinase domain (KD), where an assembled or disassembled core corresponds to low or high kinase activity, respectively. The forces that disassemble the core or stabilize the assembled conformation are not yet well understood. A bending of the C-terminal αI-helix upon binding of the N-terminal myristoyl to the KD myristate pocket observed in crystal structures appears to stabilize the assembled, inactive conformation. This has led to the development of a novel class of allosteric inhibitors which mimic myristoyl binding. However, solution experiments show that the αI-helix is flexible and also that a regulatory core with an empty myristate pocket adopts an assembled conformation. Moreover, binding of type II ATP site inhibitors, which induce an inactive activation loop conformation, also leads to core disassembly, which however can be reversed by the addition of allosteric inhibitors.

To elucidate the apparent cross talk between ATP site and αI-helix, we have systematically reduced the length of the αI-helix and quantified the opening of the regulatory core by the type II inhibitor imatinib and the enzymatic activity of the respective apo forms. The results show that the length of αI in the SH3-SH2-KD core correlates with the degree of imatinib-induced core opening and with the enzymatic activity of the apo core. This firmly establishes the αI-helix as an essential part of the disassembly and activation mechanism and proves that type II inhibitor-induced opening occurs via an allosteric coupling from αI to the ATP site. These phenomena can be rationalized by a simple mechanical model of an entropic force exerted by αI, which propagates via the KD SH2/SH3 interface to the KD N-lobe. Our results shed light on the molecular mechanism of Abl activation and its allosteric regulation and help to understand the molecular activation of Bcr-Abl and to develop new specific CML therapies.

Introduction

Abelson tyrosine kinase (Abl) is crucial for many cellular processes including proliferation, division, survival, DNA repair and migration[1, 2]. Under non-pathological conditions Abl is tightly regulated with very low intrinsic activity in unstimulated cells[3]. However, the oncogenic t(9;22)(q34;q11) chromosomal translocation (Philadelphia chromosome) leads to the expression of the highly active fusion protein Bcr-Abl and subsequently to chronic myeloid leukemia (CML)[4-6]. The ATP site inhibitors imatinib (Gleevec), nilotinib (Tasigna), and dasatinib (Sprycel) constitute the front-line therapy against CML[3, 7, 8], but the emergence of drug-resistant point mutations in a fraction of patients has created the need for alternatives[3, 9]. In particular, the recently developed allosteric inhibitor asciminib (ABL001)[10], which targets the myristoyl binding pocket (see below), shows high promise in clinical trials to overcome these resistances[11, 12]. This development now enables dual Bcr-Abl targeting and thereby therapy of patients bearing compound mutations[9, 10]. The exact functional mechanism of the allosteric inhibitors is unclear.

Under healthy conditions, Abl regulation is achieved by a set of interactions within its regulatory core consisting sequentially of the SH3 and SH2 domain and the kinase domain (KD) and the preceding ~60-80-residue-long N-terminal tail (N-cap)[13] (Figure 1A). The N-cap varies between splice variants 1a and 1b with Abl 1b being 19 residues longer and N-terminally myristoylated. Crystal structures of the autoinhibited Abl 1b core with the myristoylated N-cap[13-15] reveal a tight, almost spherical assembly (Figure 1B). This assembly appears stabilized by several interactions: (i) the docking of the SH3 domain to the proline-rich linker from the SH2 domain to the KD N-lobe, (ii) extensive contacts between the SH3 and SH2 domains and the KD C- and N-lobes, respectively, and (iii) the docking of the N-terminal myristoyl into a hydrophobic cleft at the bottom of the KD C-lobe. The assembly of the core impedes efficient substrate binding[13], presumably by hindering hinge motions between the KD C- and N-lobes[16], and reduces the kinase activity by 10- to 100-fold relative to the isolated kinase domain[16, 17]. In contrast, the active state of Abl is thought to require the disassembly of the core to make the substrate binding site accessible and expose the protein-protein contact sites of the SH2 and SH3 domains.

In crystal structures of the isolated Abl kinase domain with an empty myristoyl binding pocket (PDB code 1M52[18]), the C-terminal αI-helix (residues 504 to 522) adopts an extended straight conformation (Figure 1B). In contrast, in the assembled core structures (Figure 1B), the helix breaks into two parts αI (residues 504 to 515) and αI' (residues 520 to 531) connected by the αI–αI' loop, with the αI' part bending towards the myristoyl bound in the myristoyl

pocket (Figure 1B and D). Notably, the straight αI-helix of the isolated Abl kinase domain would clash with the SH2 domain in the assembled core. This has led to the notion that myristoyl binding induces a bend of the αI-helix and thereby stabilizes the assembled inactive core. Following this idea, so-called allosteric inhibitors have been developed that target the myristoyl pocket[19-21], leading to the highly promising drug asciminib[10]. Notably, not all myristoyl pocket binders act as allosteric inhibitors, but only those that also bend the αI-helix[20].

Several observations indicate that the described role of the αI-helix in the destabilization of the regulatory core is incomplete. First, the αI-helix is rather flexible in solution[20, 22] and may avoid the steric clash with the SH2 domain in the assembled conformation. Indeed, an Abl$^{83-534}$ construct comprising only the SH3-SH2-KD domains but not the myristoylated N-cap adopts an assembled conformation in solution[22] and has strongly reduced enzymatic activity relative to the isolated KD[16]. Second, binding of type II ATP site inhibitors[16], which induce an inactive activation loop (A-loop) conformation in the KD, disassembles the core into an arrangement where SH3 and SH2 domains move with high-amplitude nanosecond motions relative to the KD[22] (Figure 1C). This type II inhibitor-disassembled core is reassembled when allosteric inhibitors bind to the myristate pocket[22], indicating a cross talk between ATP site and the αI-helix/myristate pocket. The inhibitor-induced disassembly correlates with a slight rotation of the KD N-lobe towards the SH3 domain caused by the push of type II inhibitors onto the A-loop and subsequently the P-loop[16]. To explain these observations, we have proposed a mechanical model where both the rotation of the KD N-lobe and the flexible αI-helix exert destabilizing forces onto the SH3/SH2-KD interface, which together lead to the disassembly of the core[16].

Here, we prove and quantify this model of allosteric activation and interaction between the αI-helix and the ATP site by stepwise shortening of the Abl C-terminal αI-helix. We show that the shorter the αI-helix, the less the Abl regulatory core disassembles by imatinib as detected by NMR. This reduction in opening correlates with a simultaneous loss in kinase activity of the apo regulatory core. Thus, the αI-helix is a crucial element of Abl activation and regulation.

Results and Discussion

Expression of C-terminal Abl truncation constructs

To test the impact of the C-terminal αI part on Abl's conformational equilibrium and activity, Abl constructs of the regulatory core (Abl$^{83-534}$, 1b numbering) were expressed with decreasing length by introducing stop codons. The first truncated construct, Abl$^{83-519}$

(Figure 2A), misses the αI'-helix part of the myristoyl-bound conformation (Figure 1D). As compared to Abl$^{83-534}$, its expression yield is reduced about 4-fold as quantified by western blot (Figure 2B) and analysis of the fully purified construct (Figure 2C), presumably due to instability. Surprisingly, Abl$^{83-519}$ showed no strong effect on the disassembly induced by the type II inhibitor imatinib relative to the full-length core Abl$^{83-534}$ (see below). Thus, the impact of the αI' part on the conformational equilibrium is not very pronounced.

For this reason, the C-terminus was further reduced by one amino acid at a time until Abl$^{83-513}$, thereby removing sequentially the αI–αI' loop and the last two residues T514 and M515 of the αI-helix part of the myristoyl-bound conformation. The resulting constructs had further reduced expression yields down to less than 10 % for the least expressing Abl$^{83-513}$ relative to Abl$^{83-534}$ (Figure 2B). This reduction in yield can be rationalized by the sequential loss of stabilizing interactions between the αI-αI' loop and the αI'-helix involving residues F516, Q517, S520 and D523[13, 15] and the loss of α-helical hydrogen bonds originating at T514 and M515 (Figure 2C). Due to these severe reductions in yield, large-scale expressions of ^{15}N-labeled constructs for NMR were then only carried out for Abl$^{83-519}$, Abl$^{83-517}$, and Abl$^{83-515}$. The final yield after purification for the least expressing Abl$^{83-515}$ was 0.16 mg per liter expression culture and reduced about 20-fold relative to Abl$^{83-534}$ (3.0 mg/L) (Figure 2D).

Truncation of the C-terminal αI–αI'-loop leads to less disassembly of the Abl core by imatinib

Assembled and disassembled Abl core conformations can be readily distinguished by the ^{1}H-^{15}N chemical shifts of the SH3 and SH2 domain backbone resonances[16], with the well-resolved ^{1}H-^{15}N resonances of V130, T136, and G149 showing particularly strong effects (Figure 3). When adding the type II inhibitor imatinib to Abl$^{83-534}$, strong shifts are observed for the latter resonances that are indicative of the conformational change from the assembled to the disassembled conformation (Figure 3B). No pronounced chemical shift differences are observed between the resonances of the Abl$^{83-534}$•imatinib and the Abl$^{83-519}$•imatinib complexes, indicating that the latter is also disassembled. Upon further truncation of the C-terminal Abl end (constructs Abl$^{83-517}$ and Abl$^{83-515}$), the resonances of the respective imatinib complexes shift on a straight line towards their apo forms. For clarity, only the apo resonances of the longest (Abl$^{83-534}$) and shortest construct (Abl$^{83-515}$) are shown in Figure 3B. The other apo forms are located between those two. The same trend of the truncated Abl•imatinib complexes is observed for all chemical shift differences of the assigned SH3/SH2

residues (Figure 4A). Thus, truncating the αI–αI‘-loop reduces the tendency for the Abl core to open under the influence of imatinib.

Interestingly, albeit the resonances of the Abl^{83-519}•imatinib and Abl^{83-534}•imatinib complexes are very similar, the V130, T136, and G149 resonances of Abl^{83-534}•imatinib are slightly shifted on the straight lines connecting the resonances of the Abl^{83-519}, Abl^{83-517}, and Abl^{83-515} imatinib complexes towards the more closed Abl^{83-515}•imatinib complex (Figure 3B). This hints at a slight stabilization of the closed form by the presence of the αI’ residues, which appears to result from the salt bridge between αI‘ residue E528 and KD C-lobe residue R479 (Figure 1B). This salt bridge is destroyed by the αI‘ truncation.

A quantitative analysis of all SH3/SH2 ^{1}H-^{15}N chemical shifts by principal component analysis (PCA) comprising not only the presently described complexes but also complexes of Abl^{83-534} with further type I and type II inhibitors[16] completely confirms these qualitative observations (Figure 5A). The first principal component (PC1) distinguishes between assembled and disassembled conformation with respective clusters for type I and apo form as well as type II inhibitor complexes. Notably, almost 70 % of the data are explained by PC1 (Figure 5B). The PC1 values of the imatinib complexes of Abl^{83-519}, Abl^{83-517}, and Abl^{83-515} shift continuously on a straight from the position of the disassembled cluster towards about half of the position of the assembled cluster, indicating again that the core disassembly by imatinib is strongly reduced when the αI–αI’ loop is truncated. As observed before, the PC1 position of Abl^{83-534}•imatinib corresponds to a slightly less disassembled conformation than that of Abl^{83-519}•imatinib. All imatinib complexes are effectively inhibited. However, as shown later, the truncation of the αI–αI’ loop and the αI’-helix also leads to a reduction of kinase activity of the apo forms. Thus, the observed reduction in imatinib-induced disassembly correlates to reduced activation of Abl.

The PCA loadings plot (Figure 5C) shows the ^{1}H and ^{15}N chemical shift contribution of individual amino acids to PC1 and PC2. Not surprisingly, resonances of V130, T136, and G149, have a strong contribution on PC1, i.e. they are indicative for the assembly state. Mapping all residues that contribute strongly to PC1 ($|PC1| > 0.15$) onto the assembled core structure (PDB code 2FO0[15]) reveals a cluster located mainly within the SH3 domain in proximity to the SH2-KD-linker (Figure 5D). This agrees with the previously suggested imatinib-induced push of the KD N-lobe towards the SH3 domain[16].

Truncation of the αI-helix induces changes in the apo assembled core

In addition to PC1, the truncated apo constructs differ significantly from apo Abl$^{83-534}$ in PC2 (Figure 5A), which explains a further ~15 % of the observations (Figure 5B). Previously, the largest variations in PC2 among ATP-site inhibitor complexes and apo Abl$^{83-534}$ were observed between apo Abl$^{83-534}$ and Abl$^{83-534}$ type I inhibitor complexes, albeit both these forms adopt the assembled core conformation. Interestingly, the truncated Abl constructs shift even further away in the PC2 direction from the type I inhibitor complexes than apo Abl$^{83-534}$. While many residues contribute to both PC1 and PC2 (Figure 5C), S181, I182, and S183 contribute almost uniquely to PC2 (Figure 5C). These residues are located close to the interaction site with the αI-helix (Figure 5E). Thereby, this indicates a change of the interaction between the SH2 domain and the KD-C-lobe.

Figure 4B shows the chemical shift differences for all assigned SH3 and SH2 residues between apo Abl$^{83-534}$ and the respective apo truncated constructs. Notably, some more residues are visible in Figure 4B than in the PCA loadings (Figure 5C), since not all resonances were observable in all investigated forms and such cases were excluded from the PCA. The largest chemical shift differences between apo Abl$^{83-515}$, Abl$^{83-517}$ and Abl$^{83-519}$ relative to apo Abl$^{83-534}$ are observed for SH2 residues H148, V151, and A156. A156 is located in the helix opposite to the KD C-lobe and the other two residues are in close proximity to A156 and the SH3-SH2 and SH2-KD linkers (Figure 4C). These residues show the biggest chemical shift differences for apo Abl$^{83-517}$ and apo Abl$^{83-519}$, too. This indicates that the flexible αI-helix has a clear impact on the SH2 domain in apo Abl. The mechanical force may be transmitted to the SH3-SH2 and SH2-KD linkers and thereby influence the Abl core assembly.

Truncation of the αI-helix induces conformational changes in the KD around the ATP pocket

So far, we have only analyzed the behavior of SH3 and SH2 but not of KD resonances, since the former are best suited to monitor the Abl regulatory core assembly, while not being affected by local changes from ligand binding. However, we have also analyzed the chemical shift changes induced in the KD upon αI-helix truncation for the Abl apo forms (Supplementary Figure S1). Truncation of the αI-helix induces changes of the KD residues located between the αI-helix and the ATP binding pocket. Obviously, the shorter the αI-helix, the larger the chemical shift differences in the KD. Exemplary residues are D382, G391, F401 and Y459. Interestingly, D382 is the crucial catalytic residue.

We also compared KD chemical shifts for the imatinib-bound truncated constructs (Supplementary Figure S2). Although continuous changes are observed for some residues in close proximity to the allosteric pocket, these changes are rather minor relative to the changes in the apo forms. Interestingly, as shown for resonances E348, I379, Y459, and F505 (Supplementary Figure S2C), the initial truncation of the αI'-helix shifts the resonance in a different direction than the subsequent truncations of the αI-αI' loop. The resonances of the latter locate on a straight line. These observations correlate with the gradual trends of the imatinib-induced disassembly monitored by the SH3 and SH2 resonances in Figures 3 and 5. However, no such pronounced trends were observed for either SH3/SH2 or KD resonances for the apo forms.

The αI-helix contributes directly to Abl activation

As shown above, the αI-helix assists in Abl core disassembly induced by imatinib. To show that the αI-helix also participates in the 'real' activation process of apo Abl, we performed *in vitro* kinase activity assays for the different truncation constructs using the optimized Abl substrate Abltide (Figure 6). Indeed, the stepwise truncation of the αI-helix steadily reduces the Michaelis-Menten v_{max} from 116.9 nmol P_i min^{-1} μmol^{-1} for Abl^{83-534} down to the very small value of 3.4 nmol P_i min^{-1} μmol^{-1} for Abl^{83-515}, while substrate affinity K_M remained almost unchanged between 77 and 45 μM. This proves that the forces induced by the αI-helix are a fundamental part of the activation mechanism.

Conclusion

In summary, we have shown a correlation between the length of the Abl C-terminal αI-helix and the imatinib-induced disassembly of the Abl core as well as Abl's catalytic activity. We explain these observations by a simple mechanical model, where the flexible αI-helix samples conformational space in solution, thereby pushing onto the SH2 domain, which enables disassembly and activation of Abl. These results show that the push of the KD N-lobe alone onto the SH3 domain[16] is not sufficient to disassemble and activate the core. It is rather the combined effect of both the N-lobe and αI-helix mechanical forces which activates the kinase.

This mechanical model of Abl activation explains the inhibitory power of myristoyl-mimicking allosteric inhibitors such as asciminib, which were selected in the drug development process by their ability to bend the αI-helix[11, 20]. The bending induced by such allosteric inhibitors reduces the entropic force exerted by the αI-helix and abolishes kinase activity.

We have also shown by single-molecule FRET (smFRET) (Thesis Chapter 2) that the apo form of Abl$^{83-534}$ disassembles to about 30 % in solution. Of note, this conformation is less disassembled than the imatinib-induced conformation. We conclude from the smFRET data that this partial disassembly is a first step in kinase activation. Combined with the present data, we can definitely attribute the disassembly of the apo form to the mechanical force exerted by the αI-helix. It will be interesting to observe a reduction of apo disassembly in smFRET experiments for the αI-helix truncated constructs.

Since we showed that the αI-helix push is absolutely required for the enzymatic reaction with the small substrate Abltide and since allosteric inhibitors effectively inhibit the kinase by bending the αI-helix, it remains unclear how the kinase exerts its catalytic function in the myristoylated wildtype. One possible explanation would be that the myristoyl affinity is weaker than that of asciminib and consequently, the kinase performs its work during the periods in which the myristoyl is not bound. Indeed, the K_d of a myristoylated peptide towards Abl was determined as 2 μM[14] and that of asciminib is in the low nanomolar range[11]. A further possibility is that the low population of the disassembled state increases due to interactions with larger substrates, e.g. by the binding of substrate phosphotyrosine or polyproline motifs to Abl's SH2 and SH3 domains.

In apparent contrast to our data, a myristoylated N-cap-containing construct with the αI-helix ending at residue Q517 was reported to have an increased activity[14]. However, in this case, myristoyl binding is impaired and the pull by the 80-residue-long N-cap onto the SH3 domain may open the core and increase activity.

The myristoyl-related regulation mechanism including the αI-helix is rather unique among kinases as known so far. For example, in the structurally closely related Src and Hck kinases[13], the αI'-helix part is not present. Instead, a phosphorylated tyrosine in the C-terminal tail interacts with the SH2 domain and thereby stabilizes the assembled core[23]. Besides the Abl and Src kinase families, also the Csk, Brk, and Tec kinase families contain the regulatory SH3-SH2-KD module. It would be interesting to investigate how activation is achieved in these assemblies.

Material and Methods

Cloning, expression and purification

To generate the Abl constructs with the truncated αI-helix (Abl$^{83-513}$, Abl$^{83-514}$, Abl$^{83-515}$, Abl$^{83-516}$, Abl$^{83-517}$, Abl$^{83-518}$, and Abl$^{83-519}$; Abl 1b numbering), stop codons (TAG) were

introduced at the respective positions by site-directed QuikChange™ mutagenesis into the plasmid containing human Abl$^{83-534}$, which was described earlier[22]. For the initial expression and solubility tests, all Abl constructs were co-expressed with lambda phosphatase (LPP; to obtain purely dephosphorylated Abl) as described earlier[16] in 25 mL LB medium. After harvesting, cells were resuspended in 1 mL lysis buffer, sonicated, centrifuged and the supernatant collected for western blot analysis with a conjugated poly-histidine antibody (Sigma Aldrich, Cat.No. A7058).

All Abl constructs used for NMR experiments were co-expressed with LPP in ^{15}N-labeled M9 minimal medium and purified as described earlier[16, 22] except for the following modifications. The cell lysate was cleared by centrifugation at 30.000 g and loaded onto a His-Trap column (GE Healthcare) and eluted by applying a linear imidazole gradient from 20 mM to 200 mM within 30 CV. Further, in contrast to Abl$^{83-534}$, the truncated Abl mutants did not bind to ion exchange Q- or S-sepharose HP columns (GE Healthcare) equilibrated with 20 mM Tris-HCl, 20 mM NaCl, 2 mM TCEP, and 5 % glycerol. However, loading of Abl onto the Q-sepharose HP column helped to remove impurities that bind tightly to the column, while Abl could be collected in the flow through. *In vitro* LPP treatment was applied after the ion-exchange step as described earlier[16], if Abl was not fully dephosphorylated as indicated by electron-spray ionization (ESI) time-of-flight (TOF) mass spectrometry (MS)[16]. All purified samples were validated by ESI-TOF MS for correct protein mass and absence of contaminations by other proteins.

NMR spectroscopy

As in our previous studies[16, 22], the isotope-labeled SH3-SH2-KD Abl constructs were concentrated to 25-100 µM in 20 mM Tris·HCl (pH 8.0), 100 mM NaCl, 2 mM EDTA, 2 mM TCEP, and 0.02 % NaN_3. Ligands pre-dissolved in DMSO (stock concentration 5 mM) were added at a molar ratio of 3:1 (ligand:protein). All NMR experiments were performed at 303 K on a Bruker AVANCE 900-MHz spectrometer equipped with a TCI triple resonance cryo-probe. ^{1}H-^{15}N TROSY experiments were recorded with 224 (^{15}N) × 1024 (^{1}H) complex points and acquisition times of ~40 ms in both dimensions. All NMR data were processed with the NMRpipe software package[24]. Spectra were displayed and analyzed with the program SPARKY[25]. The chemical shift differences were calculated according to $\Delta\delta = ({\Delta\delta_N}^2/25 + {\Delta\delta_{HN}}^2)^{1/2}$. The principal component analysis (PCA) of chemical shift variations was carried out using NumPy.

PDB structure analysis

PDB structures were displayed using the PyMOL Molecular Graphics System (Schrödinger, LLC).

Activity assay

A biotinylated form of the optimized Abl substrate Abltide (biotin-GGEAIYAAPFKK, obtained from ProteoGenix, France) was incubated in concentrations from 3.125 µM to 200 µM in a total of 20 µl kinase assay buffer (20 mM Tris-HCl, 5 mM $MgCl_2$, 1 mM DTT, 10 µM bovine serum albumin, pH 7.5) with 2 ng of the respective Abl construct, 100 µM ATP and 5 µCi γ-^{32}P-ATP for 12 minutes at room temperature. The reaction was terminated by adding 10 µl of 7.5 M guanidine hydrochloride. 8 µl of this terminated reaction mixture were then applied to a streptavidin biotin capture membrane (SAM2, Promega, Cat.# V2861) and further treated following the manufacturer's recommendations. Thus, after a short drying phase, the membrane was washed for 30 s with 2 M NaCl, 3 times for 2 min with 2 M NaCl, 4 times for 2 min with 2 M NaCl in 1% H_3PO_4, 2 times for 30 s with deionized water, and finally rinsed with ethanol. The amount of ^{32}P incorporated into the Abl substrate was quantified using a liquid scintillation counter (PerkinElmer, model: Tri-Carb®4910TR).

Figure Legends

Figure 1. Conformations of the Abl core and domain organization in Abl and Bcr-Abl. (**A**) The domain organization is shown of Abl isoforms 1a and 1b, as well as of the chronic myeloid leukemia (CML)-inducing fusion protein Bcr-Abl. The Abl^{core} consists sequentially of an SH3, an SH2, and a kinase domain (KD). The N-cap varies between the two splice variants, whereby the isoform 1b is 19 amino acids longer and N-myristoylated at glycine 2. In the Bcr-Abl fusion protein the N-cap is exchanged with a fragment of the Bcr protein. (**B**) The crystal structure of the N-terminal half of Abl 1b isoform (residues 2-531), myristoylated (orange spheres) at the N-terminal glycine (PDB 2FO0[15]), shows a tight assembly with the SH3 (green) and SH2 (yellow) domains docking onto the KD (blue) N- and C-lobes. The N-cap is indicated by a dashed brown line since large parts of it (aa 2-64) are not observed in the X-ray structure probably due to high flexibility[15]. The C-terminal αI-helix is extended and straight in a KD-only crystal structure with unliganded myristoyl pocket (shown in red, PDB code 1M52[18]) and would clash with the SH2 domain in the assembled core conformation. However, the αI-helix is bent in the presence of myristoylation, which leads to a shorter αI-helix (residues 504-515, light pink) and the newly formed αI'-helix (aa 520-531), which are connected by the αI-αI'-loop[13]. This allows SH2 docking to the KD C-lobe. A salt bridge between residues R479 (KD C-lobe, sticks representation) and E528 (located toward the end of the αI'-helix, sticks representation) is observed in the crystal structure. (**C**) Type II inhibitors such as imatinib, shown in orange stick representation, induce a dynamic disassembled conformation as evident from NMR and SAXS data with nanosecond mobility of the SH3 and SH2 domains (indicated by grey arrows)[22]. One possible conformation of the deduced structural ensemble is shown. The αI'-helix is highly flexible in this conformation as shown by NMR relaxation experiments (indicated by arrows)[20, 22]. (**D**) Schematic representation of the C-terminal αI-helix. In the case of the KD-only construct without bound myristoyl (PDB code 1M52[18]), the helix extends from residue 504 to 522. In presence of the SH3 and SH2 domains and with bound myristoyl (PDB code 2FO0[15]), the αI-helix breaks after residue 515 and the newly formed αI'-helix forms (residues 520-531).

Figure 2. Production of Abl^{core} constructs with truncated αI-helix. (**A**) The interaction site between the SH2 domain (yellow surface representation) and the C-terminus of the Abl KD (blue cartoon representation) is shown for the truncated constructs used in the NMR experiments (Abl^{83-515}, Abl^{83-517}, Abl^{83-519}). The respective last amino acids, M515, Q517, and S519, are shown in stick representation. (**B**) Top: western blot of the soluble Abl fractions in the supernatant after cell lysis of several Abl constructs truncated at different positions in the αI-helix and αI-αI'-loop. Bottom: expression yields of the corresponding Abl constructs. The x-axis denotes the respective last amino acid of the respective construct Abl^{83-X}. (**C**) The side chains of H509, Q510, A511, E513, T514, and M515 at the end of the αI-helix are shown in grey stick representation and their hydrogen bonds are depicted as yellow dashed lines. (**D**) Relative yields of purified Abl constructs with truncated helix which were used for NMR experiments. The x-axis denotes the respective last amino acid of the respective construct Abl^{83-X}.

Figure 3. Selected SH3 and SH2 resonances show an influence of the helix truncation on the apo forms and the complexes with imatinib. (**A**) The residues V130, T136, and G149 are highlighted in the assembled core structure as spheres (PDB 2FO0[15]). (**B**) The resonances of V130, T136, and G149 of the different ^{1}H-^{15}N TROSY spectra are superimposed. These residues are reporters on the Abl core assembly state. The resonances are from apo Abl$^{83-534}$ (black), apo Abl$^{83-515}$ (red), Abl$^{83-534}$•imatinib (blue), Abl$^{83-519}$•imatinib (brown), Abl$^{83-517}$•imatinib (magenta), and Abl$^{83-515}$•imatinib (green). The peak centers are marked by dots. The shifts that result from helix truncation as seen in the two apo spectra are indicated by red arrows. The shifts that result from imatinib-induced core disassembly are indicated by black arrows.

Figure 4. Chemical shift differences Δδ of SH3-SH2 resonances. Averaged ^{1}H and ^{15}N chemical shift differences $\Delta\delta = (\Delta\delta_N{}^2/25 + \Delta\delta_{HN}{}^2)^{1/2}$ for all assigned SH3-SH2 resonances. (**A**) $\Delta\delta$ between the apo form and the imatinib-bound complex of the respective truncated constructs (Abl^{83-X}, where X stands for the respective last amino acid) as a function of residue number. The reporter residues of Figure 3 are labeled. (**B**) Δδ between apo Abl^{83-X} and Abl$^{83-534}$ as a function of residue number. Largest differences are observed for H148, V151, and A156, which are highlighted in (**C**) as red spheres in the assembled core structure (PDB 2FO0[15]).

Figure 5. Analysis of SH3-SH2 resonances by principle component analysis. The ^{1}H and ^{15}N chemical shifts of all assigned SH3-SH2 resonances of all truncated constructs in the apo forms and in complex with imatinib and Abl$^{83-534}$ in complex with various ATP competitive inhibitors were analyzed by principle component analysis (PCA). (**A**) The score plot reveals a cluster comprising apo Abl$^{83-534}$ and its complexes with the non-hydrolysable ATP analogue AMP-PNP and all type I ATP competitive inhibitors (green background). This represents the assembled core conformation. A second cluster (purple background), which is separated in the PC1 dimension, comprises all Abl$^{83-534}$•type II inhibitor complexes and represents the disassembled core conformation. The truncated apo Abl^{83-X} constructs have the same PC1 score as apo Abl$^{83-534}$, but are shifted in the PC2 dimension as indicated by a magenta arrow labeled 'helix truncation'. The truncated Abl^{83-X}•imatinib constructs are shifted in the PC1 dimension in dependence of the length of the construct. In particular, the Abl$^{83-515}$•imatinib complex is less disassembled compared to the Abl$^{83-534}$•imatinib complex. (**B**) Relative signal contributions of the principal components (PCs). The first two PCs explain approximately 85 % of the data (red line). (**C**) PCA loading plot showing the contributions of the ^{1}H or ^{15}N chemical shifts of individual residues to the first two PCs. (**D**) Residues that contribute most to PC1 (|PC1| > 0.15) are shown as red spheres in the assembled core structure. (**E**) Residues that contribute most to PC2 (PC2 > 0.15 or PC2 < -0.2) are shown as blue spheres in the assembled core structure.

Figure 6. The kinase activity correlates with the length of the αI-helix. The specific kinase activity of Abl$^{83-534}$ (black curve), Abl$^{83-519}$ (red), Abl$^{83-517}$ (blue), and Abl$^{83-515}$ (green) was

measured in an *in vitro* phosphorylation assay from the incorporation of ^{32}P into an optimal Abl substrate peptide (Abltide) at varying concentrations. The averages of 3 replicates are shown. The data were fitted to Michaelis-Menten kinetics and the values for v_{max} and the Michaelis-Menten constant K_M are shown below the plot.

Supplementary Figure 1. Truncation of the αI-helix influences apo KD resonances. (**A**) The chemical shift differences of KD residues between apo Abl$^{83-534}$ and apo Abl$^{83-515}$ are mapped onto the assembled core structure (PDB 2FO0[15]). KD residues with chemical shift differences $\Delta\delta \geq 0.04$ ppm are shown as red spheres; residues with $\Delta\delta < 0.04$ ppm are shown as blue spheres. Unassigned residues are shown as grey cartoon. (**B**) The chemical shift differences of KD residues between apo Abl$^{83-534}$ and apo Abl$^{83-519}$ are mapped onto the assembled core structure. KD residues with chemical shift differences $\Delta\delta > 0.04$ ppm are shown as red spheres, residues with $\Delta\delta < 0.04$ ppm are shown as blue spheres. Unassigned residues are shown as grey cartoon. (**C**) Exemplary resonances from ^{1}H-^{15}N TROSY spectra of apo Abl$^{83-534}$ (red), Abl$^{83-519}$ (black), Abl$^{83-517}$ (blue), and Abl$^{83-515}$ (yellow), which show a shift depending on the αI-helix length (indicated by arrows), and the respective residues labeled in (A) and (B).

Supplementary Figure 2. The KD resonances of Abl•imatinib complexes are less affected by αI-helix truncation. (**A**) The chemical shift differences of KD residues between Abl$^{83-534}$•imatinib and Abl$^{83-515}$•imatinib are mapped onto the assembled core structure (PDB 2FO0[15]). KD residues with chemical shift differences $\Delta\delta \geq 0.075$ ppm are shown as red spheres; residues with $\Delta\delta < 0.075$ ppm are shown as blue spheres. Unassigned residues are shown as grey cartoon. (**B**) The chemical shift differences of KD residues between Abl$^{83-534}$•imatinib and Abl$^{83-519}$•imatinib are mapped onto the assembled core structure. KD residues with chemical shift differences $\Delta\delta \geq 0.075$ ppm are shown as red spheres, residues with $\Delta\delta < 0.075$ ppm are shown as blue spheres. Unassigned residues are shown as grey cartoon. (**C**) Exemplary resonances from ^{1}H-^{15}N TROSY spectra of Abl$^{83-534}$•imatinib (magenta), Abl$^{83-519}$•imatinib (blue), Abl$^{83-517}$•imatinib (cyan), and Abl$^{83-515}$•imatinib (green), which show a shift depending on the αI-helix length (indicated by arrows), and the respective residues labeled in (A) and (B).

References

1. Van Etten, R. A., Cycling, stressed-out and nervous: cellular functions of c-Abl. *Trends Cell Biol* **1999,** *9* (5), 179-86.
2. Pendergast, A. M., The Abl family kinases: mechanisms of regulation and signaling. *Adv Cancer Res* **2002,** *85*, 51-100.
3. Hantschel, O.; Grebien, F.; Superti-Furga, G., The growing arsenal of ATP-competitive and allosteric inhibitors of BCR-ABL. *Cancer Res* **2012,** *72* (19), 4890-5.
4. Rowley, J. D., Letter: A new consistent chromosomal abnormality in chronic myelogenous leukaemia identified by quinacrine fluorescence and Giemsa staining. *Nature* **1973,** *243* (5405), 290-3.
5. Deininger, M. W.; Goldman, J. M.; Melo, J. V., The molecular biology of chronic myeloid leukemia. *Blood* **2000,** *96* (10), 3343-56.
6. Braun, T. P.; Eide, C. A.; Druker, B. J., Response and Resistance to BCR-ABL1-Targeted Therapies. *Cancer Cell* **2020,** *37* (4), 530-542.
7. Shah, N. P.; Tran, C.; Lee, F. Y.; Chen, P.; Norris, D.; Sawyers, C. L., Overriding imatinib resistance with a novel ABL kinase inhibitor. *Science* **2004,** *305* (5682), 399-401.
8. O'Hare, T., A Decade of Nilotinib and Dasatinib: From In Vitro Studies to First-Line Tyrosine Kinase Inhibitors. *Cancer Res* **2016,** *76* (20), 5911-5913.
9. Eide, C. A.; Zabriskie, M. S.; Savage Stevens, S. L.; Antelope, O.; Vellore, N. A.; Than, H.; Schultz, A. R.; Clair, P.; Bowler, A. D.; Pomicter, A. D.; Yan, D.; Senina, A. V.; Qiang, W.; Kelley, T. W.; Szankasi, P.; Heinrich, M. C.; Tyner, J. W.; Rea, D.; Cayuela, J. M.; Kim, D. W.; Tognon, C. E.; O'Hare, T.; Druker, B. J.; Deininger, M. W., Combining the Allosteric Inhibitor Asciminib with Ponatinib Suppresses Emergence of and Restores Efficacy against Highly Resistant BCR-ABL1 Mutants. *Cancer Cell* **2019,** *36* (4), 431-443 e5.
10. Wylie, A. A.; Schoepfer, J.; Jahnke, W.; Cowan-Jacob, S. W.; Loo, A.; Furet, P.; Marzinzik, A. L.; Pelle, X.; Donovan, J.; Zhu, W.; Buonamici, S.; Hassan, A. Q.; Lombardo, F.; Iyer, V.; Palmer, M.; Berellini, G.; Dodd, S.; Thohan, S.; Bitter, H.; Branford, S.; Ross, D. M.; Hughes, T. P.; Petruzzelli, L.; Vanasse, K. G.; Warmuth, M.; Hofmann, F.; Keen, N. J.; Sellers, W. R., The allosteric inhibitor ABL001 enables dual targeting of BCR-ABL1. *Nature* **2017,** *543* (7647), 733-737.
11. Schoepfer, J.; Jahnke, W.; Berellini, G.; Buonamici, S.; Cotesta, S.; Cowan-Jacob, S. W.; Dodd, S.; Drueckes, P.; Fabbro, D.; Gabriel, T.; Groell, J. M.; Grotzfeld, R. M.; Hassan, A. Q.; Henry, C.; Iyer, V.; Jones, D.; Lombardo, F.; Loo, A.; Manley, P. W.; Pelle, X.; Rummel, G.; Salem, B.; Warmuth, M.; Wylie, A. A.; Zoller, T.; Marzinzik, A. L.; Furet, P., Discovery of Asciminib (ABL001), an Allosteric Inhibitor of the Tyrosine Kinase Activity of BCR-ABL1. *J Med Chem* **2018,** *61* (18), 8120-8135.
12. Hughes, T. P.; Mauro, M. J.; Cortes, J. E.; Minami, H.; Rea, D.; DeAngelo, D. J.; Breccia, M.; Goh, Y. T.; Talpaz, M.; Hochhaus, A.; le Coutre, P.; Ottmann, O.; Heinrich, M. C.; Steegmann, J. L.; Deininger, M. W. N.; Janssen, J.; Mahon, F. X.; Minami, Y.; Yeung, D.; Ross, D. M.; Tallman, M. S.; Park, J. H.; Druker, B. J.; Hynds, D.; Duan, Y.; Meille, C.; Hourcade-Potelleret, F.; Vanasse, K. G.; Lang,

F.; Kim, D. W., Asciminib in Chronic Myeloid Leukemia after ABL Kinase Inhibitor Failure. *N Engl J Med* **2019,** *381* (24), 2315-2326.

13. Nagar, B.; Hantschel, O.; Young, M. A.; Scheffzek, K.; Veach, D.; Bornmann, W.; Clarkson, B.; Superti-Furga, G.; Kuriyan, J., Structural basis for the autoinhibition of c-Abl tyrosine kinase. *Cell* **2003,** *112* (6), 859-71.

14. Hantschel, O.; Nagar, B.; Guettler, S.; Kretzschmar, J.; Dorey, K.; Kuriyan, J.; Superti-Furga, G., A myristoyl/phosphotyrosine switch regulates c-Abl. *Cell* **2003,** *112* (6), 845-57.

15. Nagar, B.; Hantschel, O.; Seeliger, M.; Davies, J. M.; Weis, W. I.; Superti-Furga, G.; Kuriyan, J., Organization of the SH3-SH2 unit in active and inactive forms of the c-Abl tyrosine kinase. *Mol Cell* **2006,** *21* (6), 787-98.

16. Sonti, R.; Hertel-Hering, I.; Lamontanara, A. J.; Hantschel, O.; Grzesiek, S., ATP Site Ligands Determine the Assembly State of the Abelson Kinase Regulatory Core via the Activation Loop Conformation. *J Am Chem Soc* **2018,** *140* (5), 1863-1869.

17. Hantschel, O., Structure, regulation, signaling, and targeting of abl kinases in cancer. *Genes Cancer* **2012,** *3* (5-6), 436-46.

18. Nagar, B.; Bornmann, W. G.; Pellicena, P.; Schindler, T.; Veach, D. R.; Miller, W. T.; Clarkson, B.; Kuriyan, J., Crystal structures of the kinase domain of c-Abl in complex with the small molecule inhibitors PD173955 and imatinib (STI-571). *Cancer Res* **2002,** *62* (15), 4236-43.

19. Adrian, F. J.; Ding, Q.; Sim, T.; Velentza, A.; Sloan, C.; Liu, Y.; Zhang, G.; Hur, W.; Ding, S.; Manley, P.; Mestan, J.; Fabbro, D.; Gray, N. S., Allosteric inhibitors of Bcr-abl-dependent cell proliferation. *Nat Chem Biol* **2006,** *2* (2), 95-102.

20. Jahnke, W.; Grotzfeld, R. M.; Pelle, X.; Strauss, A.; Fendrich, G.; Cowan-Jacob, S. W.; Cotesta, S.; Fabbro, D.; Furet, P.; Mestan, J.; Marzinzik, A. L., Binding or bending: distinction of allosteric Abl kinase agonists from antagonists by an NMR-based conformational assay. *J Am Chem Soc* **2010,** *132* (20), 7043-8.

21. Zhang, J.; Adrian, F. J.; Jahnke, W.; Cowan-Jacob, S. W.; Li, A. G.; Iacob, R. E.; Sim, T.; Powers, J.; Dierks, C.; Sun, F.; Guo, G. R.; Ding, Q.; Okram, B.; Choi, Y.; Wojciechowski, A.; Deng, X.; Liu, G.; Fendrich, G.; Strauss, A.; Vajpai, N.; Grzesiek, S.; Tuntland, T.; Liu, Y.; Bursulaya, B.; Azam, M.; Manley, P. W.; Engen, J. R.; Daley, G. Q.; Warmuth, M.; Gray, N. S., Targeting Bcr-Abl by combining allosteric with ATP-binding-site inhibitors. *Nature* **2010,** *463* (7280), 501-6.

22. Skora, L.; Mestan, J.; Fabbro, D.; Jahnke, W.; Grzesiek, S., NMR reveals the allosteric opening and closing of Abelson tyrosine kinase by ATP-site and myristoyl pocket inhibitors. *Proc Natl Acad Sci U S A* **2013,** *110* (47), E4437-45.

23. Thomas, S. M.; Brugge, J. S., Cellular functions regulated by Src family kinases. *Annu Rev Cell Dev Biol* **1997,** *13*, 513-609.

24. Delaglio, F.; Grzesiek, S.; Vuister, G. W.; Zhu, G.; Pfeifer, J.; Bax, A., NMRPipe: a multidimensional spectral processing system based on UNIX pipes. *J Biomol NMR* **1995,** *6* (3), 277-93.

25. Lee, W.; Tonelli, M.; Markley, J. L., NMRFAM-SPARKY: enhanced software for biomolecular NMR spectroscopy. *Bioinformatics* **2015,** *31* (8), 1325-7.

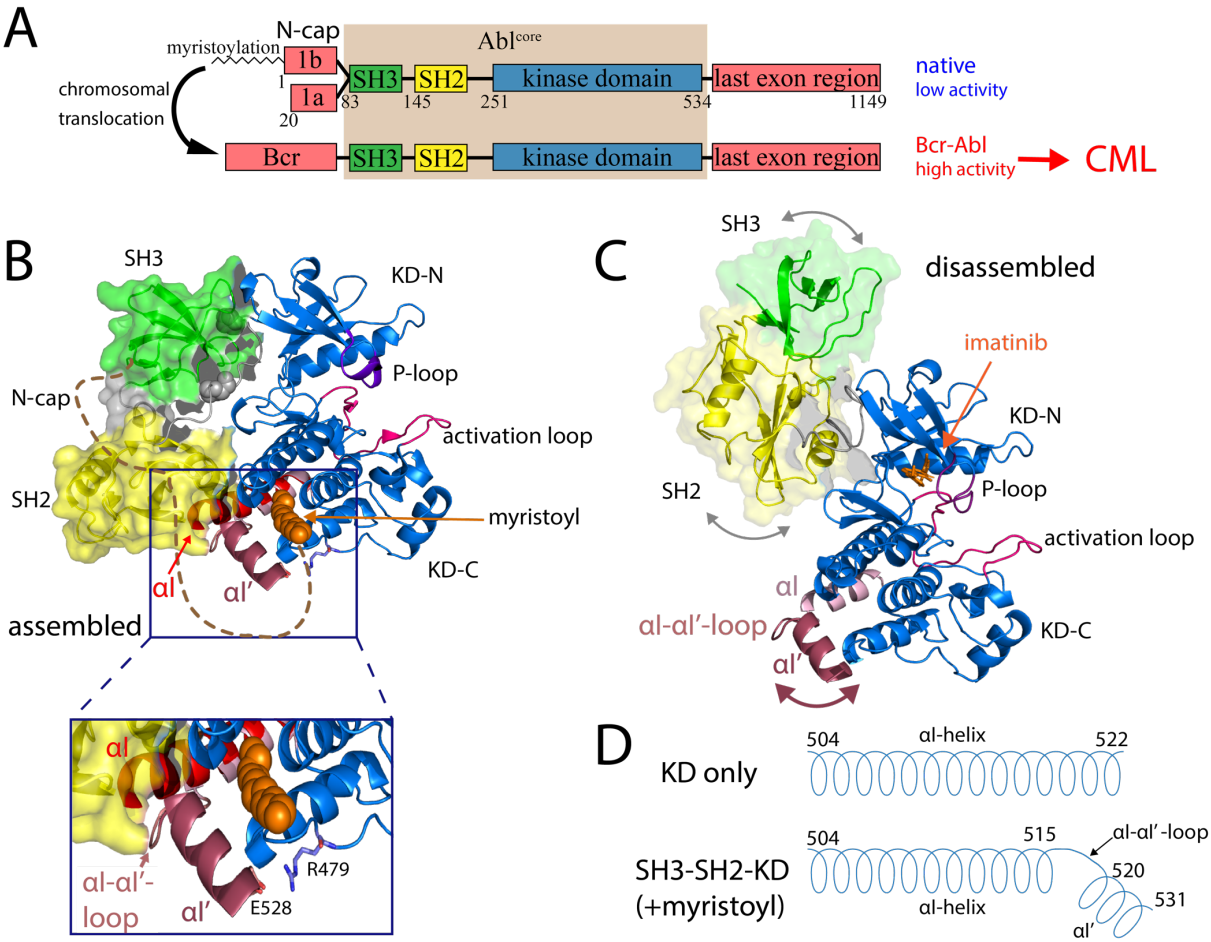
A
N-cap
myristoylation
1b
1a
1
20
Abl^core
SH3
SH2
kinase domain
last exon region
83
145
251
534
1149
chromosomal
translocation
Bcr
native
low activity
Bcr-Abl
high activity
CML
B
SH3
KD-N
N-cap
P-loop
activation loop
SH2
myristoyl
KD-C
αI
αI′
assembled
αI-αI′-
loop
R479
E528
C
SH3
disassembled
imatinib
KD-N
SH2
P-loop
activation loop
αI
αI-αI′-loop
KD-C
αI′
D
KD only
504
αI-helix
522
SH3-SH2-KD
(+myristoyl)
504
515
αI-αI′-loop
520
αI-helix
531
αI′

Figure 1

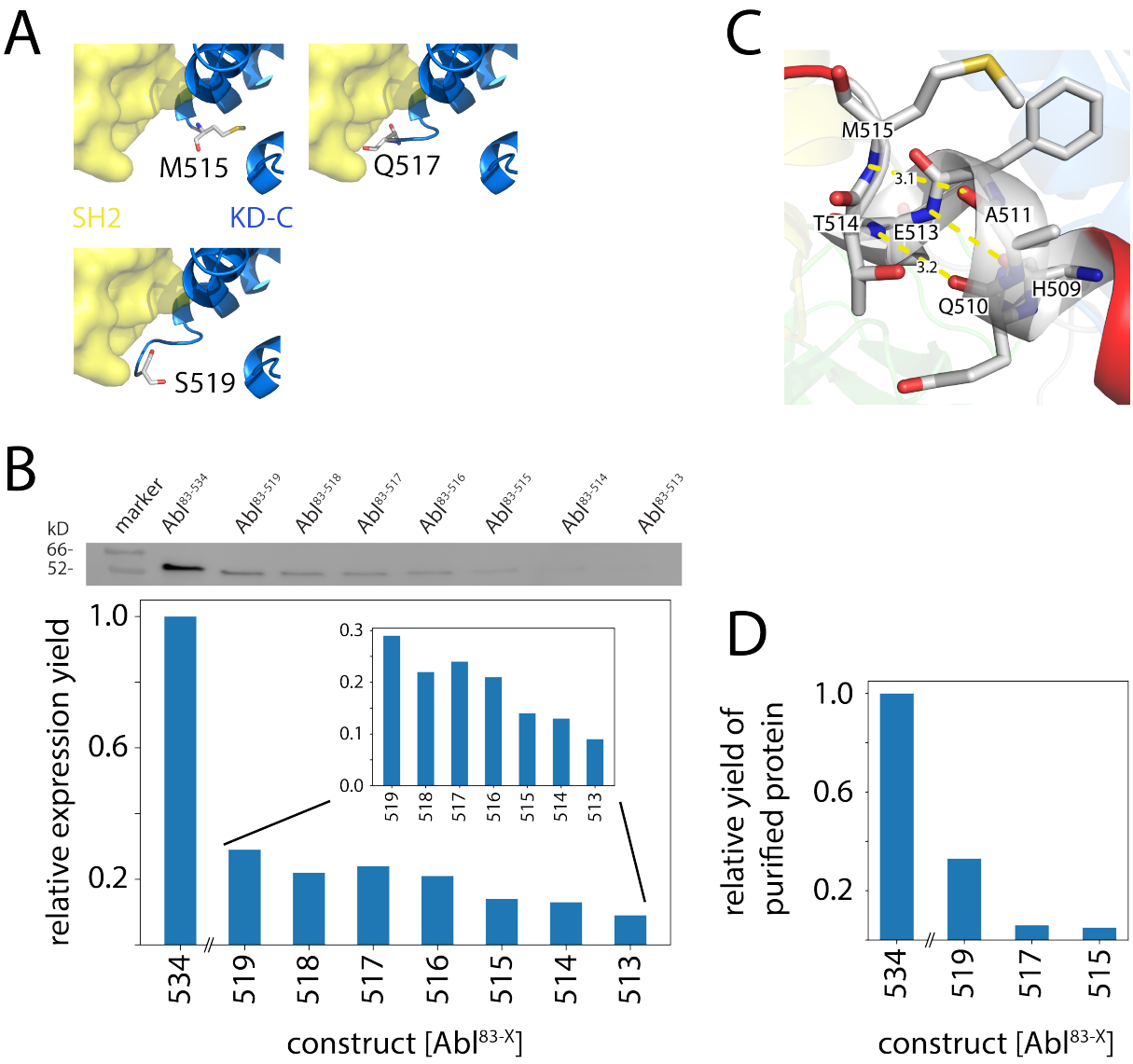
A
M515
Q517
SH2
KD-C
S519
C
M515
3.1
T514
E513
A511
3.2
H509
Q510
B
marker
Abl83-534
Abl83-519
Abl83-518
Abl83-517
Abl83-516
Abl83-515
Abl83-514
Abl83-513
kD
66-
52-
relative expression yield
1.0
0.6
0.2
0.3
0.2
0.1
0.0
519
518
517
516
515
514
513
534
519
518
517
516
515
514
513
construct [Abl83-X]
D
relative yield of purified protein
1.0
0.6
0.2
534
519
517
515
construct [Abl83-X]

Figure 2

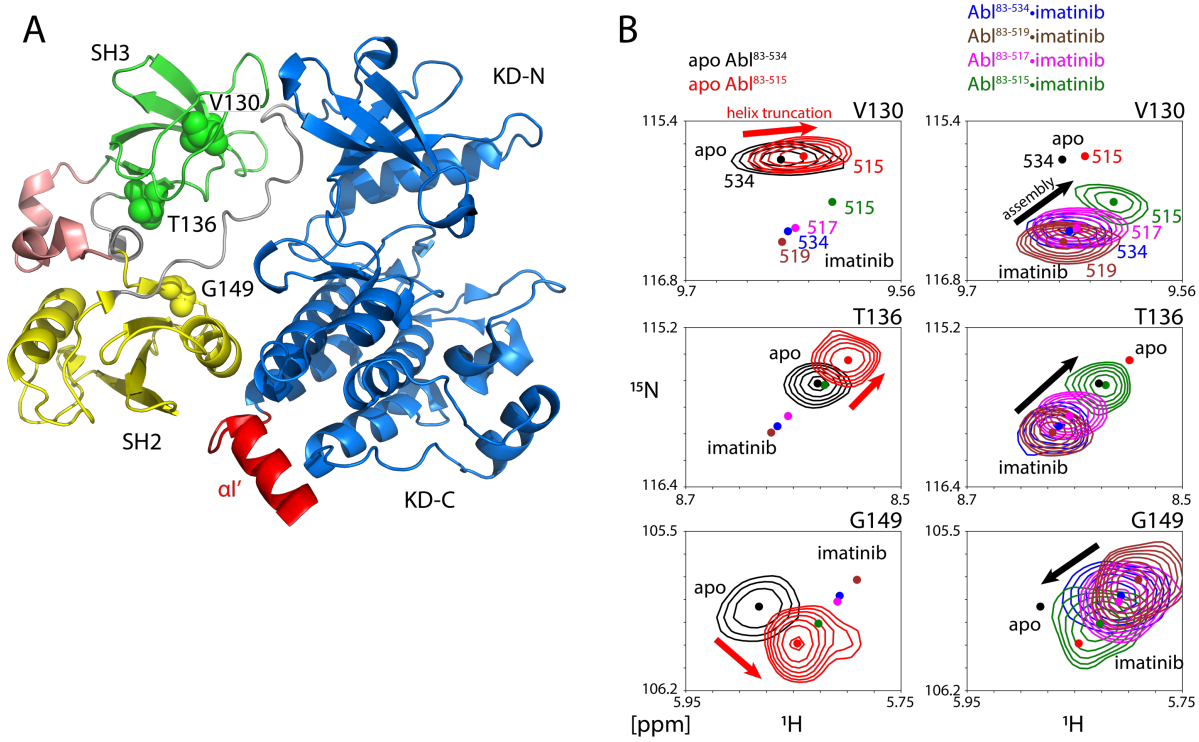
A
SH3
V130
KD-N
T136
G149
SH2
αI′
KD-C
B
Abl83-534•imatinib
Abl83-519•imatinib
Abl83-517•imatinib
Abl83-515•imatinib
apo Abl83-534
apo Abl83-515
helix truncation
V130
T136
G149
apo
imatinib
assembly
15N
[ppm]
1H

Figure 3

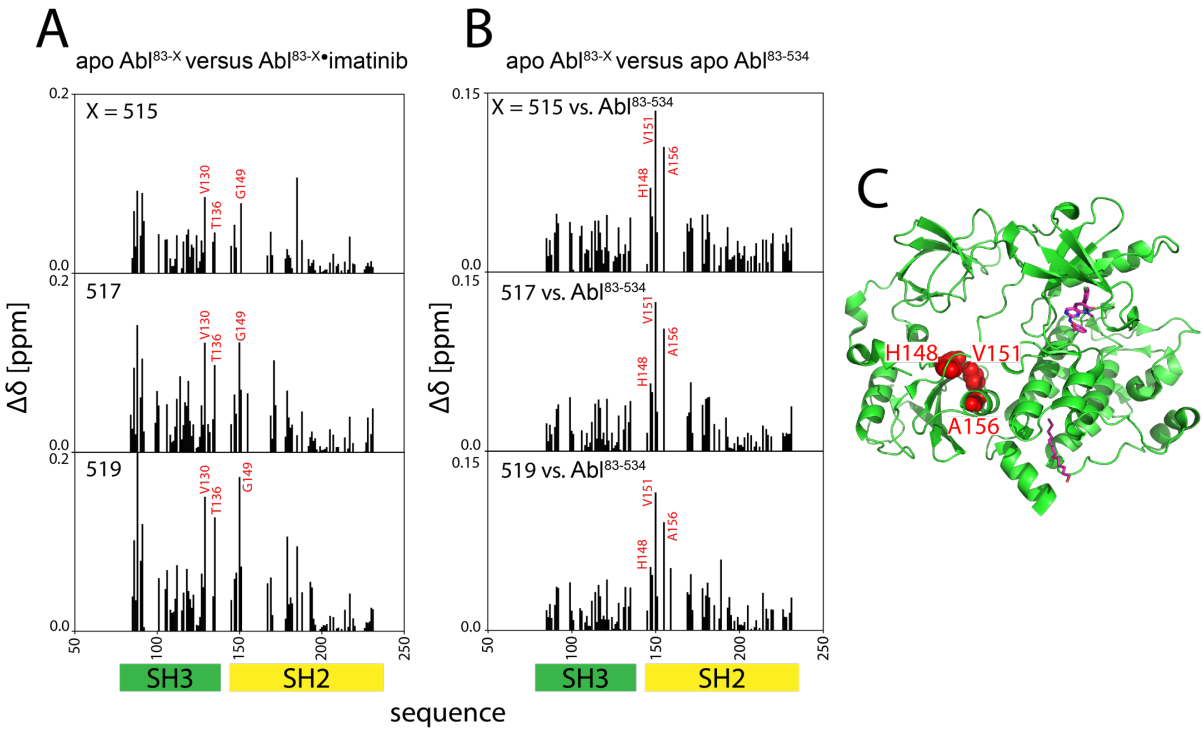
A
apo Abl83-X versus Abl83-X•imatinib
X = 515
517
519
V130
T136
G149
Δδ [ppm]
B
apo Abl83-X versus apo Abl83-534
X = 515 vs. Abl83-534
517 vs. Abl83-534
519 vs. Abl83-534
H148
V151
A156
SH3
SH2
sequence
C
H148
V151
A156

Figure 4

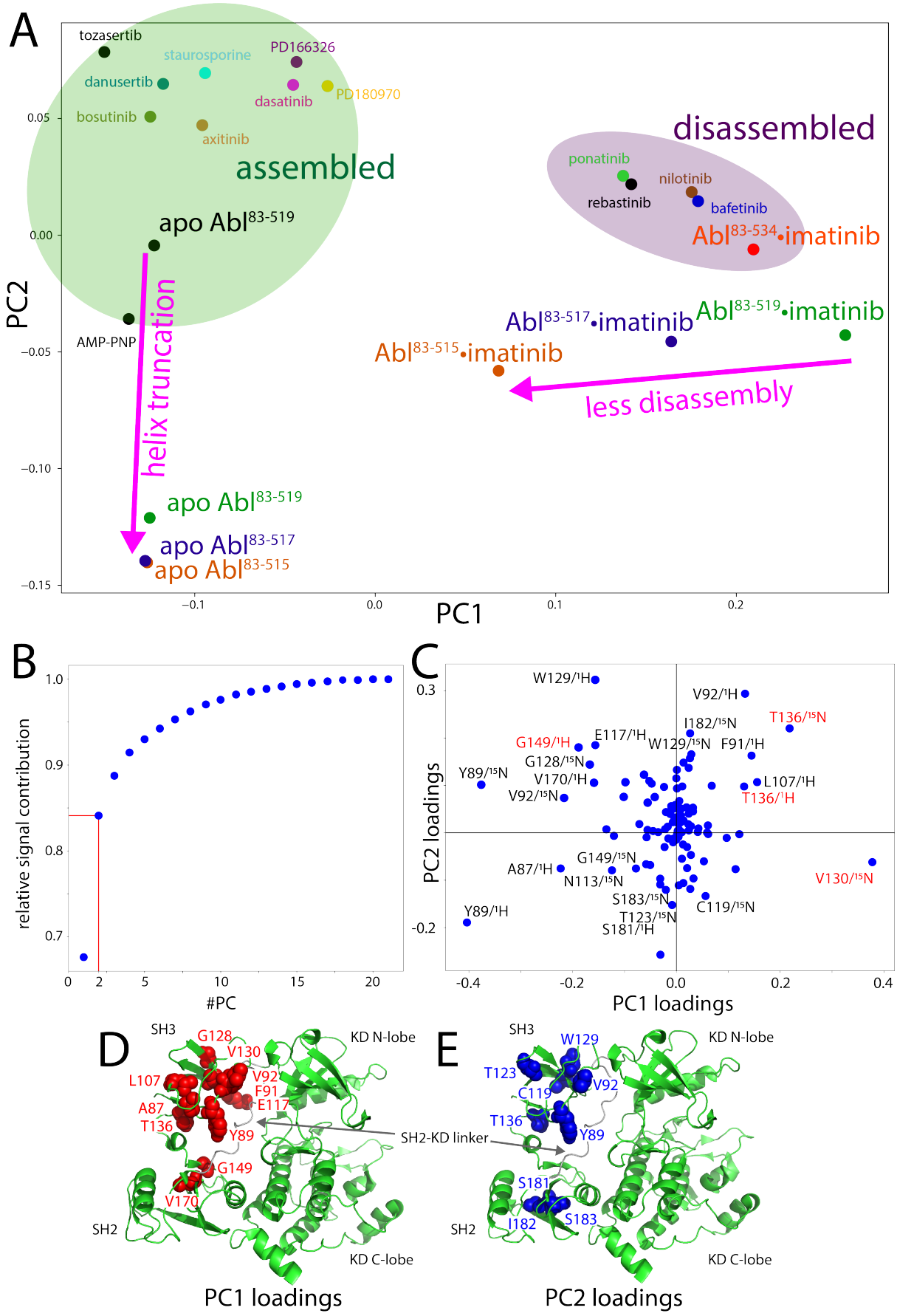
A
tozasertib
staurosporine
PD166326
danusertib
dasatinib
PD180970
bosutinib
axitinib
assembled
disassembled
ponatinib
nilotinib
rebastinib
bafetinib
Abl83-534•imatinib
apo Abl83-519
AMP-PNP
helix truncation
Abl83-517•imatinib
Abl83-519•imatinib
Abl83-515•imatinib
less disassembly
apo Abl83-519
apo Abl83-517
apo Abl83-515
PC2
PC1
B
relative signal contribution
#PC
C
PC2 loadings
PC1 loadings
W129/1H
V92/1H
T136/15N
I182/15N
E117/1H
G149/1H
W129/15N
F91/1H
G128/15N
Y89/15N
V170/1H
L107/1H
V92/15N
T136/1H
G149/15N
A87/1H
N113/15N
V130/15N
S183/15N
Y89/1H
C119/15N
T123/15N
S181/1H
D
SH3
G128
V130
KD N-lobe
L107
V92
F91
A87
E117
T136
Y89
SH2-KD linker
G149
V170
SH2
KD C-lobe
PC1 loadings
E
SH3
W129
KD N-lobe
T123
C119
V92
T136
Y89
S181
I182
S183
SH2
KD C-lobe
PC2 loadings

Figure 5

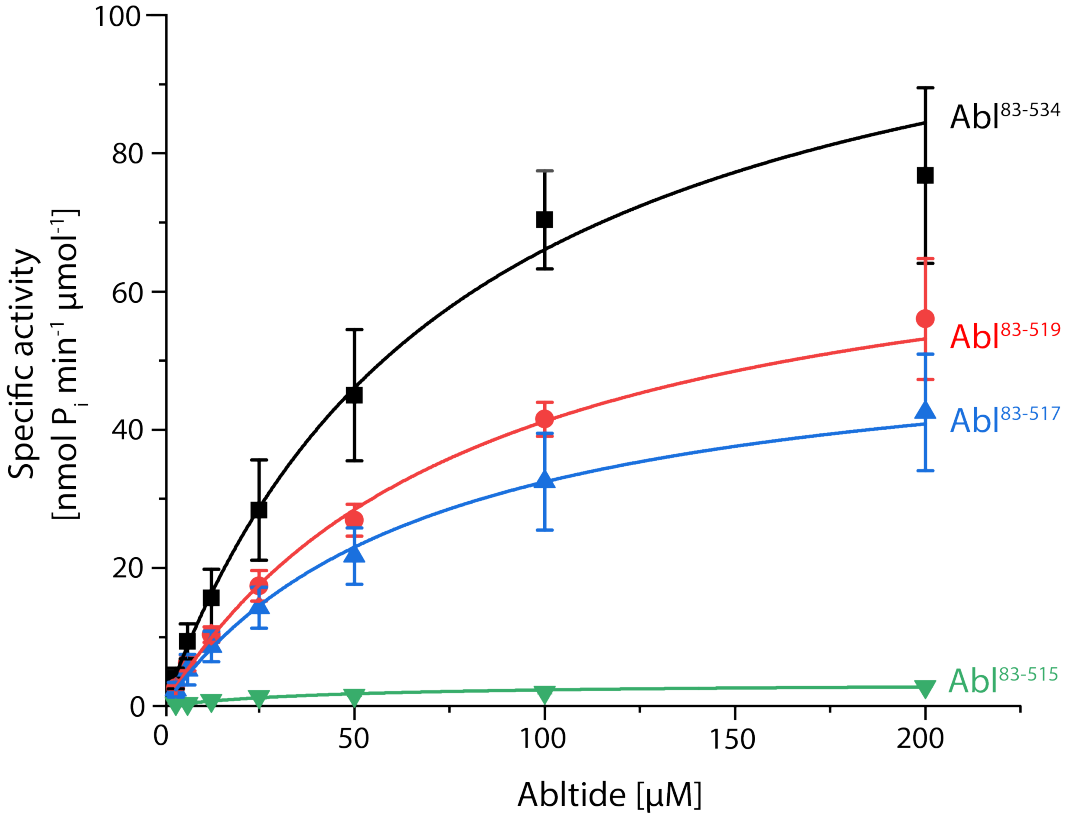

	Abl$^{83-534}$	Abl$^{83-519}$	Abl$^{83-517}$	Abl$^{83-515}$
v_{max} [nmol P_i min^{-1} µmol^{-1}]	116.9 ± 9.5	74.9 ± 5.1	55.1 ± 3.3	3.4 ± 0.2
K_M [µM]	77.0 ± 10.9	81.7 ± 8.7	69.7 ± 6.8	45.2 ± 10.9

Figure 6

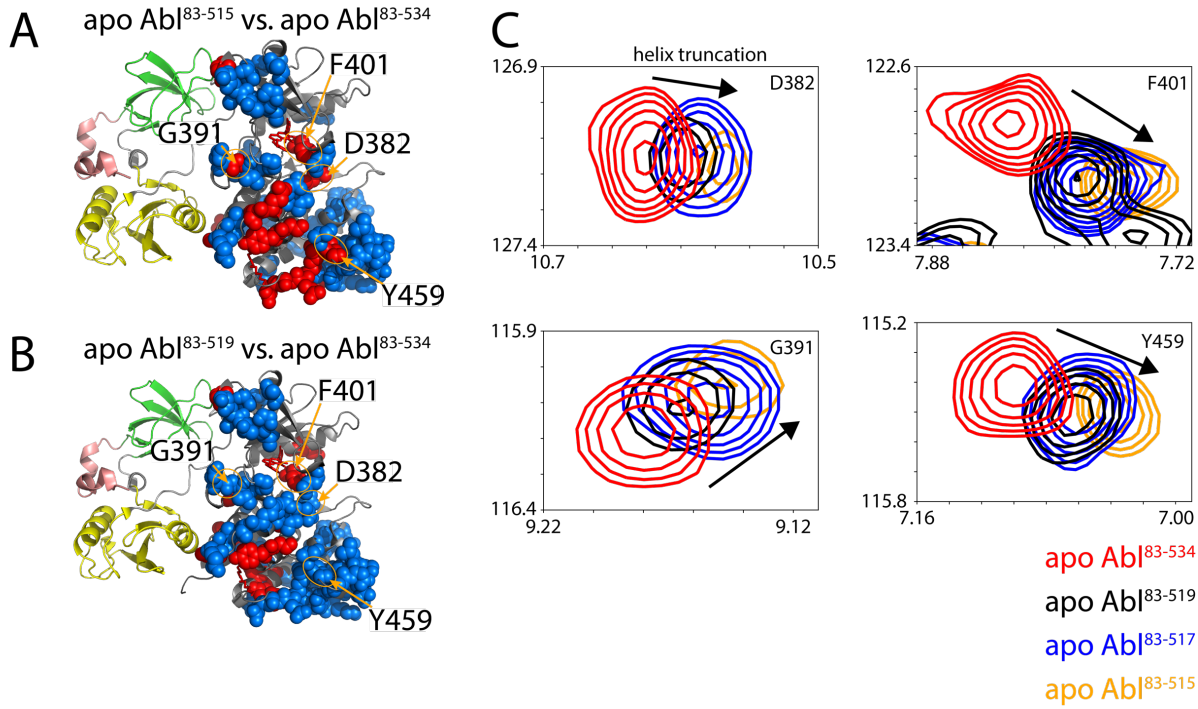

Supplementary Figure S1

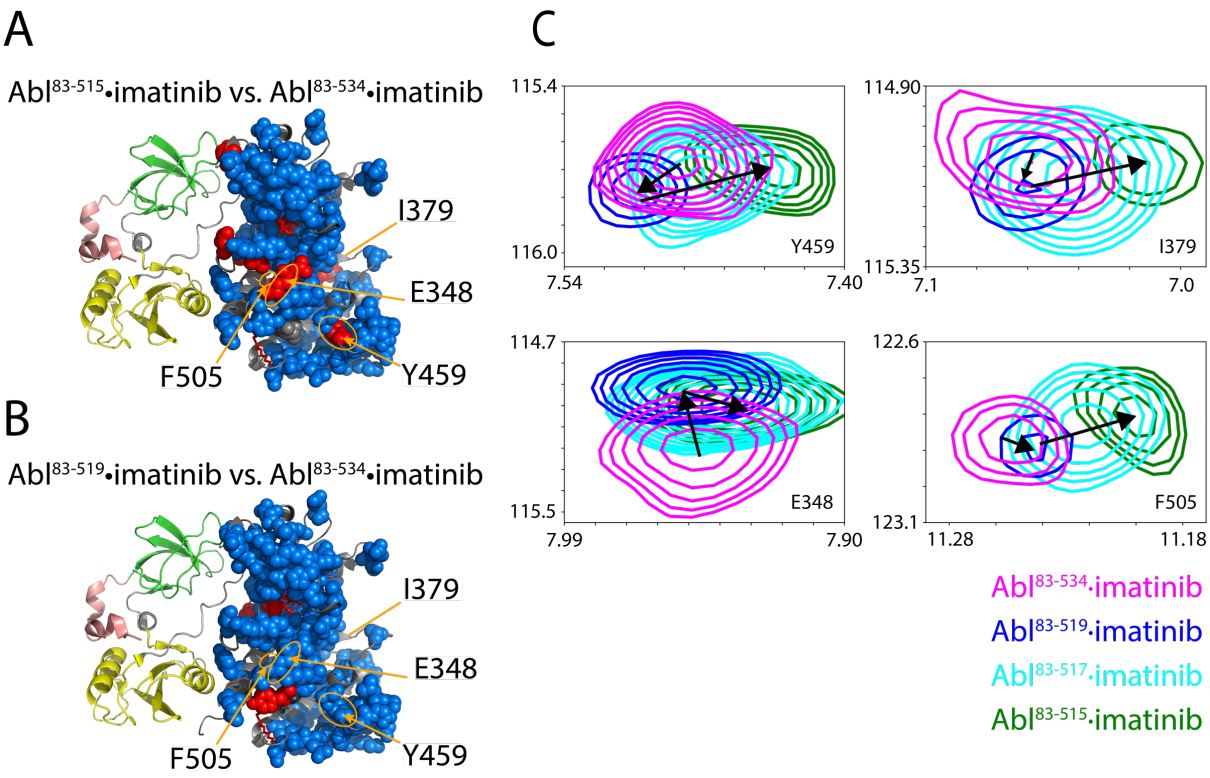

Supplementary Figure S2

3.2 Influence of the Abl N-cap on the Abl regulatory core conformational equilibrium in solution

Introduction

Based on crystal structures of myristoylated Abl$^{2-531}$ (hereafter called myr-Abl^{cap}) in complex with the type I ATP site ligand PD166326 [33, 173] the Abl N-cap and the myristoylation of the 1b isoform have been proposed to be major stabilizing elements of the autoinhibited assembled core conformation of Abl. These elements comprise a clamp around the SH2 mediated by a phosphorylated serine (pS69) of the N-cap and the myristoyl-induced bending of the C-terminal αI-helix, which allows docking of the SH2 domain onto the KD C-lobe. However, removing the N-terminus and myristoylation still results in the assembled core conformation [172]. But, it was shown in the previous Chapters that the apo form, although adopting mainly the assembled conformation in solution disassembles occasionally (Chapter 0). This disassembly seems caused by a push of the flexible αI-helix onto the SH2 domain (Chapter 3.1). Bending of the αI-helix by binding of the allosteric inhibitors such as GNF-5 and asciminib reduces the disassembly rate. This stabilizing mechanism probably resembles that of myr-Abl^{cap} (1b isoform). However, the 1a isoform is ubiquitously expressed and properly regulated despite the lack of the myristoylation [173]. The molecular basis for this and the biological relevance of the N-cap-SH2 clamp mediated by pSer-69 is yet not fully understood since the myristoylated Abl core has so far not been studied in solution at atomic detail.

Here, we successfully produced ^{15}N-labeled myristoylated Abl for NMR studies to investigate the impact of the N-cap (1b isoform) and the myristoylation on the conformation of the regulatory core.

Results and Discussion

Myristoylated Abl can be expressed ^{15}N-labeled in insect cells for NMR studies

To be able to determine the influence of the Abl N-cap onto the Abl^{core} (Abl$^{83-534}$, SH3-SH2-KD) conformation by NMR, we had to produce intact ^{15}N-labeled myr-Abl^{cap} (Abl$^{2-531}$, N-cap-SH3-SH2-KD). Abl^{core} and parts of it can be produced conveniently in *E. coli* with high ^{15}N and ^{2}H levels, which enables NMR TROSY and relaxation experiments to study its conformation and dynamics [172, 174]. Unfortunately, *E. coli* is of limited use for the production of proteins with PTMs, which are often present in proteins from higher eukaryotes [342]. In our particular case, *E. coli* cannot produce myristoylated Abl, since it lacks an endogenous N-myristoyltransferase (NMT).

Baculovirus-based insect cell expression is an alternative to *E. coli* for protein production, in particular for high-yield production of proteins originating from higher eukaryotes. However, expression of isotope-labeled proteins for NMR studies is more laborious and expensive in insect cells. Moreover, due to their lower tolerance to D_2O compared to *E. coli* and intolerance of deuterated glucose, deuteration levels achieved in insect cells are reduced. These are major drawbacks, yet in our lab recently developed protocols for cost-effective production of isotope-labeled proteins in insect cells [341, 342] encouraged us to establish isotope-labeled expression of myr-Abl^{cap} in insect cells.

We therefore first set up the expression and purification of unlabeled wt myristoylated Abl N-cap-SH3-SH2-KD (aa2-531, myr-Abl^{cap}) and various mutants (listed in Table 1) of Abl^{cap} 1a and 1b isoforms according to previous publications [33]. The expression yield was estimated by a small-scale expression test and a subsequent one-step purification using magnetic-bead-based IMAC medium 'His Mag Sepharose® Ni' (GE Healthcare), thereby removing most impurities (as judged from an SDS-PAGE). This enabled a rough quantification of the expression level from UV_{280} absorption. Results are shown in Table 1. All constructs were expressed at concentrations of several mg per L of expression culture. For comparison: the amount required for a 50-µM NMR sample of Abl^{cap} is approximately 1 mg. The best expressing construct was the kinase-defective myr-Abl^{cap} D382N mutant (~30 mg/L). The wt myr-Abl^{cap} expression was approximately half of it (15 mg/L). This expression-enhancing effect of the D382N mutation was not observed for the myristoyl-lacking G2A mutant and the 1a isoform, which were expressed at ~10-15 mg/L each. Both

poly-proline mutants, P242E,P249E in the SH2-KD linker and P15E,P18E in the N-cap, expressed at approximately 20 mg/L.

Table 1. Expression and purification yields of Abl constructs including the N-cap of isoforms 1a and 1b.

Construct[a]	**Yield small-scale test [mg/L]**[b]	**Yield purified [mg/L]**[c]
wt myr-Abl^{cap} (1b)	15.0 ± 1.4	3.9 ± 0.6
myr-Abl^{cap} D382N (1b)	32.5 ± 4.5	15.8 ± 0.2
Abl^{cap} G2A (1b)	13.0 ± 4.4	N/A
Abl^{cap} G2A,D382N (1b)	13.7 ± 3.2	2.5*
myr-Abl^{cap} P242E,P249E,D382N (1b)	22.7 ± 1.2	N/A
myr-Abl^{cap} P15E,P18E,D382N (1b)	27.5 ± 2.4	N/A
wt Abl^{cap,1a} (1a)	12.4 ± 2.7	N/A
Abl^{cap,1a} D363N (1a)	15.7 ± 3.3	N/A

[a] 1b and 1a denote the two isoforms of Abl. Constructs of 1b isoform comprise residues 2-531 of Abl 1b and 1a isoform constructs comprise residues 2-512 of Abl 1a.

[b] Yield estimates from a small-scale test expression and rough purification given in mg protein per liter of expression culture, n = 2-6.

[c] Yield of purified protein given in mg protein per liter of expression culture, n = 1-4.

* Single experiment.

Abl bears various phosphorylation sites throughout the regulatory core and other parts of the protein with various effects. Phosphorylated tyrosine 242 (pY242) in the SH2-KD linker and pY412 in the activation loop, influence the core conformation and kinase activity [26, 33, 173, 364]. Serine 69 in the N-cap was phosphorylated in the crystal structure of the assembled core and a possible stabilizing effect on this conformation was proposed [173]. Importantly, the stability of the apo Abl^{core} is significantly increased in the fully dephosphorylated state [174]. For these reasons, it is crucial to be able to produce all Abl constructs with controlled, homogeneous phosphorylation. For example, it would be interesting to produce a homogenous pS69 sample to investigate the proposed stabilizing effect of this phosphosite on the core assembled conformation. To test if we can produce protein samples homogeneously dephosphorylated and monophosphorylated at S69, which are expected to be stable at NMR experiment conditions, we expressed and purified wt myr-Abl^{cap} and its D382N and G2A,D382N mutants to high purity and analyzed the protein for posttranslational modifications, in particular phosphorylation and myristoylation, by ESI-TOF mass spectrometry. We found myr-Abl^{cap} D382N to be homogeneously myristoylated and

mono-phosphorylated as described previously [173]. By applying *in vitro* dephosphorylation with lambda phosphatase (LPP) [174] we were also able to produce completely dephosphorylated myr-Abl^{cap} D382N.

This encouraged us to purify wt myr-Abl^{cap}. Although being able to purify this protein with a yield of a few milligrams, it was widely phosphorylated and consequently instable. We hoped to overcome this issue by applying the same *in vitro* dephosphorylation step during purification as for the D382N mutant. Indeed, the phosphorylation level dropped. However, until now we have not been able to obtain a homogeneously phosphorylated wt myr-Abl^{cap}.

Since we wanted to study the effect of myristoylation, we also expressed and purified the non-myristoylated G2A,D382N mutant. The yield of this mutant was significantly lower (2.5 mg/L). However, it was possible to purify the fully dephosphorylated sample to homogeneity.

We then continued with ^{15}N-labeled expression of the kinase-defective myr-Abl^{cap} D382N mutant in insect cells to obtain an NMR sample with homogeneous phosphorylation. This mutant had also been used to determine the crystal structure of the assembled conformation [173]. We could obtain either monophosphorylated or dephosphorylated Abl, the latter by adding LPP during purification. The expression was performed based on a previously published protocol, where homegrown ^{15}N-labeled yeast extract is added to yeast- and amino acid-depleted growth medium [341]. Thereby, we reached the same expression yield as obtained from unlabeled protein expression. The ^{15}N incorporation was 75 % as determined by ESI-TOF mass spectrometry. In principle, the ^{15}N incorporation can be increased to >90 % by adding ^{15}N-labeled glutamine to the growth medium [342]. However, this increases the costs for expression dramatically and a higher ^{15}N level was not required.

A ^{1}H−^{15}N TROSY HSQC spectrum of the monophosphorylated 61-kDa myr-Abl^{cap} D382N•imatinib is shown in Figure 3.1. In the buffer used for NMR studies, the protein could be concentrated to maximally 55 µM. Together with the lower ^{15}N incorporation, the effective maximal NMR sample concentration was approximately 40 µM. Nevertheless, we were able to obtain a decent TROSY spectrum.

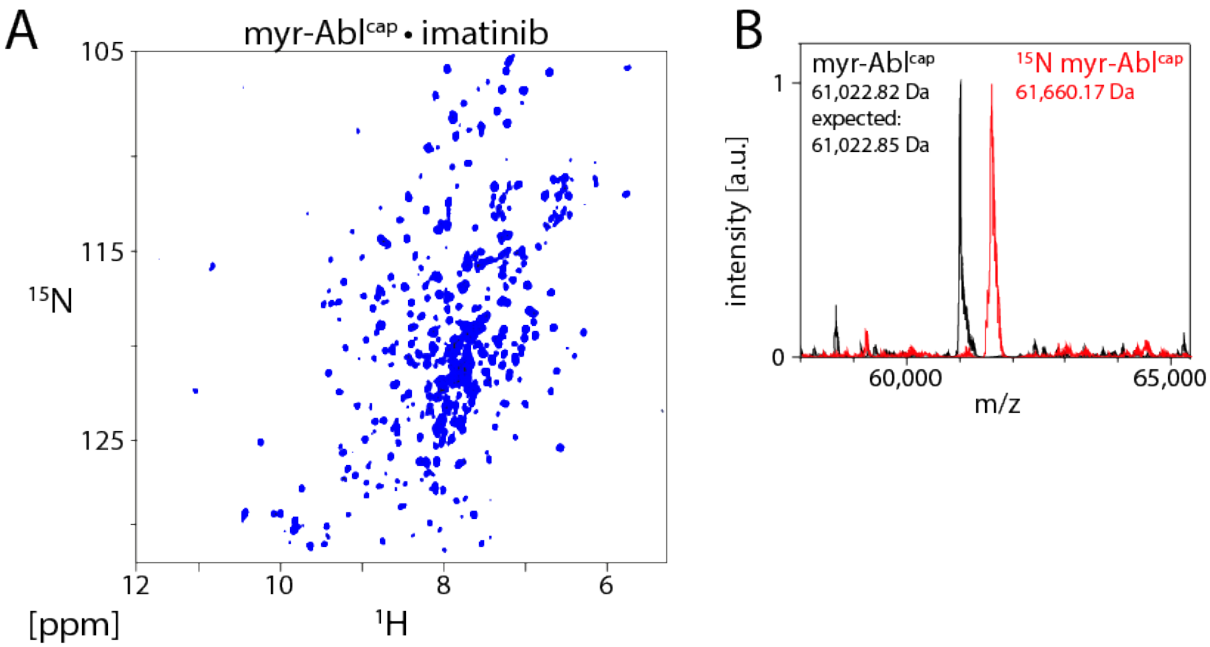

Figure 3.1. Expression of ^{15}N-labeled myristoylated Abl$^{2-531}$. A) The ^{1}H–^{15}N TROSY HSQC spectrum of monophoyphorylated myr-Abl^{cap} D382N•imatinib is shown. The protein was expressed by using baculovirus-based insect cell expression in Sf-9 cells. Yeast extract- and amino acid-depleted Sf-4 medium was supplemented by homemade ^{15}N-labeled yeast extract and ^{14}N glutamine. B) ESI-TOF mass spectra of purified unlabeled myr-Abl (black) and ^{15}N-labeled myr-Abl (red) show homogeneous samples. The expected mass for monophosphorylated and myristoylated Abl^{cap} is 61022.82 Da, which fits perfectly the measured mass of the purified unlabeled sample (black). The ^{15}N incorporation efficiency is roughly 75 %, as determined from the mass shift between the labeled and unlabeled samples.

Myr-Abl^{cap} adopts an assembled conformation in solution

The SH2 and SH3 chemical shifts can be analyzed to determine the Abl core conformation as described previously [172, 174] and as used in Chapter 3.1. In particular, the resonances of a few key residues were found to report on conformational changes of the Abl core between the assembled apo conformation and the imatinib-induced disassembled core. These resonances are V130, T136, G149, and V170. Therefore, we recorded the ^{1}H–^{15}N TROSY spectrum of the monophosphorylated apo myr-Abl^{cap} D382N and compared the resonances of the SH2 and SH3 domains with those of the wt apo Abl^{core}, which lacks the myristoylated N-cap.

The chemical shift differences ($\Delta\delta = ({\Delta\delta_N}^2/25 + {\Delta\delta_{HN}}^2)^{1/2}$) plot for all assigned SH3-SH2 resonances shows overall smaller Δδ values between wt apo Abl^{core} and apo myr-Abl^{cap} D382N compared with the core disassembly seen from the Δδ plot of apo Abl^{core} vs. Abl^{core}•imatinib (Figure 3.2A). Only a few slightly larger shifts, mainly in the SH2 domain, are observed between apo myr-Abl^{cap} D382N and apo Abl^{core}, such as W146, G149, R171, and T213 (Figure 3.2B), while upon imatinib-induced Abl^{core}

disassembly, shifts are observed throughout the SH3 and SH2 domains. This evidence supports the assumption that the apo myristoylated Abl^{cap} D382N construct adopts the assembled core conformation in solution as expected from the available crystal structure [173]. Plotted onto the assembled core structure it becomes clear that the largest shifts are located within the SH2 domain close to the N-cap clamp and the SH2-KD linker (Figure 3.2C).

Furthermore, residue W146, which is the most shifted residue, is located opposite of the phosphorylation site S69 (Figure 3.2C). According to the crystal structure of the assembled core, W146 even participates in a hydrogen network between the phosphate group, a water molecule and several surrounding residues [173]. From that it seems clear that our myr-Abl^{cap} D382N construct is phosphorylated at S69 and that the phosphorylation of S69 brings the N-cap close to the SH2 domain and in particular to W146, which results in the large shift of that resonance. Hence, the relevance of the pS69 mediated interaction between the N-cap and the SH2 domain, as presumed from the crystal structure [173], is confirmed to exist also in solution.

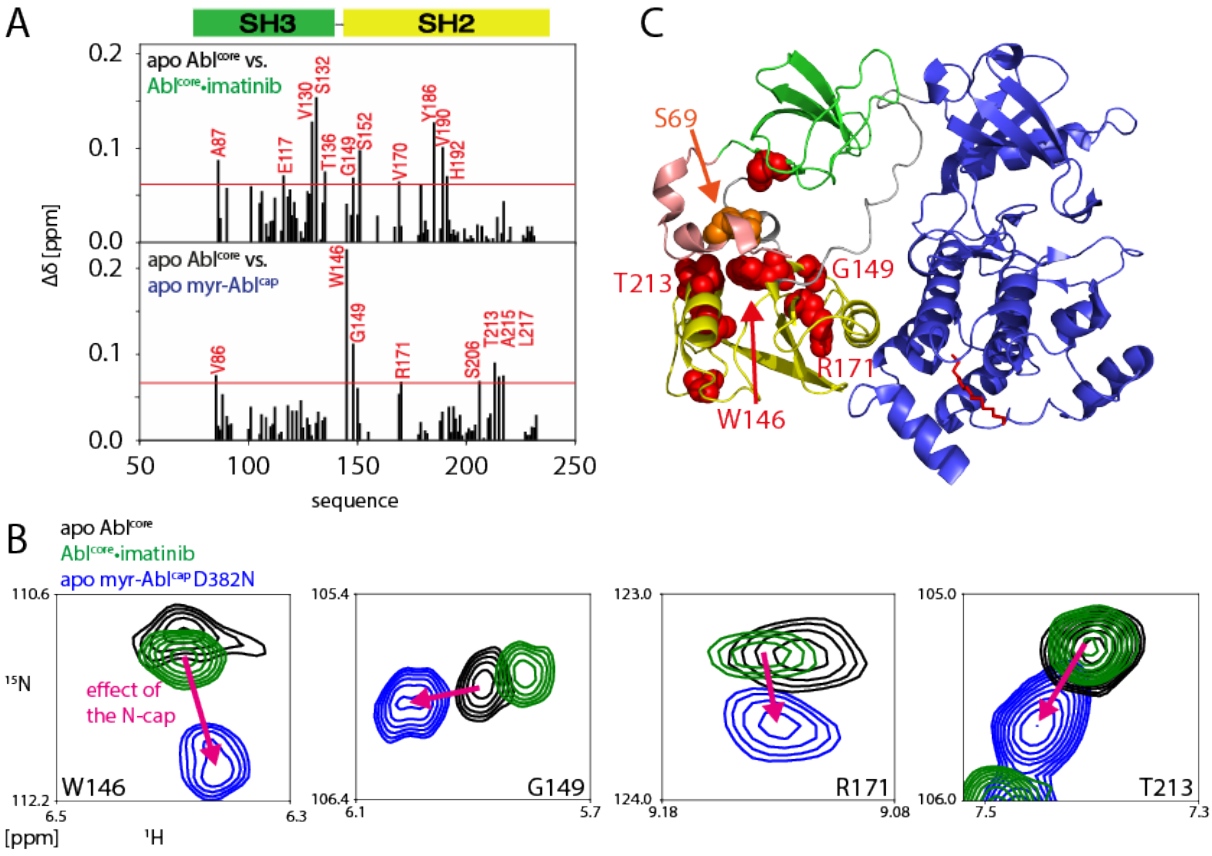

Figure 3.2. The apo myristoylated Abl^{cap} construct adopts the assembled conformation in solution. A) The chemical shift differences (Δδ) plot of apo Abl^{core} vs. Abl^{core}•imatinib shows shifts throughout the SH3 and SH2 domains upon core disassembly. Δδ values between apo Abl^{core} and apo myr-Abl^{cap} D382N are less pronounced and limited mainly to the SH2 domain, indicating no major

conformational changes. Δδ = 0.6 ppm. B) Exemplary resonances showing the largest shifts when the myristoylated N-cap is added to the apo Abl^{core}. The apo Abl^{core} resonances are plotted in black, the myr-Abl^{core} resonances in blue. Abl^{core}•imatinib resonances (green) are shown to compare the assembled with the disassembled conformation. C) Residues with the largest Δδ values in the apo myr-Abl^{cap} D382N construct are shown in the crystal structure as red spheres of the assembled core [173].

Imatinib does not fully disassemble myristoylated Abl

The Abl^{core}, which lacks the N-cap and myristoylation, resembles the disassembled conformation upon imatinib binding. However, additional binding of the myristoyl-mimicking drug GNF-5 to the Abl^{core}•imatinib complex results in a reassembly of the core [172]. Thus, we wanted to investigate next, if the myristoylated N-cap of myr-Abl^{cap}•imatinib complex has the same power to revert the imatinib-induced disassembly as GNF-5.

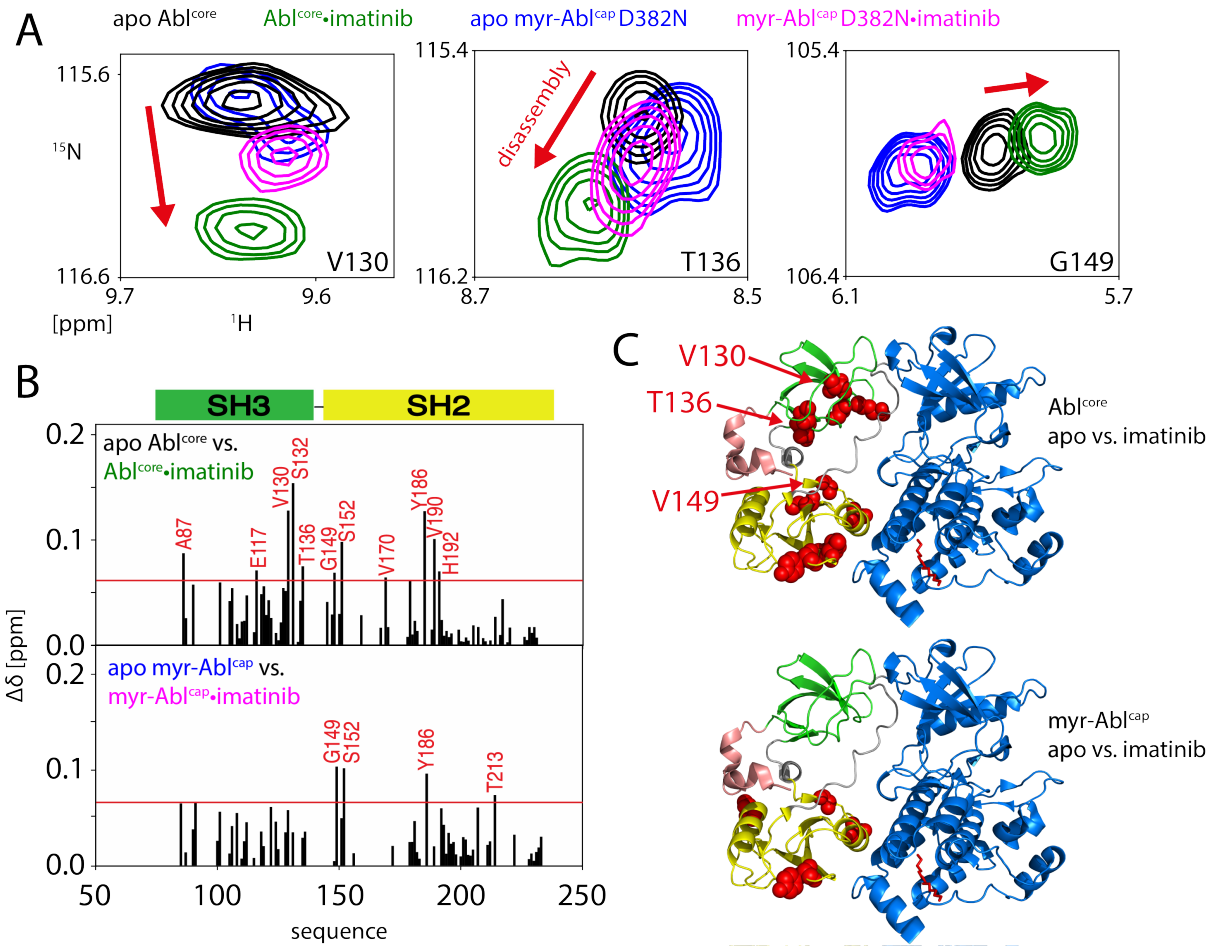

Figure 3.3. Myr-Abl^{cap}•imatinib is less disassembled than Abl^{core}•imatinib. A) Key resonances reporting on the core assembly state are shown for apo Abl^{core} (black), Abl^{core}•imatinib (green), apo myr-Abl^{cap} D382N (blue) and myr-Abl^{cap} D382N•imatinib (magenta). B) Chemical shift difference (Δδ) plots of apo Abl^{core} vs. Abl^{core}•imatinib and apo myr-Abl^{cap} vs. myr-Abl^{cap}•imatinib. The horizontal red line indicates Δδ = 0.6 ppm. C) Residues with the largest Δδ values in the two Δδ plots from B are shown as red spheres in the crystal structure of the assembled core [173].

As seen from the previously mentioned resonances of V130, T136, and G149, addition of imatinib to myr-Abl^{cap} D382N induces the disassembly to a much lesser extent than for the Abl^{core} construct, which lacks the N-cap (Figure 3.3A). The resonances are slightly shifted in the direction of disassembly, but not as far as in the Abl^{core}•imatinib complex. The SH3-SH2 chemical shifts differences of all assigned SH3-SH2 resonances between apo and the imatinib complexes of myr-Abl and Abl^{core} (Figure 3.3B) corroborate this observation. Shifts are overall smaller than for Abl^{core}, but nevertheless present. Mapping the largest shifts for myr-Abl^{cap} D382N onto the Abl structure shows that they mainly involve residues in the SH2 domain close to the SH2-KD linker and the SH2-C-lobe interface, whereas in the absence of the N-cap and myristoylation, larger changes are also observed in the SH3 domain at the interaction site with the SH2-KD linker (Figure 3.3C).

Behavior of the non-myristoylated G2A mutant

Myristoylation occurs at the N-terminal glycine of Abl. When mutated to alanine (G2A), Abl is no longer myristoylated and has nearly 10-fold increased activity compared to the myristoylated wt Abl^{cap} [176]. The $^{1}H-^{15}N$ TROSY spectrum of Abl^{cap} G2A,D382N is shown in Figure 3.4 together with those of myr-Abl^{cap} D382N and the N-cap-lacking Abl^{core} construct. Notably, the kinase-defective Abl^{cap} G2A,D382N mutant was multiply phosphorylated. In order to obtain a homogenous sample, it was treated with phosphatase *in vitro*. The protein was thus fully dephosphorylated, i.e. it misses the phosphorylation at S69, which is present in the myr-Abl^{cap} D283N sample. Interestingly, the Abl^{cap} G2A,D382N mutant adopts roughly the same assembled conformation as both myr-Abl^{cap} D382N and wt Abl^{core}, as there are no dramatic changes in the TROSY. However, a few changes are already noticeable by eye.

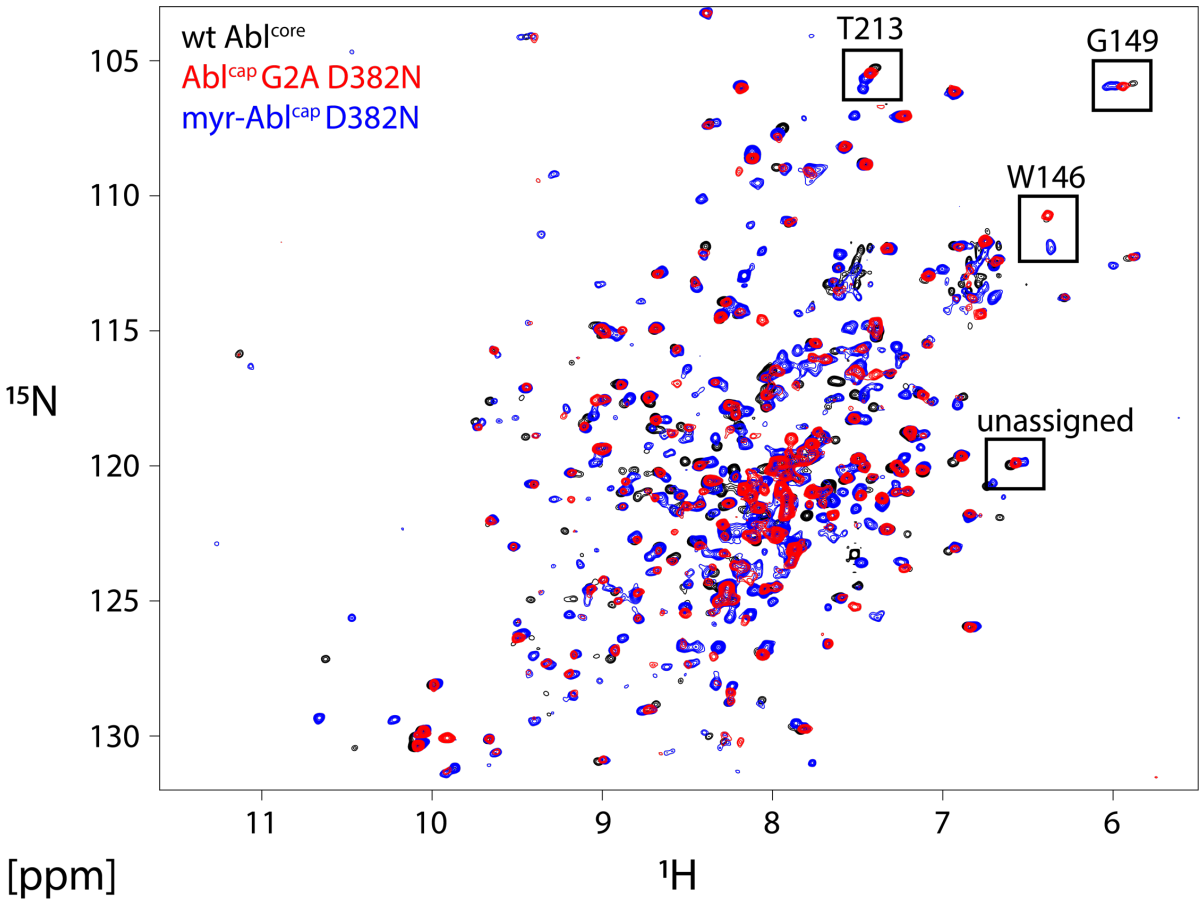

Figure 3.4. $^{1}H–^{15}N$ TROSY spectrum of apo Abl^{cap} G2A,D382N (red) in comparison to myr-Abl^{cap} D382N (blue) and wt Abl^{core} (black). A homogenous sample of fully dephosphorylated Abl^{cap} G2A D382N could be produced ^{15}N labeled. Comparison with the myristoylated and the N-cap-lacking constructs already reveals differences.

This is confirmed by calculating chemical shift differences for all assigned SH3-SH2-KD resonances (Figure 3.5). The differences are overall very small (mostly $\Delta\delta < 0.05$ ppm) compared to either myr-Abl^{cap} D382N or wt Abl^{core}. Yet, the comparison between the G2A mutant and myr-Abl^{cap} reveals resonances shifted to a larger extent, namely W146, V151, V170, and R171 ($\Delta\delta > 0.05$ ppm). Those are all located in close proximity within the SH2 domain and close to the SH2-KD linker. Further resonances with $\Delta\delta > 0.04$ ppm are located within the SH2 as well or at the beginning of the SH3 domain (Figure 3.5). Since the G2A mutant is not phosphorylated at S69, in contrast to the monophosphorylated myr-Abl^{cap}, it is obvious that these changes show the interaction between the SH2 domain and pS69.

The conformation of the G2A mutant is more similar to myr-Abl^{cap} than to the N-cap-lacking wt Abl^{core}, as the differences to the latter are overall slightly larger when excluding W146, V151, V170, and R171 (Figure 3.5). Notably, not many assignments are available within the KD due to spectral overlap in the N-cap-comprising constructs

and since assignments were simply transferred from the wt Abl^{core} constructs and not obtained de novo by heteronuclear NMR. Nevertheless, a few shifts are observed within the KD. However, they could origin in the D382N mutation that was needed to produce a homogenous sample and are thus not further discussed.

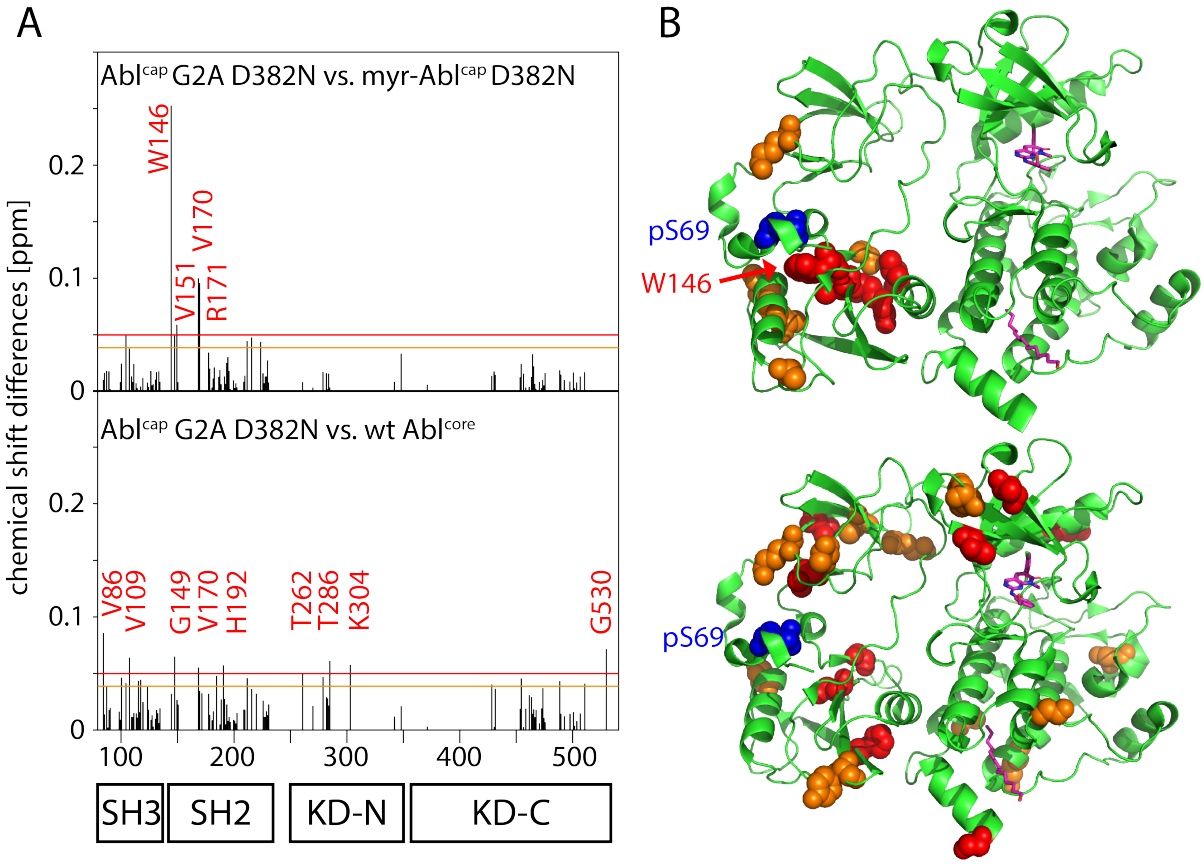

Figure 3.5. Chemical shift differences between the unphosphorylated Abl^{cap} G2A, D382N, monophosphorylated myr-Abl^{cap} D382N (top) and unphosphorylated wt Abl^{core} (bottom). A) Chemical shift differences (Δδ) of apo Abl^{cap} G2A,D382N vs. apo myr-Abl^{cap} D382N and apo Abl^{cap} G2A D382N vs. apo Abl^{core}. The red and orange line mark chemical shift difference of 0.05 ppm and 0.04 ppm, respectively. The largest chemical shift differences between the Abl^{cap} G2A D382N and myr-Abl^{cap} D382N are located within the SH2 domain close to S69 of the N-cap, which is phosphorylated only in the myr-Abl construct. Otherwise, chemical shift differences are rather small throughout the protein. The chemical shift differences are overall slightly larger between the G2A N-cap construct and the N-cap-lacking construct, although no large single shifts are observed as in the above case. B) Residues with Δδ > 0.05 are shown in the assembled core structure as red spheres.

A closer look at individual resonances reveals different classes of shifts (Figure **3.6**). First, the above discussed key reporter residues for the core assembly state show that the G2A mutant stays in the assembled conformation as exemplary shown for residues V130 and T136 (Figure 3.6A). Second, resonances that show similar shifts within both myr-Abl^{cap} D382N and the G2A,D382N mutant, but distinct from wt Abl^{core}, reveal the effect of the N-cap on the protein conformation as shown by resonances of V86 and T286 (Figure 3.6B). Mapping of all assigned resonances that show this behavior onto

the structure of the assembled core reveals that they are located mainly in the SH3 domain and in particular close to the SH3-SH2 and SH2-KD linker (residues V86 and Y89) and within the KD. However, as mentioned before, changes within the KD could also arise from the D382N mutation. Third, several resonances of the G2A mutant are positioned between myr-Abl^{cap} and Abl^{core} (Figure 3.6C). This is shown for residues G149 and T213 and, interestingly, mapping of all resonances with this behavior onto the structure shows that this is the case all across the SH3 and SH2 domains and for KD N-lobe residues at the SH3-KD interface. This intermediate shift indicates that the non-myristoylated and dephosphorylated N-cap forms the same interaction with the rest of the core, mainly the SH2 domain, but this interaction is less tight. This could be either due to the absent myristate or the absent phosphorylation at S69. Forth, mainly residue W146 shows the already discussed interaction between the phosphorylated N-cap and the SH2 domain (Figure 3.6D).

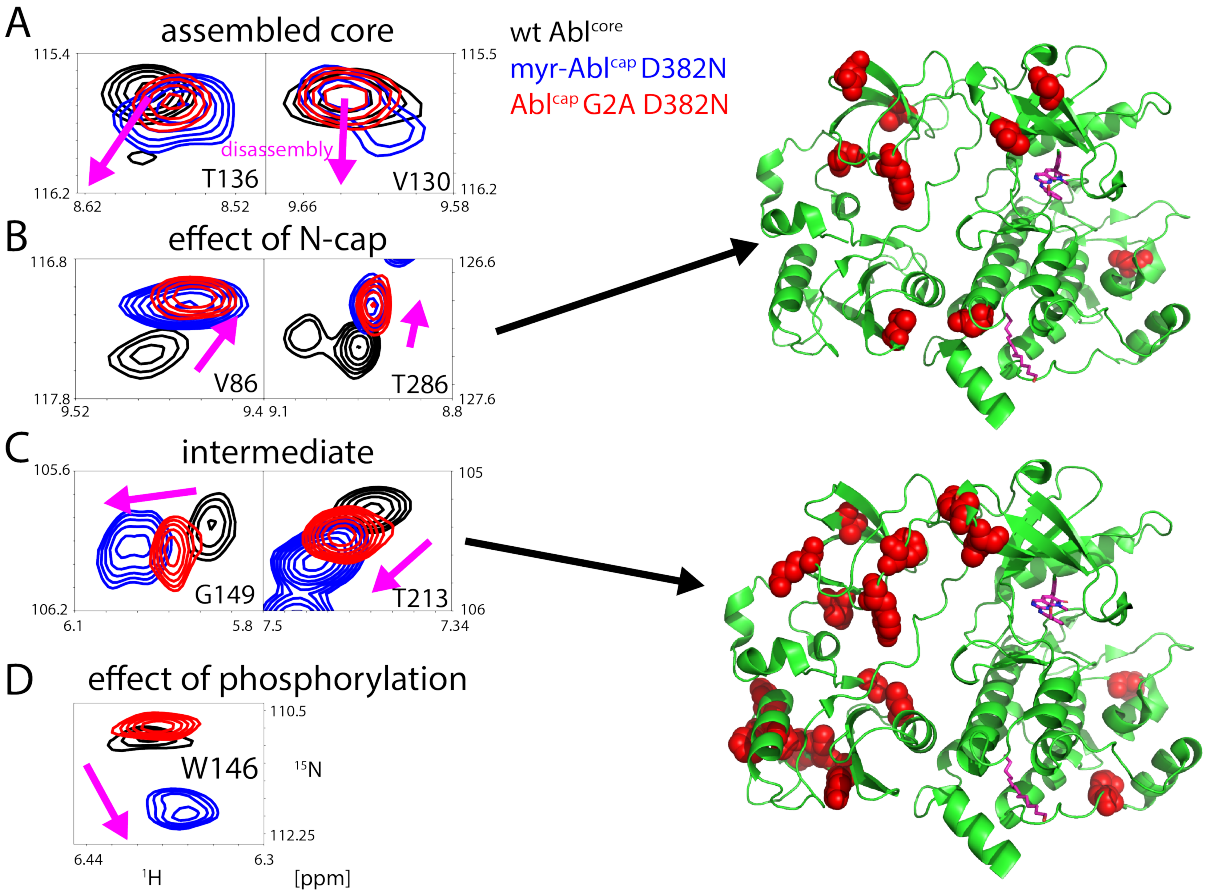

Figure 3.6. Different classes of resonance shifts from wt Abl^{core} (black), monophosphorylated myr-Abl^{cap} D382N (blue), and dephosphorylated Abl^{cap} G2A D382N (red). A) Resonances V130 and T136 show that all investigated apo constructs adopt the assembled core conformation in solution, independent of the N-cap and myristoylation. The magenta arrow indicates the direction in which the resonance of a disassembled core would shift. B) Exemplary resonances V86 and T286 show a shift

(magenta arrow), which is induced by the presence of the N-cap, independent of S69 phosphorylation. All resonances showing this behavior are mapped onto the assembled core structure (2FO0 [173]). Many shifts are observed within the SH3 domain. C) Many resonances show a linear shift (magenta arrow) from Abl^{core} over the G2A N-cap mutant to myr-Abl, as shown exemplary for resonances G149 and T213. This indicates that the G2A mutant is in some intermediate state between the other two. Mapping of all those residues onto the structure shows that this intermediate state can be observed throughout the SH3 and SH2 domains as well as in the KD N-lobe at the interface to the SH2 domain. Since not many KD resonance assignments are available, it is unclear if the observation for the two KD C-lobe resonances, K434 and R476, are artifacts due to possible wrong assignments or if the N-cap effect is transmitted through the KD. D) The phosphorylation at S69 induces a large shift of resonance W146, which was observed to take part in a hydrogen network with the phosphate group of pS69 in a crystal [173].

A numerical classification of chemical shifts summarizes the above findings on the effect of the N-cap on the Abl core conformational equilibrium.

A numerical principal component analysis (PCA) of all SH3 and SH2 chemical shifts (Figure 3.7**)** can show the assembly state and further structural features of Abl constructs and Abl•inhibitor complexes and reveal resonances that contribute most to these states on a molecular level. Here, the Abl^{cap} constructs apo myr- Abl^{cap} D382N, myr-Abl^{cap} D382N•imatinib, and apo Abl^{cap} G2A,D382N were analyzed together with apo Abl^{core}, Abl^{core}•type I inhibitors, and Abl^{core}•type II inhibitors. The scores plot (Figure 3.7A) reveals the usual discrimination between the assembled conformation (light blue cluster comprising apo Abl^{core} and Abl^{core}•type I inhibitor complexes) and the disassembled conformation (pink cluster comprising Abl^{core}•type II inhibitor complexes). Notably, this disassembly is here not simply described by the first principal component (PC1). It is important to state that the chemical shifts of W146 were excluded from the analysis, because it would appear too dominant and mask all other structural features due to its large shift upon S69 phosphorylation. The first two components, PC1 and PC2, explain more than 80% of the data (Figure 3.7B).

All N-cap-containing constructs differ clearly from Abl^{core} complexes (Figure 3.7A). This is independent of myristoylation and confirms the findings of the above analysis of individual chemical shifts. The loadings plot uncovers further residues that contribute to the N-cap-induced changes (Figure 3.7C), among others V86, V109, N125, V151, and T213.

The PCA confirms the observation that the myr-Abl^{cap} D382N, as well as the Abl^{cap} G2A D382N construct mutant, resembles the assembled conformation, whereas addition of imatinib does not fully disassemble the core of myristoylated Abl, as seen from the smaller shift upon imatinib binding for the myristoylated construct compared

to wt Abl^{core}. Strong contributing residues are, among others, V130 and T136 (Figure 3.7C), both part of the set of key residues reporting on the Abl core conformation [174].

Furthermore, the observation that several resonances of the G2A mutant are located in-between myr-Abl^{cap} and Abl^{core} is also reflected in the PCA, where the score of the G2A mutant lies in the middle as well (Figure 3.7A). Moreover, as expected from the chemical shift differences, the G2A mutant is yet closer to myr-Abl^{cap} than Abl^{core}.

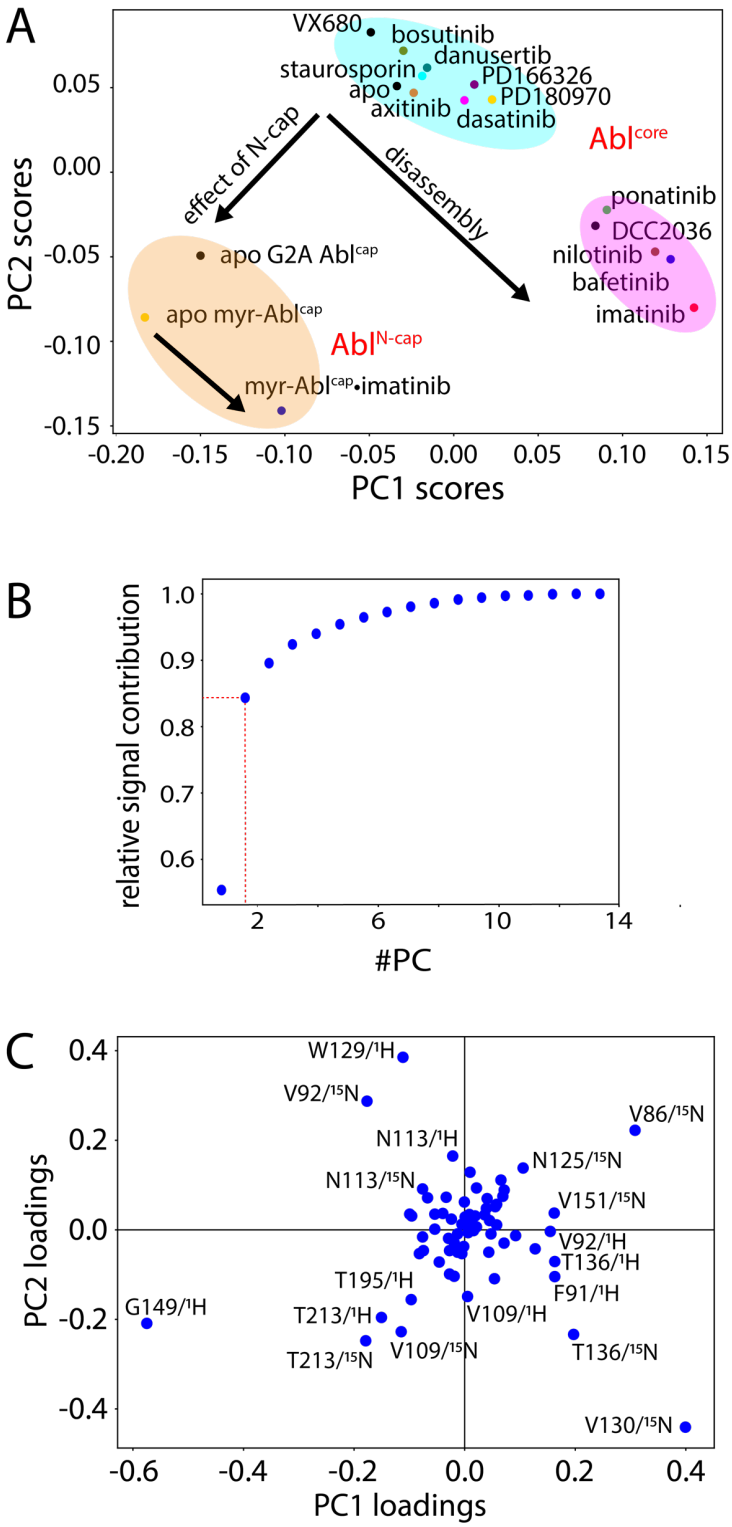

Figure 3.7. Principal component analysis of all SH3-SH2 chemical shifts of Abl^{cap} constructs and Abl^{core} in complex with type I and II ATP site inhibitors. A) The PCA scores plot distinguishes assembled core conformation (light blue cluster) adopted by apo Abl^{core} and in complex with type I inhibitors from disassembled core conformation adopting type II complexes (pink cluster) as reported previously [174]. Further, it distinguishes the N-cap-comprising constructs (orange area). Notably, the myr-Abl^{cap}•imatinib complex is less shifted in the direction of disassembly compared to the Abl^{core}•imatinib complex. B) The loadings plot reveals individual chemical shift components that contribute to either disassembly or the N-cap effect. E.g. G149 contributes strongly to the N-cap effect, whereas V130 contributes mainly to the core disassembly. C) The first two principal components (PCs) explain more than 80 % of the data.

Myristoyl binding pocket

For further interpretation of these data, it is of importance to know whether the myristoyl is indeed bound to the allosteric pocket at the KD C-lobe bottom as observed in crystals [33, 173]. So far, only a few residues forming the myristoyl pocket or close to it could be assigned. The corresponding assigned resonances of Y488, H509, L529, and G530 are depicted in Figure 3.8 for apo Abl^{core}, Abl^{core}•GNF-5, apo myr-Abl^{cap} D382N, apo Abl^{cap} G2A,D382N, and myr-Abl^{cap} D382N•imatinib. If the myristoyl binds to the allosteric pocket, one would assume a similar shift for apo myr-Abl^{cap} D382N as for the Abl^{core}•GNF-5 complex. Furthermore, resonances of the non-myristoylated apo Abl^{cap} G2A,D382N would be expected at the position of apo Abl^{core}. This behavior is clearly observed for the resonance of H509 (Figure 3.8), which is located on the αI-helix and is therefore close to the bound myristoyl moiety. The resonances of L529 overlapped partially and could not be assigned unambiguously. However, the resonance of neighboring G530 has been shown to be an excellent reporter for GNF-5 binding [172]. This resonance shows a surprising behavior in the case of the myristoylated constructs. While the G2A mutant locates at the same position as the apo core, both apo and imatinib-bound myr-Abl^{cap} D382N resonances are observed at both the positions of apo Abl^{core} and Abl^{core}•GNF-5. This hints towards a slow exchange between a filled and an empty myristoyl pocket. The myristoyl-bound fraction is about 15 % in both the apo form and the imatinib complex as judged from the peak volumes. An incompletely myristoylated sample can be excluded by the MS data, which shows a homogeneous sample (Figure 3.8). Albeit not well resolved, the resonance of Y488, sitting at the opposite site of the binding pocket, shows a similar trend.

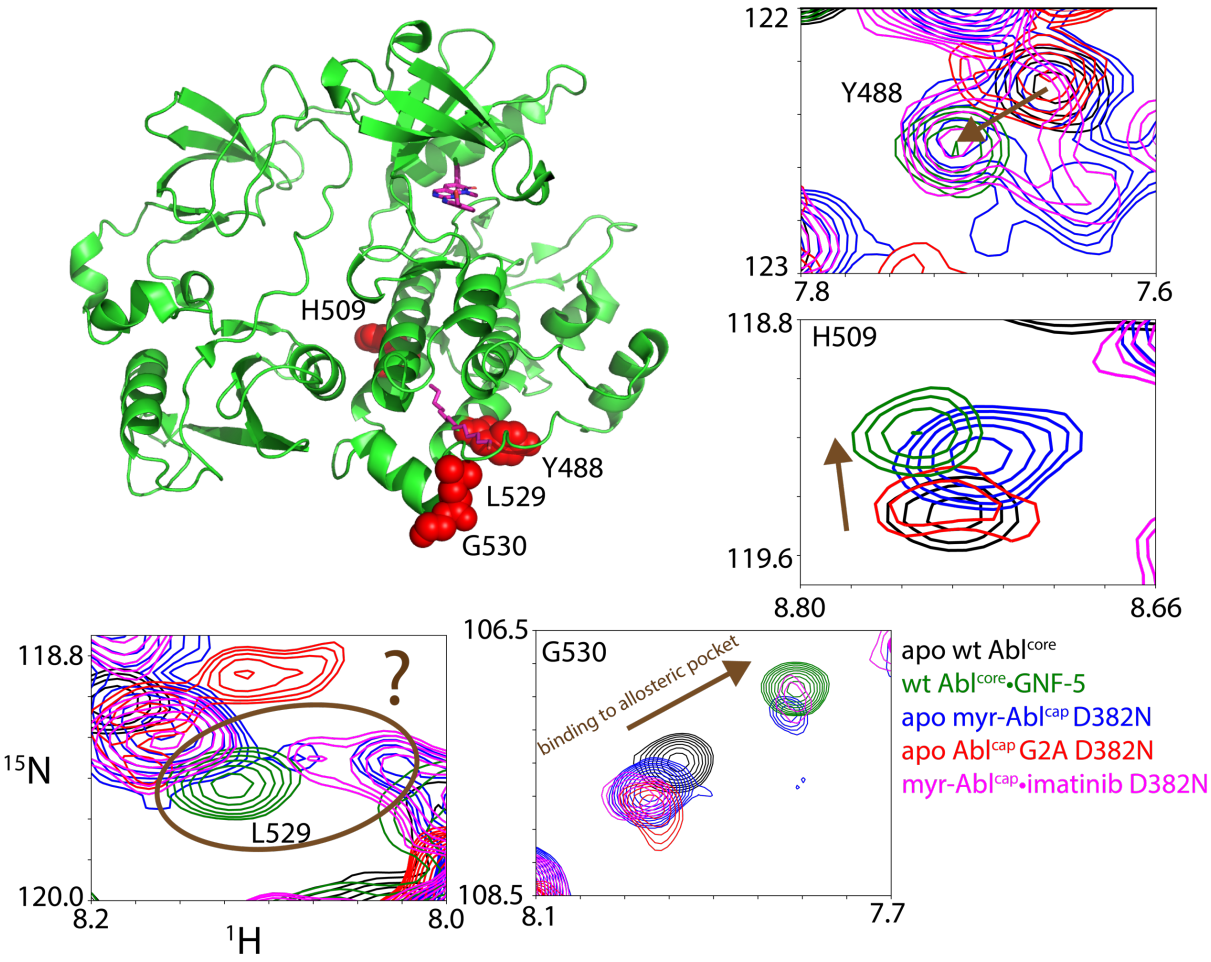

Figure 3.8. Resonances reporting on myristoyl pocket occupation. Resonances Y488, H509, L529, and G530, which are located close to the myristoyl pocket, are highlighted in the assembled core structure (pdb 2FO0 [173]). The myristoyl and PD166326 ligands are shown as purple sticks. Resonances showing binding of GNF-5 are plotted for the spectra of unliganded (black) and GNF-5 bound (green) Abl^{core}, apo (blue) and imatinib bound (magenta) myr-Abl^{cap} D382N, and apo Abl^{cap} G2A,D382N (red). Brown arrows indicate the shift induced by allosteric pocket binders. The assignment of L529 in the myristoylated constructs is ambiguous (brown circle).

Interaction between the N-terminal peptide of the Abl 1a isoform and the Abl core

Myristoylation was identified as one of the major stabilizing contributors to the assembled Abl core conformation since the αI-helix is bent in the myristoyl-bound state and thereby opens the space for SH2 docking onto the KD C-lobe [33, 176]. Although it was shown that myristoylation is not required for adopting the assembled conformation in solution [172], it will probably reduce dynamic opening of the core and thus reduce Abl kinase activity. However, the naturally abundant non-myristoylated 1a isoform is still 'properly regulated' [173].

In order to investigate how the 1a isoform of Abl achieves proper regulation, a peptide comprising the Abl 1a N-terminal residues (aa2-15) was added to wt Abl^{core} in

a ratio of 6:1 (peptide 900 µM, Abl 150 µM). If the N-terminus of Abl 1a, which contains several aliphatic amino acids (Figure 3.9A), interacted with the myristoyl pocket or other parts of the Abl core, it would be visible by chemical shift changes. Addition of the 1a peptide to apo Abl^{core} causes only small chemical shift changes in the ^{1}H-^{15}N TROSY (Figure 3.9A), which indicates as expected that the Abl core stays in its assembled conformation. However, although being very small (Δδ < 0.06 ppm) (Figure 3.9B) there are clear shifts of a residue cluster in the SH2 domain as well as of some residues located in the SH3 domain close to the SH3-SH2 (V109) and SH2-KD linkers (N115) and within the KD hinge region (N316) close to the ATP pocket (Figure 3.9C).

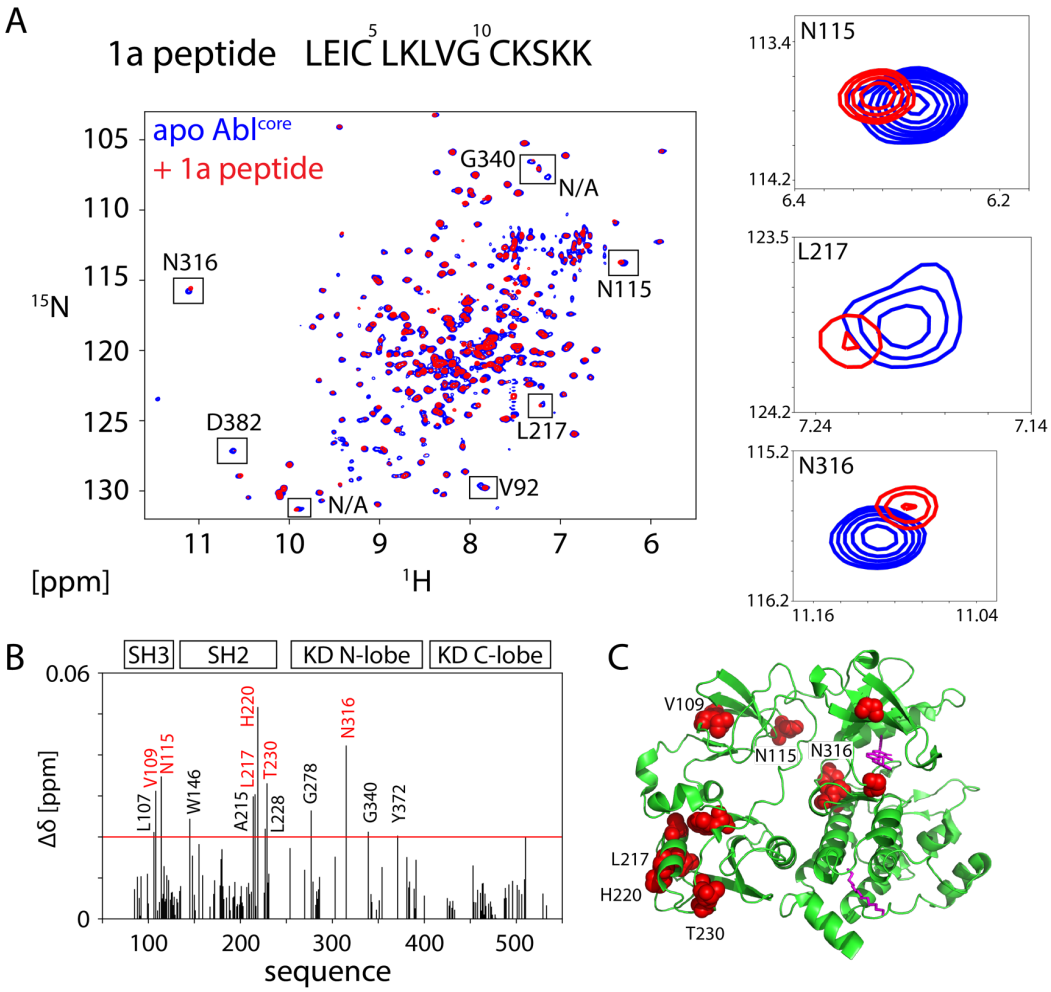

Figure 3.9. Interaction of the N-terminal 1a isoform Abl peptide with Abl^{core}. A) The peptide comprises amino acids 2-15 of Abl isoform 1a. The sequence is shown at the top. The ^{1}H-^{15}N TROSY spectra are shown for apo Abl^{core} (blue) and with 6-fold peptide added (red). A few obvious changes are highlighted in the spectrum. Resonances N115, L217, and N316 from these spectra are shown on the right. B) Chemical shift differences Δδ are very small (Δδ < 0.06) throughout the whole protein. Red line indicates Δδ = 0.02 ppm. C) Shifts larger than 0.02 ppm are mapped onto the assembled core structure (pdb 2FO0 [173]). Most changes occur within the SH2 domain, but some also in the SH3 domain and the KD hinge region.

Conclusion and Perspective

In summary, this study investigated the stabilizing effect of the Abl 1b isoform myristoylated N-cap and the 1a isoform N-terminus on the Abl core conformation in solution by NMR. This included preparation of ^{15}N-labeled N-cap-containing Abl core constructs (Abl^{cap}) for NMR studies and studying the regulatory core (SH3-SH2-KD) conformation by analyzing mainly SH3-SH2 chemical shifts obtained from ^{1}H-^{15}N TROSY experiments.

Although *E. coli* expression offers the most convenient way to produce isotope-labeled proteins for NMR studies, it cannot naturally produce myristoylated proteins due to the lack of an endogenous N-myristoyltransferase (NMT). The presented study made use of a recently developed protocol using homemade ^{15}N-labeled yeast extract [341, 342] to produce isotope-labeled proteins in insect cells for NMR studies. That enabled the expression of several milligrams of ^{15}N-labeled myristoylated Abl (myr-Abl^{cap} D382N), of its non-myristoylated G2A mutant (Abl^{cap} G2A,D382N) and of the Abl 1a isoform (Abl^{cap,1a} D363N).

The Abl core conformation was investigated for all measured constructs by analyzing the chemical shifts of the SH3-SH2 resonances as described previously [172, 174]. The regulatory core of apo myr-Abl^{cap} D382N adopts an assembled conformation as expected from the available X-ray structure [173]. In this structure, the N-cap forms a clamp around the SH2 domain and the myristoyl binds to the allosteric pocket at the KD bottom, both potentially stabilizing the assembled conformation. Most pronounced chemical shift changes were indeed observed for the SH2 domain. In particular, the resonance of W146 was found largely shifted when the sample was phosphorylated at S69 and W146 was observed to be part of a hydrogen network that mediates interaction between the phosphate group of pS69 and the SH2 domain in a crystal [173]. Thereby, this study confirms the relevance of S69 phosphorylation and its participation in N-cap-SH2 interaction in solution.

Surprisingly, there seems to exist a considerably large population of myr-Abl^{cap}, where the myristoyl is not bound to the allosteric pocket (~85 % as estimated from G530 peak volume ratios). Unfortunately, there are only a few resonances assigned around the allosteric pocket. Obtaining more assignments in the future will help to better support this conclusion. However, if this is true, it may have considerable impact on the understanding of how Abl works. For example, it has been speculated whether the active ‘top-hat’ conformation is achievable with a bound myristoyl [180]. But this

question is negligible if the myristoyl can leave the pocket, therefore allowing also other disassembled conformations. Maybe Abl can only be active if the myristoyl leaves the pocket. Then, its activity would be regulated by the myristoyl binding affinity. The binding constant of a myristoylated peptide to the isolated KD was measured as approximately 2 µM [173], which might vary in the presence of the SH3 and SH2 domain and the full N-cap.

The non-myristoylated G2A mutant has nearly 10-fold increased kinase activity compared to the myristoylated wt [176]. Furthermore, the myristoyl-induced αI-helix kink was identified as a crucial inhibition mechanism, and inhibition corresponds to a stabilization of the assembled conformation. Myristoyl-mimicking compounds such as GNF-5 and asciminib were shown to be effective kinase inhibitors and, as shown in Chapter 3.1, removal of the αI'-helix leads to a stabilized assembled core and strongly reduced kinase activity. However, the G2A mutant adopts mainly the assembled inhibited conformation in solution. Potentially, the dynamic opening of the G2A mutant is larger, as a free 80-residue-long N-cap could pull the SH3 domain off the KD N-lobe, hence explaining the increased activity. This we cannot observe with our experimental NMR setup, but future smFRET experiments with that mutant may give quantitative insights into this mechanism.

A careful analysis of all obtained chemical shifts revealed that the N-cap of the G2A mutant adopts an intermediate state between myr-Abl^{cap} and N-cap-lacking Abl^{core}, possibly indicating a weaker interaction between the G2A N-cap and the SH2 domain. This could consequently lead to an increased dynamic opening of the core as described in Chapter 0, which our NMR experiments are not capable to detect, and thus explain the increased activity. However, it is not yet clear from the presented data if this weaker interaction arises from the missing myristoylation or if the S69 phosphorylation plays a major role, since the Abl^{cap} G2A,D382N sample used here is not phosphorylated at S69, whereas it is phosphorylated in the myr-Abl^{cap} D382N sample. Comparison with a yet to be measured fully dephosphorylated myr-Abl^{cap} sample will answer this question.

In Abl^{core} constructs, binding of the type II ATP site inhibitor imatinib leads to large chemical shift changes within the SH3-SH2 domains due to disassembly of the Abl core [172]. However, as shown in this work, myr-Abl^{cap} shows smaller chemical shift changes upon imatinib binding, indicating that the myristoylated N-cap hinders the disassembly regulatory core to some extent. This finding indicates that the

myristoylated N-cap stabilizes the assembled conformation also in solution as proposed based on the crystal structure [173].

The atomic details for that observation are yet unclear. It seems obvious to compare this situation with the incomplete disassembly of the constructs with the truncated αI-helix. In both cases the entropic force exerted by the αI-helix is reduced, in one case by cutting the helix and in the other by myristoyl-induced bending of the αI-helix, such that the push by the N-lobe onto the SH3 domain is not sufficiently strong to disassemble the core. Consequently, the hinge motion of the KD is reduced in the myristoylated construct, thereby hindering efficient substrate binding and keeping the kinase activity low. However, the N-cap-lacking Abl^{core}•imatinib•GNF-5 ternary complex is fully assembled [172], albeit this situation compares to the myr-Abl^{cap}•imatinib complex – myristoyl is simply replaced by GNF-5. The possibly not permanently bound myristoyl – in the apo form as well as in the imatinib complex – could enable disassembly, which is hindered by the partial myristoyl binding.

It would be interesting to investigate the dynamics of the disassembled conformation of myr-Abl^{cap}•imatinib. If the myristoyl is still bound partially in this conformation, one would expect a hindered motion. To determine the NMR ^{15}N-relaxation rates requires deuteration, which is not easily achieved in insect cells [342], but advances in that technology may enable this in the future. In contrast, smFRET experiments can be performed, if we can prepare fluorophore-labeled myr-Abl^{cap}. For this, the expression of Abl with unnatural amino acids in insect cells or mammalian cells needs to be established first.

The conclusion that the myristoyl does not permanently occupy the allosteric pocket raises the question as to which extent it stabilizes the assembled conformation. Maybe its role is smaller than expected from its effect on the αI-helix and the success of myristoyl-mimicking allosteric inhibitors. A rather small contribution of the myristoylation to the regulation of Abl could help in understanding how the non-myristoylated 1a isoform achieves proper regulation although it lacks the myristoylation.

In order to study the regulation mechanism of the 1a isoform, this work investigated a potential role of the N-terminal residues of Abl^{cap,1a}. Only a very weak interaction between the N-terminal 1a isoform peptide and the Abl core was observed. It could be interesting to see if this interaction is stronger when the Abl^{cap,1a} construct is measured by NMR. This construct was expressed and purified. Unfortunately, the NMR sample

concentration was too low and the signal-to-noise ratio insufficient to detect enough resonances and draw any conclusions. However, future preparation should yield enough material such that proper spectra of the Abl 1a isoform can be recorded and give new insights into the N-cap^{1a}-mediated inhibition mechanism.

An important next step in this project will be the production of homogeneous wt myr-Abl^{cap} samples. These can be used to directly link NMR observations with activity data, which is impossible with the used inactive kinase mutant. The observation that the myristoyl might not occupy the allosteric pocket all the time raises new questions: What does this mean for Abl and Bcr-Abl activity? What does this mean for the development of Bcr-Abl therapy?

As shown in Chapter 0, Abl is highly dynamic. Although only the assembled conformation is observed by solution NMR, this does not mean that Abl does not disassemble occasionally. This dynamical information is crucial to understand the activity of Abl and inhibition by certain intra- or intermolecular elements. A rigorous investigation of the dynamics of myr-Abl and various activating mutants by NMR and FRET will certainly provide more answers to the above questions. However, sample production for those studies is a bottleneck. For further NMR studies, deuteration will be inevitable, which in insect cells is not as easy as in *E. coli* [342]. Possibly, expression in *E. coli* could be tried with co-expression of N-myristoyltransferase [365] in order to produce N-myristoylated proteins. For FRET studies, introduction of propargyl-lysine by amber stop codon technology is necessary for site-specific fluorophore labeling. Incorporation of unnatural amino acids in mammalian cells is an established methodology [296, 322] and should be applicable to myr-Abl as well.

Material and Methods

Constructs

The plasmids for expression of myristoylated Abl$^{2-531}$ (1b isoform, myr-Abl^{cap}) and Abl$^{2-512}$ (1a isoform, Abl^{cap,1a}) were a kind gift from Oliver Hantschel (University of Marburg, Germany). Details of these plasmids and their expression wer described previously [33]. In brief, the constructs are cloned into the pFastBac1 vector (Gibco BRL) for expression in baculovirus-infected insect cells of *Spodoptera frugiperda* (Sf-9 cells). The vector contains a C-terminal cleavage site for the Tobacco Etch Virus (TEV) protease followed by a hexa-histidine tag. Notably, the plasmids also contain two

single point mutations within the N-cap, K29R and E30D, which are, however, not functionally relevant [176]. The G2A mutation was produced by site-directed mutagenesis using a protocol adapted from the commercial QuikChange method (Agilent). The sequences of the relevant parts of all plasmids were confirmed by Sanger DNA sequencing (Microsynth AG, Balgach SG, Switzerland).

The Abl 1a N-terminal peptide with the sequence LEICLKLVGCKSKK (residues 2-15) was purchased from Sigma Aldrich.

Insect cell culture and baculovirus production

Permanent insect cell cultures were kept at 27 °C and a shaking speed of 250 rpm (25-mm orbit) in 50-mL centrifugal tubes (TPP) and subcultured in mid-log phase based on standard protocols [366].

Recombinant bacmid DNA was generated according to the supplier's protocol (Life Technologies) by transforming the plasmids into DH10bac *E. coli* cells (Thermo Fisher, USA), blue/white screening, and plasmid isolation. The baculovirus was then produced as described elsewhere [341]. In brief, first ~1 million adherent Sf-9 cells were transfected with bacmid DNA using FuGENE® HD transfection reagent (Promega), incubated at 27 °C for 3-5 days and the virus containing supernatant - virus generation P0 - eventually collected and stored at 4°C. High-titer virus stocks, P1 and P2, were generated within two subsequent amplification rounds. For P1, 50 mL cultures of Sf-9 cells at a cell density of $1x10^6$ cells/mL in full SF4 medium (BioConcept, Switzerland, # 9-00F38-K) were infected with 1 mL of P0 virus stock, incubated for 48 h at 27 °C and shaking speed of 180 rpm (50-mm orbit), and harvested at 1000 g and 10 °C for 15 min. The P2 generation was produced similarly. A 100-mL culture of Sf-9 cells at a cell density of $1x10^6$ cells/mL in full SF4 medium was infected with 200 µL of P1 virus stock, further processed as P1, and the final P2 virus stock stored at 4 °C.

Small-scale expression and solubility test

Expression level and solubility of constructs were routinely estimated from small-scale cultures. For this, 10-mL cultures of Sf-9 cells at a cell density of $1.5x10^6$ cells/mL in full SF4 medium in 50-mL centrifugal tubes (TPP) were infected with a previously determined optimum concentration of P2 virus stock (usually 4 mL/L). Cultures were then incubated at 27 °C and 250 rpm (25-mm orbit) shaking

speed for 72 h, and cells harvested at 1500 g for 15 min. Cell pellets were resuspended in 1 mL lysis buffer (50 mM Tris-HCl, 500 mM NaCl, 10 mM imidazole, 2 mM TCEP, 5 % glycerol, cOmplete^{TM} EDTA-free protease inhibitor mix (Roche), pH 8.0), lysed by sonicating at 1-s pulse – 1-s pause intervals for a total pulsing time of 20 s, and centrifuged at 16.000 g for 5 min. All steps were carried out at 4 °C or on ice. The supernatant was analyzed by SDS-gel electrophoresis and Coomassie staining.

Expression and purification of Abl^{core}

^{15}N-labeled wt Abl$^{83-534}$ was produced as described by Skora *et al.*, 2013 [172] and modified in Sonti *et al.*, 2018 [174].

Expression and purification of ^{15}N-labeled myristoylated Abl^{cap} for NMR studies

^{15}N-labeled samples were prepared from insect cells fed with a homemade ^{15}N-labeled yeast extract based on a previously described protocol [341] and modified by Bastian Franke (unpublished). In brief, 250-500 mL of expression cultures of Sf-9 cells at a cell density of 1.5x10^6 cells/mL in full SF4 medium in 600-ml TubeSpin Bioreactors (TPP) were infected with 4 mL/L P2 virus stock and incubated for 16 h at 27 °C and 180 rpm (50-mm orbit). Cultures were harvested at 300 g for 4 min at 20 °C, and cell pellets dissolved in ΔSF4 medium (depleted of amino acids and yeast extract, BioConcept, Switzerland, # 9-02S38-I). After renewed centrifugation, cells were dissolved in sterile-filtered labeling medium, incubated for additional 48 h and harvested at 1500 g for 15 min at 4 °C. The labeling medium consisted of ΔSF4 medium, 8 g/L homemade ^{15}N yeastolate [341], and 1 g/L $^{14}N_2$-glutamine. The pH was adjusted to 6.2 and the osmolality to that of the SF4 medium (usually 340 mOsmol/kg) by adding NaCl.

For purification of NMR samples, the cell pellets were resuspended in lysis buffer [50 mM Tris-HCl, 500 mM NaCl, 10 mM imidazole, 2 mM TCEP, 5 % glycerol, cOmplete^{TM} EDTA-free protease inhibitor mix (Roche), pH 8.0], and cells lysed using a dounce tissue homogenizer. After lysis, the cell extract was further purified as described for Abl^{core} (Abl$^{83-534}$) by Sonti *et al.,* 2018 [174] with the following modifications. The ion-exchange chromatography step was left out since samples were usually already pure after the Ni-His affinity chromatography step. Optionally, *in vitro* dephosphorylation by lambda phosphatase (LPP) was applied.

LC/MS

In order to verify the correct protein mass, identify possible PTMs (mainly phosphorylation and myristoylation), degradation products or impurities, and to determine the level of ^{15}N incorporation, Abl samples of 30 to 100 µL were prepared for LC/MS analysis by addition of acetic acid until the pH of the sample dropped below a value of 3. The samples were then applied to a Jupiter (5 µ, 300 Å, 157 µL) C4 reverse-phase column (Phenomenex) using an LC system (Agilent) equipped with an autosampler for injection into the ESI-TOF mass spectrometer (Bruker microTOF). The protein mass was calculated by maximum entropy deconvolution.

NMR

The NMR ^{1}H-^{15}N TROSY experiments, chemical shift difference calculation and principle component analysis were carried out as described earlier in Chapter 3.1. Assignments were transferred from Abl^{83-534} complexes [172]. The chemical shift differences were calculated according to $\Delta\delta = (\Delta\delta_N{}^2/25 + \Delta\delta_{HN}{}^2)^{1/2}$.

Molecular graphics

PDB structures were displayed using the PyMOL Molecular Graphics System (Schrödinger, LLC).

3.3 Influence of the C-terminal F-actin binding domain on the core conformation

Introduction

The C-terminal FABD of Abl has been reported to be important for Bcr-Abl's transforming potential in rat fibroblasts [367] and oncogenicity in transgenic mice [368]. A kinase inhibitory effect of F-actin was shown under certain conditions in the cell in one study [108], whereas no effect of the C-terminal tail of Abl including the FABD on the kinase activity was observed in another [175]. Additionally, an interplay between KD autophosphorylation and FABD that regulates nuclear import and imatinib sensitivity has been reported [369]. However, these biological effects could also be a simple consequence of FABD-F-actin binding and subsequent nuclear import retention [34]. Deeper insights into the molecular mechanism underlying the function of the FABD within Abl are lacking as previous studies are solely based on nuclear localization and mutagenesis experiments.

Results and Discussion

The FABD does not affect the apo Abl core conformation.

To investigate whether the C-terminal FABD of Abl interacts with the Abl regulatory core (Abl^{core}), we performed NMR titration experiments. For this, ^{1}H-^{15}N TROSY spectra were recorded for a titration of ^{15}N-labeled apo Abl^{core} with unlabeled FABD (Figure 3.10A). No significant chemical shift changes ($\Delta\delta < 0.025$ ppm) were observed in the TROSY spectra until a final FABD:Abl ratio of 4:1 (FABD 360 µM, Abl 90 µM) (Figure 3.10B). This clearly indicates that the FABD added in *trans* does not interact with the assembled apo Abl^{core} up to concentrations of hundreds of micromolar.

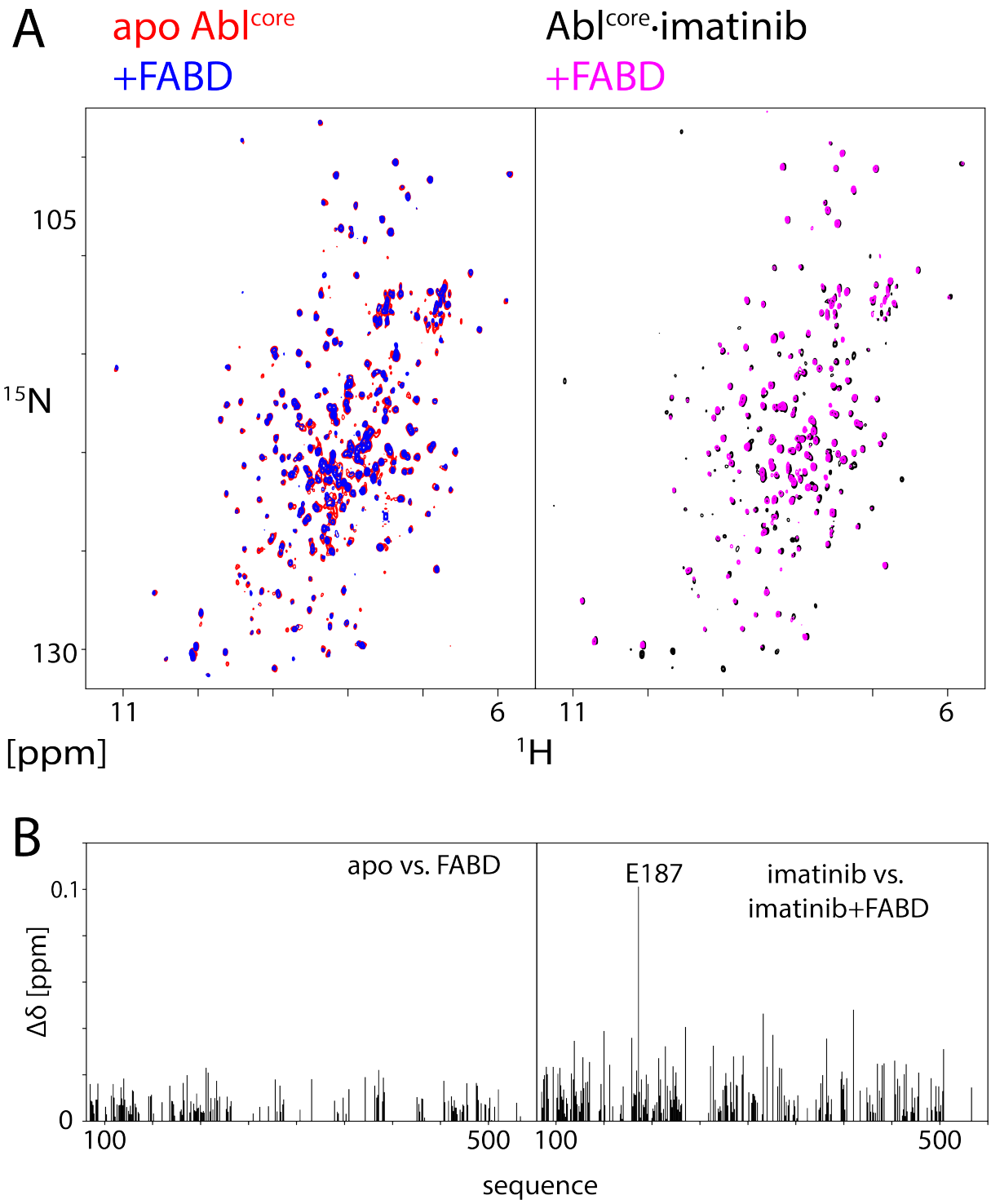

Figure 3.10. The FABD only interacts with the Abl^{core}•imatinib complex, but not with the apo Abl^{core}. A) ^{1}H–^{15}N TROSY spectra of the apo Abl^{core} (red) and Abl^{core}•FABD (blue) show no difference. Small changes are visible between Abl^{core}•imatinib (black) and Abl^{core}•imatinib•FABD (magenta). B) The chemical shift difference (Δδ) plots are shown for the comparison of apo Abl^{core} and Abl^{core}•FABD (top) and Abl^{core}•imatinib and Abl^{core}•imatinib•FABD (bottom) with $\Delta\delta = (\Delta\delta_N{}^2/25 + \Delta\delta_{HN}{}^2)^{1/2}$.

The FABD shifts the disassembled conformation towards a more active conformation.

In order to investigate whether the FABD interacts rather with the disassembled than with the assembled conformation, unlabeled FABD was added at a ratio of 4:1 (360 µM FABD, 90 µM Abl) to ^{15}N-labeled Abl^{core}•imatinib. In this case, chemical shift differences (Δδ) up to 0.05 ppm were observed throughout the Abl core (Figure **3.10**B). The chemical shift difference of E187 was even larger (Δδ = 0.1 ppm).

A quantitative analysis of all observed SH3 and SH2 chemical shifts by PCA reveals that adding FABD to the Abl^{core}•imatinib complex shifts its conformation in the direction of the activating Abl^{core} P242E,P249E mutant (Figure 3.11A). The substitution of these SH2-KD linker prolines is presumably destabilizing the interaction between the SH3 domain with the KD N-lobe via the SH2-KD linker [33] and shifts the conformational equilibrium towards a form that is even more disassembled than the wt Abl^{core}•imatinib complex (Sonti *et al.*, unpublished data).

More than 85 % of the data are explained by the first two principal components (Figure 3.11B). These two principal components describe the difference between the assembled and disassembled conformation (PC1) and the difference between the apo core and complexes with ATP pocket inhibitors (PC2) [174]. The P242E, P249E mutant is shifted even further in the PC1 dimension compared to the disassembled type II inhibitor complexes and has the same PC2 value as the apo Abl^{core} (Sonti *et al.*, unpublished data). Interestingly, both, the apo and the imatinib complex of the Abl^{core} P242E,P249E mutant are located close to each other, indicating that adding imatinib does not affect the SH3-SH2 assembly anymore in this conformation.

The Abl^{core}•imatinib•FABD sample is slightly shifted both in the PC1 and PC2 directions by about a third from the wt Abl^{core}•imatinib complex towards apo Abl^{core} P242E,P249E and Abl^{core} P242E,P249E•imatinib (Figure 3.11A). Notably, the Abl^{core}•FABD sample showed similar PC1 and PC2 scores as the apo core as already seen above from comparison of the respective spectra.

The PCA loadings plot reveals resonances that contribute most to the respective PC1 and PC2 scores (Figure 3.11C). From those, resonances F91, E120, T136, and V151 are exemplarily plotted (Figure 3.11E). Interestingly, residues C119, E120, and W129, which strongly contribute to PC2, are located in the SH3 domain and make contact to the SH2-KD-linker P249 in the assembled core conformation (PDB 2FO0 [173], Figure 3.11D). Moreover, Y89 whose chemical shifts contribute strongly to both

PC1 and PC2 is in contact with P242 in the assembled conformation. Interestingly, some resonances show a small second peak in the Abl^{core}•imatinib•FABD spectrum at the position of the Abl^{core} P242E,P249E mutant (e.g. V151) or a shoulder of the main peak reaching out to the P242E,P249E peak (e.g. E120). The PCA was only performed on SH2/SH3 chemical shifts. However, also KD N-lobe resonances follow the trend described before. This is exemplarily shown for T296, C324, and F336 (Figure 3.11E).

Together these observations suggest an altered interaction between the SH3 domain and the SH2-KD-linker as well as the KD N-lobe in the presence of the FABD. Such an altered interaction is also present in even pronounced form in the P242E,P249E mutant as indicated by the larger shift of the respective resonances (Figure 3.11E) and larger PCA scores (Figure 3.11A). However, a clear interaction site could not be defined so far, since the largest chemical shift differences are distributed across the whole protein. Additionally, not all resonances are assigned and some resonances are broadened and thus not visible in the spectrum. For example, the SH2-KD-linker residues are all not assigned and consequently, binding to this linker could not be verified.

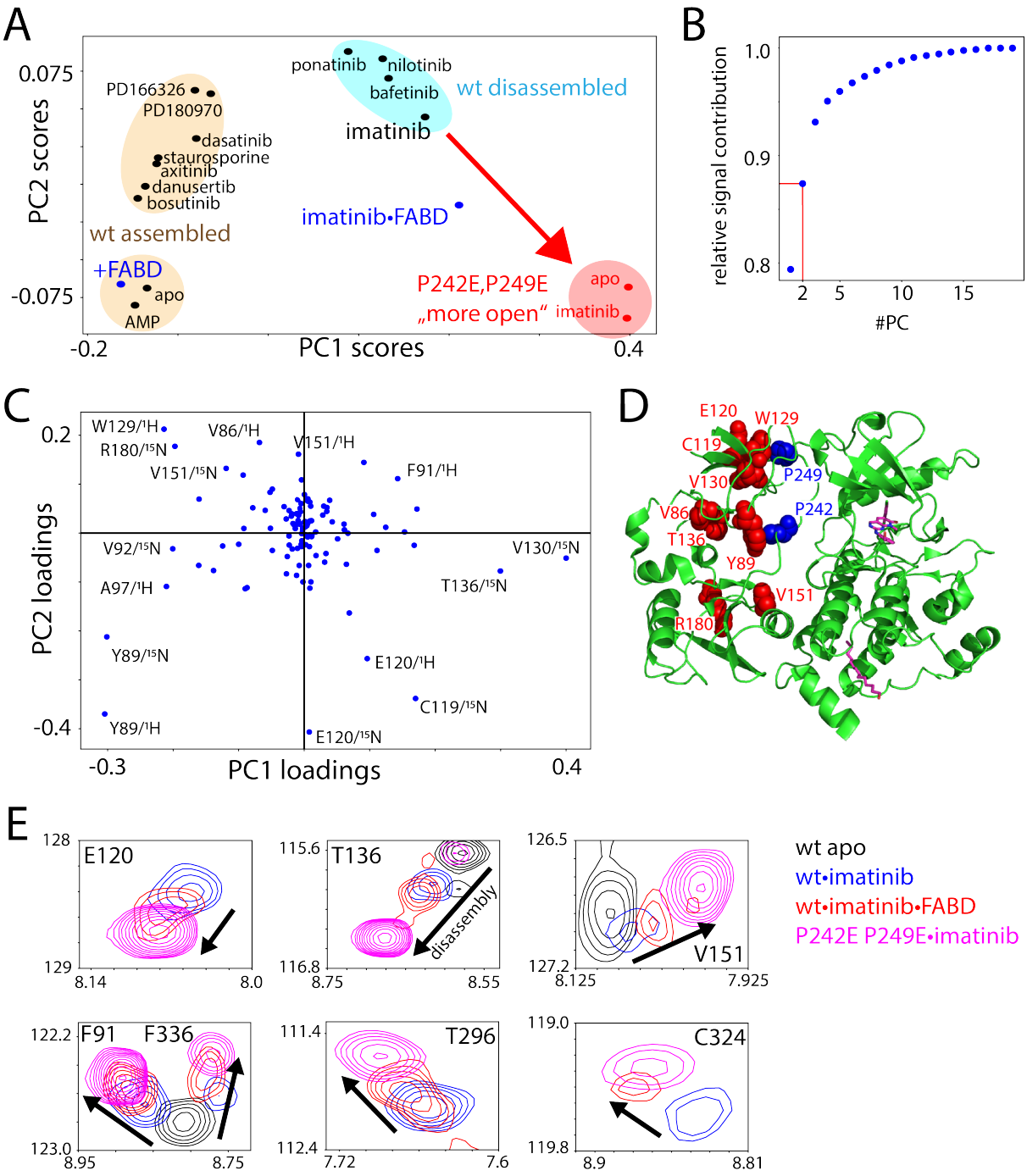

Figure 3.11. Principal component analysis of Abl SH3 and SH2 resonances shows that the interaction with the FABD induces a slightly more disassembled conformation of the Abl^{core}. A) The PCA scores plot shows the principal component (PC) 1 and 2 scores for various Abl^{core} samples. Four clusters can be identified: i) apo wt Abl^{core} and complexes with AMP-PNP or FABD, ii) complexes of wt Abl^{core} with type I inhibitors adopting the assembled conformation, iii) complexes of wt Abl^{core} with type II inhibitors adopting the disassembled conformation, and iv) Abl^{core} P242E,P249E, both apo and imatinib complex. The wt Abl^{core}•imatinib•FABD complex locates in between the Abl^{core}•imatinib complex and the Abl^{core} P242E,P249E mutant, indicated by a red arrow. B) Relative contributions of the PCs to explain the observed signal. . The first two PCs describe more than 85 % of the data. C) The loadings plot reveals which ^{1}H and ^{15}N chemical shifts contribute most to the first two PCs. D) These residues are depicted as red spheres within the assembled core structure (PDB 2FO0 [173]). Residues P242 and P249 are depicted as blue spheres. E) Exemplary residues appearing in the PCA and from visual inspection of KD resonances are shown for apo Abl^{core} (black), Abl^{core}•imatinib (blue), Abl^{core}•imatinib•FABD (red), and Abl^{core} P242E,P249E•imatinib (magenta).

Conclusion and Perspective

In summary, this study shows that the isolated FABD of Abl interacts with the disassembled Abl^{core}•imatinib regulatory core, but not with the assembled apo Abl regulatory core. Unfortunately, the binding site could not be defined, which is probably due to missing resonance assignments and resonance broadening. Surprisingly, the interaction of the FABD with the Abl regulatory core shifts the imatinib-induced disassembled core conformation towards a distinct conformation that is adopted by the SH2-KD-linker mutant P242E,P249E in the apo state or bound to imatinib.

The smallness of the chemical shift changes is likely a consequence of the experimental design. Under physiological conditions, when both the FABD and the Abl core are connected by the unstructured regions of the Abl C-terminal tail, their interaction must be much stronger.

The P242E,P249E mutations increase the catalytic activity of Abl [176] and shift the equilibrium to a 'more open' state compared to the disassembled conformation induced by type II inhibitors as seen by NMR (Sonti *et al.*, unpublished data) and comparison of SAXS-derived radii of gyration (R_g = 31 Å for the Abl^{core}•imatinib [172] and R_g = 34 Å for the 'activated' Abl^{core} P242E,P249E in complex with the ATP site ligand PD166326 [173]). This effect has been rationalized by a destabilization of the polyproline-mediated interaction between the SH3 domain and the SH2-KD-linker and hence of the assembled conformation. This is supported by the presented observations. The SH3 residues, which are located close to the SH2-KD-linker prolines, show strongest chemical shifts upon conformational change from the disassembled core to the 'more open' core both in the Abl^{core} P242E,P249E mutant as well as in the Abl^{core}•imatinib•FABD complex.

This 'more open' conformation seems to be stabilized by the FABD. However, apparently the interaction is not strong enough to open the tight assembled conformation. A possible model is that the FABD interacts with the SH-KD-linker or other regions that are not accessible in the assembled conformation. These become partly accessible in the disassembled conformation and the FABD squeezes between the KD and the SH3 and SH2 domains, thereby shifting the conformational equilibrium towards a 'more open' conformation.

Since the P242E,P249E mutation increases the activity of Abl [175] and FABD stabilizes a P242E,P249E-like 'more open' conformation, it would be interesting to measure the influence of the isolated FABD on the Abl core kinase activity. If the FABD

shifts the equilibrium to a ‘more open’ and thus more active conformation, one may expect an increase of the activity. However, the FABD may also compete with substrate binding resulting in lower catalytic activity. Indeed, it has been reported that under certain conditions, F-actin inhibits Abl kinase activity through FABD binding in the cell [108]. This could be reasoned by a model in which FABD is bound to F-actin and thus cannot activate the Abl core. However, in contrast, it was later reported that the C-terminal tail of Abl has no effect on the activity at all [175]. So far, no activity data recorded under well controlled *in vitro* conditions are available.

To prove the hypothesis of an FABD-induced conformational change of the Abl core, it would be necessary to directly observe the interaction site between the FABD and the Abl core. This will be done after improving the assignments of the Abl core. Recording TROSY spectra of ^{15}N-labeled FABD and titrating unlabeled Abl core could also identify the interaction site within the FABD.

In addition, single-molecule FRET experiments could be very helpful to investigate the assumed interaction. If the FABD shifts the dynamic equilibrium of the Abl•imatinib complex to a ‘more open’ conformation, this can be readily observed with the experimental setup developed in Chapter 0. Furthermore, donor and acceptor fluorophores could be placed separately on the Abl core and the FABD. FRET would then directly show the interaction. Furthermore, placing the fluorophore at different positions on the Abl core could help to identify the interaction site.

Our observation of a direct interaction between FABD and the Abl^{core} suggests that the smFRET experiments should be expanded to full-length Abl, possibly in cells, where also F-actin is present. Thereby, one could not only investigate the molecular mechanism of an FABD-Abl^{core} interaction, but also its biological consequences. Questions that could be addressed are for example: Is there a competition between F-actin and the Abl^{core} for FABD binding? Does this influence nuclear localization? Is the Abl kinase activity influenced by the cytoskeleton, and what are the consequences for leukemogenesis and drug development?

Material and Methods

Expression and Purification

The plasmid harboring the construct for FABD expression in *E. coli* in a modified pET24d vector (Novagen) was a kind gift of Oliver Hantschel (University of Marburg,

Germany). As described previously [370], the vector comprises FABD residues 1026-1149 of the Abl 1b isoform, which are preceded by an N-terminal His-tag followed by GST and a TEV cleavage site. Expression and purification of unlabeled FABD was carried out as described previously [370]. The vector was transformed into BL21(DE3) *E. coli* cells and grown in LB medium at 37 °C. The expression was induced at an OD of 0.8 by addition of 1 mM IPTG, and temperature was reduced to 20 °C. Cells were harvested 4-6 h after induction. After cleavage, the purified FABD sequence is GAMA-^{1026}STRVS…DIVQR^{1049}-LE (superscript indicates Abl isoform 1b numbering).

^{15}N-labeled wt Abl$^{83-534}$ was produced as described [174].

NMR

The NMR ^{1}H-^{15}N TROSY experiments and chemical shift difference calculations were performed as described in Chapter 3.1. Unlabeled FABD was buffer-exchanged into the 'NMR buffer' [20 mM Tris·HCl (pH 8.0), 100 mM NaCl, 2 mM EDTA, 2 mM TCEP, and 0.02% NaN_3] using a 30-kDa molecular weight cutoff centrifugal filter (Amicon) and concentrated to 740 µM. FABD was titrated from that stock solution to the ^{15}N-labeled wt Abl^{core} NMR sample. The final concentrations were 90 µM wt Abl$^{83-534}$ and 360 µM FABD.

All NMR experiments were performed at 303 K on a Bruker AVANCE 900-MHz spectrometer equipped with a TCI triple resonance cryoprobe. ^{1}H-^{15}N TROSY experiments were recorded as 224 (^{15}N) × 1024 (^{1}H) complex points with acquisition times of ~40 ms in both dimensions. All NMR data were processed with the NMRPipe software package [371] and analyzed with SPARKY [372]. The chemical shift differences were calculated according to $\Delta\delta = ({\Delta\delta_N}^2/25 + {\Delta\delta_{HN}}^2)^{1/2}$.

4 High-pressure NMR study of the Abl regulatory core conformation

4.1 Introduction

Pressure changes the equilibrium of protein conformations, if they occupy different volumina [373]. Such changes can be observed by high-pressure NMR at atomic resolution [373-376]. Thus, certain conformational states may be trapped and investigated by NMR without the need to change the temperature, mutate the protein or add binding partners. However, mostly local conformation changes at the active site pocket of a protein have been described using high-pressure NMR [377-381]. Recently, a pressure-induced global structural transition between two functionally relevant states has been reported for the β1-adrenergic receptor [382].

In this context, it was interesting to test if also conformational changes of multidomain proteins can be induced and observed by high-pressure NMR. The Abl^{core} (SH3-SH2-KD, Abl^{83-534}) construct with its large assembled-to-disassembled transition, two distinct ligand pockets and regulation by various interdomain interactions appears as an interesting subject for such a high-pressure NMR study. This could provide new insights about the Abl conformational equilibrium, in particular about the assembled apo conformation. Since the C-terminal αI-helix assists in Abl^{core} activation by pushing onto the SH2 domain (see Chapter 3.1), it may be hypothesized that the assembled conformation of the apo form is slightly less compact than allosteric inhibitor-bound complexes, where the αI-helix is bent and the pressure onto the SH2 domain is reduced. This hypothetic difference in compactness might be revealed by high-pressure NMR. Additionally, further void volumes between the SH3, SH2, and kinase domains could be uncovered, which can be eventually related to Abl function.

4.2 Results and Discussion

Pressure does not change the disassembled Abl^{core}•imatinib conformation

In order to test the applicability of high-pressure NMR to Abl, first ^{1}H-^{15}N TROSY spectra of Abl^{core}•imatinib were recorded at 1, 750, 1500, and 2500 bar (Figure **4.1**A), since Abl is most stable in this complex. Indeed, Abl stayed intact up to 2500 bar. Small reversible and linear pressure-dependent chemical shift changes were observed for all resonances as it is commonly observed. Interestingly, besides these

pressure-induced chemical shift changes, major changes indicating a conformational transition from the disassembled to the assembled or another, unknown conformation were not observed for the Abl^{core}•imatinib complex.

The chemical shift differences Δδ between the 1 bar and 2500 bar spectra were calculated for all assigned resonances (Figure 4.1B). The largest Δδ were observed mainly within the KD and in particular around the ATP binding pocket (Figure 4.1C). This indicates that, although occupied by imatinib, the ATP site is still compressible and not completely filled by the ligand.

Interestingly, the resonances of S457, R476, and A493 also have Δδ > 0.25 ppm between 1 bar and 2500 bar. These residues are clustered at the bottom of the KD C-lobe close to the myristoyl pocket (Figure 4.1C). Unfortunately, there are very few assignments of residues forming the allosteric pocket, which is empty in our case and therefore expected to experience bigger pressure effects. Possibly, the changes of the aforementioned KD C-lobe residues are a consequence of allosteric pocket compression.

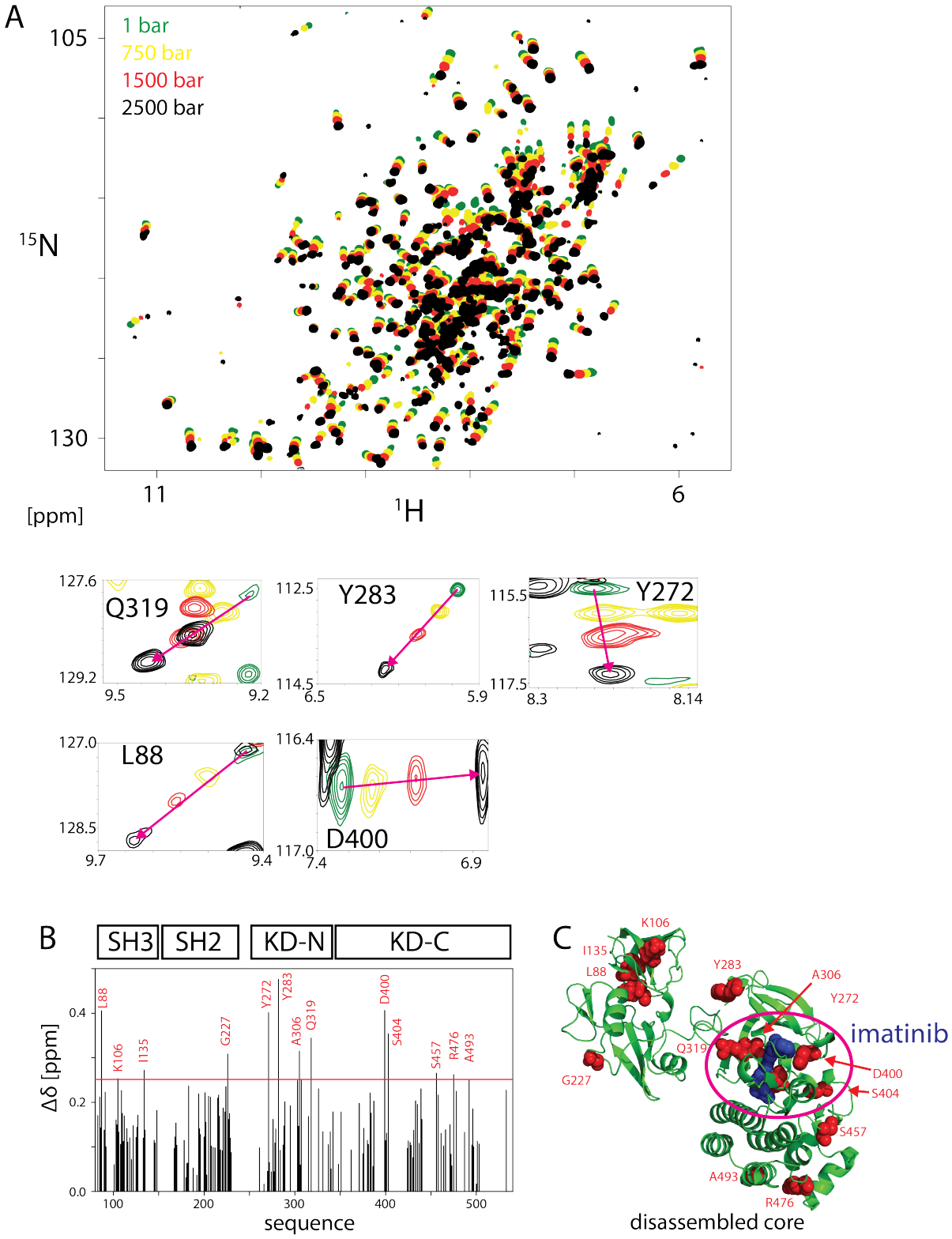

Figure 4.1. Abl^{core}•imatinib under high pressure. A) The $^{1}H-^{15}N$ TROSY spectra and selected resonances of Abl^{core}•imatinib are shown at 1, 750, 1500, and 2500 bar. All resonances show a pressure-induced linear shift indicated by a magenta arrow. B) The chemical shift differences (Δδ) between 1 and 2500 bar are shown for all assigned resonances. Red line indicates Δδ = 0.25 ppm. C) Residues with Δδ > 0.25 ppm are highlighted and mapped onto a model of the disassembled Abl core structure [172]. The ATP pocket is highlighted by a magenta circle. Imatinib is depicted as blue spheres.

The apo Abl^{core} disassembles under pressure, but is unstable

Since high pressure had no strong effect on the imatinib-disassembled Abl^{core}, we wanted to test if high pressure affects the assembled conformation of the apo Abl^{core}. In contrast to the Abl^{core}•imatinib complex, the apo form was not stable at high pressure (≥1500 bar). However, before the protein was lost, several resonances did not simply shift linearly with increasing pressure, but moved towards the resonances of the imatinib complex (Figure 4.2). The respective residues were not only located in the SH3 and SH2 domains, like V92, G149, and A225, which report on the Abl^{core} conformation, but also close to the catalytic site (D382) (Figure 4.2). At 750 bar, the apo resonances are split into two for V92, G149, and D382, with one resonance following the linear shift of the assembled conformation, and the other shifted to the resonance position of the disassembled Abl^{core}•imatinib conformation. This indicates that the Abl^{core} is in slow conformational exchange between the assembled and the disassembled conformation at 750 bar. At 1500 bar, only one apo resonance is observed which is close to the one for the disassembled Abl^{core}•imatinib conformation.

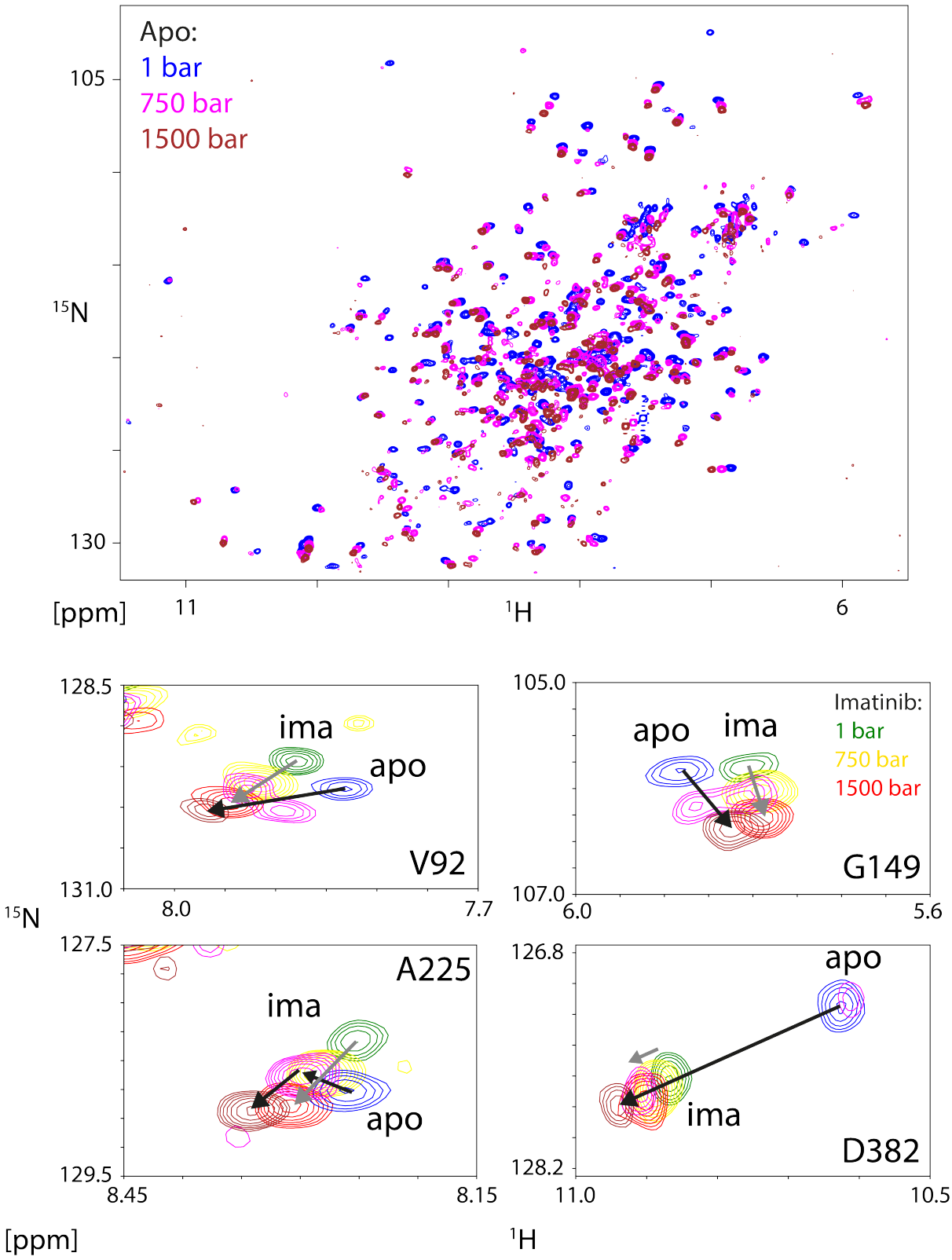

Figure 4.2. Apo Abl^{core} under high pressure. The ^{1}H-^{15}N TROSY spectra and selected resonances of apo Abl^{core} are shown at 1, 750, and 1500 bar (blue, magenta, and brown for apo resonances; green, yellow, and red for imatinib complex resonances). The pressure-induced shift of the imatinib complex resonances is indicated by grey arrows, the shift of the apo resonances by black arrows.

The assembled Abl^{core} •dasatinib complex conformation is not substantially affected by pressure

Since the apo state of Abl^{core} was not stable under high pressure, we added the type I ATP-competitive inhibitor dasatinib to increase the stability of the Abl^{core}. Thereby, we were able to study the effect of high pressure onto the assembled core conformation. It was possible to record ^{1}H-^{15}N TROSY spectra of Abl^{core}•dasatinib at 1, 750, 1500, and 2500 bar (Figure 4.3A). Unfortunately, less KD resonances could be assigned for the high-pressure spectra compared to the Abl^{core}•imatinib sample. Thus, not many chemical shift differences Δδ between 1 bar and 2500 bar could be calculated for the KD domain (Figure 4.3B). Nevertheless, a cluster of larger chemical shift changes was detected for residues T286, L317, and Q319 between the ATP pocket and the SH3-KD interface (Figure 4.3B and C). Analysis of the assembled core structure by the program Hollow 1.2 [383] revealed a void volume in this area (Figure 4.3C). Hence, these larger Δδ values could be attributed to a compression of the void volume between the KD and the SH3 domain around the SH2-KD linker.

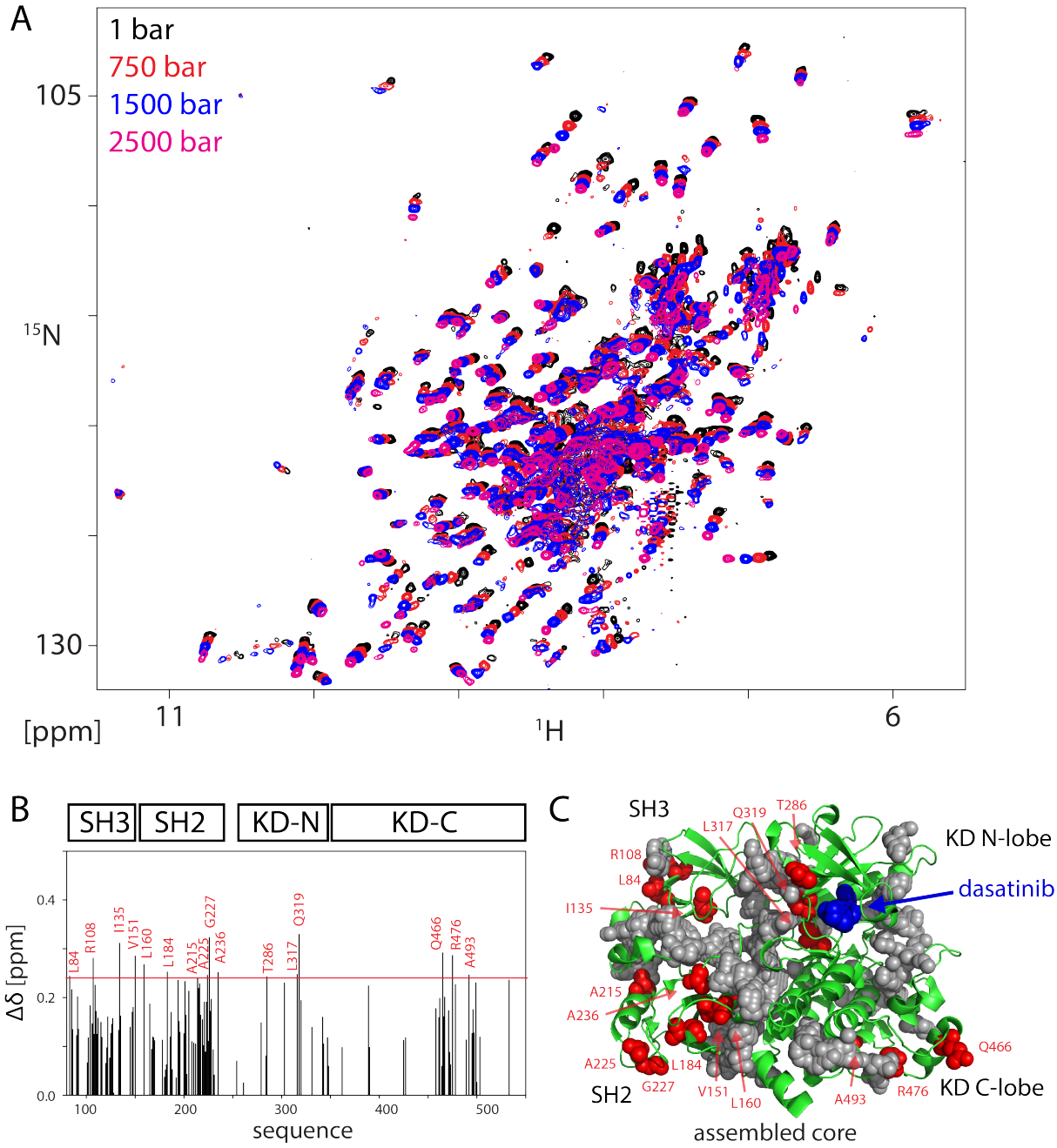

Figure 4.3. Abl^{core}•dasatinib under high pressure. A) ^{1}H-^{15}N TROSY spectra of Abl^{core}•dasatinib at 1, 750, 1500, and 2500 bar. B) Chemical shift differences Δδ between 1 and 2500 bar for all assigned resonances. Red line indicates Δδ = 0.24 ppm. C) Residues with Δδ > 0.24 ppm are mapped onto the assembled Abl^{core} structure (PDB 2FO0 [173]) with the type I ATP site ligand dasatinib (blue spheres). Void volumes calculated with the program Hollow 1.2.[383] (see Material and Methods for details) are shown as grey spheres.

Interestingly, a second cluster of larger chemical shift differences at the bottom of the KD C-lobe (residues S466, R476, and A493) is very similar to the Abl^{core}•imatinib complex. This supports the aforementioned interpretation that these shifts are arising from compression of the nearby allosteric myristoyl pocket, which is empty in both cases.

In contrast to the Abl^{core}•imatinib complex, more changes were observed within the SH3-SH2 module. These could arise from void volumes between the individual domains (Figure 4.3C). Apparently, these void volumes exist in the assembled conformation, but not in the imatinib-induced disassembled conformation, where the SH3 and SH2 domains move rather freely in the aqueous solution.

Besides these specific effects, overall the chemical shifts follow a nearly linear shift with increasing pressure, which indicates that the Abl^{core}•dasatinib remains roughly unchanged in the assembled conformation.

4.3 Conclusion and Perspective

In summary, this study has shown that pressure up to 2500 bar does not strongly change the type I inhibitor complex assembled Abl^{core} conformation or the type II-induced disassembled Abl^{core} conformation. However, pressure disassembles the apo Abl^{core}, which eventually precipitates at pressures higher than 1500 bar.

The apo form was extremely unstable under high pressure. Before precipitating, the apo core disassembles as indicated by SH3 and SH2 resonances. Indeed, it was observed that the apo form of the Abl^{core} is less stable compared to inhibitor-bound complexes in NMR [172] and during the copper-catalyzed fluorophore labeling reaction (Chapter 0). This instability possibly arises from increased dynamics of the apo KD [172, 174]. Therefore, a pressure-induced instability after Abl^{core} disassembly and hence further increase of the molecules dynamics is not entirely surprising.

However, the observed disassembly of the Abl^{core} at pressures below 1500 bar with the observed slow exchange between the assembled and the disassembled conformation at 750 bar is very exciting. Probably, the apo form bears compressible void volumes between the core domains, which are not present in the disassembled conformation. Application of high pressure then leads to compression of these voids and consequently disassembly of the core, which indicates that these voids are important for kinase regulation. Further investigation of this process by measuring more pressure points, calculating the populations of the assembled and disassembled conformation, as well as error estimation will enable calculation of the free energy difference as described elsewhere [382].

As no major conformational changes up to 2500 bar were observed for complexes with the ATP-competitive inhibitors imatinib and dasatinib, the analysis focused on local changes. The biggest local changes are observed around the ATP pocket for the

Abl^{core}•imatinib complex, whereas larger changes happen at the SH3-SH2-KD interface for the Abl^{core}•dasatinib complex. The latter suggests that the assembled conformation induced by type-I ATP site inhibitors is not yet completely compact.

This could arise from a force exerted by the flexible C-terminal αI-helix directed onto the SH2 domain as shown above (Chapter 3.1). Thereby, the SH2 domain might be slightly pushed away. It will be interesting to see if the pressure-induced changes, in particular at the SH2-KD interface, are smaller when the allosteric pocket is filled by GNF-5 or asciminib. In this case, the αI-helix is bent away from the SH2 domain and consequently the force directed towards the SH2 domain is reduced and the assembly could be slightly more compact. In fact, however, the crystal structure of the myristoylated Abl (bent αI-helix) complex with the type I inhibitor PD166326 reveals still many cavities between the SH3, SH2, and kinase domain (Figure 4.3).

Nevertheless, since no disassembly, as for the apo form, was observed for the assembled conformation of Abl^{core}•dasatinib, we speculate that the proposed cavities in this conformation are smaller and the free energy difference to the disassembled conformation is bigger. Possibly, 2500 bar are just not enough to also open the core conformation of the Abl^{core}•dasatinib complex. Unfortunately, not significantly higher pressure are currently reachable for NMR solution conditions.

4.4 Material and Methods

Protein expression and purification

^{15}N-labeled wt Abl$^{83-534}$ was produced as described [174].

High-pressure NMR

The NMR ^{1}H-^{15}N TROSY experiments at 1 bar were recorded as described earlier in Chapter 3.1. High-pressure NMR experiments were carried out as described [382]. In short, 250 µL of the NMR sample with protein concentration of typically 50 µM were placed into the high-pressure NMR tube of a commercial high-pressure NMR cell (Daedalus Innovations LLC) with an inner diameter of 3 mm and an active volume of 120 µL. The sample was covered with extra-low viscosity paraffin wax (Sigma Aldrich id 95369). The pressure cell was connected to a pressure line filled with low-viscosity paraffin oil that connects the pressure cell with a pressure generator (High Pressure Equipment Company). The tube is rated up to 2500 bar.

^{1}H-^{15}N TROSY experiments of wt Abl$^{83-534}$ in its apo state and in complex with ATP-site inhibitors were recorded at various pressures. All NMR experiments were performed at 303 K on a Bruker AVANCE 900-MHz spectrometer equipped with a TCI triple resonance cryoprobe. ^{1}H-^{15}N TROSY experiments were recorded as 224 (^{15}N) × 1024 (^{1}H) complex points with acquisition times of ~40 ms in both dimensions. All NMR data were processed with the NMRPipe software package [371] and analyzed with SPARKY [372].

The chemical shift differences were calculated according to $\Delta\delta = (\Delta\delta_N{}^2/25 + \Delta\delta_{HN}{}^2)^{1/2}$.

Void volumes in the crystal structure were quantified using the program Hollow 1.2. [383] with a grid spacing of 1.0 Å and a sphere size of 4 Å for the definition of the outer Abl surface. Water molecules and ligands were removed before the analysis.

5 References

1. Manning, G.; Whyte, D. B.; Martinez, R.; Hunter, T.; Sudarsanam, S., The protein kinase complement of the human genome. *Science* **2002,** *298* (5600), 1912-34.
2. Hunter, T., A thousand and one protein kinases. *Cell* **1987,** *50* (6), 823-9.
3. Blume-Jensen, P.; Hunter, T., Oncogenic kinase signalling. *Nature* **2001,** *411* (6835), 355-65.
4. Lahiry, P.; Torkamani, A.; Schork, N. J.; Hegele, R. A., Kinase mutations in human disease: interpreting genotype-phenotype relationships. *Nat Rev Genet* **2010,** *11* (1), 60-74.
5. Fabbro, D.; Cowan-Jacob, S. W.; Moebitz, H., Ten things you should know about protein kinases: IUPHAR Review 14. *Br J Pharmacol* **2015,** *172* (11), 2675-700.
6. Burnett, G.; Kennedy, E. P., The enzymatic phosphorylation of proteins. *J Biol Chem* **1954,** *211* (2), 969-80.
7. Cohen, P., The origins of protein phosphorylation. *Nat Cell Biol* **2002,** *4* (5), E127-30.
8. Krebs, E. G.; Graves, D. J.; Fischer, E. H., Factors Affecting the Activity of Muscle Phosphorylase B Kinase. *Journal of Biological Chemistry* **1959,** *234* (11), 2867-2873.
9. Robinson, D. R.; Wu, Y. M.; Lin, S. F., The protein tyrosine kinase family of the human genome. *Oncogene* **2000,** *19* (49), 5548-57.
10. Gschwind, A.; Fischer, O. M.; Ullrich, A., The discovery of receptor tyrosine kinases: targets for cancer therapy. *Nat Rev Cancer* **2004,** *4* (5), 361-70.
11. Lemmon, M. A.; Schlessinger, J., Cell signaling by receptor tyrosine kinases. *Cell* **2010,** *141* (7), 1117-34.
12. Segaliny, A. I.; Tellez-Gabriel, M.; Heymann, M. F.; Heymann, D., Receptor tyrosine kinases: Characterisation, mechanism of action and therapeutic interests for bone cancers. *J Bone Oncol* **2015,** *4* (1), 1-12.
13. Du, Z.; Lovly, C. M., Mechanisms of receptor tyrosine kinase activation in cancer. *Mol Cancer* **2018,** *17* (1), 58.
14. Hubbard, S. R.; Till, J. H., Protein tyrosine kinase structure and function. *Annu Rev Biochem* **2000,** *69*, 373-98.
15. Knighton, D. R.; Zheng, J. H.; Ten Eyck, L. F.; Ashford, V. A.; Xuong, N. H.; Taylor, S. S.; Sowadski, J. M., Crystal structure of the catalytic subunit of cyclic adenosine monophosphate-dependent protein kinase. *Science* **1991,** *253* (5018), 407-14.
16. Knighton, D. R.; Zheng, J. H.; Ten Eyck, L. F.; Xuong, N. H.; Taylor, S. S.; Sowadski, J. M., Structure of a peptide inhibitor bound to the catalytic subunit of cyclic adenosine monophosphate-dependent protein kinase. *Science* **1991,** *253* (5018), 414-20.

17. Johnson, L. N.; Noble, M. E.; Owen, D. J., Active and inactive protein kinases: structural basis for regulation. *Cell* **1996,** *85* (2), 149-58.

18. Huse, M.; Kuriyan, J., The conformational plasticity of protein kinases. *Cell* **2002,** *109* (3), 275-82.

19. Hubbard, S. R.; Wei, L.; Ellis, L.; Hendrickson, W. A., Crystal structure of the tyrosine kinase domain of the human insulin receptor. *Nature* **1994,** *372* (6508), 746-54.

20. Hubbard, S. R., Crystal structure of the activated insulin receptor tyrosine kinase in complex with peptide substrate and ATP analog. *EMBO J* **1997,** *16* (18), 5572-81.

21. Russo, A. A.; Jeffrey, P. D.; Patten, A. K.; Massague, J.; Pavletich, N. P., Crystal structure of the p27(Kip1) cyclin-dependent-kinase inhibitor bound to the cyclin A Cdk2 complex. *Nature* **1996,** *382* (6589), 325-331.

22. Yamaguchi, H.; Hendrickson, W. A., Structural basis for activation of human lymphocyte kinase Lck upon tyrosine phosphorylation. *Nature* **1996,** *384* (6608), 484-489.

23. Canagarajah, B. J.; Khokhlatchev, A.; Cobb, M. H.; Goldsmith, E. J., Activation mechanism of the MAP kinase ERK2 by dual phosphorylation. *Cell* **1997,** *90* (5), 859-69.

24. Sadowski, I.; Stone, J. C.; Pawson, T., A Noncatalytic Domain Conserved among Cytoplasmic Protein-Tyrosine Kinases Modifies the Kinase Function and Transforming Activity of Fujinami Sarcoma-Virus P130gag-Fps. *Molecular and Cellular Biology* **1986,** *6* (12), 4396-4408.

25. Mayer, B. J., The discovery of modular binding domains: building blocks of cell signalling. *Nat Rev Mol Cell Biol* **2015,** *16* (11), 691-8.

26. Lamontanara, A. J.; Georgeon, S.; Tria, G.; Svergun, D. I.; Hantschel, O., The SH2 domain of Abl kinases regulates kinase autophosphorylation by controlling activation loop accessibility. *Nat Commun* **2014,** *5*, 5470.

27. Liu, B. A.; Engelmann, B. W.; Nash, P. D., The language of SH2 domain interactions defines phosphotyrosine-mediated signal transduction. *FEBS Lett* **2012,** *586* (17), 2597-605.

28. Waksman, G.; Kumaran, S.; Lubman, O., SH2 domains: role, structure and implications for molecular medicine. *Expert Rev Mol Med* **2004,** *6* (3), 1-18.

29. Mayer, B. J., SH3 domains: complexity in moderation. *J Cell Sci* **2001,** *114* (Pt 7), 1253-63.

30. Kurochkina, N.; Guha, U., SH3 domains: modules of protein-protein interactions. *Biophys Rev* **2013,** *5* (1), 29-39.

31. Supertifurga, G.; Fumagalli, S.; Koegl, M.; Courtneidge, S. A.; Draetta, G., Csk Inhibition of C-Src Activity Requires Both the Sh2 and Sh3 Domains of Src. *Embo Journal* **1993,** *12* (7), 2625-2634.

32. Xu, W.; Harrison, S. C.; Eck, M. J., Three-dimensional structure of the tyrosine kinase c-Src. *Nature* **1997,** *385* (6617), 595-602.

33. Nagar, B.; Hantschel, O.; Young, M. A.; Scheffzek, K.; Veach, D.; Bornmann, W.; Clarkson, B.; Superti-Furga, G.; Kuriyan, J., Structural basis for the autoinhibition of c-Abl tyrosine kinase. *Cell* **2003,** *112* (6), 859-71.

34. Hantschel, O.; Wiesner, S.; Guttler, T.; Mackereth, C. D.; Rix, L. L.; Mikes, Z.; Dehne, J.; Gorlich, D.; Sattler, M.; Superti-Furga, G., Structural basis for the cytoskeletal association of Bcr-Abl/c-Abl. *Mol Cell* **2005,** *19* (4), 461-73.

35. Colicelli, J., ABL tyrosine kinases: evolution of function, regulation, and specificity. *Sci Signal* **2010,** *3* (139), re6.

36. Van Etten, R. A., Cycling, stressed-out and nervous: cellular functions of c-Abl. *Trends Cell Biol* **1999,** *9* (5), 179-86.

37. Bradley, W. D.; Koleske, A. J., Regulation of cell migration and morphogenesis by Abl-family kinases: emerging mechanisms and physiological contexts. *J Cell Sci* **2009,** *122* (Pt 19), 3441-54.

38. Greuber, E. K.; Smith-Pearson, P.; Wang, J.; Pendergast, A. M., Role of ABL family kinases in cancer: from leukaemia to solid tumours. *Nat Rev Cancer* **2013,** *13* (8), 559-71.

39. Tybulewicz, V. L.; Crawford, C. E.; Jackson, P. K.; Bronson, R. T.; Mulligan, R. C., Neonatal lethality and lymphopenia in mice with a homozygous disruption of the c-abl proto-oncogene. *Cell* **1991,** *65* (7), 1153-63.

40. Schwartzberg, P. L.; Stall, A. M.; Hardin, J. D.; Bowdish, K. S.; Humaran, T.; Boast, S.; Harbison, M. L.; Robertson, E. J.; Goff, S. P., Mice Homozygous for the Ablm1 Mutation Show Poor Viability and Depletion of Selected B-Cell and T-Cell Populations. *Cell* **1991,** *65* (7), 1165-1175.

41. Li, B. J.; Boast, S.; de los Santos, K.; Schieren, I.; Quiroz, M.; Teitelbaum, S. L.; Tondravi, M. M.; Goff, S. P., Mice deficient in Abl are osteoporotic and have defects in osteoblast maturation. *Nature Genetics* **2000,** *24* (3), 304-308.

42. Chen, S.; Wang, R.; Li, Q. F.; Tang, D. D., Abl knockout differentially affects p130 Crk-associated substrate, vinculin, and paxillin in blood vessels of mice. *Am J Physiol Heart Circ Physiol* **2009,** *297* (2), H533-9.

43. Qiu, Z.; Cang, Y.; Goff, S. P., c-Abl tyrosine kinase regulates cardiac growth and development. *Proc Natl Acad Sci U S A* **2010,** *107* (3), 1136-41.

44. Silberman, I.; Sionov, R. V.; Zuckerman, V.; Haupt, S.; Goldberg, Z.; Strasser, A.; Ben-Sasson, Z. S.; Baniyash, M.; Koleske, A. J.; Haupt, Y., T cell survival and function requires the c-Abl tyrosine kinase. *Cell Cycle* **2008,** *7* (24), 3847-57.

45. Brightbill, H.; Schlissel, M. S., The effects of c-Abl mutation on developing B cell differentiation and survival. *Int Immunol* **2009,** *21* (5), 575-85.

46. Liberatore, R. A.; Goff, S. P., c-Abl-deficient mice exhibit reduced numbers of peritoneal B-1 cells and defects in BCR-induced B cell activation. *Int Immunol* **2009,** *21* (4), 403-14.

47. Koleske, A. J.; Gifford, A. M.; Scott, M. L.; Nee, M.; Bronson, R. T.; Miczek, K. A.; Baltimore, D., Essential roles for the Abl and Arg tyrosine kinases in neurulation. *Neuron* **1998,** *21* (6), 1259-72.

48. Gourley, S. L.; Koleske, A. J.; Taylor, J. R., Loss of dendrite stabilization by the Abl-related gene (Arg) kinase regulates behavioral flexibility and sensitivity to cocaine. *Proc Natl Acad Sci U S A* **2009,** *106* (39), 16859-64.

49. De Braekeleer, E.; Douet-Guilbert, N.; Morel, F.; Le Bris, M. J.; Basinko, A.; De Braekeleer, M., ETV6 fusion genes in hematological malignancies: a review. *Leuk Res* **2012,** *36* (8), 945-61.

50. Hantschel, O., Structure, regulation, signaling, and targeting of abl kinases in cancer. *Genes Cancer* **2012,** *3* (5-6), 436-46.

51. Khatri, A.; Wang, J.; Pendergast, A. M., Multifunctional Abl kinases in health and disease. *J Cell Sci* **2016,** *129* (1), 9-16.

52. Schlatterer, S. D.; Acker, C. M.; Davies, P., c-Abl in neurodegenerative disease. *J Mol Neurosci* **2011,** *45* (3), 445-52.

53. Renshaw, M. W.; Capozza, M. A.; Wang, J. Y., Differential expression of type-specific c-abl mRNAs in mouse tissues and cell lines. *Mol Cell Biol* **1988,** *8* (10), 4547-51.

54. Van Etten, R. A.; Jackson, P. K.; Baltimore, D.; Sanders, M. C.; Matsudaira, P. T.; Janmey, P. A., The COOH terminus of the c-Abl tyrosine kinase contains distinct F- and G-actin binding domains with bundling activity. *J Cell Biol* **1994,** *124* (3), 325-40.

55. Taagepera, S.; McDonald, D.; Loeb, J. E.; Whitaker, L. L.; McElroy, A. K.; Wang, J. Y.; Hope, T. J., Nuclear-cytoplasmic shuttling of C-ABL tyrosine kinase. *Proc Natl Acad Sci U S A* **1998,** *95* (13), 7457-62.

56. Antoku, S.; Saksela, K.; Rivera, G. M.; Mayer, B. J., A crucial role in cell spreading for the interaction of Abl PxxP motifs with Crk and Nck adaptors. *J Cell Sci* **2008,** *121* (Pt 18), 3071-82.

57. Kipreos, E. T.; Wang, J. Y., Cell cycle-regulated binding of c-Abl tyrosine kinase to DNA. *Science* **1992,** *256* (5055), 382-5.

58. Dikstein, R.; Agami, R.; Heffetz, D.; Shaul, Y., p140/c-Abl that binds DNA is preferentially phosphorylated at tyrosine residues. *Proceedings of the National Academy of Sciences of the United States of America* **1996,** *93* (6), 2387-2391.

59. David-Cordonnier, M. H.; Hamdane, M.; Bailly, C.; D'Halluin, J. C., Determination of the human c-Abl consensus DNA binding site. *FEBS Lett* **1998,** *424* (3), 177-82.

60. David-Cordonnier, M. H.; Payet, D.; D'Halluin, J. C.; Waring, M. J.; Travers, A. A.; Bailly, C., The DNA-binding domain of human c-Abl

tyrosine kinase promotes the interaction of a HMG chromosomal protein with DNA. *Nucleic Acids Res* **1999,** *27* (11), 2265-70.

61. Wetzler, M.; Talpaz, M.; Van Etten, R. A.; Hirsh-Ginsberg, C.; Beran, M.; Kurzrock, R., Subcellular localization of Bcr, Abl, and Bcr-Abl proteins in normal and leukemic cells and correlation of expression with myeloid differentiation. *J Clin Invest* **1993,** *92* (4), 1925-39.

62. Shaul, Y.; Ben-Yehoyada, M., Role of c-Abl in the DNA damage stress response. *Cell Res* **2005,** *15* (1), 33-35.

63. Van Etten, R. A.; Jackson, P.; Baltimore, D., The Mouse Type IV c-abl Gene Product Is a Nuclear Protein, and Activation of transforming ability is associated with cytoplasmic localization. *Cell* **1989**, 669-678.

64. Wen, S. T.; Jackson, P. K.; VanEtten, R. A., The cytostatic function of c-Abl is controlled by multiple nuclear localization signals and requires the p53 and Rb tumor suppressor gene products. *Embo Journal* **1996,** *15* (7), 1583-1595.

65. Kharbanda, S.; Yuan, Z. M.; Weichselbaum, R.; Kufe, D., Functional role for the c-Abl protein tyrosine kinase in the cellular response to genotoxic stress. *Biochim Biophys Acta* **1997,** *1333* (2), O1-7.

66. Sawyers, C. L., Disabling Abl-perspectives on Abl kinase regulation and cancer therapeutics. *Cancer Cell* **2002,** *1* (1), 13-5.

67. Yuan, Z. M.; Utsugisawa, T.; Ishiko, T.; Nakada, S.; Huang, Y.; Kharbanda, S.; Weichselbaum, R.; Kufe, D., Activation of protein kinase C delta by the c-Abl tyrosine kinase in response to ionizing radiation. *Oncogene* **1998,** *16* (13), 1643-8.

68. Ren, R.; Mayer, B. J.; Cicchetti, P.; Baltimore, D., Identification of a ten-amino acid proline-rich SH3 binding site. *Science* **1993,** *259* (5098), 1157-61.

69. Sudol, M., From Src Homology domains to other signaling modules: proposal of the 'protein recognition code'. *Oncogene* **1998,** *17* (11), 1469-1474.

70. Kay, B. K.; Williamson, M. P.; Sudol, P., The importance of being proline: the interaction of proline-rich motifs in signaling proteins with their cognate domains. *Faseb J* **2000,** *14* (2), 231-241.

71. Tong, A. H.; Drees, B.; Nardelli, G.; Bader, G. D.; Brannetti, B.; Castagnoli, L.; Evangelista, M.; Ferracuti, S.; Nelson, B.; Paoluzi, S.; Quondam, M.; Zucconi, A.; Hogue, C. W.; Fields, S.; Boone, C.; Cesareni, G., A combined experimental and computational strategy to define protein interaction networks for peptide recognition modules. *Science* **2002,** *295* (5553), 321-4.

72. Shi, Y.; Alin, K.; Goff, S. P., Abl-interactor-1, a novel SH3 protein binding to the carboxy-terminal portion of the Abl protein, suppresses v-abl transforming activity. *Genes Dev* **1995,** *9* (21), 2583-97.

73. Dai, Z.; Pendergast, A. M., Abi-2, a novel SH3-containing protein interacts with the c-Abl tyrosine kinase and modulates c-Abl transforming activity. *Genes Dev* **1995,** *9* (21), 2569-82.

74. Cao, X.; Tanis, K. Q.; Koleske, A. J.; Colicelli, J., Enhancement of ABL kinase catalytic efficiency by a direct binding regulator is independent of other regulatory mechanisms. *J Biol Chem* **2008,** *283* (46), 31401-7.

75. Feller, S. M.; Knudsen, B.; Hanafusa, H., c-Abl kinase regulates the protein binding activity of c-Crk. *The EMBO Journal* **1994,** *13* (10), 2341-2361.

76. Ren, R. B.; Ye, Z. S.; Baltimore, D., Abl Protein-Tyrosine Kinase Selects the Crk Adapter as a Substrate Using Sh3-Binding Sites. *Gene Dev* **1994,** *8* (7), 783-795.

77. Sattler, M.; Salgia, R., Role of the adapter protein CRKL in signal transduction of normal hematopoietic and BCR/ABL-transformed cells. *Leukemia* **1998,** *12* (5), 637-44.

78. Smith, J. M.; Katz, S.; Mayer, B. J., Activation of the Abl tyrosine kinase in vivo by Src homology 3 domains from the Src homology 2/Src homology 3 adaptor Nck. *J Biol Chem* **1999,** *274* (39), 27956-62.

79. Feller, S. M., Crk family adaptors - signalling complex formation and biological roles. *Oncogene* **2001,** *20* (44), 6348-6371.

80. Jankowski, W.; Saleh, T.; Pai, M. T.; Sriram, G.; Birge, R. B.; Kalodimos, C. G., Domain organization differences explain Bcr-Abl's preference for CrkL over CrkII. *Nat Chem Biol* **2012,** *8* (6), 590-6.

81. Tani, K.; Sato, S.; Sukezane, T.; Kojima, H.; Hirose, H.; Hanafusa, H.; Shishido, T., Abl interactor 1 promotes tyrosine 296 phosphorylation of mammalian enabled (Mena) by c-Abl kinase. *J Biol Chem* **2003,** *278* (24), 21685-92.

82. Lin, T.-Y.; Huang, C.-H.; Chou, W.-G.; Juang, J.-L., Abi Enhances Abl-Mediated Cdc2 Phosphorylation and Inactivation. *Journal of Biomedical Science* **2004,** *11* (6), 902-910.

83. Leng, Y.; Zhang, J.; Badour, K.; Arpaia, E.; Freeman, S.; Cheung, P.; Siu, M.; Siminovitch, K., Abelson-interactor-1 promotes WAVE2 membrane translocation and Abelson-mediated tyrosine phosphorylation required for WAVE2 activation. *Proc Natl Acad Sci U S A* **2005,** *102* (4), 1098-103.

84. Xiong, X.; Cui, P.; Hossain, S.; Xu, R.; Warner, B.; Guo, X.; An, X.; Debnath, A. K.; Cowburn, D.; Kotula, L., Allosteric inhibition of the nonMyristoylated c-Abl tyrosine kinase by phosphopeptides derived from Abi1/Hssh3bp1. *Biochim Biophys Acta* **2008,** *1783* (5), 737-47.

85. Kim, N.; Kim, S.; Nahm, M.; Kopke, D.; Kim, J.; Cho, E.; Lee, M. J.; Lee, M.; Kim, S. H.; Broadie, K.; Lee, S., BMP-dependent synaptic development requires Abi-Abl-Rac signaling of BMP receptor macropinocytosis. *Nat Commun* **2019,** *10* (1), 684.

86. Chorzalska, A.; Salloum, I.; Shafqat, H.; Khan, S.; Marjon, P.; Treaba, D.; Schorl, C.; Morgan, J.; Bryke, C. R.; Falanga, V.; Zhao, T. C.; Reagan, J.; Winer, E.; Olszewski, A. J.; Al-Homsi, A. S.; Kouttab, N.; Dubielecka, P. M., Low expression of Abelson interactor-1 is linked to acquired drug resistance in Bcr-Abl-induced leukemia. *Leukemia* **2014,** *28* (11), 2165-77.

87. Hu, H.; Bliss, J. M.; Wang, Y.; Colicelli, J., RIN1 is an ABL tyrosine kinase activator and a regulator of epithelial-cell adhesion and migration. *Curr Biol* **2005,** *15* (9), 815-23.

88. Ting, P. Y.; Damoiseaux, R.; Titz, B.; Bradley, K. A.; Graeber, T. G.; Fernandez-Vega, V.; Bannister, T. D.; Chase, P.; Nair, R.; Scampavia, L.; Hodder, P.; Spicer, T. P.; Colicelli, J., Identification of small molecules that disrupt signaling between ABL and its positive regulator RIN1. *PLoS One* **2015,** *10* (3), e0121833.

89. Liu, X.; Li, Y.; Wen, L.; Tao, K.; Xiao, Q.; Cao, W.; Huang, Z.; Gao, M.; Li, H.; Wang, F.; Feng, W., ABL SH3 mutant inhibits BCR-ABL activity and increases imatinib sensitivity by targeting RIN1 protein in CML cell. *Cancer Lett* **2015,** *369* (1), 222-8.

90. Pawson, T.; Scott, J. D., Signaling through scaffold, anchoring, and adaptor proteins. *Science* **1997,** *278* (5346), 2075-2080.

91. Flynn, D. C., Adaptor proteins. *Oncogene* **2001,** *20* (44), 6270-2.

92. Luo, L. Y.; Hahn, W. C., Oncogenic Signaling Adaptor Proteins. *J Genet Genomics* **2015,** *42* (10), 521-529.

93. Gotoh, N., Regulation of growth factor signaling by FRS2 family docking/scaffold adaptor proteins. *Cancer Sci* **2008,** *99* (7), 1319-25.

94. ten Hoeve, J.; Morris, C.; Heisterkamp, N.; Groffen, J., Isolation and chromosomal localization of CRKL, a human crk-like gene. *Oncogene* **1993,** *8* (9), 2469-2474.

95. Nichols, G. L.; Raines, M. A.; Vera, J. C.; Lacomis, L.; Tempst, P.; Golde, D. W., Identification of Crkl as the Constitutively Phosphorylated 39-Kd Tyrosine Phosphoprotein in Chronic Myelogenous Leukemia-Cells. *Blood* **1994,** *84* (9), 2912-2918.

96. ten Hoeve, J.; Arlinghaus, R. B.; Guo, J. Q.; Heisterkamp, N.; Groffen, J., Tyrosine phosphorylation of CRKL in Philadelphia+ leukemia. *Blood* **1994,** *84* (6), 1731-6.

97. Senechal, K.; Halpern, J.; Sawyers, C. L., The CRKL adaptor protein transforms fibroblasts and functions in transformation by the BCR-ABL oncogene. *J Biol Chem* **1996,** *271* (38), 23255-61.

98. Luo, B.; Cheung, H. W.; Subramanian, A.; Sharifnia, T.; Okamoto, M.; Yang, X.; Hinkle, G.; Boehm, J. S.; Beroukhim, R.; Weir, B. A.; Mermel, C.; Barbie, D. A.; Awad, T.; Zhou, X.; Nguyen, T.; Piqani, B.; Li, C.; Golub, T. R.; Meyerson, M.; Hacohen, N.; Hahn, W. C.; Lander, E. S.; Sabatini, D. M.; Root, D. E., Highly parallel identification of essential genes in cancer cells. *Proc Natl Acad Sci U S A* **2008,** *105* (51), 20380-5.

99. Seo, J. H.; Wood, L. J.; Agarwal, A.; O'Hare, T.; Elsea, C. R.; Griswold, I. J.; Deininger, M. W.; Imamoto, A.; Druker, B. J., A specific need for CRKL in p210BCR-ABL-induced transformation of mouse hematopoietic progenitors. *Cancer Res* **2010,** *70* (18), 7325-35.

100. Lucas, C. M.; Harris, R. J.; Giannoudis, A.; Knight, K.; Watmough, S. J.; Clark, R. E., BCR-ABL1 tyrosine kinase activity at diagnosis, as determined via the pCrkL/CrkL ratio, is predictive of clinical outcome in chronic myeloid leukaemia. *Brit J Haematol* **2010,** *149* (3), 458-460.

101. Eide, C. A.; Zabriskie, M. S.; Savage Stevens, S. L.; Antelope, O.; Vellore, N. A.; Than, H.; Schultz, A. R.; Clair, P.; Bowler, A. D.; Pomicter, A. D.; Yan, D.; Senina, A. V.; Qiang, W.; Kelley, T. W.; Szankasi, P.; Heinrich, M. C.; Tyner, J. W.; Rea, D.; Cayuela, J. M.; Kim, D. W.; Tognon, C. E.; O'Hare, T.; Druker, B. J.; Deininger, M. W., Combining the Allosteric Inhibitor Asciminib with Ponatinib Suppresses Emergence of and Restores Efficacy against Highly Resistant BCR-ABL1 Mutants. *Cancer Cell* **2019,** *36* (4), 431-443 e5.

102. Wylie, A. A.; Schoepfer, J.; Jahnke, W.; Cowan-Jacob, S. W.; Loo, A.; Furet, P.; Marzinzik, A. L.; Pelle, X.; Donovan, J.; Zhu, W.; Buonamici, S.; Hassan, A. Q.; Lombardo, F.; Iyer, V.; Palmer, M.; Berellini, G.; Dodd, S.; Thohan, S.; Bitter, H.; Branford, S.; Ross, D. M.; Hughes, T. P.; Petruzzelli, L.; Vanasse, K. G.; Warmuth, M.; Hofmann, F.; Keen, N. J.; Sellers, W. R., The allosteric inhibitor ABL001 enables dual targeting of BCR-ABL1. *Nature* **2017,** *543* (7647), 733-737.

103. Mcwhirter, J. R.; Wang, J. Y. J., Activation of Tyrosine Kinase and Microfilament-Binding Functions of C-Abl by Bcr Sequences in Bcr/Abl Fusion Proteins. *Molecular and Cellular Biology* **1991,** *11* (3), 1553-1565.

104. Plattner, R.; Kadlec, L.; DeMali, K. A.; Kazlauskas, A.; Pendergast, A. M., c-Abl is activated by growth factors and Src family kinases and has a role in the cellular response to PDGF. *Gene Dev* **1999,** *13* (18), 2400-2411.

105. Zukerberg, L. R.; Patrick, G. N.; Nikolic, M.; Humbert, S.; Wu, C. L.; Lanier, L. M.; Gertler, F. B.; Vidal, M.; Van Etten, R. A.; Tsai, L. H., Cables links Cdk5 and c-Abl and facilitates Cdk5 tyrosine phosphorylation, kinase upregulation, and neurite outgrowth. *Neuron* **2000,** *26* (3), 633-46.

106. Kain, K. H.; Klemke, R. L., Inhibition of cell migration by Abl family tyrosine kinases through uncoupling of Crk-CAS complexes. *J Biol Chem* **2001,** *276* (19), 16185-92.

107. Woodring, P. J.; Hunter, T.; Wang, J. Y., Regulation of F-actin-dependent processes by the Abl family of tyrosine kinases. *J Cell Sci* **2003,** *116* (Pt 13), 2613-26.

108. Woodring, P. J.; Hunter, T.; Wang, J. Y., Inhibition of c-Abl tyrosine kinase activity by filamentous actin. *J Biol Chem* **2001,** *276* (29), 27104-10.

109. Wang, Y.; Miller, A. L.; Mooseker, M. S.; Koleske, A. J., The Abl-related gene (Arg) nonreceptor tyrosine kinase uses two F-actin-binding domains to bundle F-actin. *Proc Natl Acad Sci U S A* **2001,** *98* (26), 14865-70.

110. Hernandez, S. E.; Krishnaswami, M.; Miller, A. L.; Koleske, A. J., How do Abl family kinases regulate cell shape and movement? *Trends Cell Biol* **2004,** *14* (1), 36-44.

111. Miller, A. L.; Wang, Y.; Mooseker, M. S.; Koleske, A. J., The Abl-related gene (Arg) requires its F-actin-microtubule cross-linking activity to regulate lamellipodial dynamics during fibroblast adhesion. *J Cell Biol* **2004,** *165* (3), 407-19.

112. Nowell, P. C.; Hungerford, D. A., Chromosome studies on normal and leukemic human leukocytes. *J Natl Cancer Inst* **1960,** *25*, 85-109.

113. Nowell, P. C., Discovery of the Philadelphia chromosome: a personal perspective. *J Clin Invest* **2007,** *117* (8), 2033-5.

114. Rowley, J. D., Letter: A new consistent chromosomal abnormality in chronic myelogenous leukaemia identified by quinacrine fluorescence and Giemsa staining. *Nature* **1973,** *243* (5405), 290-3.

115. Gale, R. P.; Canaani, E., An 8-kilobase abl RNA transcript in chronic myelogenous leukemia. *Proc Natl Acad Sci U S A* **1984,** *81* (18), 5648-52.

116. Shtivelman, E.; Lifshitz, B.; Gale, R. P.; Canaani, E., Fused transcript of abl and bcr genes in chronic myelogenous leukaemia. *Nature* **1985,** *315* (6020), 550-4.

117. Deininger, M. W.; Goldman, J. M.; Melo, J. V., The molecular biology of chronic myeloid leukemia. *Blood* **2000,** *96* (10), 3343-56.

118. Rowley, J. D., Chromosomal translocations: revisited yet again. *Blood* **2008,** *112* (6), 2183-9.

119. Wang, J.; Pendergast, A. M., The Emerging Role of ABL Kinases in Solid Tumors. *Trends Cancer* **2015,** *1* (2), 110-123.

120. Tripathi, R.; Liu, Z.; Plattner, R., EnABLing Tumor Growth and Progression: Recent progress in unraveling the functions of ABL kinases in solid tumor cells. *Curr Pharmacol Rep* **2018,** *4* (5), 367-379.

121. Eide, C. A.; O'Hare, T., Chronic myeloid leukemia: advances in understanding disease biology and mechanisms of resistance to tyrosine kinase inhibitors. *Curr Hematol Malig Rep* **2015,** *10* (2), 158-66.

122. Faderl, S.; Talpaz, M.; Estrov, Z.; O'Brien, S.; Kurzrock, R.; Kantarjian, H. M., The biology of chronic myeloid leukemia. *N Engl J Med* **1999,** *341* (3), 164-72.

123. Wong, S.; Witte, O. N., The BCR-ABL story: bench to bedside and back. *Annu Rev Immunol* **2004,** *22*, 247-306.

124. Mcwhirter, J. R.; Galasso, D. L.; Wang, J. Y. J., A Coiled-Coil Oligomerization Domain of Bcr Is Essential for the Transforming Function of Bcr-Abl Oncoproteins. *Molecular and Cellular Biology* **1993,** *13* (12), 7587-7595.

125. Zhao, X.; Ghaffari, S.; Lodish, H.; Malashkevich, V. N.; Kim, P. S., Structure of the Bcr-Abl oncoprotein oligomerization domain. *Nat Struct Biol* **2002,** *9* (2), 117-20.

126. Taylor, C. M.; Keating, A. E., Orientation and oligomerization specificity of the Bcr coiled-coil oligomerization domain. *Biochemistry* **2005,** *44* (49), 16246-56.

127. Beissert, T.; Hundertmark, A.; Kaburova, V.; Travaglini, L.; Mian, A. A.; Nervi, C.; Ruthardt, M., Targeting of the N-terminal coiled coil oligomerization interface by a helix-2 peptide inhibits unmutated and imatinib-resistant BCR/ABL. *Int J Cancer* **2008,** *122* (12), 2744-52.

128. Mian, A. A.; Oancea, C.; Zhao, Z.; Ottmann, O. G.; Ruthardt, M., Oligomerization inhibition, combined with allosteric inhibition, abrogates the transformation potential of T315I-positive BCR/ABL. *Leukemia* **2009,** *23* (12), 2242-7.

129. Woessner, D. W.; Eiring, A. M.; Bruno, B. J.; Zabriskie, M. S.; Reynolds, K. R.; Miller, G. D.; O'Hare, T.; Deininger, M. W.; Lim, C. S., A coiled-coil mimetic intercepts BCR-ABL1 dimerization in native and kinase-mutant chronic myeloid leukemia. *Leukemia* **2015,** *29* (8), 1668-75.

130. Bruno, B. J.; Lim, C. S., Inhibition of bcr-abl in human leukemic cells with a coiled-coil protein delivered by a leukemia-specific cell-penetrating Peptide. *Mol Pharm* **2015,** *12* (5), 1412-21.

131. Cornillie, S. P.; Bruno, B. J.; Lim, C. S.; Cheatham, T. E., 3rd, Computational Modeling of Stapled Peptides toward a Treatment Strategy for CML and Broader Implications in the Design of Lengthy Peptide Therapeutics. *J Phys Chem B* **2018,** *122* (14), 3864-3875.

132. Reckel, S.; Gehin, C.; Tardivon, D.; Georgeon, S.; Kukenshoner, T.; Lohr, F.; Koide, A.; Buchner, L.; Panjkovich, A.; Reynaud, A.; Pinho, S.; Gerig, B.; Svergun, D.; Pojer, F.; Guntert, P.; Dotsch, V.; Koide, S.; Gavin, A. C.; Hantschel, O., Structural and functional dissection of the DH and PH domains of oncogenic Bcr-Abl tyrosine kinase. *Nat Commun* **2017,** *8* (1), 2101.

133. Rossman, K. L.; Der, C. J.; Sondek, J., GEF means go: turning on RHO GTPases with guanine nucleotide-exchange factors. *Nat Rev Mol Cell Biol* **2005,** *6* (2), 167-80.

134. Lemmon, M. A., Membrane recognition by phospholipid-binding domains. *Nat Rev Mol Cell Biol* **2008,** *9* (2), 99-111.

135. Snyder, J. T.; Worthylake, D. K.; Rossman, K. L.; Betts, L.; Pruitt, W. M.; Siderovski, D. P.; Der, C. J.; Sondek, J., Structural basis for the selective activation of Rho GTPases by Dbl exchange factors. *Nat Struct Biol* **2002,** *9* (6), 468-75.

136. Pendergast, A. M.; Quilliam, L. A.; Cripe, L. D.; Bassing, C. H.; Dai, Z. H.; Li, N. X.; Batzer, A.; Rabun, K. M.; Der, C. J.; Schlessinger, J.; Gishizky, M. L., Bcr-Abl-Induced Oncogenesis Is Mediated by Direct Interaction with the Sh2 Domain of the Grb-2 Adapter Protein. *Cell* **1993,** *75* (1), 175-185.

137. Million, R. P.; Van Etten, R. A., The Grb2 binding site is required for the induction of chronic myeloid leukemia-like disease in mice by the Bcr/Abl tyrosine kinase. *Blood* **2000,** *96* (2), 664-670.

138. Green, M. R.; Newton, M. D.; Fancher, K. M., Off-Target Effects of BCR-ABL and JAK2 Inhibitors. *American Journal of Clinical Oncology* **2016,** *39* (1), 76-84.

139. Chaar, M.; Kamta, J.; Ait-Oudhia, S., Mechanisms, monitoring, and management of tyrosine kinase inhibitors-associated cardiovascular toxicities. *Onco Targets Ther* **2018,** *11*, 6227-6237.

140. Ferguson, F. M.; Gray, N. S., Kinase inhibitors: the road ahead. *Nat Rev Drug Discov* **2018,** *17* (5), 353-377.

141. Bond, D. A.; Woyach, J. A., Targeting BTK in CLL: Beyond Ibrutinib. *Curr Hematol Malig Rep* **2019,** *14* (3), 197-205.

142. Silver, R. T.; Woolf, S. H.; Hehlmann, R.; Appelbaum, F. R.; Anderson, J.; Bennett, C.; Goldman, J. M.; Guilhot, F.; Kantarjian, H. M.; Lichtin, A. E.; Talpaz, M.; Tura, S., An evidence-based analysis of the effect of busulfan, hydroxyurea, interferon, and allogeneic bone marrow transplantation in treating the chronic phase of chronic myeloid leukemia: developed for the American Society of Hematology. *Blood* **1999,** *94* (5), 1517-36.

143. Doney, K.; Buckner, C. D.; Sale, G. E.; Ramberg, R.; Boyd, C.; Thomas, E. D., Treatment of chronic granulocytic leukemia by chemotherapy, total body irradiation and allogeneic bone marrow transplantation. *Experimental hematology* **1978,** *6* (9), 738-747.

144. McGlave, P. B.; Miller, W. J.; Hurd, D. D.; Arthur, D. C.; Kim, T., Cytogenetic conversion following allogeneic bone marrow transplantation for advanced chronic myelogenous leukemia. *Blood* **1981,** *58* (5), 1050-2.

145. Talpaz, M.; Kantarjian, H. M.; McCredie, K.; Trujillo, J. M.; Keating, M. J.; Gutterman, J. U., Hematologic remission and cytogenetic improvement induced by recombinant human interferon alpha A in chronic myelogenous leukemia. *N Engl J Med* **1986,** *314* (17), 1065-9.

146. Druker, B. J.; Tamura, S.; Buchdunger, E.; Ohno, S.; Segal, G. M.; Fanning, S.; Zimmermann, J.; Lydon, N. B., Effects of a selective inhibitor of the Abl tyrosine kinase on the growth of Bcr-Abl positive cells. *Nat Med* **1996,** *2* (5), 561-6.

147. Homewood, J.; Watson, M.; Richards, S. M.; Halsey, J.; Shepherd, P. C. A.; Adult Leukaemia Working, P., Treatment of CML using IFN-alpha: impact on quality of life. *Hematol J* **2003,** *4* (4), 253-262.

148. Buchdunger, E.; Zimmermann, J.; Mett, H.; Meyer, T.; Muller, M.; Druker, B. J.; Lydon, N. B., Inhibition of the Abl protein-tyrosine kinase in vitro and in vivo by a 2-phenylaminopyrimidine derivative. *Cancer Res* **1996,** *56* (1), 100-4.

149. Capdeville, R.; Buchdunger, E.; Zimmermann, J.; Matter, A., Glivec (STI571, imatinib), a rationally developed, targeted anticancer drug. *Nat Rev Drug Discov* **2002,** *1* (7), 493-502.

150. Hantschel, O.; Grebien, F.; Superti-Furga, G., The growing arsenal of ATP-competitive and allosteric inhibitors of BCR-ABL. *Cancer Res* **2012,** *72* (19), 4890-5.

151. Hughes, T. P.; Mauro, M. J.; Cortes, J. E.; Minami, H.; Rea, D.; DeAngelo, D. J.; Breccia, M.; Goh, Y. T.; Talpaz, M.; Hochhaus, A.; le Coutre, P.; Ottmann, O.; Heinrich, M. C.; Steegmann, J. L.; Deininger, M. W. N.; Janssen, J.; Mahon, F. X.; Minami, Y.; Yeung, D.; Ross, D. M.; Tallman, M. S.; Park, J. H.; Druker, B. J.; Hynds, D.; Duan, Y.; Meille, C.; Hourcade-Potelleret, F.; Vanasse, K. G.; Lang, F.; Kim, D. W., Asciminib in Chronic Myeloid Leukemia after ABL Kinase Inhibitor Failure. *N Engl J Med* **2019,** *381* (24), 2315-2326.

152. Mahon, F. X.; Deininger, M. W. N.; Schultheis, B.; Chabrol, J.; Reiffers, J.; Goldman, J. M.; Melo, J. V., Selection and characterization of BCR-ABL positive cell lines with differential sensitivity to the tyrosine kinase inhibitor STI571: diverse mechanisms of resistance. *Blood* **2000,** *96* (3), 1070-1079.

153. Gorre, M. E.; Mohammed, M.; Ellwood, K.; Hsu, N.; Paquette, R.; Rao, P. N.; Sawyers, C. L., Clinical resistance to STI-571 cancer therapy caused by BCR-ABL gene mutation or amplification. *Science* **2001,** *293* (5531), 876-80.

154. Illmer, T.; Schaich, M.; Platzbecker, U.; Freiberg-Richter, J.; Oelschlagel, U.; von Bonin, M.; Pursche, S.; Bergemann, T.; Ehninger, G.; Schleyer, E., P-glycoprotein-mediated drug efflux is a resistance mechanism of chronic myelogenous leukemia cells to treatment with imatinib mesylate. *Leukemia* **2004,** *18* (3), 401-8.

155. Gadzicki, D.; von Neuhoff, N.; Steinemann, D.; Just, M.; Busche, G.; Kreipe, H.; Wilkens, L.; Schlegelberger, B., BCR-ABL gene amplification and overexpression in a patient with chronic myeloid leukemia treated with imatinib. *Cancer Genet Cytogenet* **2005,** *159* (2), 164-7.

156. Khorashad, J. S.; Anand, M.; Marin, D.; Saunders, S.; Al-Jabary, T.; Iqbal, A.; Margerison, S.; Melo, J. V.; Goldman, J. M.; Apperley, J. F.; Kaeda, J., The presence of a BCR-ABL mutant allele in CML does not always explain clinical resistance to imatinib. *Leukemia* **2006,** *20* (4), 658-63.

157. O'Hare, T.; Zabriskie, M. S.; Eiring, A. M.; Deininger, M. W., Pushing the limits of targeted therapy in chronic myeloid leukaemia. *Nat Rev Cancer* **2012,** *12* (8), 513-26.

158. O'Hare, T.; Eide, C. A.; Deininger, M. W., Bcr-Abl kinase domain mutations, drug resistance, and the road to a cure for chronic myeloid leukemia. *Blood* **2007,** *110* (7), 2242-9.

159. Azam, M.; Latek, R. R.; Daley, G. Q., Mechanisms of autoinhibition and STI-571/imatinib resistance revealed by mutagenesis of BCR-ABL. *Cell* **2003,** *112* (6), 831-43.

160. Sherbenou, D. W.; Hantschel, O.; Kaupe, I.; Willis, S.; Bumm, T.; Turaga, L. P.; Lange, T.; Dao, K. H.; Press, R. D.; Druker, B. J.; Superti-Furga, G.; Deininger, M. W., BCR-ABL SH3-SH2 domain mutations in chronic myeloid leukemia patients on imatinib. *Blood* **2010,** *116* (17), 3278-85.

161. Rossari, F.; Minutolo, F.; Orciuolo, E., Past, present, and future of Bcr-Abl inhibitors: from chemical development to clinical efficacy. *J Hematol Oncol* **2018,** *11* (1), 84.

162. Latifi, Y.; Moccetti, F.; Wu, M.; Xie, A.; Packwood, W.; Qi, Y.; Ozawa, K.; Shentu, W. H.; Brown, E.; Shirai, T.; McCarty, O. J.; Ruggeri, Z.; Moslehi, J.; Chen, J. M.; Druker, B. J.; Lopez, J. A.; Lindner, J. R., Thrombotic microangiopathy as a cause of cardiovascular toxicity from the BCR-ABL1 tyrosine kinase inhibitor ponatinib. *Blood* **2019,** *133* (14), 1597-1606.

163. Schoepfer, J.; Jahnke, W.; Berellini, G.; Buonamici, S.; Cotesta, S.; Cowan-Jacob, S. W.; Dodd, S.; Drueckes, P.; Fabbro, D.; Gabriel, T.; Groell, J. M.; Grotzfeld, R. M.; Hassan, A. Q.; Henry, C.; Iyer, V.; Jones, D.; Lombardo, F.; Loo, A.; Manley, P. W.; Pelle, X.; Rummel, G.; Salem, B.; Warmuth, M.; Wylie, A. A.; Zoller, T.; Marzinzik, A. L.; Furet, P., Discovery of Asciminib (ABL001), an Allosteric Inhibitor of the Tyrosine Kinase Activity of BCR-ABL1. *J Med Chem* **2018,** *61* (18), 8120-8135.

164. Adrian, F. J.; Ding, Q.; Sim, T.; Velentza, A.; Sloan, C.; Liu, Y.; Zhang, G.; Hur, W.; Ding, S.; Manley, P.; Mestan, J.; Fabbro, D.; Gray, N. S., Allosteric inhibitors of Bcr-abl-dependent cell proliferation. *Nat Chem Biol* **2006,** *2* (2), 95-102.

165. Zhan, J. Y.; Ma, J.; Zheng, Q. C., Molecular dynamics investigation on the Asciminib resistance mechanism of I502L and V468F mutations in BCR-ABL. *J Mol Graph Model* **2019,** *89*, 242-249.

166. Vajpai, N.; Strauss, A.; Fendrich, G.; Cowan-Jacob, S. W.; Manley, P. W.; Grzesiek, S.; Jahnke, W., Solution conformations and dynamics of ABL kinase-inhibitor complexes determined by NMR substantiate the different binding modes of imatinib/nilotinib and dasatinib. *J Biol Chem* **2008,** *283* (26), 18292-302.

167. Cowan-Jacob, S. W.; Fendrich, G.; Floersheimer, A.; Furet, P.; Liebetanz, J.; Rummel, G.; Rheinberger, P.; Centeleghe, M.; Fabbro, D.; Manley, P. W., Structural biology contributions to the discovery of drugs to treat chronic myelogenous leukaemia. *Acta Crystallogr D Biol Crystallogr* **2007,** *63* (Pt 1), 80-93.

168. Tokarski, J. S.; Newitt, J. A.; Chang, C. Y.; Cheng, J. D.; Wittekind, M.; Kiefer, S. E.; Kish, K.; Lee, F. Y.; Borzillerri, R.; Lombardo, L. J.; Xie, D.; Zhang, Y.; Klei, H. E., The structure of Dasatinib (BMS-354825) bound to activated ABL kinase domain elucidates its inhibitory activity against imatinib-resistant ABL mutants. *Cancer Res* **2006,** *66* (11), 5790-7.

169. Schindler, T.; Bornmann, W.; Pellicena, P.; Miller, W. T.; Clarkson, B.; Kuriyan, J., Structural mechanism for STI-571 inhibition of abelson tyrosine kinase. *Science* **2000,** *289* (5486), 1938-42.

170. Nagar, B.; Bornmann, W. G.; Pellicena, P.; Schindler, T.; Veach, D. R.; Miller, W. T.; Clarkson, B.; Kuriyan, J., Crystal structures of the kinase domain of c-Abl in complex with the small molecule inhibitors PD173955 and imatinib (STI-571). *Cancer Res* **2002,** *62* (15), 4236-43.

171. Jahnke, W.; Grotzfeld, R. M.; Pelle, X.; Strauss, A.; Fendrich, G.; Cowan-Jacob, S. W.; Cotesta, S.; Fabbro, D.; Furet, P.; Mestan, J.; Marzinzik, A. L., Binding or bending: distinction of allosteric Abl kinase agonists from antagonists by an NMR-based conformational assay. *J Am Chem Soc* **2010,** *132* (20), 7043-8.

172. Skora, L.; Mestan, J.; Fabbro, D.; Jahnke, W.; Grzesiek, S., NMR reveals the allosteric opening and closing of Abelson tyrosine kinase by ATP-site and myristoyl pocket inhibitors. *Proc Natl Acad Sci U S A* **2013,** *110* (47), E4437-45.

173. Nagar, B.; Hantschel, O.; Seeliger, M.; Davies, J. M.; Weis, W. I.; Superti-Furga, G.; Kuriyan, J., Organization of the SH3-SH2 unit in active and inactive forms of the c-Abl tyrosine kinase. *Mol Cell* **2006,** *21* (6), 787-98.

174. Sonti, R.; Hertel-Hering, I.; Lamontanara, A. J.; Hantschel, O.; Grzesiek, S., ATP Site Ligands Determine the Assembly State of the Abelson Kinase Regulatory Core via the Activation Loop Conformation. *J Am Chem Soc* **2018,** *140* (5), 1863-1869.

175. Pluk, H.; Dorey, K.; Superti-Furga, G., Autoinhibition of c-Abl. *Cell* **2002,** *108* (2), 247-59.

176. Hantschel, O.; Nagar, B.; Guettler, S.; Kretzschmar, J.; Dorey, K.; Kuriyan, J.; Superti-Furga, G., A myristoyl/phosphotyrosine switch regulates c-Abl. *Cell* **2003,** *112* (6), 845-57.

177. Schindler, T.; Sicheri, F.; Pico, A.; Gazit, A.; Levitzki, A.; Kuriyan, J., Crystal structure of Hck in complex with a Src family-selective tyrosine kinase inhibitor. *Mol Cell* **1999,** *3* (5), 639-48.

178. Brasher, B. B.; Van Etten, R. A., c-Abl has high intrinsic tyrosine kinase activity that is stimulated by mutation of the Src homology 3 domain and by autophosphorylation at two distinct regulatory tyrosines. *J Biol Chem* **2000,** *275* (45), 35631-7.

179. Lorenz, S.; Deng, P.; Hantschel, O.; Superti-Furga, G.; Kuriyan, J., Crystal structure of an SH2-kinase construct of c-Abl and effect of the SH2 domain on kinase activity. *Biochem J* **2015,** *468* (2), 283-91.

180. Saleh, T.; Rossi, P.; Kalodimos, C. G., Atomic view of the energy landscape in the allosteric regulation of Abl kinase. *Nat Struct Mol Biol* **2017,** *24* (11), 893-901.

181. Jura, N.; Zhang, X.; Endres, N. F.; Seeliger, M. A.; Schindler, T.; Kuriyan, J., Catalytic control in the EGF receptor and its connection to general kinase regulatory mechanisms. *Mol Cell* **2011,** *42* (1), 9-22.

182. De Bondt, H. L.; Rosenblatt, J.; Jancarik, J.; Jones, H. D.; Morgan, D. O.; Kim, S. H., Crystal structure of cyclin-dependent kinase 2. *Nature* **1993,** *363* (6430), 595-602.

183. Bayliss, R.; Sardon, T.; Vernos, I.; Conti, E., Structural basis of Aurora-A activation by TPX2 at the mitotic spindle. *Molecular Cell* **2003,** *12* (4), 851-862.

184. Filippakopoulos, P.; Kofler, M.; Hantschel, O.; Gish, G. D.; Grebien, F.; Salah, E.; Neudecker, P.; Kay, L. E.; Turk, B. E.; Superti-Furga, G.; Pawson, T.; Knapp, S., Structural coupling of SH2-kinase domains links Fes and Abl substrate recognition and kinase activation. *Cell* **2008,** *134* (5), 793-803.

185. Duarte, D. P.; Lamontanara, A. J.; La Sala, G.; Jeong, S.; Sohn, Y. K.; Panjkovich, A.; Georgeon, S.; Kukenshoner, T.; Marcaida, M. J.; Pojer, F.; De Vivo, M.; Svergun, D.; Kim, H. S.; Dal Peraro, M.; Hantschel, O., Btk SH2-kinase interface is critical for allosteric kinase activation and its targeting inhibits B-cell neoplasms. *Nat Commun* **2020,** *11* (1), 2319.

186. Grebien, F.; Hantschel, O.; Wojcik, J.; Kaupe, I.; Kovacic, B.; Wyrzucki, A. M.; Gish, G. D.; Cerny-Reiterer, S.; Koide, A.; Beug, H.; Pawson, T.; Valent, P.; Koide, S.; Superti-Furga, G., Targeting the SH2-kinase interface in Bcr-Abl inhibits leukemogenesis. *Cell* **2011,** *147* (2), 306-19.

187. Cox, S.; Radzio-Andzelm, E.; Taylor, S. S., Domain movements in protein kinases. *Curr Opin Struct Biol* **1994,** *4* (6), 893-901.

188. Lakowicz, J. R., *Principles of Fluorescence Spectroscopy*. 3rd ed.; 2006.

189. Cavanagh, J.; Wayne, J. F.; Palmer, A. G.; Rance, M.; Skelton, N. J., *Protein NMR Spectroscopy*

Principles and Practice. Second Edition ed.; 2007.

190. Garcia-Rubio, I., EPR of site-directed spin-labeled proteins: A powerful tool to study structural flexibility. *Arch Biochem Biophys* **2020,** *684*, 108323.

191. Hodge, E. A.; Benhaim, M. A.; Lee, K. K., Bridging protein structure, dynamics, and function using hydrogen/deuterium-exchange mass spectrometry. *Protein Sci* **2020,** *29* (4), 843-855.

192. Förster, T., Zwischenmolekulare Energiewanderung Und Fluoreszenz. *Ann Phys-Berlin* **1948,** *2* (1-2), 55-75.

193. Förster, T., Experimentelle Und Theoretische Untersuchung Des Zwischenmolekularen Ubergangs Von Elektronenanregungsenergie. *Z Naturforsch A* **1949,** *4* (5), 321-327.

194. Hellenkamp, B.; Schmid, S.; Doroshenko, O.; Opanasyuk, O.; Kuhnemuth, R.; Rezaei Adariani, S.; Ambrose, B.; Aznauryan, M.; Barth, A.; Birkedal, V.; Bowen, M. E.; Chen, H.; Cordes, T.; Eilert, T.; Fijen, C.; Gebhardt, C.; Gotz, M.; Gouridis, G.; Gratton, E.; Ha, T.; Hao, P.; Hanke, C. A.; Hartmann, A.; Hendrix, J.; Hildebrandt, L. L.; Hirschfeld, V.; Hohlbein, J.; Hua, B.; Hubner, C. G.; Kallis, E.; Kapanidis, A. N.; Kim, J. Y.; Krainer, G.; Lamb, D. C.; Lee, N. K.; Lemke, E. A.; Levesque, B.; Levitus, M.; McCann, J. J.; Naredi-Rainer, N.; Nettels, D.; Ngo, T.; Qiu, R.; Robb, N. C.; Rocker, C.; Sanabria, H.; Schlierf, M.; Schroder, T.; Schuler, B.; Seidel, H.; Streit, L.; Thurn, J.; Tinnefeld, P.; Tyagi, S.; Vandenberk, N.; Vera, A. M.; Weninger, K. R.; Wunsch, B.; Yanez-Orozco, I. S.; Michaelis, J.; Seidel, C. A. M.; Craggs, T. D.; Hugel, T., Precision and accuracy of single-molecule FRET

measurements-a multi-laboratory benchmark study. *Nat Methods* **2018,** *15* (9), 669-676.

195. Felekyan, S.; Kühnemuth, R.; Kudryavtsev, V.; Sandhagen, C.; Becker, W.; Seidel, C. A. M., Full correlation from picoseconds to seconds by time-resolved and time-correlated single photon detection. *Review of Scientific Instruments* **2005,** *76* (8).

196. Felekyan, S.; Sanabria, H.; Kalinin, S.; Kuhnemuth, R.; Seidel, C. A., Analyzing Forster resonance energy transfer with fluctuation algorithms. *Methods Enzymol* **2013,** *519*, 39-85.

197. Gauer, J. W.; LeBlanc, S.; Hao, P.; Qiu, R.; Case, B. C.; Sakato, M.; Hingorani, M. M.; Erie, D. A.; Weninger, K. R., Single-Molecule FRET to Measure Conformational Dynamics of DNA Mismatch Repair Proteins. *Methods Enzymol* **2016,** *581*, 285-315.

198. Kalinin, S.; Peulen, T.; Sindbert, S.; Rothwell, P. J.; Berger, S.; Restle, T.; Goody, R. S.; Gohlke, H.; Seidel, C. A., A toolkit and benchmark study for FRET-restrained high-precision structural modeling. *Nat Methods* **2012,** *9* (12), 1218-25.

199. Dimura, M.; Peulen, T. O.; Hanke, C. A.; Prakash, A.; Gohlke, H.; Seidel, C. A., Quantitative FRET studies and integrative modeling unravel the structure and dynamics of biomolecular systems. *Curr Opin Struct Biol* **2016,** *40*, 163-185.

200. Hellenkamp, B.; Wortmann, P.; Kandzia, F.; Zacharias, M.; Hugel, T., Multidomain structure and correlated dynamics determined by self-consistent FRET networks. *Nat Methods* **2017,** *14* (2), 174-180.

201. Al-Soufi, W.; Reija, B.; Novo, M.; Felekyan, S.; Kuhnemuth, R.; Seidel, C. A., Fluorescence correlation spectroscopy, a tool to investigate supramolecular dynamics: inclusion complexes of pyronines with cyclodextrin. *J Am Chem Soc* **2005,** *127* (24), 8775-84.

202. Martin, S. F.; Tatham, M. H.; Hay, R. T.; Samuel, I. D., Quantitative analysis of multi-protein interactions using FRET: application to the SUMO pathway. *Protein Sci* **2008,** *17* (4), 777-84.

203. Jiang, L.; Xiong, Z.; Song, Y.; Lu, Y.; Chen, Y.; Schultz, J. S.; Li, J.; Liao, J., Protein-Protein Affinity Determination by Quantitative FRET Quenching. *Sci Rep* **2019,** *9* (1), 2050.

204. Ben-Johny, M.; Yue, D. N.; Yue, D. T., Detecting stoichiometry of macromolecular complexes in live cells using FRET. *Nat Commun* **2016,** *7*, 13709.

205. Mattiroli, F.; Gu, Y.; Luger, K., FRET-based Stoichiometry Measurements of Protein Complexes in vitro. *Bio Protoc* **2018,** *7* (3).

206. Hochreiter, B.; Kunze, M.; Moser, B.; Schmid, J. A., Advanced FRET normalization allows quantitative analysis of protein interactions including stoichiometries and relative affinities in living cells. *Sci Rep* **2019,** *9* (1), 8233.

207. Marshall, R. A.; Aitken, C. E.; Dorywalska, M.; Puglisi, J. D., Translation at the single-molecule level. *Annu Rev Biochem* **2008,** *77*, 177-203.

208. Dunkle, J. A.; Cate, J. H., Ribosome structure and dynamics during translocation and termination. *Annu Rev Biophys* **2010,** *39*, 227-44.

209. Wang, J.; Johnson, A. G.; Lapointe, C. P.; Choi, J.; Prabhakar, A.; Chen, D. H.; Petrov, A. N.; Puglisi, J. D., eIF5B gates the transition from translation initiation to elongation. *Nature* **2019,** *573* (7775), 605-608.

210. Smiley, R. D.; Hammes, G. G., Single molecule studies of enzyme mechanisms. *Chem Rev* **2006,** *106* (8), 3080-94.

211. Mickler, M.; Hessling, M.; Ratzke, C.; Buchner, J.; Hugel, T., The large conformational changes of Hsp90 are only weakly coupled to ATP hydrolysis. *Nat Struct Mol Biol* **2009,** *16* (3), 281-6.

212. Ha, T.; Kozlov, A. G.; Lohman, T. M., Single-molecule views of protein movement on single-stranded DNA. *Annu Rev Biophys* **2012,** *41*, 295-319.

213. Park, H.; Kang, H.; Ko, W.; Lee, W.; Jo, K.; Lee, H. S., FRET-based analysis of protein-nucleic acid interactions by genetically incorporating a fluorescent amino acid. *Amino Acids* **2015,** *47* (4), 729-734.

214. Aleman, E. A.; Lamichhane, R.; Rueda, D., Exploring RNA folding one molecule at a time. *Curr Opin Chem Biol* **2008,** *12* (6), 647-54.

215. Schuler, B.; Hofmann, H., Single-molecule spectroscopy of protein folding dynamics--expanding scope and timescales. *Curr Opin Struct Biol* **2013,** *23* (1), 36-47.

216. Aznauryan, M.; Delgado, L.; Soranno, A.; Nettels, D.; Huang, J. R.; Labhardt, A. M.; Grzesiek, S.; Schuler, B., Comprehensive structural and dynamical view of an unfolded protein from the combination of single-molecule FRET, NMR, and SAXS. *Proc Natl Acad Sci U S A* **2016,** *113* (37), E5389-98.

217. Borgia, A.; Borgia, M. B.; Bugge, K.; Kissling, V. M.; Heidarsson, P. O.; Fernandes, C. B.; Sottini, A.; Soranno, A.; Buholzer, K. J.; Nettels, D.; Kragelund, B. B.; Best, R. B.; Schuler, B., Extreme disorder in an ultrahigh-affinity protein complex. *Nature* **2018,** *555* (7694), 61-66.

218. LeBlanc, S. J.; Kulkarni, P.; Weninger, K. R., Single Molecule FRET: A Powerful Tool to Study Intrinsically Disordered Proteins. *Biomolecules* **2018,** *8* (4).

219. Sakon, J. J.; Weninger, K. R., Detecting the conformation of individual proteins in live cells. *Nat Methods* **2010,** *7* (3), 203-5.

220. Kravets, E.; Degrandi, D.; Ma, Q.; Peulen, T. O.; Klumpers, V.; Felekyan, S.; Kuhnemuth, R.; Weidtkamp-Peters, S.; Seidel, C. A.; Pfeffer, K., Guanylate binding proteins directly attack Toxoplasma gondii via supramolecular complexes. *Elife* **2016,** *5*.

221. Plitzko, J. M.; Schuler, B.; Selenko, P., Structural Biology outside the box-inside the cell. *Curr Opin Struct Biol* **2017,** *46*, 110-121.

222. Moerner, W. E.; Kador, L., Optical detection and spectroscopy of single molecules in a solid. *Phys Rev Lett* **1989,** *62* (21), 2535-2538.

223. Orrit, M.; Bernard, J., Single pentacene molecules detected by fluorescence excitation in a p-terphenyl crystal. *Phys Rev Lett* **1990,** *65* (21), 2716-2719.

224. Brooks Shera, E.; Seitzinger, N. K.; Davis, L. M.; Keller, R. A.; Soper, S. A., Detection of single fluorescent molecules. *Chemical Physics letters* **1990,** *174* (6), 553-557.

225. Ha, T.; Enderle, T.; Ogletree, D. F.; Chemla, D. S.; Selvin, P. R.; Weiss, S., Probing the interaction between two single molecules: Fluorescence resonance energy transfer between a single donor and a single acceptor. *Proceedings of the National Academy of Sciences of the United States of America* **1996,** *93* (13), 6264-6268.

226. Lu, H. P.; Xun, L.; Xie, X. S., Single-molecule enzymatic dynamics. *Science* **1998,** *282* (5395), 1877-82.

227. van Oijen, A. M.; Blainey, P. C.; Crampton, D. J.; Richardson, C. C.; Ellenberger, T.; Xie, X. S., Single-molecule kinetics of lambda exonuclease reveal base dependence and dynamic disorder. *Science* **2003,** *301* (5637), 1235-8.

228. Flomenbom, O.; Velonia, K.; Loos, D.; Masuo, S.; Cotlet, M.; Engelborghs, Y.; Hofkens, J.; Rowan, A. E.; Nolte, R. J.; Van der Auweraer, M.; de Schryver, F. C.; Klafter, J., Stretched exponential decay and correlations in the catalytic activity of fluctuating single lipase molecules. *Proc Natl Acad Sci U S A* **2005,** *102* (7), 2368-72.

229. English, B. P.; Min, W.; van Oijen, A. M.; Lee, K. T.; Luo, G.; Sun, H.; Cherayil, B. J.; Kou, S. C.; Xie, X. S., Ever-fluctuating single enzyme molecules: Michaelis-Menten equation revisited. *Nat Chem Biol* **2006,** *2* (2), 87-94.

230. Rissin, D. M.; Gorris, H. H.; Walt, D. R., Distinct and long-lived activity states of single enzyme molecules. *J Am Chem Soc* **2008,** *130* (15), 5349-53.

231. Kapanidis, A. N.; Strick, T., Biology, one molecule at a time. *Trends Biochem Sci* **2009,** *34* (5), 234-43.

232. Binnig, G.; Quate, C. F.; Gerber, C., Atomic force microscope. *Phys Rev Lett* **1986,** *56* (9), 930-933.

233. Krieg, M.; Fläschner, G.; Alsteens, D.; Gaub, B. M.; Wuite, G. J. L.; Roos, W. H.; Gaub, H. E.; Gerber, C.; Dufrene, Y. F.; Müller, D. J., Atomic force microscopy - based mechanobiology. *Nature Reviews Physics* **2019**, 42-57.

234. Ashkin, A., Acceleration and Trapping of Particles by Radiation Pressure. *Physical Review Letters* **1970,** *24* (4), 156-159.

235. Ashkin, A.; Dziedzic, J. M.; Bjorkholm, J. E.; Chu, S., Observation of a single-beam gradient force optical trap for dielectric particles. *Opt Lett* **1986,** *11* (5), 288.

236. Ashkin, A., Forces of a single-beam gradient laser trap on a dielectric sphere in the ray optics regime. *Biophys J* **1992,** *61* (2), 569-82.

237. Arai, Y.; Yasuda, R.; Akashi, K.; Harada, Y.; Miyata, H.; Kinosita, K., Jr.; Itoh, H., Tying a molecular knot with optical tweezers. *Nature* **1999,** *399* (6735), 446-8.

238. Gao, D.; Ding, W.; Nieto-Vesperinas, M.; Ding, X.; Rahman, M.; Zhang, T.; Lim, C.; Qiu, C. W., Optical manipulation from the microscale to the nanoscale: fundamentals, advances and prospects. *Light Sci Appl* **2017,** *6* (9), e17039.

239. Strick, T. R.; Allemand, J. F.; Bensimon, D.; Bensimon, A.; Croquette, V., The elasticity of a single supercoiled DNA molecule. *Science* **1996,** *271* (5257), 1835-7.

240. Sarkar, R.; Rybenkov, V. V., A Guide to Magnetic Tweezers and Their Applications. *Frontiers in Physics* **2016,** *4*.

241. Walla, P. J., *Modern Biophysical Chemistry*

Detection and Analysis of Biomolecules. 2009.

242. Ando, T., High-speed atomic force microscopy and its future prospects. *Biophys Rev* **2018,** *10* (2), 285-292.

243. Uchihashi, T.; Scheuring, S., Applications of high-speed atomic force microscopy to real-time visualization of dynamic biomolecular processes. *Biochim Biophys Acta Gen Subj* **2018,** *1862* (2), 229-240.

244. Sun, Z.; Juriani, A.; Meininger, G. A.; Meissner, K. E., Probing cell surface interactions using atomic force microscope cantilevers functionalized for quantum dot-enabled Forster resonance energy transfer. *J Biomed Opt* **2009,** *14* (4), 040502.

245. He, Y.; Lu, M.; Cao, J.; Lu, H. P., Manipulating protein conformations by single-molecule AFM-FRET nanoscopy. *ACS Nano* **2012,** *6* (2), 1221-9.

246. Heath, G. R.; Scheuring, S., High-speed AFM height spectroscopy reveals micros-dynamics of unlabeled biomolecules. *Nat Commun* **2018,** *9* (1), 4983.

247. Neher, E.; Sakmann, B., Single-channel currents recorded from membrane of denervated frog muscle fibres. *Nature* **1976,** *260* (5554), 799-802.

248. Sakmann, B.; Neher, E., Patch clamp techniques for studying ionic channels in excitable membranes. *Annu Rev Physiol* **1984,** *46*, 455-72.

249. Stryer, L.; Haugland, R. P., Energy transfer: a spectroscopic ruler. *Proc Natl Acad Sci U S A* **1967,** *58* (2), 719-26.

250. Sisamakis, E.; Valeri, A.; Kalinin, S.; Rothwell, P. J.; Seidel, C. A. M., Accurate Single-Molecule FRET Studies Using Multiparameter Fluorescence Detection. In *Single Molecule Tools, Part B:Super-Resolution, Particle Tracking, Multiparameter, and Force Based Methods*, 2010; pp 455-514.

251. van der Meer, B. W., Kappa-squared: from nuisance to new sense. *J Biotechnol* **2002,** *82* (3), 181-96.

252. Pawley, J. B., *Handbook Of Biological Confocal Microscopy*. 2006.

253. Eggeling, C.; Fries, J. R.; Brand, L.; Gunther, R.; Seidel, C. A., Monitoring conformational dynamics of a single molecule by selective fluorescence spectroscopy. *Proc Natl Acad Sci U S A* **1998,** *95* (4), 1556-61.

254. Becker, W., *Advanced Time-Correlated Single Photon Counting Techniques*. 2005.

255. Widengren, J.; Kudryavtsev, V.; Antonik, M.; Berger, S.; Gerken, M.; Seidel, C. A., Single-molecule detection and identification of multiple species by multiparameter fluorescence detection. *Anal Chem* **2006,** *78* (6), 2039-50.

256. Muller, B. K.; Zaychikov, E.; Brauchle, C.; Lamb, D. C., Pulsed interleaved excitation. *Biophys J* **2005,** *89* (5), 3508-22.

257. Magde, D.; Elson, E.; Webb, W. W., Thermodynamic Fluctuations in a Reacting System—Measurement by Fluorescence Correlation Spectroscopy. *Physical Review Letters* **1972,** *29* (11), 705-708.

258. Felekyan, S.; Kalinin, S.; Sanabria, H.; Valeri, A.; Seidel, C. A., Filtered FCS: species auto- and cross-correlation functions highlight binding and dynamics in biomolecules. *Chemphyschem* **2012,** *13* (4), 1036-53.

259. Böhmer, M. W., M.; Rahn, H.-J.; Erdmann, R.; Enderlein, J., Time-resolved fluorescence correlation spectroscopy. *Chemical Physics letters* **2002,** *353*, 439-445.

260. Gregor, I.; Enderlein, J., Time-resolved methods in biophysics. 3. Fluorescence lifetime correlation spectroscopy. *Photochem Photobiol Sci* **2007,** *6* (1), 13-8.

261. Kapusta, P.; Wahl, M.; Benda, A.; Hof, M.; Enderlein, J., Fluorescence lifetime correlation spectroscopy. *J Fluoresc* **2007,** *17* (1), 43-8.

262. Wohland, T.; Shi, X.; Sankaran, J.; Stelzer, E. H., Single plane illumination fluorescence correlation spectroscopy (SPIM-FCS) probes inhomogeneous three-dimensional environments. *Opt Express* **2010,** *18* (10), 10627-41.

263. Ries, J.; Schwille, P., Fluorescence correlation spectroscopy. *Bioessays* **2012,** *34* (5), 361-8.

264. Zhuang, X.; Kim, H.; Pereira, M. J.; Babcock, H. P.; Walter, N. G.; Chu, S., Correlating structural dynamics and function in single ribozyme molecules. *Science* **2002,** *296* (5572), 1473-6.

265. Tan, E.; Wilson, T. J.; Nahas, M. K.; Clegg, R. M.; Lilley, D. M.; Ha, T., A four-way junction accelerates hairpin ribozyme folding via a discrete intermediate. *Proc Natl Acad Sci U S A* **2003,** *100* (16), 9308-13.

266. Nahas, M. K.; Wilson, T. J.; Hohng, S.; Jarvie, K.; Lilley, D. M.; Ha, T., Observation of internal cleavage and ligation reactions of a ribozyme. *Nat Struct Mol Biol* **2004,** *11* (11), 1107-13.

267. Lee, J. Y.; Okumus, B.; Kim, D. S.; Ha, T., Extreme conformational diversity in human telomeric DNA. *Proc Natl Acad Sci U S A* **2005,** *102* (52), 18938-43.

268. McKinney, S. A.; Freeman, A. D. J.; Lilley, D. M. J.; Ha, T. J., Observing spontaneous branch migration of Holliday junctions one step at a time. *Proceedings of the National Academy of Sciences of the United States of America* **2005,** *102* (16), 5715-5720.

269. McKinney, S. A.; Joo, C.; Ha, T., Analysis of single-molecule FRET trajectories using hidden Markov modeling. *Biophys J* **2006,** *91* (5), 1941-51.

270. Kalinin, S.; Valeri, A.; Antonik, M.; Felekyan, S.; Seidel, C. A., Detection of structural dynamics by FRET: a photon distribution and fluorescence lifetime analysis of systems with multiple states. *J Phys Chem B* **2010,** *114* (23), 7983-95.

271. Palo, K.; Mets, U.; Loorits, V.; Kask, P., Calculation of photon-count number distributions via master equations. *Biophys J* **2006,** *90* (6), 2179-91.

272. Gopich, I. V.; Szabo, A., Single-molecule FRET with diffusion and conformational dynamics. *J Phys Chem B* **2007,** *111* (44), 12925-12932.

273. Kalinin, S.; Felekyan, S.; Antonik, M.; Seidel, C. A., Probability distribution analysis of single-molecule fluorescence anisotropy and resonance energy transfer. *J Phys Chem B* **2007,** *111* (34), 10253-62.

274. Martynov, V. I.; Pakhomov, A. A.; Popova, N. V.; Deyev, I. E.; Petrenko, A. G., Synthetic Fluorophores for Visualizing Biomolecules in Living Systems. *Acta Naturae* **2016,** *8* (4), 33-46.

275. Fu, Y.; Finney, N. S., Small-molecule fluorescent probes and their design. *RSC Advances* **2018,** *8* (51), 29051-29061.

276. Richardson, F. S., Terbium(III) and Europium(III) Ions as Luminescent Probes and Stains for Biomoiecular Systems. *Chem Rev* **1982,** *82*, 541-552.

277. Balzani, V.; Ballardini, R., New Trends in the Design of Luminescent Metal-Complexes. *Photochem Photobiol* **1990,** *52* (2), 409-416.

278. Sabbatini, N.; Guardigli, M.; Bolletta, F.; Manet, I.; Ziessel, R., Luminescent Eu3+ and Tb3+ Complexes of a Branched Macrocyclic Ligand Incorporating 2,2'-Bipyridine in the Macrocycle and Phosphinate Esters in the Side Arms. *Angew Chem Int Edit* **1994,** *33* (14), 1501-1503.

279. Guo, Z.; Park, S.; Yoon, J.; Shin, I., Recent progress in the development of near-infrared fluorescent probes for bioimaging applications. *Chem Soc Rev* **2014,** *43* (1), 16-29.

280. Li, Q.; Liu, W.; Wu, J.; Zhou, B.; Niu, G.; Zhang, H.; Ge, J.; Wang, P., Deep-red to near-infrared fluorescent dyes: Synthesis, photophysical properties, and application in cell imaging. *Spectrochim Acta A Mol Biomol Spectrosc* **2016,** *164*, 8-14.

281. Grzybowski, M.; Taki, M.; Senda, K.; Sato, Y.; Ariyoshi, T.; Okada, Y.; Kawakami, R.; Imamura, T.; Yamaguchi, S., A Highly Photostable Near-Infrared Labeling Agent Based on a Phospha-rhodamine for Long-Term and Deep Imaging. *Angew Chem Int Ed Engl* **2018,** *57* (32), 10137-10141.

282. Shimomura, O.; Johnson, F. H.; Saiga, Y., Extraction, Purification and Properties of Aequorin, a Bioluminescent Protein from the Luminous Hydromedusan, Aequorea. *Journal of Cellular and Comparative Physiology* **1962,** *59* (3), 223-239.

283. Greife, A.; Felekyan, S.; Ma, Q.; Gertzen, C. G.; Spomer, L.; Dimura, M.; Peulen, T. O.; Wohler, C.; Haussinger, D.; Gohlke, H.; Keitel, V.; Seidel, C. A., Structural assemblies of the di- and oligomeric G-protein coupled receptor TGR5 in live cells: an MFIS-FRET and integrative modelling study. *Sci Rep* **2016,** *6*, 36792.

284. Ebbinghaus, S.; Dhar, A.; McDonald, J. D.; Gruebele, M., Protein folding stability and dynamics imaged in a living cell. *Nat Methods* **2010,** *7* (4), 319-23.

285. Pantoja, R.; Rodriguez, E. A.; Dibas, M. I.; Dougherty, D. A.; Lester, H. A., Single-molecule imaging of a fluorescent unnatural amino acid incorporated into nicotinic receptors. *Biophys J* **2009,** *96* (1), 226-37.

286. Ko, W.; Kim, S.; Lee, S.; Jo, K.; Lee, H. S., Genetically encoded FRET sensors using a fluorescent unnatural amino acid as a FRET donor. *RSC Advances* **2016,** *6* (82), 78661-78668.

287. Hilaire, M. R.; Ahmed, I. A.; Lin, C. W.; Jo, H.; DeGrado, W. F.; Gai, F., Blue fluorescent amino acid for biological spectroscopy and microscopy. *Proc Natl Acad Sci U S A* **2017,** *114* (23), 6005-6009.

288. Crankshaw, M. W.; Grant, G. A., Modification of Cysteine. *Current Protocols in Protein Science* **1996,** *3* (1), 15.1.1-15.1.18.

289. Hermanson, G. T., *Bioconjugate Techniques*. 2nd ed.; 2008.

290. Chalker, J. M.; Bernardes, G. J.; Lin, Y. A.; Davis, B. G., Chemical modification of proteins at cysteine: opportunities in chemistry and biology. *Chem Asian J* **2009,** *4* (5), 630-40.

291. Stephanopoulos, N.; Francis, M. B., Choosing an effective protein bioconjugation strategy. *Nat Chem Biol* **2011,** *7* (12), 876-84.

292. Liu, C. C.; Schultz, P. G., Adding new chemistries to the genetic code. *Annu Rev Biochem* **2010,** *79*, 413-44.

293. Young, T. S.; Schultz, P. G., Beyond the canonical 20 amino acids: expanding the genetic lexicon. *J Biol Chem* **2010,** *285* (15), 11039-44.

294. Chin, J. W., Expanding and reprogramming the genetic code of cells and animals. *Annu Rev Biochem* **2014,** *83*, 379-408.

295. Lemke, E. A., *Noncanonical Amino Acids*. 2018.

296. Young, D. D.; Schultz, P. G., Playing with the Molecules of Life. *ACS Chem Biol* **2018,** *13* (4), 854-870.

297. Mukai, T.; Kobayashi, T.; Hino, N.; Yanagisawa, T.; Sakamoto, K.; Yokoyama, S., Adding l-lysine derivatives to the genetic code of mammalian cells with engineered pyrrolysyl-tRNA synthetases. *Biochem Biophys Res Commun* **2008,** *371* (4), 818-22.

298. Nguyen, D. P.; Lusic, H.; Neumann, H.; Kapadnis, P. B.; Deiters, A.; Chin, J. W., Genetic encoding and labeling of aliphatic azides and alkynes in recombinant proteins via a pyrrolysyl-tRNA Synthetase/tRNA(CUA) pair and click chemistry. *J Am Chem Soc* **2009,** *131* (25), 8720-1.

299. Plass, T.; Milles, S.; Koehler, C.; Schultz, C.; Lemke, E. A., Genetically encoded copper-free click chemistry. *Angew Chem Int Ed Engl* **2011,** *50* (17), 3878-81.

300. Grunbeck, A.; Huber, T.; Sachdev, P.; Sakmar, T. P., Mapping the ligand-binding site on a G protein-coupled receptor (GPCR) using genetically encoded photocrosslinkers. *Biochemistry* **2011,** *50* (17), 3411-3.

301. Coin, I.; Katritch, V.; Sun, T.; Xiang, Z.; Siu, F. Y.; Beyermann, M.; Stevens, R. C.; Wang, L., Genetically encoded chemical probes in cells reveal the binding path of urocortin-I to CRF class B GPCR. *Cell* **2013,** *155* (6), 1258-69.

302. Rannversson, H.; Andersen, J.; Sorensen, L.; Bang-Andersen, B.; Park, M.; Huber, T.; Sakmar, T. P.; Stromgaard, K., Genetically encoded photocrosslinkers locate the high-affinity binding site of antidepressant drugs in the human serotonin transporter. *Nat Commun* **2016,** *7*, 11261.

303. Freinkman, E.; Chng, S. S.; Kahne, D., The complex that inserts lipopolysaccharide into the bacterial outer membrane forms a two-protein plug-and-barrel. *Proc Natl Acad Sci U S A* **2011,** *108* (6), 2486-91.

304. Ye, S.; Huber, T.; Vogel, R.; Sakmar, T. P., FTIR analysis of GPCR activation using azido probes. *Nat Chem Biol* **2009,** *5* (6), 397-9.

305. Hemphill, J.; Borchardt, E. K.; Brown, K.; Asokan, A.; Deiters, A., Optical Control of CRISPR/Cas9 Gene Editing. *J Am Chem Soc* **2015,** *137* (17), 5642-5.

306. Ma, J. S.; Kim, J. Y.; Kazane, S. A.; Choi, S. H.; Yun, H. Y.; Kim, M. S.; Rodgers, D. T.; Pugh, H. M.; Singer, O.; Sun, S. B.; Fonslow, B. R.; Kochenderfer, J. N.; Wright, T. M.; Schultz, P. G.; Young, T. S.; Kim, C. H.; Cao, Y., Versatile strategy for controlling the specificity and activity of engineered T cells. *Proc Natl Acad Sci U S A* **2016,** *113* (4), E450-8.

307. Kalstrup, T.; Blunck, R., Dynamics of internal pore opening in K(V) channels probed by a fluorescent unnatural amino acid. *Proc Natl Acad Sci U S A* **2013,** *110* (20), 8272-7.

308. Mitchell, A. L.; Addy, P. S.; Chin, M. A.; Chatterjee, A., A Unique Genetically Encoded FRET Pair in Mammalian Cells. *Chembiochem* **2017,** *18* (6), 511-514.

309. Liang, L.; Astruc, D., The copper(I)-catalyzed alkyne-azide cycloaddition (CuAAC) “click” reaction and its applications. An overview. *Coordination Chemistry Reviews* **2011,** *255* (23-24), 2933-2945.

310. Kiick, K. L.; Saxon, E.; Tirrell, D. A.; Bertozzi, C. R., Incorporation of azides into recombinant proteins for chemoselective modification by the Staudinger ligation. *Proceedings of the National Academy of Sciences of the United States of America* **2002,** *99* (1), 19-24.

311. Shao, N.; Singh, N. S.; Slade, S. E.; Jones, A. M.; Balasubramanian, M. K., Site Specific Genetic Incorporation of Azidophenylalanine in Schizosaccharomyces pombe. *Sci Rep* **2015,** *5*, 17196.

312. Besanceney-Webler, C.; Jiang, H.; Zheng, T.; Feng, L.; Soriano del Amo, D.; Wang, W.; Klivansky, L. M.; Marlow, F. L.; Liu, Y.; Wu, P., Increasing the efficacy of bioorthogonal click reactions for bioconjugation: a comparative study. *Angew Chem Int Ed Engl* **2011,** *50* (35), 8051-6.

313. Kucher, S.; Korneev, S.; Tyagi, S.; Apfelbaum, R.; Grohmann, D.; Lemke, E. A.; Klare, J. P.; Steinhoff, H. J.; Klose, D., Orthogonal spin labeling using click chemistry for in vitro and in vivo applications. *J Magn Reson* **2017,** *275*, 38-45.

314. Plass, T.; Milles, S.; Koehler, C.; Szymanski, J.; Mueller, R.; Wiessler, M.; Schultz, C.; Lemke, E. A., Amino acids for Diels-Alder reactions in living cells. *Angew Chem Int Ed Engl* **2012,** *51* (17), 4166-70.

315. Wang, L.; Zhang, Z.; Brock, A.; Schultz, P. G., Addition of the keto functional group to the genetic code of Escherichia coli. *Proc Natl Acad Sci U S A* **2003,** *100* (1), 56-61.

316. Ai, H. W.; Shen, W.; Brustad, E.; Schultz, P. G., Genetically encoded alkenes in yeast. *Angew Chem Int Ed Engl* **2010,** *49* (5), 935-7.

317. Addy, P. S.; Erickson, S. B.; Italia, J. S.; Chatterjee, A., A Chemoselective Rapid Azo-Coupling Reaction (CRACR) for Unclickable Bioconjugation. *J Am Chem Soc* **2017,** *139* (34), 11670-11673.

318. Spicer, C. D.; Davis, B. G., Rewriting the bacterial glycocalyx via Suzuki-Miyaura cross-coupling. *Chem Commun (Camb)* **2013,** *49* (27), 2747-9.

319. Sanabria, H.; Rodnin, D.; Hemmen, K.; Peulen, T. O.; Felekyan, S.; Fleissner, M. R.; Dimura, M.; Koberling, F.; Kuhnemuth, R.; Hubbell, W.; Gohlke, H.; Seidel, C. A. M., Resolving dynamics and function of transient states in single enzyme molecules. *Nat Commun* **2020,** *11* (1), 1231.

320. Kim, J.; Seo, M. H.; Lee, S.; Cho, K.; Yang, A.; Woo, K.; Kim, H. S.; Park, H. S., Simple and efficient strategy for site-specific dual labeling of proteins for single-molecule fluorescence resonance energy transfer analysis. *Anal Chem* **2013,** *85* (3), 1468-74.

321. Lee, T. C.; Kang, M.; Kim, C. H.; Schultz, P. G.; Chapman, E.; Deniz, A. A., Dual Unnatural Amino Acid Incorporation and Click-Chemistry Labeling to Enable Single-Molecule FRET Studies of p97 Folding. *Chembiochem* **2016,** *17* (11), 981-4.

322. Chatterjee, A.; Xiao, H.; Bollong, M.; Ai, H. W.; Schultz, P. G., Efficient viral delivery system for unnatural amino acid mutagenesis in mammalian cells. *Proc Natl Acad Sci U S A* **2013,** *110* (29), 11803-8.

323. Ernst, R. J.; Krogager, T. P.; Maywood, E. S.; Zanchi, R.; Beranek, V.; Elliott, T. S.; Barry, N. P.; Hastings, M. H.; Chin, J. W., Genetic code expansion in the mouse brain. *Nat Chem Biol* **2016,** *12* (10), 776-778.

324. Zheng, Y.; Lewis, T. L., Jr.; Igo, P.; Polleux, F.; Chatterjee, A., Virus-Enabled Optimization and Delivery of the Genetic Machinery for Efficient Unnatural Amino Acid Mutagenesis in Mammalian Cells and Tissues. *ACS Synth Biol* **2017,** *6* (1), 13-18.

325. Lajoie, M. J.; Rovner, A. J.; Goodman, D. B.; Aerni, H. R.; Haimovich, A. D.; Kuznetsov, G.; Mercer, J. A.; Wang, H. H.; Carr, P. A.; Mosberg, J. A.; Rohland, N.; Schultz, P. G.; Jacobson, J. M.; Rinehart, J.; Church, G. M.; Isaacs, F. J., Genomically recoded organisms expand biological functions. *Science* **2013,** *342* (6156), 357-60.

326. Mukai, T.; Hoshi, H.; Ohtake, K.; Takahashi, M.; Yamaguchi, A.; Hayashi, A.; Yokoyama, S.; Sakamoto, K., Highly reproductive Escherichia coli cells with no specific assignment to the UAG codon. *Sci Rep* **2015,** *5*, 9699.

327. Hong, V.; Presolski, S. I.; Ma, C.; Finn, M. G., Analysis and optimization of copper-catalyzed azide-alkyne cycloaddition for bioconjugation. *Angew Chem Int Ed Engl* **2009,** *48* (52), 9879-83.

328. Narayanan, C.; Bafna, K.; Roux, L. D.; Agarwal, P. K.; Doucet, N., Applications of NMR and computational methodologies to study protein dynamics. *Arch Biochem Biophys* **2017,** *628*, 71-80.

329. Kay, L. E., New Views of Functionally Dynamic Proteins by Solution NMR Spectroscopy. *J Mol Biol* **2016,** *428* (2 Pt A), 323-331.

330. Wider, G.; Wuthrich, K., NMR spectroscopy of large molecules and multimolecular assemblies in solution. *Curr Opin Struct Biol* **1999,** *9* (5), 594-601.

331. Sekhar, A.; Kay, L. E., An NMR View of Protein Dynamics in Health and Disease. *Annu Rev Biophys* **2019,** *48*, 297-319.

332. Pervushin, K.; Riek, R.; Wider, G.; Wuthrich, K., Attenuated T2 relaxation by mutual cancellation of dipole-dipole coupling and chemical shift anisotropy indicates an avenue to NMR structures of very large biological macromolecules in solution. *Proc Natl Acad Sci U S A* **1997,** *94* (23), 12366-71.

333. Tugarinov, V.; Hwang, P. M.; Ollerenshaw, J. E.; Kay, L. E., Cross-correlated relaxation enhanced 1H-13C NMR spectroscopy of methyl groups in very high molecular weight proteins and protein complexes. *J Am Chem Soc* **2003,** *125* (34), 10420-8.

334. Joss, D.; Haussinger, D., Design and applications of lanthanide chelating tags for pseudocontact shift NMR spectroscopy with biomacromolecules. *Prog Nucl Magn Reson Spectrosc* **2019,** *114-115*, 284-312.

335. Chen, K.; Tjandra, N., The use of residual dipolar coupling in studying proteins by NMR. *Top Curr Chem* **2012,** *326*, 47-67.

336. Boisbouvier, J.; Kay, L. E., Advanced isotopic labeling for the NMR investigation of challenging proteins and nucleic acids. *J Biomol NMR* **2018,** *71* (3), 115-117.

337. Rosenzweig, R.; Kay, L. E., Bringing dynamic molecular machines into focus by methyl-TROSY NMR. *Annu Rev Biochem* **2014,** *83*, 291-315.

338. Huang, C.; Kalodimos, C. G., Structures of Large Protein Complexes Determined by Nuclear Magnetic Resonance Spectroscopy. *Annu Rev Biophys* **2017,** *46*, 317-336.

339. Jiang, Y.; Kalodimos, C. G., NMR Studies of Large Proteins. *J Mol Biol* **2017,** *429* (17), 2667-2676.

340. Sprangers, R.; Velyvis, A.; Kay, L. E., Solution NMR of supramolecular complexes: providing new insights into function. *Nat Methods* **2007,** *4* (9), 697-703.

341. Opitz, C.; Isogai, S.; Grzesiek, S., An economic approach to efficient isotope labeling in insect cells using homemade 15N-, 13C- and 2H-labeled yeast extracts. *J Biomol NMR* **2015,** *62* (3), 373-85.

342. Franke, B.; Opitz, C.; Isogai, S.; Grahl, A.; Delgado, L.; Gossert, A. D.; Grzesiek, S., Production of isotope-labeled proteins in insect cells for NMR. *J Biomol NMR* **2018,** *71* (3), 173-184.

343. Sitarska, A.; Skora, L.; Klopp, J.; Roest, S.; Fernandez, C.; Shrestha, B.; Gossert, A. D., Affordable uniform isotope labeling with (2)H, (13)C and (15)N in insect cells. *J Biomol NMR* **2015,** *62* (2), 191-7.

344. Mittermaier, A. K.; Kay, L. E., Observing biological dynamics at atomic resolution using NMR. *Trends Biochem Sci* **2009,** *34* (12), 601-11.

345. Farrow, N. A.; Zhang, O.; Forman-Kay, J. D.; Kay, L. E., A heteronuclear correlation experiment for simultaneous determination of 15N longitudinal decay and chemical exchange rates of systems in slow equilibrium. *J Biomol NMR* **1994,** *4* (5), 727-34.

346. Li, Y.; Palmer, A. G., 3rd, TROSY-selected ZZ-exchange experiment for characterizing slow chemical exchange in large proteins. *J Biomol NMR* **2009,** *45* (4), 357-60.

347. Anthis, N. J.; Clore, G. M., Visualizing transient dark states by NMR spectroscopy. *Q Rev Biophys* **2015,** *48* (1), 35-116.

348. Vallurupalli, P.; Bouvignies, G.; Kay, L. E., Studying "invisible" excited protein states in slow exchange with a major state conformation. *J Am Chem Soc* **2012,** *134* (19), 8148-61.

349. Grahl, A.; Abiko, L. A.; Isogai, S.; Sharpe, T.; Grzesiek, S., A high-resolution description of beta1-adrenergic receptor functional dynamics and allosteric coupling from backbone NMR. *Nat Commun* **2020,** *11* (1), 2216.

350. Nikolova, E. N.; Kim, E.; Wise, A. A.; O'Brien, P. J.; Andricioaei, I.; Al-Hashimi, H. M., Transient Hoogsteen base pairs in canonical duplex DNA. *Nature* **2011,** *470* (7335), 498-502.

351. Clore, G. M.; Iwahara, J., Theory, Practice, and Applications of Paramagnetic Relaxation Enhancement for the Characterization of Transient Low-Population States of Biological Macromolecules and Their Complexes. *Chemical Reviews* **2009,** *109* (9), 4108-4139.

352. Wagner, G., Characterization of the distribution of internal motions in the basic pancreatic trypsin inhibitor using a large number of internal NMR probes. *Quarterly Reviews of Biophysics* **1983,** *16* (1), 1-57.

353. Karplus, M.; Kuriyan, J., Molecular dynamics and protein function. *Proc Natl Acad Sci U S A* **2005,** *102* (19), 6679-85.

354. Karplus, M.; McCammon, J. A., Molecular dynamics simulations of biomolecules. *Nat Struct Biol* **2002,** *9* (9), 646-52.

355. Hollingsworth, S. A.; Dror, R. O., Molecular Dynamics Simulation for All. *Neuron* **2018,** *99* (6), 1129-1143.

356. Lindorff-Larsen, K.; Maragakis, P.; Piana, S.; Eastwood, M. P.; Dror, R. O.; Shaw, D. E., Systematic validation of protein force fields against experimental data. *PLoS One* **2012,** *7* (2), e32131.

357. Lopes, P. E. M.; Guvench, O.; MacKerell, A. D., Current Status of Protein Force Fields for Molecular Dynamics Simulations. In *Molecular Modeling of Proteins*, Kukol, A., Ed. Springer New York: New York, NY, 2015; pp 47-71.

358. Nerenberg, P. S.; Head-Gordon, T., New developments in force fields for biomolecular simulations. *Curr Opin Struct Biol* **2018,** *49*, 129-138.

359. Hata, H.; Nishiyama, M.; Kitao, A., Molecular dynamics simulation of proteins under high pressure: Structure, function and thermodynamics. *Biochim Biophys Acta Gen Subj* **2020,** *1864* (2), 129395.

360. Magalhães, R. P.; Fernandes, H. S.; Sousa, S. F., Modelling Enzymatic Mechanisms with QM/MM Approaches: Current Status and Future Challenges. *Israel Journal of Chemistry* **2020**.

361. Lindorff-Larsen, K.; Piana, S.; Dror, R. O.; Shaw, D. E., How fast-folding proteins fold. *Science* **2011,** *334* (6055), 517-20.

362. Latorraca, N. R.; Wang, J. K.; Bauer, B.; Townshend, R. J. L.; Hollingsworth, S. A.; Olivieri, J. E.; Xu, H. E.; Sommer, M. E.; Dror, R. O., Molecular mechanism of GPCR-mediated arrestin activation. *Nature* **2018,** *557* (7705), 452-456.

363. Robustelli, P.; Stafford, K. A.; Palmer, A. G., 3rd, Interpreting protein structural dynamics from NMR chemical shifts. *J Am Chem Soc* **2012,** *134* (14), 6365-74.

364. Hantschel, O.; Superti-Furga, G., Regulation of the c-Abl and Bcr-Abl tyrosine kinases. *Nat Rev Mol Cell Biol* **2004,** *5* (1), 33-44.

365. Gluck, J. M.; Hoffmann, S.; Koenig, B. W.; Willbold, D., Single vector system for efficient N-myristoylation of recombinant proteins in E. coli. *PLoS One* **2010,** *5* (4), e10081.

366. O'Reilly, D. R.; Miller, L.; Luckow, V. A., *Baculovirus expression vectors : a laboratory manual*. Oxford University Press: 1994.

367. McWhirter, J. R.; Wang, J. Y., An actin-binding function contributes to transformation by the Bcr-Abl oncoprotein of Philadelphia chromosome-positive human leukemias. *The EMBO Journal* **1993,** *12* (4), 1533-1546.

368. Heisterkamp, N.; Voncken, J. W.; Senadheera, D.; Gonzalez-Gomez, I.; Reichert, A.; Haataja, L.; Reinikainen, A.; Pattengale, P. K.; Groffen, J., genicity of p190 Bcr/Abl F-actin-binding domain mutants. *Blood* **2000,** *96* (6), 2226-2232.

369. Preyer, M.; Vigneri, P.; Wang, J. Y., Interplay between kinase domain autophosphorylation and F-actin binding domain in regulating imatinib sensitivity and nuclear import of BCR-ABL. *PLoS One* **2011,** *6* (2), e17020.

370. Wiesner, S.; Hantschel, O.; Mackereth, C. D.; Superti-Furga, G.; Sattler, M., NMR Assignment Reveals an α-Helical Fold for the F-Actin Binding Domain of Human Bcr-Abl/c-Abl. *Journal of Biomolecular NMR* **2005,** *32* (4), 335-335.

371. Delaglio, F.; Grzesiek, S.; Vuister, G. W.; Zhu, G.; Pfeifer, J.; Bax, A., NMRPipe: a multidimensional spectral processing system based on UNIX pipes. *J Biomol NMR* **1995,** *6* (3), 277-93.

372. Lee, W.; Tonelli, M.; Markley, J. L., NMRFAM-SPARKY: enhanced software for biomolecular NMR spectroscopy. *Bioinformatics* **2015,** *31* (8), 1325-7.

373. Frauenfelder, H.; Alberding, N. A.; Ansari, A.; Braunstein, D.; Cowen, B. R.; Hong, M. K.; Iben, I. E. T.; Johnson, J. B.; Luck, S.; Marden, M. C.; Mourant, J. R.; Ormos, P.; Reinisch, L.; Scholl, R.; Schulte, A.; Shyamsunder, E.; Sorensen, L. B.; Steinbach, P. J.; Xie, A. H.; Young, R. D.; Yue, K. T., Proteins and Pressure. *J Phys Chem-Us* **1990,** *94* (3), 1024-1037.

374. Kitahara, R.; Okuno, A.; Kato, M.; Taniguchi, Y.; Yokoyama, S.; Akasaka, K., Cold denaturation of ubiquitin at high pressure. *Magn Reson Chem* **2006,** *44 Spec No*, S108-13.

375. Kremer, W.; Arnold, M.; Munte, C. E.; Hartl, R.; Erlach, M. B.; Koehler, J.; Meier, A.; Kalbitzer, H. R., Pulsed pressure perturbations, an extra dimension in NMR spectroscopy of proteins. *J Am Chem Soc* **2011,** *133* (34), 13646-51.

376. Vajpai, N.; Nisius, L.; Wiktor, M.; Grzesiek, S., High-pressure NMR reveals close similarity between cold and alcohol protein denaturation in ubiquitin. *Proc Natl Acad Sci U S A* **2013,** *110* (5), E368-76.

377. Nisius, L.; Grzesiek, S., Key stabilizing elements of protein structure identified through pressure and temperature perturbation of its hydrogen bond network. *Nat Chem* **2012,** *4* (9), 711-7.

378. Kalbitzer, H. R.; Rosnizeck, I. C.; Munte, C. E.; Narayanan, S. P.; Kropf, V.; Spoerner, M., Intrinsic allosteric inhibition of signaling proteins by targeting rare interaction states detected by high-pressure NMR spectroscopy. *Angew Chem Int Ed Engl* **2013,** *52* (52), 14242-6.

379. Munte, C. E.; Beck Erlach, M.; Kremer, W.; Koehler, J.; Kalbitzer, H. R., Distinct conformational states of the Alzheimer beta-amyloid peptide can be detected by high-pressure NMR spectroscopy. *Angew Chem Int Ed Engl* **2013,** *52* (34), 8943-7.

380. Maeno, A.; Sindhikara, D.; Hirata, F.; Otten, R.; Dahlquist, F. W.; Yokoyama, S.; Akasaka, K.; Mulder, F. A.; Kitahara, R., Cavity as a source of conformational fluctuation and high-energy state: high-pressure NMR study of a cavity-enlarged mutant of T4 lysozyme. *Biophys J* **2015,** *108* (1), 133-45.

381. Alderson, T. R.; Roche, J.; Gastall, H. Y.; Dias, D. M.; Pritisanac, I.; Ying, J.; Bax, A.; Benesch, J. L. P.; Baldwin, A. J., Local unfolding of the HSP27 monomer regulates chaperone activity. *Nat Commun* **2019,** *10* (1), 1068.

382. Abiko, L. A.; Grahl, A.; Grzesiek, S., High Pressure Shifts the beta1-Adrenergic Receptor to the Active Conformation in the Absence of G Protein. *American Chemical Society* **2019**, 16663-16670.

383. Ho, B. K.; Gruswitz, F., HOLLOW: generating accurate representations of channel and interior surfaces in molecular structures. *BMC Struct Biol* **2008,** *8*, 49.